



HAL
open science

Electronic Structure and Molecular Dynamics Applications of Carbon Nanotubes

Stefano Battaglia

► **To cite this version:**

Stefano Battaglia. Electronic Structure and Molecular Dynamics Applications of Carbon Nanotubes. Theoretical and/or physical chemistry. Université Paul Sabatier - Toulouse III; Università degli studi (Pérouse, Italie), 2018. English. NNT : 2018TOU30341 . tel-02479457

HAL Id: tel-02479457

<https://theses.hal.science/tel-02479457>

Submitted on 14 Feb 2020

HAL is a multi-disciplinary open access archive for the deposit and dissemination of scientific research documents, whether they are published or not. The documents may come from teaching and research institutions in France or abroad, or from public or private research centers.

L'archive ouverte pluridisciplinaire **HAL**, est destinée au dépôt et à la diffusion de documents scientifiques de niveau recherche, publiés ou non, émanant des établissements d'enseignement et de recherche français ou étrangers, des laboratoires publics ou privés.



THÈSE

En vue de l'obtention du **DOCTORAT DE L'UNIVERSITÉ DE TOULOUSE**

Délivré par l'Université Toulouse 3 - Paul Sabatier
Cotutelle internationale : Università degli Studi di Perugia

Présentée et soutenue par
Stefano BATTAGLIA

Le 16 octobre 2018

Applications de Structure Électronique et Dynamique Moléculaire des Nanotubes de Carbone

Ecole doctorale : **SDM - SCIENCES DE LA MATIERE - Toulouse**

Spécialité : **Physico-Chimie Théorique**

Unité de recherche :
LCPQ-IRSAMC - Laboratoire de Chimie et Physique Quantiques

Thèse dirigée par
Thierry LEININGER et Maria Noelia FAGINAS LAGO

Jury

M. Alfredo SÁNCHEZ DE MERÁS, Rapporteur
Mme Cecilia COLETTI, Examineur
M. Romuald POTEAU, Examineur
M. Roland LINDH, Examineur
M. Thierry LEININGER, Directeur de thèse
Mme Noelia FAGINAS LAGO, Co-directeur de thèse

"Consciousness is a much smaller part of our mental life than we are conscious of, because we cannot be conscious of what we are not conscious of."

Julian Jaynes

Acknowledgements

First and foremost, my acknowledgements go to my thesis supervisors, Prof. Thierry Leininger, Prof. Stefano Evangelisti and Dr. Noelia Faginas Lago, without whom I was certainly not able to carry out this PhD thesis. I deeply thank you for the freedom and trust you gave me since the beginning; I believe this has been a fundamental point that allowed me to be happy and motivated during the entire course of the thesis and develop my knowledge on theoretical chemistry and physics at incredible pace. The relationship resulted from these three years goes beyond that of merely a supervisor and I am very grateful for that.

Being this PhD part of a greater project, I cannot thank enough the coordinator of the Theoretical Chemistry and Computational Modelling (TCCM) programme, Prof. Manuel Yañez, and all other collaborators who have worked for a long time behind the scenes. The effort that made this adventure possible is immense, thank you!

La mia famiglia è sempre presente e disponibile nella mia vita, e per questo vorrei ringraziare tanto i miei genitori, Evelyne e Michele, quanto i miei fratelli Marco e Valerio. Anche se negli ultimi tre anni sono stato poco presente, ogni volta che sono tornato a casa vi ho sempre trovati con un sorriso e felici di passare del tempo insieme. Il vostro supporto ed interesse in quello che faccio, così come il vostro rispetto nelle mie scelte è molto importante per me e per questo ve ne sono grato.

Special friends remain such despite the distance, this is now a fact(!), Pitti, Tiz and Andy. Thank you very much for making our friendship a stronghold of my life, by organizing trips and adventures together, by visiting me around Europe, for the long calls discussing everyday's matter as much as serious issues. I am very happy and lucky to have found some people on whom I can always count.

A special person who deserves special acknowledgements is Oriana. Since we met we had a great time together and besides the nice moments spent going out in Toulouse, you were always available to help me with any scientific issue. On one side you changed my mind on computational chemists and on the other you proved the power of binary trees. Thank you for this and much more.

I would like to thank the people in Toulouse for making my stay in *La Ville Rose* an incredible time of my life. Particulièrement à Nico et Stan, qui n'ont pas été simplement des coloc, mais des vrais amis. On était une coloc géniale: soirées grandioses, adventures aux festivals et une vie très sportive (sous forme de tournois à fifa haha). C'était toujours un endroit vivant grâce aux nombreux amis de la coloc, lesquels je remercie aussi pour les moments passés ensemble.

The number of people at IRSAMC who deserve acknowledgement is certainly too long to go name by name, I therefore thank all of them indistinctly here. Anyhow, I cannot spare some personal thoughts for a few people. First, I would like to thank my officemates, Léa and Francesco, whom I bothered so much with basic chemistry questions and have listened so many times to my scientific problems, that is a miracle if they still do not hate me. A lot of thanks go to Patri, who was always up and available for going

out, for interesting discussions and even for being a tour guide in Madrid. I found a good friend in her. Special thanks go to Jean-Paul, always showing interest in the work I was doing and available to discuss on my preferred topic of the field, quantum chemical methods. I would also like to thank David, for the technical support provided not only while I was in Toulouse, but also during my time in Perugia as well as Martial for the many times I asked advice from him.

Di tutte le persone che ho conosciuto all'università di Perugia, vorrei specialmente ringraziare quelle del laboratorio di organica, che mi hanno accolto nella loro piccola famiglia e mi hanno permesso di boicottare la liomatic insieme a loro; un grazie particolare va a Federica e Francesco. Inoltre, per motivi più scientifici questa volta, vorrei ringraziare Prof. Fernando Pirani per il lavoro svolto insieme.

A big *thank you* goes to my friend and officemate Jelle, who also always answered to my chemistry questions with patience: I think, I might actually have developed some chemical intuition after all. Although, to be fair, I should acknowledge Jelle for much more than that. During the time spent in Perugia we developed a friendship well beyond that of science and I am very happy for that, even though you stole my shark. Special thanks also go to Maike, whose incredible positive energy was a real uplift after stressful days of work.

During these three years, I regularly met with the other students of the TCCM PhD program, whom I thank for the nice moments passed together as well as for the occasional struggles shared. More specifically, I would like to thank for “the true friendship I developed with some of them” (yes, I am quoting you Martina), namely with Jelle, Andi, Martina and Carles.

At last, as the number of people I met and interacted with during the course of the thesis is so large, I would like to thank all those people that in one way or another made this time more valuable than it would have been without them.

Abstract

Carbon nanotubes (CNTs), synthesized for the first time in 1991, have shown great promise on a wide range of areas and are a current topic of research, both on a theoretical and an experimental level. In this thesis, molecular properties of short CNTs as well as possible applications exploiting them as hosting systems were investigated by means of *ab initio* and molecular dynamics calculations.

Single units of zigzag CNTs, namely cyclacenes, were hypothesized more than 50 years ago. With the successful synthesis of CNTs, the interest in such systems and other types of carbon nanobelts considerably increased, although their experimental realization has not been achieved yet. Therefore, predicting the molecular properties, the prospective applications and possibly providing important insight for the synthesis process based on theoretical approaches is of major interest. Notwithstanding, the challenges associated to cyclacenes are not only experimental, as previous theoretical works show controversial results about the electronic structure of this system.

In this thesis, several electronic properties were derived analytically within the tight-binding approximation, providing asymptotic results at the thermodynamic limit for the total position spread tensor and the polarizability. The tight-binding trends were assessed by high level *ab initio* calculations, finding a good agreement between both approaches. One major issue related to cyclacenes is the description of the electronic configuration of their ground state. By studying a wide range of system sizes, the polyradical character of the ground state was found to increase for increasing system size, whereas the opposite trend was found for the singlet-triplet energy gap.

Polynitrogen clusters have been suggested as environmentally friendly high energy-density material due to their particular bond energetics and their decomposition pathways into molecular nitrogen. However, their stability at ambient conditions is particularly poor, making their storage a major problem. An attempt to solve this challenge and stabilize polynitrogen systems is to confine them in nanomaterials.

The encapsulation of different nitrogen clusters inside CNTs was studied by *ab initio* calculations, finding that some systems are favorably stabilized, whereas others undergo decomposition. The nature of the interaction between polynitrogen ions and CNTs was also subject of investigation, uncovering the role of electrostatic and induction effects. Based on the *ab initio* data, a novel intermolecular potential was derived and implemented in the DL POLY 4 program in order to perform molecular dynamics simulations.

Linear beryllium chains show fascinating magnetic properties due to their half-filled edge orbitals. The ground state of an isolated chain is antiferromagnetic, with an exponentially decreasing coupling as a function of the chain length. It was predicted that interaction of the chain with carbon nanomaterials can change the nature of the ground state from antiferromagnetic to ferromagnetic depending on the distance between the fragments.

As part of this thesis, a study of the chain confinement inside CNTs was carried out, providing a straightforward approach to control the strength of the interaction according to the CNT diameter. Furthermore, the geometrical constraints imposed by the cavity size prevent the chain from folding into a lower energy isomer, thus preserving the magnetic properties of the system.

Contents

Acknowledgements	v
Abstract	vii
1 Introduction	1
2 Theoretical Methods	7
2.1 Quantum Chemistry	7
2.1.1 The Schrödinger Equation	7
2.1.2 Hückel Theory	10
2.1.3 Hartree-Fock Theory	13
2.1.4 Many-Body Perturbation Theory	18
2.1.5 Coupled Cluster Theory	23
2.1.6 Multireference Methods	26
2.1.7 Density Functional Theory	31
2.1.8 Basis Sets in Quantum Chemistry	36
2.2 Molecular Dynamics	40
2.2.1 The Model System	40
2.2.2 Classical Force Fields	42
2.2.3 Newton's Equation of Motion	46
2.2.4 Statistical Thermodynamics	47
2.2.5 Molecular Dynamics Algorithm	49
3 Cyclacenes	51
3.1 Introduction	51
3.2 Analytical Tight-Binding	53
3.2.1 The Tight-Binding Energies and Orbitals	54
3.2.2 Molecular Properties of Cyclacenes	56
3.2.3 Axial Component of TPS and Polarizability	58
3.2.4 Planar Components of TPS and Polarizability	60
3.3 <i>Ab Initio</i>	63
3.3.1 Methodology	63
3.3.2 Minimal Active Space	64
3.3.3 Dynamical Active Space	69
3.4 Conclusions	79

4	Carbon Nanotubes	81
4.1	N_3^- Confinement in Carbon Nanotubes	81
4.1.1	<i>Ab Initio</i> Methodology – Part I	83
4.1.2	<i>Ab Initio</i> Interaction Energies – Part I	84
4.1.3	Charge Distribution and Interaction Nature	88
4.1.4	<i>Ab Initio</i> Methodology – Part II	90
4.1.5	<i>Ab Initio</i> Interaction Energies – Part II	92
4.1.6	Intermolecular Potential	93
4.1.7	Molecular Dynamics	102
4.2	N_5^+ and N_8 Confinement in Carbon Nanotubes	105
4.2.1	Methodology	105
4.2.2	N_5^+ Interaction Energy and Relaxation	106
4.2.3	Confinement of N_8	109
4.3	Be_n Confinement in Carbon Nanotubes	112
4.3.1	Methodology	112
4.3.2	Stability of Be_n Chains	114
4.3.3	Magnetic Coupling	115
4.4	Conclusions	118
5	General Conclusions	123
A	Appendix	149
A.1	Geometry Optimization of N_3^- in CNTs – Part II	149
A.2	Analytical Gradients	153
A.2.1	Improved Lennard-Jones Potential	153
A.2.2	Induction Potential	155
A.3	Virial	157
A.3.1	Induction Potential	157
A.4	Distributed Gaussian Orbitals for Molecular Calculations: Application to Simple Systems	159
A.5	Signatures of Wigner Localization in One-dimensional Systems	199
A.6	Front Cover Image	209
A.7	Résumé Substantiel	213
A.8	Sintesi Sostanziale	235

List of Figures

1.1	A C ₆₀ fullerene (left), a carbon nanotube (center) and graphene (right). . .	1
1.2	Graphene sheet with CNT structural parameters (left) and example of arm-chair, zigzag and chiral nanotubes (right).	2
1.3	Cycloparaphenylene (left), a carbon nanobelt (center) and a cyclacene (right).	4
2.1	The CASSCF orbital spaces.	29
2.2	Model system example in a two-dimensional square box with periodic boundary conditions. Red discs represent the position of the particles, black arrows their velocity vector. As can be seen, the central highlighted box is replicated in both dimensions.	41
2.3	Example of the Lennard-Jones potential. All values are in arbitrary units. .	44
2.4	Example depicting the concept of cutoff radius and minimum image convention.	46
3.1	Wrapping of a linear octacene into an [8]cyclacene.	51
3.2	Simplified scheme of a cyclacene.	54
3.3	Scheme of the unit cell μ of the cyclacene with attached basis functions. . .	54
3.4	Energy bands (in t units) at Hückel level of theory for $a = 0$ and $t = 1$. . .	55
3.5	Nonvanishing integrals (left) and squared integrals (right) in b and b^2 units, respectively, contributing to the axial component of the TPS.	58
3.6	$1 \rightarrow 4$ (left) and $2 \rightarrow 3$ (right) contribution to α_{zz} in $\frac{b^2}{t}$ units.	60
3.7	Squared integral in b^2 units contributing to the planar components of the TPS.	61
3.8	Planar component of the per-electron TPS (left) and per-electron polarizability (right) in b^2 units and $\frac{b^2}{t}$, respectively.	62
3.9	Symmetric (left) and antisymmetric (right) MOs constituting the HOMO–LUMO pair for a [12]cyclacene. Hydrogen atoms are omitted.	64
3.10	Two-electron integrals as a function of the system size n	67
3.11	One-electron integrals as a function of the system size n	67
3.12	Hückel energy bands in t units for a [6]cyclacene (left) and for a [16]cyclacene (right). Note that the points at $k\theta = 2\pi$ are the same as those at $k\theta = 0$ because of periodic boundary conditions.	70
3.13	Symmetric (left) and antisymmetric (right) MO associated to the energies $\varepsilon_1(k\theta = \pi)$ and $\varepsilon_4(k\theta = \pi)$ for a [12]cyclacene. Hydrogen atoms are omitted.	70

3.14	Hückel energy bands in t units for a [6]cyclacene (left) and for a [16]cyclacene (right).	71
3.15	CASSCF(k, k) singlet–triplet energy gaps calculated with the ANO-DZ (green squares) and the ANO-DZP (red circles) basis sets as a function of n	72
3.16	CASSCF NOONs. Note that all unique π orbitals are plotted, including those not included in the ASs.	76
3.17	Effective number of unpaired electrons with respect to the system size. . .	77
3.18	The total axial component of the TPS computed with the CASSCF wave function.	78
4.1	Side (a) and front (b) view of the geometry used for the unrelaxed interaction energy calculations.	84
4.2	Unrelaxed interaction energies as a function of the nanotube diameter. . .	85
4.3	Starting orientations of the confined N_3^- ion. In the last two cases (e) and (f), N_3^- is closer to the edge of the CNT, while in the other cases is at the midpoint.	86
4.4	Starting (a) and final (b) position of the N_3^- ion inside the the (5,5)CNT. .	86
4.5	Relaxed geometry of N_3^- inside a CNT(6,6).	87
4.6	Relaxed interaction energies as a function of the CNT diameter.	87
4.7	Partial atomic charges of the isolated (a) N_3^- fragment and confined (b) inside a CNT(5,5).	88
4.8	Molecular electrostatic potential of the unperturbed (5,5) CNT (a) and perturbed (b) by the presence of the azide ion. The isosurface value was set to 0.02. The energy scale is given in kcal/mol.	89
4.9	Interaction energy as a function of tube length. The solid lines are fits to the RI-SCS-MP2/cc-pVDZ and the approximate DLPNO-CCSD(T)/cc-pVTZ points.	92
4.10	Comparison of classical and quantum-chemical interaction energies for $\beta = 8$	97
4.11	Individual potential contributions to the interaction energy.	98
4.12	Scheme showing the three different ways in which the azide was moved to generate the energy profiles.	99
4.13	Potential energy profiles for (5,5), (7,7) and (9,9) CNTs from top to bottom. The dashed vertical lines show the position of the nanotube wall. . .	100
4.14	Potential energy profiles for (5,5), (7,7) and (9,9) CNTs from top to bottom. The dashed vertical lines show the position of the nanotube openings. .	101
4.15	Potential energy profiles for (5,5), (7,7) and (9,9) CNTs from top to bottom. .	102
4.16	Adsorption energy of the azide anion inside different carbon nanotubes. .	104
4.17	Unrelaxed interaction energies as a function of the CNT diameter.	106
4.18	Relative energies with respect to step zero during the relaxation process. Geometries at steps 7, 11 and 26 are depicted along the curve without the surrounding nanotube for better representation.	107

4.19	Final structure of $N_5^+@CNT(4,4)$	107
4.20	Partial atomic charges of the isolated N_5^+ cation.	107
4.21	Partial atomic charges of the N_5^+ cation confined inside the cavity of a (5,5) CNT.	108
4.22	Partial atomic charges of the decomposed fragments after relaxation inside the cavity of a (5,5) CNT.	108
4.23	EEE conformation (1) and EZE conformation (2) of N_8	109
4.24	Potential energy surface showing the N_8 decomposition pathways in gas phase. Molecules and numbers depicted correspond to the EZE conformer, while the values in parenthesis refer to the EEE conformer.	110
4.25	Transition state structures of the decomposition reactions in gas phase for the EEE conformer (1a and 1b) and the EZE conformer (2a and 2b).	110
4.26	Edge molecular orbitals included in the active space.	113
4.27	Front and side view of a Be_5 chain inside a $CNT(5,5)$	115
A.1	Bond (left), hollow (center) and zigzag (right) starting sites.	149
A.2	Central starting geometry.	150
A.3	Geometrical parameters.	150

List of Tables

2.1	Most common statistical ensembles.	48
3.1	ΔE_{ST} , NOONs of π_+ and π_- and configuration weights C_+ and C_- of the ground state CASSCF(2,2) wave function.	65
3.2	ΔE_{ST} , NOONs of π_+ and π_- and configuration weights C_+ and C_- of the CASCI(2,2) wave function using the orbitals obtained from CASSCF calculations with larger ASs. Note that the first column labeled (2,2) corresponds to full CASSCF(2,2) calculations.	68
3.3	Two-electron integral for [8]cyclacene and [20]cyclacene and one-electron integral gap δ . All values are given in eV.	69
3.4	Active space sizes resulting from the selection scheme.	71
3.5	ΔE_{ST} , NOONs of π_+ and π_- and configuration weights C_+ and C_- of the 1A_g ground state CASSCF(k,k) wave function.	71
3.6	Predicted singlet–triplet energy gap by the NEVPT2 and CASPT2 methods.	73
3.7	Effect of the active space size on the CASSCF energy gap for a [10]cyclacene and a [16]cyclacene using the ANO-DZP basis. All values are given in eV.	75
3.8	Effect of the basis set on the CASSCF(k,k) gap for [8]cyclacene and for [20]cyclacene.	75
3.9	Axial and longitudinal components of the polarizability (in au) computed with the CASSCF method. The last column lists the NOONs of the HOMO–LUMO pair.	78
4.1	Potential parameters for carbon and carbon–hydrogen interactions. Polarizability given in \AA^3 , energies in meV and distance in \AA	96
4.2	Potential parameters for hydrogen and hydrogen–nitrogen interactions. Polarizability given in \AA^3 , energies in meV and distance in \AA	96
4.3	<i>Ab initio</i> and classical interaction energies and their difference. All energies are given in kcal/mol, Λ represents the number of units in the nanotube.	98
4.4	Be_n bond lengths in \AA obtained at NEVPT2/cc-pVTZ level of theory.	113
4.5	Structural parameters of the CNTs used in this work.	113
4.6	Summary of electronic energy (with and without zero-point vibrational energy correction), enthalpy and free energy differences between the linear and the cluster geometries. All values are given in kcal/mol.	114
4.7	CASSCF magnetic coupling J for different CNT diameters and chain lengths. All values are given in meV.	116

4.8	NEVPT2 magnetic coupling J for different CNT diameters and chain lengths. All values are given in meV.	116
4.9	Magnetic coupling J for different CNT diameters and chain lengths obtained with a larger (6,6) active space. All values are given in meV.	117
4.10	Magnetic coupling J for Be ₅ confined in longer CNTs. All values are given in meV.	117
A.1	Conformational parameters and interaction energy differences with respect to the (c) geometry. Distances are given in Å, angles in degrees and energies in kcal/mol.	151

Acronyms

QM quantum mechanics

QC quantum chemistry

TISE time-independent Schrödinger equation

au atomic units

BO Born-Oppenheimer

HMO Hückel molecular orbital

MO molecular orbital

LCAO linear combination of atomic orbitals

AO atomic orbital

HF Hartree-Fock

SD Slater determinant

SCF self-consistent field

RHF restricted Hartree-Fock

UHF unrestricted Hartree-Fock

MBPT many-body perturbation theory

MPPT Møller-Plesset perturbation theory

MP2 second order Møller-Plesset

CC coupled cluster

CCD coupled cluster doubles

CCSD coupled cluster singles and doubles

CCSD(T) coupled cluster singles doubles and parenthesis triples

CCSDT coupled cluster singles doubles and triples

DLPNO-CCSD(T) domain based local pair natural orbital CCSD(T)

CASSCF complete active space self-consistent field

CSF configuration state function

CI configuration interaction

FCI full configuration interaction

CISD configuration interaction singles and doubles

CISDT configuration interaction singles doubles and triples

CASCI complete active space configuration interaction

AS active space

MRPT multireference perturbation theory

NEVPT2 second order n -electron valence perturbation theory

DFT density functional theory

HK Hohenberg-Kohn

KS Kohn-Sham

LDA local density approximation

GGA generalized gradient approximation

GTO Gaussian type orbital

STO Slater type orbital

SZ single zeta

DZ double zeta

TZ triple zeta

CBS complete basis set

BSSE basis set superposition error

MD molecular dynamics

MC Monte Carlo

PBC periodic boundary conditions

OBC open boundary conditions

VdW Van der Waals

LJ Lennard-Jones

ILJ Improved Lennard-Jones

CNT carbon nanotube

TAO-DFT thermally-assisted-occupation DFT

TPS total position spread

LT localization tensor

ANO atomic natural orbital

HOMO highest occupied molecular orbital

LUMO lowest unoccupied molecular orbital

NOON natural orbital occupation number

CASPT2 second order complete active space perturbation theory

MRMP2 second order multireference Møller-Plesset

PNC polynitrogen compound

HEDM high energy-density material

AIMD *ab initio* molecular dynamics

NBO natural bond orbital

NPA natural population analysis

MEP molecular electrostatic potential

FF force field

RI-SCS-MP2 density-fitted spin-component-scaled MP2

EA electron affinity

IP ionization potential

1 Introduction

The last twenty five years of carbon chemistry have been full of surprises, from only two known carbon allotropes, diamond and graphite, and the belief to have a very deep knowledge in the basic element of life, the incredible discovery of three new forms of pure carbon gave substantially rise to a completely new field of research in chemistry and physics.

It is in 1985, that researchers at Rice University in collaboration with the University of Sussex detected a clear signal of a molecule composed by 60 carbon atoms only: the 0-dimensional *Buckminsterfullerene*, or simply *fullerene*, was identified for the first time¹. It took only 6 years to enlarge another time the family of carbon allotropes, when in 1991, 1-dimensional *carbon nanotubes* (CNTs) were obtained and undisputably recognized from electron microscopy images by Iijima². At last, in 2004 the circle was closed with the first synthesis of *graphene*³, which is essentially a 2-dimensional, one-atom thick sheet of graphite. A picture of these three new types of carbon structures is shown in Figure 1.1. The exciting properties of these low-dimensional carbon materials have generated an incredible wave of new research in the field, and has become a stronghold of the European research panorama⁴ set to revolutionize multiple industries.

In this PhD thesis, carbon nanotubes were the central subject of study, for which several theoretical investigations were carried out, envisioning different potential applications.

After the first successful synthesis of carbon nanotubes in 1991, research on these promising systems took off quite rapidly. In the original paper by Iijima², only *multi-wall* CNTs were observed, i.e. nanotubes made by several layers of graphene wrapped around concentrically. However, only two years later the first nanotubes composed by a single rolled up sheet of carbon atoms, namely *single-wall* CNTs, were experimentally obtained by the same group of researchers⁵. Actually, the latter started to be subject of theoretical investigations before they were synthesized in 1993, and the notation used

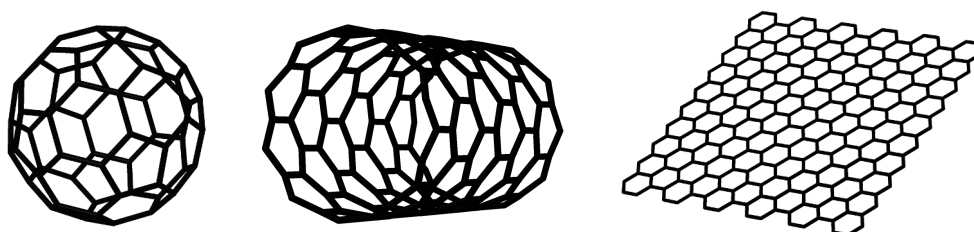


FIGURE 1.1: A C_{60} fullerene (left), a carbon nanotube (center) and graphene (right).

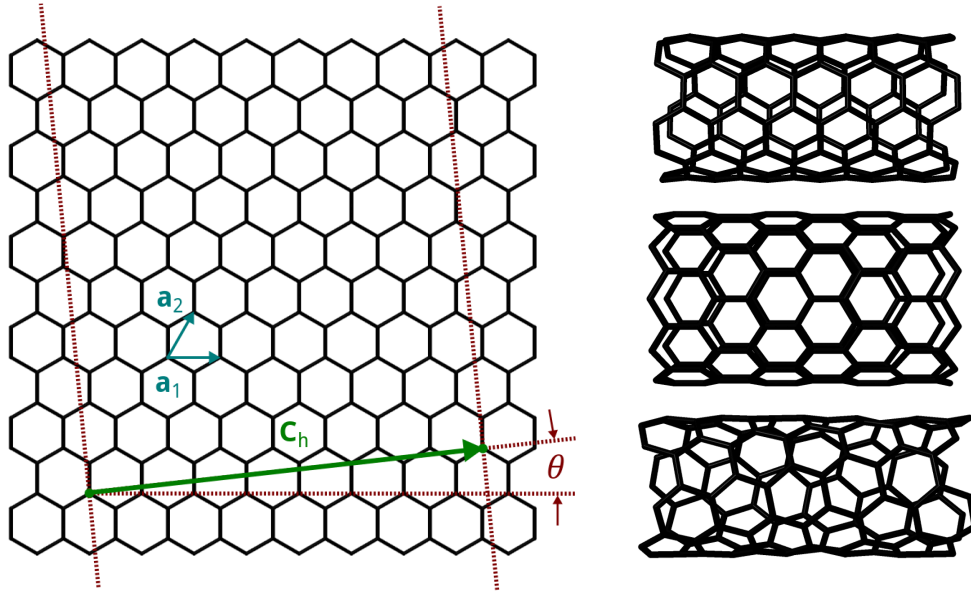


FIGURE 1.2: Graphene sheet with CNT structural parameters (left) and example of armchair, zigzag and chiral nanotubes (right).

today to differentiate the possible types of nanotubes comes from the pioneering work of Saito et al.⁶. Since a single-wall CNT essentially consists of a rolled up graphene layer, but the edges of such layer are different, there are several ways to fold it and connect the edges, giving rise to three classes (or *helicities*): *armchair*, *zigzag* and *chiral*. Formally, in the definition introduced by Saito et al.⁶, the *chiral vector*

$$\mathbf{c}_h = n\mathbf{a}_1 + m\mathbf{a}_2 \equiv (n, m) \quad (1.1)$$

completely characterizes the nanotube, where n and m are integer numbers and $n \geq m \geq 0$, while \mathbf{a}_1 and \mathbf{a}_2 represent the unit vectors of graphene. Depending on the values of n and m , the nanotube falls in one of the three classes just mentioned: armchair for $n = m$, zigzag for $n \neq 0$ and $m = 0$ and chiral for $n \neq m \neq 0$. An image depicting the graphene layer along with these structural parameters is reported in Figure 1.2, where we also note that the chiral angle θ uniquely defines the helicity as well.

The geometry of (infinitely long) defect-free carbon nanotubes¹ is uniquely defined by the chiral vector \mathbf{c}_h ⁶⁻⁸. This has allowed the precise experimental characterization of CNTs and their relationship to the observed properties. On the other hand, a particularly challenging parameter to obtain experimentally has been the sp^2 hybridized carbon-carbon bond length a_{CC} due to the curvature of the nanotube. Therefore, throughout the literature of the early days, either speculative estimates or the experimental value for graphite was used. The accurate structural investigation of carbon nanotubes has been therefore a topic in the domain of theoreticians ever since, who studied it extensively⁹⁻²⁰. In general, CNTs can be modeled in two ways, either by applying periodic boundary

¹From now on we will always use the general term carbon nanotube to refer to single-wall CNTs only.

conditions (PBC) and considering it as an infinitely long system or by open boundary conditions (OBC) and saturating the dangling carbon atoms with hydrogens in order to fill the valence shell. In the former case, there cannot be more than three symmetry-different carbon–carbon bonds, whereas in the latter, finite-size effects are important and both very short and long bond lengths are observed at the edges. These effects on, but not limited to, the geometry were subject to several investigations^{14–18,20} and are known to generate a specific pattern in the carbon–carbon bonding network, whose average bond length tends to that of an infinitely long nanotube. The value of a_{CC} is also clearly dependent on the curvature of the nanotube and hence by its diameter. For an infinitely large CNT, the bond length has to be the same as that of graphene, a value which is approached from above since the effect of curvature is to stretch the bonds¹².

One of the exceptional characteristics of CNTs is the dependence of their electronic properties to their helicity. In pioneering works^{6,21,22} based on tight-binding Hamiltonians and density functional theory (DFT) it was found that CNTs with indices satisfying the relation

$$2n + m = 3q \quad (1.2)$$

where q is an integer number, have populated energy bands at the Fermi level, thus showing a metallic behavior. In practice, this means that all armchair as well as zigzag nanotubes where n is a multiple of 3 are metallic. Systems for which Equation (1.2) is not satisfied have a gap at the Fermi level which is dependent on the diameter, making them semi-conductors.

Experimentally, although the electronic properties of CNTs were probed early on^{23–27}, it was only in 1998 that their relationship with the helicity was proven by spectroscopy and scanning tunneling microscopy^{7,28}. Due to their nanoscale dimension and their electronic properties, carbon nanotubes are a promising material for a number of applications in electronics, e.g. they can be used as transistors, allowing to shrink the size below the limit imposed today by silicon²⁹. On the other hand, due to their ballistic conductance and capability to withstand large current densities, they can be employed as molecular interconnects, for instance outperforming copper for nanometer-sized junctions²⁹.

In order to push forward the actual development of new technologies based on carbon nanotubes, their synthesis, purification and sorting play a fundamental role. The first CNTs were synthesized by arc-discharge methods and were mostly of the multi-wall type², despite the early theoretical studies being focused on the simpler single-wall class^{6,21,22}. However, the synthesis of the latter was achieved already in 1993, where it was found that instead of growing on the carbon cathode, they were forming in the gas phase⁵. Since then, other approaches were developed allowing for a more effective synthesis, in particular chemical vapor deposition which is now usually preferred over arc-discharge and laser ablation techniques, since the low temperature of the former method permits a finer control over the type of nanotubes fabricated^{29–31}. Yet, nanotube synthesis is still the major challenge despite the big steps forward achieved in this domain, as demonstrated by the large number of recent reviews^{32–35}. Most importantly,

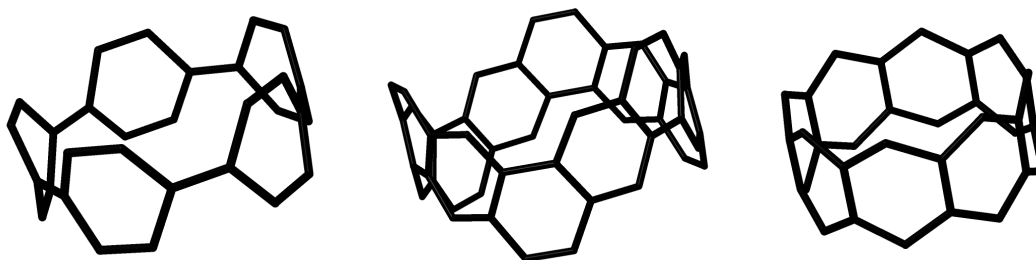


FIGURE 1.3: Cycloparaphenylene (left), a carbon nanobelt (center) and a cyclacene (right).

considering the direct relation between chirality and properties, the ability to produce chirality-defined nanotubes is essential for many types of applications, even more so given that a-posteriori sorting procedures can introduce defects in the structures and alter their properties. A promising approach becoming increasingly viable, is to use carbon caps precursors on which the nanotube can grow or carbon *nanorings* and *nanobelts* as template to initiate the CNT synthesis of a well-defined chirality^{33,34,36–39}. An advantage of such a bottom-up fabrication technique is that also the final length of the nanotube can be relatively well controlled. This synthetic route was made possible essentially by the great research effort put into the templating units, the carbon macrocycles, which are generally very challenging to obtain and an active field of research as well^{40–43}. For instance, it was only in 2008 that cycloparaphenylene, the basic carbon nanoring unit of an armchair nanotube, was experimentally obtained⁴⁴ (Figure 1.3 left), and in 2017, the first nanobelt composed by fully-fused edge-sharing benzene rings⁴⁵ (Figure 1.3 center). Whereas cyclacenes, the basic unit of zigzag nanotubes, still remain a theoretical structure only⁴⁶ (Figure 1.3 right). It is therefore clear how theory plays an important role here, the insight gained by the study of these systems *in silico* can provide crucial information for their experimental discovery.

Depending on the synthetic approach, carbon nanotubes are either terminated by end caps at the extremities, essentially half fullerenes, or are left open, likely saturated by hydrogen atoms. From a theoretical perspective on the other hand, CNTs can be modeled either by a crystal or a cluster approach. In the former case, a unit cell of desired size is defined, which is then repeated periodically along the direction of the principal axis, modeling the nanotube as an infinite system. This approach is for most purposes, but in particular to study the material-like properties of carbon nanotubes, the preferred one. On the other hand, if edge effects, short systems or insertion and extraction processes from the cavity are the subject of investigation, the cluster approach should be used. From the methodological point of view, the implications of this choice are important, especially in regards to the electronic structure^{15,25,47–53}. In the cluster approach, the electronic structure might be substantially different from the crystal case, for instance all armchair nanotubes show a metallic behavior in the latter case, but for short finite nanotubes the HOMO–LUMO gap is finite and their ground state is a closed-shell singlet.

This clearly suggests that certain properties are affected by the length of the nanotube and that a *critical* length must exist, such that a transition from the nanostructure to the thermodynamic regime occurs. In the last 20 years the finite-size effects were studied for a number of properties, e.g. structural^{14,16,18,20,54}, optical^{20,49,55,56}, aromatic^{14,17,18,57} and electronic^{15,16,54,58–63}. The most limiting issue for finite-size models has been the choice of methodology. On one side, computationally expensive approaches are required in order to obtain accurate values, but on the other hand, by investigating the dependence of the properties with respect to the CNT length, an expensive methodology is typically not affordable in practice. Nevertheless, with the increasing computational power at our disposal and the development of reduced-scaling techniques, this problem is slowly fading away.

In the early days, the first carbon nanotubes to be produced by the arc-discharge method were in general capped at both ends. Considering the hollow structure of these systems, it did not take long for experimentalists to find a way to open and fill them^{64,65}. Anyhow, the potential of CNTs in host-guest chemistry is obvious⁶⁶. Since then, a lot of work has been carried out in this direction, both experimentally and theoretically, and CNTs were used to host a large variety of systems, among others fullerenes and related molecules^{67,68}, metals^{69–77}, energetic compounds^{78–81}, and many more.

The encapsulation of molecular systems inside nanotubes can alter the chemical properties of the confined species or give rise to new phases of materials, leading to surprising results. Most notably, new phases of water confined in carbon nanotubes were predicted and experimentally observed almost 20 years ago^{82,83}, but are still investigated these days, resulting in new exciting discoveries⁸⁴.

Considering the one-dimensional structure of nanotubes, ideal candidates for confinement are linear molecules, nanowires and alike. For instance, experimental evidence of linear polyyne chains encaged in single-wall CNTs was reported some 10 years ago⁸⁵, while very recently the polymerization of white phosphorus was observed to take place inside the cavity by transmission electron microscopy⁸⁶. The latter results is illustrative for two remarkable properties of nanotubes: on one side their action as “nanoreactors” favors the formation of new compounds inside the cavity and on the other side their application as a device preventing the enclosed substances to react, decompose or fold.

In the last few pages we illustrated several properties and applications of carbon nanotubes which are relevant to the work carried out in this thesis, but we shall stop here and not dwell into a full-fledged review of CNTs applications as this would go beyond the scope of this introduction.

The structure of this manuscript is the following. In chapter 2, a long theoretical section goes over the quantum chemical methods which were used at least once in the calculations carried out during this thesis, whereas a second shorter section introduces the basics of molecular dynamics. In chapter 3, the results obtained in the investigation of [*n*]cyclacenes are reported and discussed. In chapter 4, several studies involving molecular confinement inside carbon nanotubes are presented. Different sections report results

of different systems, as well as the details regarding the methodological development carried out in this context. Despite the presence of specific conclusions at the end of chapters 3 and 4, general conclusions for this entire PhD thesis are drawn in chapter 5. Finally, supplementary material to the results presented in chapter 4 can be found in the appendix, as well as additional publications achieved during these 3 years which were not directly connected to the main topic of the thesis.

2 Theoretical Methods

In this chapter we shall briefly review the theoretical background of all the methods used throughout this PhD thesis. In particular, we shall particularly focus on quantum chemical approaches, as these were used extensively in the majority of the investigations carried out. Nevertheless, a section completely dedicated to molecular dynamics is also present, as part of the research work was the development and implementation of a new classical force field.

The following sections are not an in-depth review of the methodologies, and are only meant to give the reader the general idea of the methods and their working principles and equations. The material presented here is based on different books⁸⁷⁻⁹², so that the reader can always refer to any of them if certain parts are unclear or more details are desired.

2.1 Quantum Chemistry

With the advent of *quantum mechanics* (QM) at the beginning of the 20th century, chemistry has undergone an incredible revolution thanks to a deeper understanding of the physics governing the behavior of particles at the (sub-)atomic scale. The application of quantum mechanical laws and principles to atoms and molecules led to the birth of a new branch in theoretical chemistry, named *quantum chemistry* (QC). At its core, there is one fundamental equation describing the behavior of any molecular system, the *Schrödinger equation*, whose solution provides a mean to interpret, understand and predict virtually any property of the system and their evolution in time.

2.1.1 The Schrödinger Equation

The non-relativistic *time-dependent Schrödinger equation*, proposed by Austrian physicist Erwin Schrödinger in 1926, is given by

$$i\hbar\frac{\partial}{\partial t}\Psi_{td}(\mathbf{q},t) = \hat{H}\Psi_{td}(\mathbf{q},t) \quad (2.1)$$

where i is the imaginary unit, \hbar is Planck's constant divided by 2π , t refers to time while \mathbf{q} is a compound variable containing the position of all particles in the system. The *wave function* Ψ_{td} depends both on time and position of the particles and \hat{H} is the Hamiltonian operator, or simply *Hamiltonian*.

As long as static properties of a system are concerned, there exists a simpler, time-independent version of Equation (2.1), which is sufficient for many applications of QM to chemistry.

The non-relativistic *time-independent Schrödinger equation (TISE)* has the form

$$\hat{H}\Psi_{mol}(\mathbf{q}) = E\Psi_{mol}(\mathbf{q}) \quad (2.2)$$

where E is a scalar value representing the energy associated to the wave function $\Psi_{mol}(\mathbf{q})$, which depends on positions only¹. Despite the compactness of Equation (2.2), its exact solution is known only for a handful of systems, often of little practical interest.

The complexity of Equation (2.2) resides in the Hamiltonian \hat{H} , which depends on the system and contains all the information about the type of interactions occurring within it. In the absence of external fields, the Hamiltonian for a molecular system (in atomic units (au))² is given by

$$\begin{aligned} \hat{H} &= -\sum_{I=1}^{N_n} \frac{1}{2M_I} \nabla_I^2 - \sum_{i=1}^{N_e} \frac{1}{2} \nabla_i^2 - \sum_{i=1}^{N_e} \sum_{I=1}^{N_n} \frac{Z_I}{r_{iI}} + \sum_{i=1}^{N_e} \sum_{j>i}^{N_e} \frac{1}{r_{ij}} + \sum_{I=1}^{N_n} \sum_{J>I}^{N_n} \frac{Z_I Z_J}{r_{IJ}} \\ &= \hat{T}_n + \hat{T}_e + \hat{V}_{ne} + \hat{V}_{ee} + \hat{V}_{nn} \end{aligned} \quad (2.3)$$

Uppercase indices refer to nuclei, while lowercase ones to electrons, and N_n and N_e denote the total number of nuclei and electrons, respectively. M_I is the ratio between the mass of nucleus I and the mass of one electron, whereas the scalar value Z_I represents its atomic number, i.e. its charge in au. The variables r_{iI} , r_{ij} and r_{IJ} correspond to distances between electron i and nucleus I , electrons i and j , and nuclei I and J , respectively.

The first two terms of Equation (2.3), \hat{T}_n and \hat{T}_e , account for the total kinetic energy of the nuclei and the electrons, respectively, while the term \hat{V}_{ne} describes the electron–nuclear Coulomb attraction. The fourth term, \hat{V}_{ee} , is the Coulomb repulsion between the electrons and the fifth one, \hat{V}_{nn} , between the nuclei. The wave function $\Psi_{mol}(\mathbf{q})$ appearing in Equation (2.2) explicitly depends on both the nuclear and electronic coordinates and in order to distinguish between them, we introduce the notation

$$\Psi_{mol}(\mathbf{q}) = \Psi_{mol}(\mathbf{r}, \mathbf{R}) \quad (2.4)$$

where \mathbf{r} denotes the position of all electron whereas \mathbf{R} that of all nuclei.

By realizing that nuclei are much heavier than electrons, and that electrons move considerably faster than nuclei, the latter can, in good approximation, be considered fixed while the electrons are orbiting around them. This assumption allows the molecular wave function to be decoupled into electronic and nuclear parts, where the former depends explicitly on \mathbf{r} and parametrically on \mathbf{R} , while the latter on \mathbf{R} only. This approximation is central to modern quantum chemistry and is called the *Born-Oppenheimer (BO) approximation*³.

The molecular wave function $\psi_n(\mathbf{r}, \mathbf{R})$ is thus expressed within the BO approximation as

$$\Psi_{mol}(\mathbf{r}, \mathbf{R}) = \Psi_{el}(\mathbf{r}; \mathbf{R})\Psi_{nuc}(\mathbf{R}) \quad (2.5)$$

¹Equation (2.2) is derived from Equation (2.1) by assuming a time-independent \hat{H} and restricting the solutions to a separable ansatz of the form $\Psi_{td}(\mathbf{q}, t) = f(t)\Psi_{mol}(\mathbf{q})$.

²The use of au is standard in QC and it will be assumed from now on for the rest of this chapter.

³The BO approximation is not always valid, but its breakdown will not be discussed here.

where the semicolon appearing in Ψ_{el} highlights the parametric dependence on the nuclear coordinates \mathbf{R} . Within this framework, since the nuclei are considered to be fixed, their kinetic energy can be neglected altogether, resulting in the *electronic Schrödinger equation*

$$(\hat{H}_{el} + \hat{V}_{nn})\Psi_{el}(\mathbf{r}; \mathbf{R}) = E_{el}\Psi_{el}(\mathbf{r}; \mathbf{R}) \quad (2.6)$$

where \hat{V}_{nn} is the same as in Equation (2.3) and the *electronic Hamiltonian* \hat{H}_{el} is given by

$$\begin{aligned} \hat{H}_{el} &= \hat{T}_e + \hat{V}_{ne} + \hat{V}_{ee} \\ &= \sum_{i=1}^{N_e} \hat{t}_e(i) + \sum_{i=1}^{N_e} \hat{v}_{ne}(i) + \sum_{i=1}^{N_e} \sum_{j>i}^{N_e} \hat{v}_{ee}(i, j) \\ &= \sum_{i=1}^{N_e} \hat{h}(i) + \sum_{i=1}^{N_e} \sum_{j>i}^{N_e} \hat{v}_{ee}(i, j) \end{aligned} \quad (2.7)$$

where the terms on the right-hand side of the first line are the same as in Equation (2.3). Note that because it is a multiplicative operator, the nuclear–nuclear repulsion term \hat{V}_{nn} still appears in Equation (2.6) even though Ψ_{el} does not explicitly depend on the nuclear positions. However, as the nuclear coordinates are fixed, \hat{V}_{nn} is a constant term which only shifts the electronic energy.

In Equation (2.7) we have introduced the shorthand notation for the mono-electronic operator $\hat{h}(i)$ which is the sum of the kinetic energy operator $\hat{t}_e(i)$ of electron i and the nuclear attraction operator $\hat{v}_{ne}(i)$ of electron i and all nuclei. Similarly, the bi-electronic operator $\hat{v}_{ee}(i, j)$ is a short-hand notation for the electron–electron repulsion between the pair of electrons (i, j) .

In practice, solving the electronic Schrödinger equation is a formidable task and much of the effort of the last century has been put into the development of numerical methods seeking approximate solutions to Equation (2.6).

In the following subsections, some of these methods are presented, in particular those that have been employed during the course of this PhD thesis. The discussion will not be limited to numerical approaches used to solve Equation (2.6) only, but will also show further possible approximations of the electronic Hamiltonian given in Equation (2.7), such that its solution becomes more tractable.

As from now on we are only concerned with the electronic problem, we shall introduce a slight change in notation, by noting that in principles there is an infinite number of solutions to Equation (2.6), such that

$$\hat{H}_{el}\Psi_i(\mathbf{r}; \mathbf{R}) = E_i\Psi_i(\mathbf{r}; \mathbf{R}) \quad (2.8)$$

where the integer subscript i denotes the particular electronic state of interest, e.g. $i = 0$ refers to the electronic ground state.

2.1.2 Hückel Theory

Hückel molecular orbital (HMO) theory, developed in the 1930s, is a semi-empirical approach used to study, in first approximation, π -conjugated systems; usually hydrocarbons. Within the HMO method, the electronic Hamiltonian of Equation (2.7) is approximated by effective one-electron operators which treat the complicated electron-electron repulsion in average way, providing qualitative insight on the electronic structure of the system.

Given a π -conjugated molecular system composed by n electrons, the basic assumption is that σ and π electrons do not interact with each other and can be thus treated separately, such that the total energy of the system E_{tot} is given by⁴

$$E_{tot} = E_{\sigma} + E_{\pi} \quad (2.9)$$

It follows directly that

$$\Psi(1, 2, \dots, n) = \Psi_{\pi}(1, 2, \dots, k) \Psi_{\sigma}(k + 1, \dots, n) \quad (2.10)$$

and

$$\hat{H}(1, 2, \dots, n) = \hat{H}_{\pi}(1, 2, \dots, k) + \hat{H}_{\sigma}(k + 1, \dots, n) \quad (2.11)$$

where the arguments $1, \dots, n$ refer to electron coordinates. Note that for this entire section on Hückel theory we assume that all wave function products, either between one-electron or many-electron functions, are properly normalized and antisymmetrized. The explicit form of \hat{H}_{π} is

$$\hat{H}_{\pi}(1, \dots, k) = \sum_{i=1}^k \hat{t}_e(i) + \sum_{i=1}^k \hat{v}_{ne}(i) + \sum_{i=1}^k \sum_{j>i}^k \hat{v}_{ee}(i, j) \quad (2.12)$$

where all the terms are the same as introduced above in Equation (2.7). The two-electron operator \hat{v}_{ee} which makes the Hamiltonian complicated is still present in Equation (2.12). However, the starting assumption of Hückel theory is that \hat{H}_{π} can be approximated by a sum of effective one-electron operators that take into account the action of \hat{v}_{ee} in an average way and such that the resulting wave function Ψ_{π} is represented by a product of one-electron functions. Thus, we have

$$\hat{H}_{\pi}(1, \dots, k) = \hat{H}_{\pi}(1) + \dots + \hat{H}_{\pi}(k) \quad (2.13)$$

$$\Psi_{\pi}(1, \dots, k) = \phi_1(1) \phi_2(2) \dots \phi_k(k) \quad (2.14)$$

where the functions $\phi_i(i)$ appearing on the right-hand side of Equation (2.14) are called *molecular orbitals (MOs)*. The one-electron structure of Equation (2.13) implies that the total π energy is given by a sum of one-electron energies, i.e.

$$E_{\pi} = E_{\pi,1} + E_{\pi,2} + \dots + E_{\pi,k} \quad (2.15)$$

⁴Note that $E_{tot} = E_{el} + V_{nn}$, but since V_{nn} is just a constant it can be added at the end of the calculation, so that here we can focus on the total electronic part E_{el} only.

where the TISE still holds for the π subsystem

$$\hat{H}_\pi \psi_\pi = E_\pi \psi_\pi \quad (2.16)$$

The crudest assumption in HMO theory is that the electrons are treated independently from one another, although this is clearly not true in reality. The correlation between them is accounted for by the effective one-electron operators appearing in $\hat{H}_\pi(i)$, through the introduction of empirical parameters.

In order to describe the one-electron functions in Equation (2.14), HMO theory introduces an important concept which is used throughout modern electronic structure theory: the *linear combination of atomic orbitals (LCAO)* approach. A molecular orbital $\phi_i(\vec{r})$ (note how when discussing the general form of one-electron functions we drop the explicit index notation labeling electron i)⁵ is expressed as a linear combination of a finite set of basis functions $\{\chi_\mu(\vec{r})\}$, which are centered on each atomic nucleus and are called *atomic orbitals (AOs)*. In this way we have

$$\phi_i(\vec{r}) = \sum_{\mu=1}^M c_{i\mu} \chi_\mu(\vec{r}) \quad (2.17)$$

where M is the size of the basis set and the coefficients $c_{i\mu}$ become the unknowns of the problem to be determined. Within the Hückel method, the basis set comprises AOs contributing to the π system only, thus the size M of the basis is equal the number of atoms with a p orbital involved in the π electron cloud. As mentioned in the introduction of this subsection, HMO theory is usually applied for hydrocarbon systems, thus M is commonly equal to the number of carbon atoms in the molecule, whereas hydrogens are completely neglected. Note how the introduction of a finite basis reduced the problem from an infinite-dimensional case to a finite-dimensional one that we can treat in practice. Consider now Equation (2.16), and plug in Equations (2.13) to (2.15), such that we obtain a series of one-electron equations of the form

$$\hat{H}_\pi(i) \phi_i(i) = E_{\pi,i} \phi_i(i), \quad i = 1, 2, \dots, N \quad (2.18)$$

By rearranging this last expression and introducing the expansion of Equation (2.17) for a single electron i , we obtain

$$\sum_{\nu=1}^M [\hat{H}_\pi(i) - E_{\pi,i}] c_{i\nu} \chi_\nu(i) = 0 \quad (2.19)$$

⁵There is no particular connection between the MO subscript and the coordinate variable, both labeled with the index i . In principle any arbitrary index k can be used to label the MO and any arbitrary variable q for the coordinate, resulting in $\phi_k(q)$. However, in practice, using the same index for both will result more convenient later on with the introduction of *Slater determinants*.

If we now multiply from the left with $\chi_\mu^*(i)$ and integrate over all space, we get

$$\sum_{v=1}^M [(H_{\mu v} - S_{\mu v} E_{\pi,i}) c_{iv}] = 0, \quad \mu = 1, 2, \dots, M \quad (2.20)$$

where the elements $H_{\mu v}$ represent the Hamiltonian operator expressed in the basis of atomic orbitals forming an $M \times M$ matrix, while the elements $S_{\mu v}$ form the AO *overlap* matrix. The elements of these matrices are the integrals

$$H_{\mu v} = \langle \chi_\mu | \hat{H}_\pi | \chi_v \rangle = \int \chi_\mu^*(i) \hat{H}_\pi(i) \chi_v(i) d\vec{r}_i \quad (2.21)$$

$$S_{\mu v} = \langle \chi_\mu | \chi_v \rangle = \int \chi_\mu^*(i) \chi_v(i) d\vec{r}_i \quad (2.22)$$

Note the introduction of a short-hand notation for integrals (over operators and functions), called *braket notation*, which will be used from now on⁶.

The orbital energy $E_{\pi,i}$ associated to $\phi_i(i)$ is obtained by solving the secular equation

$$\det(H_{\mu v} - S_{\mu v} E_{\pi,i}) = 0 \quad (2.23)$$

So far, we have only discuss the general approach to express the Hamiltonian operator in a given basis of one-electron functions (which is common to all quantum chemical methods that we will see throughout this section), but we have not discuss yet their actual form. Here is where HMO theory becomes in practice an effective theory, by assigning parametric values to the integrals introduced above. The first approximation is that only *connected* atoms interact with each other, whereas disconnected ones do not. The Hamiltonian elements are thus given by

$$\langle \chi_\mu | \hat{H}_\pi | \chi_v \rangle = \begin{cases} a(\mu) & \text{for } \mu = v \\ -t(\mu, v) & \text{for } \mu \text{ and } v \text{ nearest neighbors} \\ 0 & \text{otherwise} \end{cases} \quad (2.24)$$

by noting that AOs χ_μ and χ_v are centered on different atomic nuclei. In principle, it is known if the atoms corresponding to the pair of labels μ and v are topologically connected, such that Equation (2.24) can be easily constructed. Furthermore, the AOs are assumed to be orthogonal to each other, with overlap matrix elements $S_{\mu v}$ equal to

$$\langle \chi_\mu | \chi_v \rangle = \delta_{\mu v} \quad (2.25)$$

where $\delta_{\mu v}$ is the Kronecker delta.

In Hückel terminology, a is called the Coulomb integral while $-t$ is called the resonance or bond integral. The parameters a and t can be obtained experimentally, providing more quantitative results from the theory or can be set arbitrarily (usually $a = 0$ and $t = 1$) if

⁶Expressions of the form $\langle \phi | \hat{O} | \phi \rangle$ imply an integral over the entire space of all variables appearing in both the functions and the operator. The function $|\phi\rangle$ is called *ket* while its complex conjugate $\langle \phi |$ is called *bra*.

the interest lies more in the qualitative features of the electronic structure of the studied system.

In practice, a Hückel calculation consists in constructing the Hamiltonian matrix H_π according to Equation (2.24) and subsequently diagonalize it to obtain the energy of the MOs and the coefficients $c_{i\mu}$ defining them in terms of AOs. The total electronic energy of the system is then simply given by the sum of the occupied orbitals.

The power of HMO theory resides in the simplicity of the Hamiltonian, which allows for a quick construction and diagonalization, yielding qualitative results that often provide valuable insight into the problem. Furthermore, the size of the molecular system is practically only limited by the matrix diagonalization algorithm employed to solve the eigenvalue problem, or, in certain cases, analytical expressions for energies and orbitals can be derived, thus allowing the investigation of systems up to the thermodynamic limit. On the other hand, besides the narrow applicability of HMO theory, the price to pay for such a simple treatment of the electronic problem is its limited accuracy due to the several approximations introduced. Probably, the crudest one is the form the overlap integral, which completely neglects overlap of adjacent orbitals, whereas this is usually between 0.2 and 0.3 for neighboring atomic orbitals.

2.1.3 Hartree-Fock Theory

After a subsection on a semi-empirical theory, we shall now turn the discussion to the more challenging *ab initio* approaches, starting with *Hartree-Fock (HF) theory*.

The HF approximation is a fundamental milestone of electronic structure theory, as it introduces many important concepts of theoretical chemistry as well as constituting the starting point for most methods used nowadays.

Let us start by recalling an important idea introduced in the previous discussion on Hückel theory, namely the concept of LCAO presented in Equation (2.17). The molecular orbitals $\phi_i(\vec{r})$ (as well as the atomic orbitals $\chi_\mu(\vec{r})$ in which the MOs are expanded) are functions of the three-dimensional space only⁷. However, electrons are *fermions* and hence possess an intrinsic *spin*, which in their case is equal to one half.

In order to completely describe them we need to introduce appropriate spin functions, $\alpha(\omega)$ and $\beta(\omega)$, characterizing an electron being either in a spin up or in a spin down state, respectively. These functions depend on an arbitrary variable ω , they span the entire spin space and are orthonormal to each other, such that

$$\begin{aligned}\langle\alpha|\alpha\rangle &= \int \alpha^*(\omega)\alpha(\omega)d\omega = \int \beta^*(\omega)\beta(\omega)d\omega = \langle\beta|\beta\rangle = 1 \\ \langle\alpha|\beta\rangle &= \int \alpha^*(\omega)\beta(\omega)d\omega = \int \beta^*(\omega)\alpha(\omega)d\omega = \langle\beta|\alpha\rangle = 0\end{aligned}\tag{2.26}$$

Accounting for spin, the state of an electron does not depend anymore only on its position in space \vec{r} , but also on the spin variable ω . We can define one-electron functions

⁷For this reason it is usual to refer to molecular orbitals also as *spatial orbitals*.

that consider both space and spin by multiplying molecular orbitals with spin functions, generating a new type of orbitals called *spin orbitals*

$$\psi_i(\vec{r}, \omega) = \begin{cases} \psi_i^\alpha(\vec{r}, \omega) = \phi_i(\vec{r})\alpha(\omega) \\ \psi_i^\beta(\vec{r}, \omega) = \phi_i(\vec{r})\beta(\omega) \end{cases} \quad (2.27)$$

that fully describe the state of electrons⁸.

Note the slight change of notation from the previous sections, in which ψ_i will from now on exclusively refer to spin orbitals, whereas molecular orbitals will continue to be represented by ϕ_i .

Albeit spin orbitals fully describe the state of a single electron, we are mostly interested in many-particle systems, thus we need to find a way to combine these mono-electronic functions to yield a valid many-body state⁹. In this context, a valid many-electron wave function has to account for the indistinguishability of electrons as well as for the *antisymmetry principle*, stating that a wave function which describes a system of fermions has to be antisymmetric upon interchange of the coordinates of two particles.

Consider for example a two-electron system with coordinates $(\vec{r}_1, \omega_1) \equiv 1$ and $(\vec{r}_2, \omega_2) \equiv 2$, we see that the simple product function

$$\tilde{\Phi}(1, 2) = \psi_1(1)\psi_2(2) \neq \psi_1(2)\psi_2(1) = \tilde{\Phi}(2, 1) \quad (2.28)$$

does not satisfy either of the conditions stated above since it is not antisymmetric and we can distinguish which electron is in which spin orbital. On the other hand, the linear combination

$$\Phi(1, 2) = \psi_1(1)\psi_2(2) - \psi_1(2)\psi_2(1) = -\Phi(2, 1) \quad (2.29)$$

makes the electrons indistinguishable from one another and is antisymmetric.

The generalization of the above approach to the N -electron case defines a special type of wave function called *Slater determinant (SD)*, denoted as

$$\Phi_{SD}(1, 2, \dots, N) = \frac{1}{\sqrt{N!}} \begin{vmatrix} \psi_1(1) & \psi_2(1) & \dots & \psi_N(1) \\ \psi_1(2) & \psi_2(2) & \dots & \psi_N(2) \\ \vdots & \vdots & \ddots & \vdots \\ \psi_1(N) & \psi_2(N) & \dots & \psi_N(N) \end{vmatrix} \quad (2.30)$$

$$= |\psi_1\psi_2 \dots \psi_N\rangle \quad (2.31)$$

$$= |\Phi_{SD}\rangle \quad (2.32)$$

The SD consists in a linear combination of all possible spin orbital products in which the coordinates of two electrons have been interchanged. The factor in front of the SD is such

⁸In general we will drop the explicit superscript indicating the spin, such that ψ_i simply refers to a single spin orbital of unspecified spin.

⁹In the framework of HMO theory, this was achieved by simply multiplying molecular orbitals together, however such an ansatz did not account for spin.

that $\langle \Phi_{SD} | \Phi_{SD} \rangle = 1$ if the spin orbitals are orthonormal to each other (this is usually the case). The second line of Equation (2.30) shows a short-hand notation of the diagonal, where it is assumed that the electron coordinates are ordered according to the spin orbital index.

Note that SDs satisfy the *Pauli exclusion principle*¹⁰, i.e. the fact that two electrons with same spin cannot be found simultaneously at the same position in space. In other words, Slater determinants account for (the so-called) *exchange correlation*: a *Fermi hole* exists around each electron. Even though same-spin correlation effects are fully accounted for in a SD, opposite-spin correlation is still missing completely. Hence, a single SD is typically considered to be an *uncorrelated* wave function¹¹.

Having defined a suitable form for the wave function describing an N -electron state, the Slater determinant, we shall now see how to use it in practice.

A general principle that we can use to obtain the ground state energy and the associated wave function of a system described by the Hamiltonian \hat{H}_{el} , is the *variational principle*. Consider a normalized trial wave function $\tilde{\Psi}_0$, the ground state solution of the Schrödinger equation can be obtained by minimizing the energy expectation value with respect to variations of the trial function $\tilde{\Psi}_0$, i.e.

$$E_0 = \min_{\tilde{\Psi}_0} \langle \tilde{\Psi}_0 | \hat{H}_{el} | \tilde{\Psi}_0 \rangle \quad (2.33)$$

Within the Hartree-Fock approximation, we assume that the wavefunction $\tilde{\Psi}_0$ is represented by a single Slater determinant Φ_{SD} .

Thus, according to Equation (2.7) we have

$$\begin{aligned} \langle \Phi_{SD} | \hat{H}_{el} | \Phi_{SD} \rangle &= \sum_{i=1}^{N_e} \langle \Phi_{SD} | \hat{h}(i) | \Phi_{SD} \rangle + \sum_{i=1}^{N_e} \sum_{j>i}^{N_e} \langle \Phi_{SD} | \hat{v}_{ee}(i, j) | \Phi_{SD} \rangle \\ &= \sum_{i=1}^{N_e} \langle \psi_i | \hat{h}(i) | \psi_i \rangle + \sum_{i=1}^{N_e} \sum_{j>i}^{N_e} \langle \psi_i \psi_j | | \psi_i \psi_j \rangle \\ &= E_{HF} \end{aligned} \quad (2.34)$$

where the second step comes from the application of the *Slater-Condon rules* and where we have introduced the notation

$$\langle \psi_i \psi_j | | \psi_i \psi_j \rangle = \langle \psi_i \psi_j | \psi_i \psi_j \rangle - \langle \psi_i \psi_j | \psi_j \psi_i \rangle \quad (2.35)$$

for the two-electron integrals over the operator $\hat{v}_{ee}(i, j)$.

In practice, the application of Equation (2.33) to Equation (2.34) leads to a set of equations

¹⁰This is nothing but the consequence of the indistinguishability of the electrons and the antisymmetry principle.

¹¹A clear definition of electron correlation within the field of quantum chemistry will be given later on.

called the *Hartree-Fock equations*, given by

$$\hat{f}(1)\psi_i(1) = \left[\hat{h}(1) + \hat{v}_{HF}(1) \right] \psi_i(1) = \varepsilon_i \psi_i(1) \quad \text{for } i = 1, 2, \dots, N_e \quad (2.36)$$

where the mono-electronic operator $\hat{f}(1)$ is called *Fock operator* and the *Hartree-Fock potential* $\hat{v}_{HF}(1)$ is given by

$$\hat{v}_{HF}(1) = \sum_{j=1}^{N_e} \hat{J}_j(1) - \hat{K}_j(1) \quad (2.37)$$

Note that to improve clarity in this subsection, we changed the electronic variable from i to 1 as this does not make any difference since all electrons are indistinguishable.

The operators $\hat{J}_j(1)$ and $\hat{K}_j(1)$ are called *Coulomb operator* and *exchange operator*, respectively, and are formally defined as follows

$$\hat{J}_j(1)\psi_i(1) = \left(\int \int \psi_j^*(2) \frac{1}{r_{12}} \psi_j(2) d\vec{r}_2 d\omega_2 \right) \psi_i(1) \quad (2.38)$$

$$\hat{K}_j(1)\psi_i(1) = \left(\int \int \psi_j^*(2) \frac{1}{r_{12}} \psi_i(2) d\vec{r}_2 d\omega_2 \right) \psi_j(1) \quad (2.39)$$

In order to construct the operators just introduced in Equations (2.38) and (2.39) and hence to define the Fock operator $\hat{f}(1)$ appearing in Equation (2.36), a set of spin orbitals is necessary. This fact makes the Hartree-Fock equations a nonlinear problem that has to be solved self-consistently.

In order to do so, we rely on an iterative procedure called *self-consistent field (SCF) method*, which can be summarized in the following steps:

- start with an initial guess for the spin orbitals $\{\psi_i\}$
- calculate the HF potential \hat{v}_{HF}
- find the eigensolutions of the HF equations (Equation (2.36))
- with the new set of spin orbitals $\{\psi_i\}$ recompute \hat{v}_{HF}
- iterate this procedure until the set $\{\psi_i\}$ does not change anymore (i.e. self-consistency is reached)

The SCF method provides a practical way to solve the HF equations, generating a set of optimized spin orbitals $\{\psi_i\}$ whose spatial part, i.e. the set of MOs $\{\phi_i\}$, are called *canonical orbitals* or *Hartree-Fock orbitals*. Associated to each ϕ_i there is an energy ε_i , which is called orbital energy.

The HF orbitals are *optimal*, in the sense that they minimize Equation (2.34) under the constraint to remain orthonormal among each other. In principle, there is an infinite number of solutions to the HF equations and thus the set $\{\psi_i\}$ contains an infinite number of elements. However, for an N -electron system, only the N spin orbitals associated with the lowest energy eigenvalues provide the best variational estimate of the ground state energy and wave function.

The Slater determinant constructed with this set of orbitals is called *Hartree-Fock determinant*, and the associated energy is the *Hartree-Fock energy*. The orbitals which are occupied in a Slater determinant are referred to as *occupied orbitals*, while all the remaining empty ones are called *virtual orbitals*. Note that the HF energy E_{HF} is not simply the sum of the one-electron energies ε_i of the occupied orbitals as it was the case for the HMO method, but instead is given by

$$\begin{aligned} E_{HF} &= \sum_{i=1}^{occ} \langle \psi_i | \hat{h}(i) | \psi_i \rangle + \sum_{i=1}^{occ} \sum_{j>i}^{occ} \langle \psi_i \psi_j | | \psi_i \psi_j \rangle \\ &= \sum_{i=1}^{occ} \varepsilon_i + \sum_{i=1}^{occ} \sum_{j>i}^{occ} \langle \psi_i \psi_j | | \psi_i \psi_j \rangle \end{aligned} \quad (2.40)$$

Although in principle there is an infinite number of orbitals ψ_i which are solution to Equation (2.36), in practice the HF equations are solved in a finite basis of spatial orbitals ϕ_i , which are expanded in a linear combination of atomic orbitals according to Equation (2.17), with atomic orbitals χ_μ , as

$$\phi_i = \sum_{\mu=1}^M c_{i\mu} \chi_\mu \quad (2.41)$$

The molecular orbitals ϕ_i can contain up to two electrons, one with spin α and one with spin β , such that the total number of spin orbitals ψ_i in such basis can be $2M$. The introduction of the expansion Equation (2.41) into Equation (2.36), results in a set of (matrix) eigenvalue equations known as the *Roothaan-Hall equations*, whose solution provides the expansion coefficients $c_{i\mu}$ of the orbitals. Generally, the number $2M$ of spin orbitals is larger than the number N of electrons in the system, such that at the end of the SCF procedure there are $2M - N$ virtual orbitals. By increasing the number M of functions in the basis set, more flexibility is provided to the wave function, decreasing the HF energy E_{HF} obtained through the SCF procedure, eventually reaching for $M \rightarrow \infty$ the *Hartree-Fock limit*.

Note that in the definition of spin orbitals introduced in Equation (2.27), we restricted the spatial part ϕ_i to be the same for both the α and the β spin functions. This choice is not indispensable, the HF equations and the SCF procedure are equally well defined in the case where the spatial part of the spin orbitals is allowed to *relax* separately for the α spin orbitals and for the β spin orbitals. For the *restricted* case that we just have presented, the method is called *restricted Hartree-Fock (RHF)*, whereas in the other case is named *unrestricted Hartree-Fock (UHF)*.

To finish this subsection, we shall briefly mention ups and downs of HF theory.

Albeit being a cornerstone of theoretical chemistry HF theory still provides only qualitative results which compare poorly to experiments. The reason for this is the lack of opposite-spin electron correlation in the HF wave function, which is essential to capture the correct physics of the electronic system. Nonetheless, as we shall see in the following

sections, the HF determinant and the set of canonical orbitals obtained through the SCF approach form in many cases a suitable basis to recover the missing electron correlation. On the other hand, a major drawback of HF theory appears in the case of quasi-degenerate states. When several Slater determinants are energetically very close to one another, the SCF method might fail to converge to a single solution as there is no obvious choice for the best SD, they are all equally valid choices. This problem is intrinsic to the *mono-determinantal*, or *single reference*, nature of the HF wave function, which can be circumvented by more elaborate schemes that we shall discuss later on.

2.1.4 Many-Body Perturbation Theory

As mentioned in the previous subsection, a wave function composed by a single SD only and the corresponding HF energy, do not include the effects of opposite-spin electron correlation. A more formal definition (within the field of theoretical chemistry) of the *correlation energy* is given as the difference between the exact nonrelativistic and the HF energies i.e.

$$E_{corr} = E_{exact} - E_{HF} \quad (2.42)$$

From now on, the opposite spin electron correlation, sometimes also called Coulomb electron correlation (in contrast to the Fermi correlation due to the Pauli exclusion principle), will be simply called *electron correlation*.

Although E_{corr} accounts only for a fraction of the total energy, it turns out that this small part is actually fundamental to correctly describe almost any chemical process of interest and hence has to be taken into account, even in an approximate way. Typically, the error in total energies (or energy differences) should be in the order of ≈ 1 kcal/mol to reach the so-called *chemical accuracy*.

The usual way to compute E_{corr} consists in building upon the HF approximation. In this context, an Hartree-Fock calculation consists in the first step towards the final solution and is usually followed by the application of a *post Hartree-Fock* method.

Different approaches exist to derive post HF methods, and arguably the simplest one is based on *many-body perturbation theory* (MBPT) that we shall introduce in the following.

The main idea of perturbation theory is to divide the problem at hand in an *easy* part, whose solution is known, and a *hard* part, which shall be treated as a perturbation to the easy problem.

Let us first consider the general case for non-degenerate perturbation theory¹², known as *Rayleigh-Schrödinger perturbation theory*, for an arbitrary system described by the Hamiltonian \hat{H} . We are seeking solutions to the eigenvalue problem

$$\hat{H} |\Psi_i\rangle = (\hat{H}^{(0)} + \hat{V}) |\Psi_i\rangle \quad (2.43)$$

$$= \mathcal{E}_i |\Psi_i\rangle \quad (2.44)$$

¹²The general *degenerate* case will not be discussed here, note however that the underlying idea is the same.

where the eigenfunctions and eigenvalues of the operator $\hat{H}^{(0)}$ are known, and are given by

$$\hat{H}^{(0)} |\Phi_i^{(0)}\rangle = E_i^{(0)} |\Phi_i^{(0)}\rangle \quad (2.45)$$

The operator $\hat{H}^{(0)}$ is called *zeroth-order Hamiltonian* while \hat{V} is named *perturbation operator*. If the effects introduced by \hat{V} are sufficiently small compared to $\hat{H}^{(0)}$, or in other words, if $\hat{H}^{(0)}$ is a good approximation of \hat{H} , we can introduce a parameter $\lambda \in [0, 1]$ controlling the perturbation strength, writing

$$\hat{H}(\lambda) |\Psi_i\rangle = (\hat{H}^{(0)} + \lambda \hat{V}) |\Psi_i\rangle = \mathcal{E}_i |\Psi_i\rangle \quad (2.46)$$

A Taylor expansion around $\lambda = 0$ of the exact energy and wave function for the state i results in

$$\mathcal{E}_i = E_i^{(0)} + \lambda E_i^{(1)} + \lambda^2 E_i^{(2)} + \dots \quad (2.47)$$

$$|\Psi_i\rangle = |\Phi_i^{(0)}\rangle + \lambda |\Phi_i^{(1)}\rangle + \lambda^2 |\Phi_i^{(2)}\rangle + \dots \quad (2.48)$$

where the superscripts in parenthesis indicate the *order* of the perturbation.

The idea is now to find a way to express higher-order terms as a function of lower order ones.

By inserting Equations (2.47) and (2.48) into Equation (2.46), we obtain

$$\left(\hat{H}^{(0)} + \lambda \hat{V} \right) \left(\sum_{n=0}^{\infty} \lambda^n |\Phi_i^{(n)}\rangle \right) = \left(\sum_{n=0}^{\infty} \lambda^n E_i^{(n)} \right) \left(\sum_{n=0}^{\infty} \lambda^n |\Phi_i^{(n)}\rangle \right) \quad (2.49)$$

Since Taylor expansions are unique, we can multiply out all terms of the Equation (2.49) and equate all terms appearing at the same order in λ separately, yielding

$$\hat{H}^{(0)} |\Phi_i^{(0)}\rangle = E_i^{(0)} |\Phi_i^{(0)}\rangle \quad (2.50)$$

$$\hat{H}^{(0)} |\Phi_i^{(1)}\rangle + \hat{V} |\Phi_i^{(0)}\rangle = E_i^{(0)} |\Phi_i^{(1)}\rangle + E_i^{(1)} |\Phi_i^{(0)}\rangle \quad (2.51)$$

$$\hat{H}^{(0)} |\Phi_i^{(2)}\rangle + \hat{V} |\Phi_i^{(1)}\rangle = E_i^{(0)} |\Phi_i^{(2)}\rangle + E_i^{(1)} |\Phi_i^{(1)}\rangle + E_i^{(2)} |\Phi_i^{(0)}\rangle \quad (2.52)$$

...

The first line corresponds to order $n = 0$ (no perturbation), the second line to order $n = 1$, and so on.

Projecting the above equations onto $\langle \Phi_i^{(0)} |$ and rearranging the terms, provides the following expressions for the energies at the various orders of the perturbation

$$E_i^{(0)} = \langle \Phi_i^{(0)} | \hat{H}^{(0)} | \Phi_i^{(0)} \rangle \quad (2.53)$$

$$E_i^{(1)} = \langle \Phi_i^{(0)} | \hat{V} | \Phi_i^{(0)} \rangle \quad (2.54)$$

$$E_i^{(2)} = \langle \Phi_i^{(0)} | \hat{V} | \Phi_i^{(1)} \rangle \quad (2.55)$$

$$E_i^{(3)} = \langle \Phi_i^{(0)} | \hat{V} | \Phi_i^{(2)} \rangle \quad (2.56)$$

...

where we assumed intermediate normalization, i.e. $\langle \Phi_i^{(0)} | \Psi_i \rangle = 1$, allowing us to eliminate all overlaps $\langle \Phi_i^{(0)} | \Phi_i^{(n)} \rangle$ for $n > 0$.

The energy corrections starting at $n = 2$ require the knowledge of the wave function correction at the previous order. To illustrate a possible way to obtain the wave function correction and compute the energy, let us consider the case $n = 2$. To determine $|\Phi_i^{(1)}\rangle$ we need to solve Equation (2.51), i.e.

$$(E_i^{(0)} - \hat{H}^{(0)}) |\Phi_i^{(1)}\rangle = (\hat{V} - E_i^{(1)}) |\Phi_i^{(0)}\rangle \quad (2.57)$$

The eigenfunctions of $\hat{H}^{(0)}$ form a complete orthonormal set spanning the entire (many-particle) space and since we assumed from the beginning to know all these solutions, they can be used to express $|\Phi_i^{(1)}\rangle$ on the left-hand side by an appropriate linear combination according to

$$|\Phi_i^{(1)}\rangle = \sum_{j=0}^{\infty} C_j^{(1)} |\Phi_j^{(0)}\rangle = \sum_{j=0}^{\infty} |\Phi_j^{(0)}\rangle \langle \Phi_j^{(0)} | \Phi_i^{(1)} \rangle \quad (2.58)$$

Note that $C_j^{(1)} = \langle \Phi_j^{(0)} | \Phi_i^{(1)} \rangle \neq 0$ for all j but $j = i$ because of intermediate normalization. Multiplying Equation (2.57) from the left with $\langle \Phi_j^{(0)} |$ results in

$$(E_i^{(0)} - E_j^{(0)}) \langle \Phi_j^{(0)} | \Phi_i^{(1)} \rangle = \langle \Phi_j^{(0)} | \hat{V} | \Phi_i^{(0)} \rangle \quad (2.59)$$

which can be rearranged as

$$\langle \Phi_j^{(0)} | \Phi_i^{(1)} \rangle = \frac{\langle \Phi_j^{(0)} | \hat{V} | \Phi_i^{(0)} \rangle}{E_i^{(0)} - E_j^{(0)}} \quad (2.60)$$

Now, by introducing the expansion in Equation (2.58) into the expression for the second order energy correction, Equation (2.55), we obtain

$$E_i^{(2)} = \langle \Phi_i^{(0)} | \hat{V} | \Phi_i^{(1)} \rangle = \sum_{j=0}^{\infty} \langle \Phi_i^{(0)} | \hat{V} | \Phi_j^{(0)} \rangle \langle \Phi_j^{(0)} | \Phi_i^{(1)} \rangle \quad (2.61)$$

which, by replacing $\langle \Phi_j^{(0)} | \Phi_i^{(1)} \rangle$ according to Equation (2.60), gives the final expression for $E_i^{(2)}$ as

$$E_i^{(2)} = \sum_{\substack{j=0 \\ j \neq i}}^{\infty} \frac{\langle \Phi_i^{(0)} | \hat{V} | \Phi_j^{(0)} \rangle \langle \Phi_j^{(0)} | \hat{V} | \Phi_i^{(0)} \rangle}{E_i^{(0)} - E_j^{(0)}} \quad (2.62)$$

where we highlighted that the sum is restricted to $j \neq i$ according to intermediate normalization, since this is not directly visible in the last expression. Higher order corrections to the energy can be obtained in a similar fashion to the above derivation of the case $n = 2$.

We shall now consider a more specific type of perturbation theory known within the realm of quantum chemistry as *Møller-Plesset perturbation theory (MPPT)*, in particular we will focus on *second order Møller-Plesset (MP2)* theory.

MPPT is a ground state theory, meaning that it is used to compute the correlation energy of the *ground state* of a system. The zeroth-order Hamiltonian is chosen to be the sum over Fock operators $\hat{f}(k)$. This particular choice of $\hat{H}^{(0)}$ fulfills the requirement that solutions to the unperturbed problem should be known, since these are given by SDs constructed with the set of spin orbitals obtained from the SCF method. Specifically, given N_e electrons and $M > N_e$ spin orbitals, a total of $\binom{M}{N_e}$ determinants can be created from all possible combinations of placing the N_e electrons in the M spin orbitals. A determinant where an electron is *excited* from an occupied orbital of the HF ground state to a virtual (unoccupied) orbital is named *excited determinant*.

Henceforth, with the following choice of zeroth-order Hamiltonian

$$\hat{H}^{(0)} = \sum_{k=1}^{N_e} \hat{f}(k) \quad (2.63)$$

the perturbation operator \hat{V} is given by

$$\begin{aligned} \hat{V} = \hat{H} - \hat{H}^{(0)} &= \sum_{k=1}^{N_e} \sum_{j>k}^{N_e} \hat{v}_{ee}(k, j) - \sum_{k=1}^{N_e} \hat{v}_{HF}(k) \\ &= \sum_{k=1}^{N_e} \sum_{j>k}^{N_e} \hat{v}_{ee}(k, j) - \sum_{k=1}^{N_e} \sum_{j=1}^{N_e} \hat{J}_j(k) - \hat{K}_j(k) \end{aligned} \quad (2.64)$$

To obtain the energy corrections we just have to use Equations (2.53) to (2.55) and plug in the particular definition of $\hat{H}^{(0)}$ and V .

The zeroth-order energy for the ground state is then equal to

$$E_{MP0} = E_0^{(0)} = \langle \Phi_0^{(0)} | \hat{H}^{(0)} | \Phi_0^{(0)} \rangle \quad (2.65)$$

$$= \sum_{k=1}^{N_e} \langle \Phi_{HF} | \hat{f}(k) | \Phi_{HF} \rangle \quad (2.66)$$

$$= \sum_{k=1}^{N_e} \varepsilon_{kk} \quad (2.67)$$

which is the sum of all occupied orbital energies. Note that E_{MP0} is *not* equal to the HF energy.

The first order correction to the energy is computed similarly, according to

$$E_{MP1} = E_0^{(1)} = \langle \Phi_0^{(0)} | \hat{V} | \Phi_0^{(0)} \rangle \quad (2.68)$$

$$= \langle \Phi_{HF} | \sum_{k=1}^{N_e} \sum_{j>k}^{N_e} \hat{v}_{ee}(k, j) | \Phi_{HF} \rangle - \langle \Phi_{HF} | \sum_{k=1}^{N_e} \hat{v}_{HF}(k) | \Phi_{HF} \rangle \quad (2.69)$$

$$= \sum_{k=1}^{N_e} \sum_{j>k}^{N_e} \langle \psi_k \psi_j | | \psi_k \psi_j \rangle - \sum_{k=1}^{N_e} \langle \psi_k | v_{HF} | \psi_k \rangle \quad (2.70)$$

$$= \frac{1}{2} \sum_{k=1}^{N_e} \sum_{j=1}^{N_e} \langle \psi_k \psi_j | | \psi_k \psi_j \rangle - \sum_{k=1}^{N_e} \sum_{j=1}^{N_e} \langle \psi_k \psi_j | | \psi_k \psi_j \rangle \quad (2.71)$$

$$= -\frac{1}{2} \sum_{k=1}^{N_e} \sum_{j=1}^{N_e} \langle \psi_k \psi_j | | \psi_k \psi_j \rangle \quad (2.72)$$

which summed together with the zeroth-order one gives the HF energy

$$E_{MP0} + E_{MP1} = \sum_{k=1}^{N_e} \epsilon_{kk} - \frac{1}{2} \sum_{k=1}^{N_e} \sum_{j=1}^{N_e} \langle \psi_k \psi_j | | \psi_k \psi_j \rangle \quad (2.73)$$

$$= E_{HF} \quad (2.74)$$

Thus far we have only recovered the HF energy. The first order at which electron correlation is introduced is $n = 2$, which, by recalling Equation (2.62), is given by

$$E_{MP2} = E_0^{(2)} = \sum_{j>0} \frac{\langle \Phi_0^{(0)} | \hat{V} | \Phi_j^{(0)} \rangle \langle \Phi_j^{(0)} | \hat{V} | \Phi_0^{(0)} \rangle}{E_0^{(0)} - E_j^{(0)}} \quad (2.75)$$

$$= \sum_{j>0} \frac{\langle \Phi_{HF} | \hat{V} | \Phi_j^{(0)} \rangle \langle \Phi_j^{(0)} | \hat{V} | \Phi_{HF} \rangle}{E_0^{(0)} - E_j^{(0)}} \quad (2.76)$$

$$(2.77)$$

where in this case the functions $|\Phi_j^{(0)}\rangle$ correspond to excited determinants.

The energies in the denominator are just sums of spin orbital energies, such that they can be easily simplified, whereas the terms in the numerator can be reduced according to the Slater-Condon rules, such that the final expression of the MP2 energy reads

$$E_{MP2} = \sum_{b>a}^M \sum_{a=N_e+1}^M \sum_{j>k}^{N_e} \sum_{k=1}^{N_e} \frac{\langle \psi_a \psi_b | | \psi_k \psi_j \rangle \langle \psi_k \psi_j | | \psi_a \psi_b \rangle}{\epsilon_k + \epsilon_j - \epsilon_a - \epsilon_b} \quad (2.78)$$

where M is the total number of orbitals (occupied and virtual).

As it is the case for the general MBPT, one can derive higher order corrections within MPPT, albeit other methods are commonly used to go beyond MP2. Every theory comes

with advantages and shortcomings, MPPT is not for less. The most restricting assumption of perturbation theory is the requirement for $\hat{H}^{(0)}$ to be a good approximation of the real system, in other words, that $|\Phi_0^{(0)}\rangle (= |\Phi_{HF}\rangle)$ is a good approximation of the true ground state wave function $|\Psi_0\rangle$. This is usually the case for closed-shell systems, as well as for system in which the separation between the ground and excited state is large enough. If this is not the case and near-degenerate solutions to Equation (2.46) exist, it is likely that the perturbation series does not converge and the values obtained are simply wrong. This can be seen particularly well considering the energies appearing in the denominators; too closed values make the denominator very small, which in turn makes the energy correction diverge.

Nevertheless, MP2 has been an incredibly successful theory because it is able to recover a very large portion of the electron correlation within an acceptable amount of time. Moreover, in the last decades a lot of effort has been put into developing approximate linear-scaling variations of MP2, allowing to treat very large systems.

2.1.5 Coupled Cluster Theory

Although MP2 is a conceptually simple and a widely used method to account for electron correlation, its results might be too inaccurate for a number of applications. Instead to simply go to higher orders in the perturbation series, an alternative, more powerful theory which generally produces better results than MPPT is *coupled cluster (CC) theory*. As in MP2, the coupled cluster approach is based on a previous HF reference calculation and the Hartree-Fock determinant $|\Phi_{HF}\rangle = |\Phi_0\rangle$. The main ingredient of CC theory is to use a more sophisticated wave function ansatz to approximate the exact wave function $|\Psi\rangle$, given by

$$|\Psi\rangle = e^{\hat{T}} |\Phi_0\rangle \quad (2.79)$$

where the exponential operator $e^{\hat{T}}$ can be expanded in a Taylor series as

$$e^{\hat{T}} = 1 + \hat{T} + \frac{\hat{T}^2}{2!} + \frac{\hat{T}^3}{3!} + \dots = \sum_{k=0}^{\infty} \frac{\hat{T}^k}{k!} \quad (2.80)$$

and the *cluster operator* \hat{T} is given by

$$\hat{T} = \hat{T}_1 + \hat{T}_2 + \dots + \hat{T}_{N_e} \quad (2.81)$$

The operators on the right-hand side of Equation (2.81) are called *excitation operators* and their effect on Slater determinants is to move one or more electrons from occupied orbitals to a virtual ones, thus generating a new SD.

Specifically, the one- and two-particle excitation operators are defined as follows

$$\hat{T}_1 |\Phi_0\rangle = \sum_{a=N_e+1}^M \sum_{i=1}^{N_e} t_i^a |\Phi_i^a\rangle \quad (2.82)$$

$$\hat{T}_2 |\Phi_0\rangle = \sum_{b>a}^M \sum_{a=N_e+1}^M \sum_{j>i}^{N_e} \sum_{i=1}^{N_e} t_{ij}^{ab} |\Phi_{ij}^{ab}\rangle \quad (2.83)$$

where $|\Phi_i^a\rangle$ represents a singly-excited determinant in which an electron has been moved from the occupied orbital ψ_i to the virtual orbital ψ_a . Similarly, $|\Phi_{ij}^{ab}\rangle$ is a doubly-excited determinant, and so on. The coefficients t_i^a and t_{ij}^{ab} are called *amplitudes* and they are yet to be determined. Clearly higher-order excitation operators can be defined in a similar manner.

Depending on the order of the excitation operators (i.e. the number of electrons simultaneously excited) included in the cluster operator \hat{T} , different CC schemes can be derived. As an example, by including only double excitations, i.e. $\hat{T} = \hat{T}_2$, we define the coupled cluster doubles (CCD) method; adding single excitations too, i.e. $\hat{T} = \hat{T}_1 + \hat{T}_2$, we define the coupled cluster singles and doubles (CCSD) method, and so on.

In order to determine the amplitudes and compute the CC energy, one could apply the variational principle introduced in Equation (2.33), however that would lead to a set of nonlinear equations involving *all* possible excited determinants, whose number increases exponentially with the size of the basis set. Instead, the solution of the CC equations can be obtained by projection. By introducing the ansatz given in Equation (2.79) into the Schrödinger equation, we get

$$\hat{H}e^{\hat{T}} |\Phi_0\rangle = E_{CC}e^{\hat{T}} |\Phi_0\rangle \quad (2.84)$$

The above equation is then multiplied from the left with the HF determinant and integrated over all space, resulting in

$$\langle \Phi_0 | \hat{H}e^{\hat{T}} | \Phi_0 \rangle = E_{CC} \langle \Phi_0 | e^{\hat{T}} | \Phi_0 \rangle = E_{CC} \langle \Phi_0 | \Phi_0 \rangle = E_{CC} \quad (2.85)$$

where we have used the fact that $\langle \Phi_0 | e^{\hat{T}} | \Phi_0 \rangle = 1$ since all generated excited determinants are orthogonal to $|\Phi_0\rangle$. Projection onto $|\Phi_0\rangle$ provides an expression to determine the energy, Equation (2.85), on the other hand the amplitudes are still unknown. Anyhow, they can be obtained in a similar manner, by projecting Equation (2.84) onto each excited determinant corresponding to an unknown amplitude appearing in \hat{T} . Note that Equation (2.84) is valid if and only if $e^{\hat{T}}$ is the *untruncated* excitation operator, i.e. $e^{\hat{T}} |\Phi_0\rangle$ corresponds to a full configuration interaction (FCI) wave function. Therefore, it is only in Equation (2.85) that we introduce a *truncated* version of \hat{T} , ultimately producing an *approximation* E_{CC} to the true energy.

As an example, consider the CCSD ansatz, with $\hat{T} = \hat{T}_1 + \hat{T}_2$. The expansion of Equation (2.79) is given in this case by

$$\begin{aligned}
e^{\hat{T}} |\Phi_0\rangle &= e^{\hat{T}_1 + \hat{T}_2} |\Phi_0\rangle \\
&= \left(1 + \hat{T}_1 + \hat{T}_2 + \frac{1}{2}(\hat{T}_1 + \hat{T}_2)^2 + \dots \right) |\Phi_0\rangle \\
&= \left(1 + \hat{T}_1 + \hat{T}_2 + \frac{1}{2}\hat{T}_1^2 + \frac{1}{2}\hat{T}_2^2 + \dots \right) |\Phi_0\rangle \\
&= |\Phi_0\rangle + \sum_{ia} t_i^a |\Phi_i^a\rangle + \sum_{ijab} t_{ij}^{ab} |\Phi_{ij}^{ab}\rangle + \frac{1}{2} \sum_{iajb} t_i^a t_j^b |\Phi_{ij}^{ab}\rangle \\
&\quad + \frac{1}{2} \sum_{ijab} \sum_{klcd} t_{ij}^{ab} t_{kl}^{cd} |\Phi_{ijkl}^{abcd}\rangle + \dots
\end{aligned} \tag{2.86}$$

where we notice that although the operator \hat{T} formally contains only single and double excitation operators, in Equation (2.86) excitations going beyond double are present due to the exponential ansatz. On the other hand, the only amplitudes appearing in Equation (2.86) are of the type t_i^a and t_{ij}^{ab} and products thereof. This is the particularly powerful characteristic of the CC ansatz, it generates two distinct types of excitations: terms t_i^a and t_{ij}^{ab} appearing alone are called *connected terms*, while products of amplitudes are called *disconnected terms*.

Since there are only as many amplitudes as single and double excitations, we project Equation (2.84) onto $\langle \Phi_i^a |$ and $\langle \Phi_{ij}^{ab} |$ only and integrate, giving the following equations

$$\langle \Phi_i^a | (\hat{H} - E_{CC}) e^{\hat{T}_1 + \hat{T}_2} |\Phi_0\rangle = 0 \tag{2.87}$$

$$\langle \Phi_{ij}^{ab} | (\hat{H} - E_{CC}) e^{\hat{T}_1 + \hat{T}_2} |\Phi_0\rangle = 0 \tag{2.88}$$

The presence of disconnected terms in the CC wave function makes Equations (2.87) and (2.88) nonlinear and thus have to be solved iteratively, e.g. with the Newton method or variations thereof. Once such a procedure (hopefully) converges and the amplitudes are known, the energy is computed using Equation (2.85).

It should be noted that Equations (2.87) and (2.88) are not the unique way to obtain the CC amplitudes. Alternatively, one can derive a set of nonlinear equations using the *similarity-transformed Hamiltonian* $e^{-\hat{T}} \hat{H} e^{\hat{T}}$, resulting in

$$\langle \Phi_0 | e^{-\hat{T}} \hat{H} e^{\hat{T}} |\Phi_0\rangle = E_{CC} \langle \Phi_I | \Phi_0\rangle = 0 \tag{2.89}$$

with the advantage that they do not explicitly depend on the energy E_{CC} as this vanishes due to the overlap of the HF reference $|\Phi_0\rangle$ and excited determinants $|\Phi_I\rangle$.

The success of coupled cluster theory is best appreciated with the CCSD(T) scheme, which includes single and double excitations as usual, but also triple excitations are taken

into account, albeit only in a perturbative manner (denoted by the use of parenthesis)¹³. The CCSD(T) method is considered the *gold standard* of quantum chemistry for its remarkable accuracy and hence commonly used as a benchmark for other approaches. An important property of CCSD(T) and of all CC schemes in general, is *size-consistency*. The formidable accuracy of the CC approach comes at the price of a higher computational complexity. The family of coupled cluster methods has a very steep scaling in this sense, with the CCSD method scaling as $O(N^6)$, the CCSD(T) as $O(N^7)$, the CCSDT as $O(N^8)$ and so on, with N being a measure of the system size.

In recent years, there has been a lot of research targeted towards approximate coupled cluster schemes, in particular in the framework of linear scaling techniques. Among others variants, the domain based local pair natural orbital CCSD(T) (DLPNO-CCSD(T)) method resulted quite successful⁹³, where upon localization of the molecular orbitals, the exponential decay of the overlap w.r.t. the distance between their centers is exploited, avoiding the calculation of a large number of amplitudes due to their insignificant contribution to the correlation energy.

Although coupled cluster theory has provided a great tool to theoretical chemists, and the advent of linear scaling techniques has opened their use to systems of unprecedented size, there are yet cases in which they miserably fail. The next few subsections are devoted to methods complementing the well established *single reference* theories with some of their *multireference* counterparts.

2.1.6 Multireference Methods

All post-HF approaches considered thus far have used HF theory, in particular the HF Slater determinant, as a starting point to introduce the effects of electron correlation into the formalism. This is a reasonable choice whenever the wave function is qualitatively well described by a single SD, in such case it is called a *single reference* wave function. Yet, this might not always be the case.

It turns out that quite often the single reference picture is not sufficient to correctly reproduce the main features of the true wave function, leading to wrong results or simply breaking the underlying theoretical assumptions. This situation is typical for bond breaking processes, in the calculation of excited states as well as quite common for transition metals with a partially filled d shell. In practice, the HF approximation is inadequate whenever there is more than one possibility to place electrons in near-degenerate MOs, generating several SDs with comparable energies. Instead of selecting only one them, they should all be included on equal footing into the wave function, thus becoming of *multireference* character.

This type of situation is, again, due to electron correlation. The fact that its manifestation appears to be different in the case when the mono-determinantal picture is a good or bad approximation of the true wave function, suggests that the electron correlation can be (although somewhat arbitrarily) categorized in two classes. On one side, when a single

¹³We shall not discuss how this is done in practice as the theory is quite involved, going beyond the scope of this chapter.

determinant provides a qualitatively correct wave function, electron correlation appears to be tied to the instantaneous Coulomb repulsion between the electrons at short range, an effect which is well captured by the inclusion in the wave function of a large number of SDs as it is done in single reference approaches such as MPPT and CC theory. This *type* of electron correlation is called *dynamic correlation*.

On the other side, when the wave function is indisputably of multireference character and a number of determinants is strictly required to provide enough flexibility, the correlation is tightly connected to the degeneracy of the configurations, meaning that they cannot be treated in isolation from one another as they interact strongly. When this is the case, the electron correlation is called *static correlation*.

In principle, the general theory developed for single reference approaches can be extended to the multireference world, by trivially substituting the mono-determinantal wave function on which they are build upon with a multireference one. Nevertheless, the outcoming methodologies result much more involved and complicated to their single reference counterparts, such that method developers are still actively working on it. In the remainder of this subsection, we shall see two well-established methods that combined together recover at first the static electron correlation, and in a second moment the dynamic electron correlation, in a so-called *diagonalize-then-perturb* fashion.

Complete Active Space Self-Consistent Field

The first method that we shall introduce is the *complete active space self-consistent field* (CASSCF) method⁹⁴, probably the most famous approach to treat static electron correlation. It is based on a linear expansion ansatz of the wave function in terms of SDs, known as *configuration interaction* (CI)¹⁴.

The basic idea of the CI approach is very similar to that of CC theory, where the wave function is expanded in a superposition of Slater determinants as

$$|\Psi_{CI}\rangle = C_0 |\Phi_0\rangle + \sum_{ia} C_i^a |\Phi_i^a\rangle + \sum_{ijab} C_{ij}^{ab} |\Phi_{ij}^{ab}\rangle + \dots \quad (2.90)$$

which practically corresponds to the direct application of the excitation operator \hat{T} appearing in Equation (2.81) to the HF determinant, while replacing (in reality relabeling) the amplitudes $t_i^a, t_{ij}^{ab}, \dots$ with CI coefficients $C_i^a, C_{ij}^{ab}, \dots$. The main difference between the CI and CC approaches lies in the fact that the CC expansion is nonlinear, leading to connected and disconnected terms, whereas the CI one is linear, generating only, in CC terminology, connected terms. The latter fact implies that in the wave function there are as many determinants as there are coefficients. When a *full* expansion is used, the method is called *F*CI, and all possible excited determinants are explicitly included in the wave function and treated on equal footing. On the other hand, by truncating the excitations to a lower degree, different schemes are generated, named similarly to CC theory,

¹⁴Note that the entire discussion in multireference method is also valid when using configuration state functions (CSFs) instead of Slater determinants.

i.e. CISD, CISDT, and so on.

Differently than the CC case, the optimization of the CI wave function, i.e. the CI coefficients, can be carried out by applying the variational principle stated in Equation (2.33). Insertion of the CI wave function into the expectation value gives a minimization problem over the vector of coefficients C , i.e.

$$E_{CI} = \min_C \langle \Psi_{CI} | \hat{H} | \Psi_{CI} \rangle \quad (2.91)$$

where we assume that the $|\Psi_{CI}\rangle$ is normalized, such that $\langle \Psi_{CI} | \Psi_{CI} \rangle = 1$. The minimization process results in a matrix eigenvalue problem of the form

$$\mathbf{H}C = E_{CI}C \quad (2.92)$$

where in this context \mathbf{H} is usually referred to as the *CI matrix* with elements $H_{IJ} = \langle \Phi_I | \hat{H} | \Phi_J \rangle$, C is a vector containing the expansion coefficients of the state of interest and E_{CI} is the CI energy associated to that state. Note that diagonalization of \mathbf{H} provides the entire set of eigenstates and eigenvalues, which correspond to the electronically excited states of the system.

Since the CI matrix elements are simple expectation values over excited SDs, different levels of truncation of the CI scheme simply correspond to diagonalizing a part of the FCI matrix. Nevertheless, the size of \mathbf{H} is usually very large, such that the diagonalization is in practice carried out by iterative solvers.

With the introduction of the configuration interaction method, it is now possible to present the first step towards CASSCF, i.e. the *complete active space configuration interaction (CASCI)* method. The underlying idea is the following, considering that in the presence of static correlation the problematic part of the wave function is given by those electrons that can be placed in several different ways into energetically near-degenerate MOs, instead of selecting only a single SD to represent the wave function (such as in HF), a FCI expansion in a reduced space of electrons and orbitals is used for the ansatz. In particular, the space of orbitals is partitioned in three subspaces. The *occupied space* contains all orbitals which are unambiguously doubly occupied, the *virtual space* contains all orbitals which are clearly unoccupied, and lastly the *active space (AS)* is composed by those n electrons and m orbitals which are problematic. This partitioning of the orbitals is schematized in Figure 2.1. The FCI expansion is generated with all possible determinants arising from placing the n electrons into the m orbitals. Hence, the size of the active space determines the total number of SDs in the wave function, and thus its complexity. The optimal coefficients are then obtained by solving Equation (2.92) as one would do in a normal CI calculation. Clearly, these orbitals have to come from somewhere, so anyhow an underlying *guess* calculation is required to obtain them, typically an HF one.

The CASCI approach solves the problem of having several near-degenerate determinants included into the wave function, however the fact that the orbitals were generated from a single reference method such as HF, still poses some difficulties. In particular we can

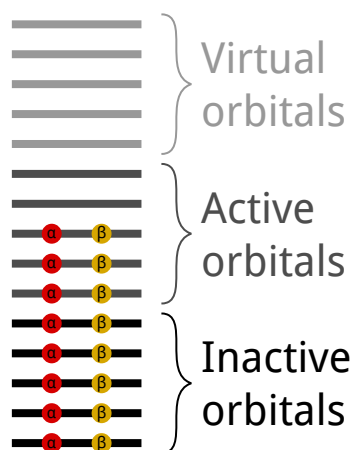


FIGURE 2.1: The CASSCF orbital spaces.

imagine that as much as doubly occupied orbitals are likely to be well represented within the HF approximation, AS orbitals are probably not. The intuitive remedy to this problem is to also optimize the MOs along with the CI coefficients, leading to the CASSCF method.

Within the CASSCF approach, the wave function is given by

$$|\Psi_{\text{CASSCF}}\rangle = \sum_I C_I |\Phi_I(c)\rangle \quad (2.93)$$

where the sum over I goes through all possible determinants $|\Phi_I(c)\rangle$ generated within the AS. Note the dependence of the SDs on the orbital coefficients c . The minimization process of the CASSCF wave function is again carried out by applying the variational principle, however the minimum has to be found with respect to both the CI expansion coefficients C and the MOs coefficients c , i.e.

$$E_{\text{CASSCF}} = \min_{C,c} \langle \Psi_{\text{CASSCF}}(C,c) | \hat{H} | \Psi_{\text{CASSCF}}(C,c) \rangle \quad (2.94)$$

Although the general formulation of the variational principle to the CASSCF wavefunction appears simple, its practical realization is a complicated minimization problem which is not guaranteed to converge. Different approaches are available to optimize the CASSCF wavefunction, however their discussion goes beyond the scope of this subsection.

One of the limits of the CASSCF method is the maximum size of the active space. The number of determinants increases factorially with the size of the AS, such that on nowadays hardware it is usually not possible to go beyond roughly 18 electrons in 18 MOs. Furthermore, the choice of the orbitals is crucial. Different selections of MOs and electrons can lead to very different results, thus introducing some degree of arbitrariness into the formalism. This fact makes this method different from the single reference approaches seen in precedence, which worked fairly in an unsupervised, blackbox manner.

The CASSCF method consists in a FCI expansion within the active orbital space, generating a vast number of determinants. Nevertheless these configurations are only restricted to the AS; the effect of the many determinants arising from excitations to virtual orbitals is therefore not taken into account. Albeit the static correlation is accounted for, the effects of dynamic correlation still have to be introduced into the formalism in some way. This is usually done by applying the single reference techniques presented in the previous subsections to the CASSCF wave function instead of the HF one, resulting in a series of multireference methodologies. In this context, the CASSCF wavefunction can be considered the multireference counterpart of the HF determinant.

Second Order n -Electron Valence Perturbation Theory

The CASSCF method only captures static correlation, however in order to obtain quantitative results, inclusion of dynamic correlation is necessary. To this end, we shall focus on the multireference implementation of MBPT, namely *multireference perturbation theory (MRPT)*. As for any perturbative approach, there is no unique way to derive an MBPT formalism, such that during the years different *types* of MRPT have been developed, each with their own particular feature.. In this subsection we will briefly present only one of these methodologies, called *second order n -electron valence perturbation theory (NEVPT2)*^{95–97}.

The basic idea remains the same as in the case of single reference theories, i.e. the is split into a simple part, described by the zeroth order Hamiltonian $\hat{H}^{(0)}$ and a hard part, described by the perturbation operator $\hat{V} = \hat{H} - \hat{H}^{(0)}$. In the particular case of MRPT, the new ingredient is the use of a multireference zeroth order wave function, in particular based on the CASSCF method.

In NEVPT2, the zeroth order Hamiltonian is chosen to be *Dyall's Hamiltonian*, reading

$$\hat{H}^{(0)} = \hat{H}_D = \hat{H}_i + \hat{H}_v + C \quad (2.95)$$

where \hat{H}_i is a one-electron Hamiltonian defined in the occupied and virtual orbital spaces as

$$\hat{H}_i = \sum_i^{occ} \hat{f}(i) + \sum_r^{virt} \hat{f}(r) \quad (2.96)$$

where \hat{f} are Fock operators and the sums go over doubly occupied and virtual orbitals only. One particular feature of NEVPT2 compared to other MRPT approaches is the form of \hat{H}_v , which is a two-electron operator of the form

$$\hat{H}_v = \sum_a^{act} \hat{h}^{eff}(a) + \frac{1}{2} \sum_{ab}^{act} \hat{v}_{ee}(a, b) \quad (2.97)$$

which is similar to the usual electronic Hamiltonian besides the fact the \hat{h}^{eff} is an effective one-electron operator which takes into account the field created by the core electrons in an effective way. The last term C is a constant which is chosen such that \hat{H}_D is equal to the normal electronic Hamiltonian within the AS.

The second order energy can then be obtained according to the usual expression

$$E^{(2)} = \langle \Psi^{(0)} | \hat{V} | \Psi^{(1)} \rangle \quad (2.98)$$

Since the reference wave function $\Psi^{(0)} = \sum_I C_I \Phi_I^{(0)}$ is not anymore composed by a single determinant, the concept of *first order interacting space* is introduced, i.e. the space spanned by all determinants external to the AS which have nonvanishing interactions with $\Psi^{(0)}$. In general, it is possible to divide this space in smaller subspaces, labeled by the number of electrons excited and from their origin (occupied, active or virtual orbital space). Working within these subspaces simplifies the formalism. As it is the case for MPPT, the first order wave function $\Psi^{(1)}$ is expanded in so called *perturbers*, i.e. eigenfunctions of the zeroth order Hamiltonian. However, the choice here is not so straightforward as in MPPT. In particular, an *uncontracted* approach where the perturbbers are simple SDs results in a very computationally demanding algorithm. To remedy to this, *internally contracted* correction functions are used, which decrease the dimension of the first order interacting subspaces, making the methodology applicable to larger ASs. On the other hand, a disadvantage of using internal contraction is the (possible) linear dependence of the basis. In order to make these functions actual eigenfunctions of the zeroth order Hamiltonian, projectors are introduced into the definition of $\hat{H}^{(0)}$.

The technical derivation of the NEVPT2 working equations is quite involved and is therefore left out from the current manuscript.

To conclude the section on multireference methods, let us list the properties of NEVPT2. The theory is invariant under unitary transformations of active orbitals as well as size-consistent. Another convenient feature of NEVPT2 is the (practical) absence of *intruder states*, i.e. states that are quasi-degenerate at zeroth order, but not in the full quantum chemical treatment. These states are responsible for the divergence of the perturbation series and make the denominator in the second order energy correction small, with a consequent explosion of the energy correction. The use of a bi-electronic Hamiltonian within the active space is the key factor eliminating this problematic states.

2.1.7 Density Functional Theory

In the last decades, a different approach than wave function theory has emerged as one of the most successful and used one in theoretical chemistry, namely *DFT*.

DFT is based upon the realization that the electron density, a function of the three dimensional space, is a much more tractable object than the wave function, which lives in a $4N$ -dimensional space (considering also the electronic spin). We shall see that in general, the electron density is sufficient for obtaining most of the properties of interest, such as the electronic energy and one-electron properties.

The density of an N -electron system is defined as the integral over all space (and spin) coordinates of $N - 1$ electrons, i.e.

$$\rho(\vec{r}) = N \int \Psi^*(\vec{r}, \vec{r}_2, \dots, \vec{r}_N) \Psi(\vec{r}, \vec{r}_2, \dots, \vec{r}_N) d\vec{r}_2 \dots d\vec{r}_N \quad (2.99)$$

where the factor N ensures that integrating the electron density

$$\int \rho(\vec{r}) d\vec{r} = N \quad (2.100)$$

yields the total number of electrons in the system.

At the very base of density functional theory there are two theorems, proposed by Hohenberg and Kohn in 1964. The *first Hohenberg-Kohn (HK) theorem* states:

The ground state density $\rho_0(\vec{r})$ determines (up to a constant) the external potential $V_{ne}(\vec{r})$ and thus the total electronic Hamiltonian \hat{H}_{el} too. This implies that also the ground state wave function Ψ_0 is uniquely determined by ρ_0 .

The strong implication of this theorem is that there is a one to one map between $V_{ne}(\vec{r})$ and $\rho_0(\vec{r})$. In order to prove the first HK theorem, one usually shows by contradiction that two external potentials cannot lead to the same ground state density, however we shall not demonstrate that here. Note that the original formulation of the above theorem was restricted to the case of non-degenerate ground states only, however it was later demonstrated by Levy in 1979⁹⁸ that the same result applies for degenerate ground state densities too.

Consider the electronic Hamiltonian of Equation (2.7). The only term which explicitly depends on the system, i.e. on the particular arrangement of the nuclei and their charge, is the electron-nuclear attraction given by

$$\hat{V}_{ne} = \hat{V}_{ext} = - \sum_{i=1}^{N_e} \sum_{I=1}^{N_n} \frac{Z_I}{r_{iI}} \quad (2.101)$$

Within the context of DFT, this term is usually called the *external potential*. The other terms of the electronic Hamiltonian, namely the kinetic energy and the electron-electron repulsion operators, are instead independent from the nuclear coordinates and thus the same for every system.

According to the first HK theorem, the ground state wave function Ψ_0 is a unique functional of ρ_0 . Therefore, the expectation value of any operator \hat{O} over Ψ_0 is also a unique functional of the ground state density, i.e.

$$O[\rho_0] = \langle \Psi_0[\rho_0] | \hat{O} | \Psi_0[\rho_0] \rangle \quad (2.102)$$

As an example, the ground state energy can be expressed as a functional of ρ_0 according to

$$E_0[\rho_0] = \langle \Psi_0[\rho_0] | \hat{H} | \Psi_0[\rho_0] \rangle \quad (2.103)$$

$$= \langle \Psi_0[\rho_0] | \hat{T} + \hat{V}_{ee} + \hat{V}_{ne} | \Psi_0[\rho_0] \rangle \quad (2.104)$$

$$= \int \hat{V}_{ne}(\mathbf{r}) \rho_0(\mathbf{r}) d\mathbf{r} + F_{HK}[\rho_0] \quad (2.105)$$

where we have introduced the universal *Hohenberg-Kohn functional* $F_{HK}[\rho_0]$ given by

$$F_{HK}[\rho_0] = \langle \Psi_0[\rho_0] | \hat{T} + \hat{V}_{ee} | \Psi_0[\rho_0] \rangle \quad (2.106)$$

which does not depend on the system. However, no analytical form of this functional is known.

The first HK theorem is an existence theorem. The *second Hohenberg-Kohn theorem* instead tells us about the properties of ρ_0 and $E_0[\rho_0]$, stating that

The exact ground state density ρ_0 minimizes the ground state energy $E_0[\rho_0]$.

This result assures that it is possible to find the "best" density among all possible densities and is in fact the analogous of the variational principle for ground state wave functions. The proof of the second theorem is also quite straightforward, and relies on the knowledge given by the first one, i.e. that to every ground state density there exists a one to one relation with the external potential. Therefore, for a given external potential, the energy $E_0[\tilde{\rho}]$ obtained with any trial density $\tilde{\rho}$ will always be above the one obtained with the exact ground state density ρ_0 associated with that particular choice of external potential. The HK theorems provide the theoretical foundations of DFT, however they do not prescribe a practical way to obtain the ground state density.

Nevertheless, one year after the publication of the HK theorems, Kohn and Sham presented a way to make DFT practical, by a clever mapping of a problem into another, simpler one⁹⁹. Their idea was the following: consider a system of non-interacting electrons described by

$$\hat{H}_{KS} = \hat{T} + \hat{V}_{KS} = \sum_{i=1}^{N_e} \left(\frac{-\nabla_i^2}{2} + v_{KS}(i) \right) \quad (2.107)$$

which is a sum of one-electron operators, with the usual kinetic energy operator and an effective local potential $v_{KS}(\vec{r})$, named the *Kohn-Sham potential*.

The exact solution to this problem is known, and is given by a single Slater determinant with orbitals obtained through the solution of the *Kohn-Sham equations*

$$\left(\frac{-\nabla^2}{2} - v_{KS}(\vec{r}) \right) \phi_i^{KS}(\vec{r}) = \varepsilon_i^{KS} \phi_i^{KS}(\vec{r}) \quad (2.108)$$

The ground state density of this system is easily obtained, by summing the square of the occupied orbitals, i.e.

$$\rho_{KS} = \sum_{i=1}^{occ} |\phi_i^{KS}(\vec{r})|^2 \quad (2.109)$$

The energy of the Kohn-Sham system is given by the following functional

$$\begin{aligned}
E_{KS}[\rho_{KS}] &= \langle \Phi[\rho_{KS}] | \hat{H}_{KS} | \Phi[\rho_{KS}] \rangle \\
&= \langle \Phi[\rho_{KS}] | \hat{T} + \hat{V}_{KS} | \Phi[\rho_{KS}] \rangle \\
&= \langle \Phi[\rho_{KS}] | \hat{T} | \Phi[\rho_{KS}] \rangle + \langle \Phi[\rho_{KS}] | \hat{V}_{KS} | \Phi[\rho_{KS}] \rangle \\
&= T_{KS} + \langle \Phi[\rho_{KS}] | \sum_{i=1}^{N_e} \hat{v}_{KS}(i) | \Phi[\rho_{KS}] \rangle \\
&= T_{KS} + \int \rho_{KS}(\vec{r}) v_{KS}(\vec{r}) d\vec{r}
\end{aligned} \tag{2.110}$$

The assumption of Kohn and Sham is that there exists an effective local potential $v_{KS}(\vec{r})$ of the non-interacting system, whose ground state density ρ_{KS} is the same as the ground state density ρ_0 of the interacting system.

In order to calculate ρ_{KS} , we need to define the Kohn-Sham (KS) potential $v_{KS}(\vec{r})$. Let us first consider the energy functional for the interacting system, Equation (2.103), and note that we can rewrite it as follows

$$E_0[\rho] = T[\rho] + V_{ne}[\rho] + V_{ee}[\rho] \tag{2.111}$$

$$= T_{KS}[\rho] + V_{ne}[\rho] + E_H[\rho] + E_{xc}[\rho] \tag{2.112}$$

$$= T_{KS}[\rho] + \int \rho(\vec{r}) v_{ne}(\vec{r}) d\vec{r} + \frac{1}{2} \int \int \frac{\rho(\vec{r})\rho(\vec{r}')}{|\vec{r} - \vec{r}'|} d\vec{r}d\vec{r}' + E_{xc}[\rho] \tag{2.113}$$

where we have explicitly defined the (classical) Coulomb interaction of two electron densities in the *Hartree functional* $E_H[\rho]$ and we have grouped all unknown terms into the *exchange-correlation functional* $E_{xc}[\rho]$, given by

$$E_{xc}[\rho] = (T[\rho] - T_{KS}[\rho]) + (V_{ee}[\rho] - E_H[\rho]) \tag{2.114}$$

One can check that by inserting Equation (2.114) into Equation (2.112), the original formulation for the ground state energy is recovered.

The only term which is not known in Equation (2.112) is the exchange and correlation functional $E_{xc}[\rho]$, which describes electronic exchange, electron correlation and the missing kinetic energy portion. The expression for $E_0[\rho]$ can be minimized with respect to the density, yielding, besides the kinetic energy of the KS system, the Kohn-Sham potential

$$v_{KS}(\vec{r}) = v_{ne}(\vec{r}) + v_H(\vec{r}) + v_{xc}(\vec{r}) \tag{2.115}$$

where $v_{xc} = \delta E_{xc} / \delta \rho$. This potential can now be inserted into the Kohn-Sham equations, Equation (2.108), such that we can now solve them in a self-consistent way, as it was done for HF theory.

As the analytical form of the exchange-correlation potential is not known, in the last decades a lot of effort in the field of DFT has been put into the development of better and better approximations of this potential. Considerable work has been carried out also in

the analysis of the exact form and constraints that such potential has to obey. We shall not discuss here in too much detail all the possible approximations, but rather give an overview of the different types of functional available.

The main ingredients characterizing the different types of functionals are the quantities on which they depend on. Namely, at the simplest level of approximation, the functional dependence is on the electron density only, i.e. $E_{xc} = E_{xc}[\rho]$. This typology of functional falls under the name local density approximation (LDA). LDA functionals usually tend to underestimate bond lengths and overestimate binding energies. They are the computationally least expensive and some notable examples are the X_α and Slater functionals^{99–101} as well as the VWN functional¹⁰². However, nowadays these functionals are almost not used anymore. An improvement upon LDA is obtained when also the information on the gradient of the density is included into the functional, namely $E_{xc} = E_{xc}[\rho, \nabla\rho]$. Such functionals are called GGA (generalized gradient approximation) functionals. GGA functionals behave roughly in the opposite way as LDA functionals do. Namely, they overestimate bond length, while underestimating binding energies. On the computational side, because the gradient of the density is required, they are more expensive than LDA. Notable examples of GGA functionals are PBE^{103,104}, BLYP^{105–107}, B97D¹⁰⁸. If also information on the second derivative of the density is included, e.g. the kinetic energy density through the occupied Kohn-Sham orbitals, the functional $E_{xc} = E_{xc}[\rho, \nabla\rho, \nabla^2\rho]$ is of meta-GGA type. In general, meta-GGA functionals provide reasonable results (on par with GGAs) for a larger number of system types (e.g. molecules, surfaces, etc.) at a slightly higher computational cost. Notable functionals in this class are TPSS¹⁰⁹, M06L¹¹⁰ and M11L¹¹¹. In combination with any of the above mentioned types of functionals, another class of approximation can be obtained by mixing a fraction of *exact exchange* into the exchange-correlation functional, e.g.

$$E_{xc} = aE_x^{DFT} + (1 - a)E_x^{HF} + E_c^{DFT} \quad (2.116)$$

where E_x^{HF} is obtained from Hartree-Fock theory as given in Equation (2.39) (note however that KS orbitals are used instead of canonical orbitals). Such functionals are named *hybrid functionals*. Hybrids improve upon GGAs on the most common properties: energies, geometries, reaction barriers, and so on. However, because of the introduction of the non-local HF exchange term, they are more expensive than GGA functionals although still applicable to large systems. This class of functionals contains some of the most famous names, among others B3LYP^{105,112}, PBE0¹¹³, TPSSh^{109,114,115} and APFD¹¹⁶. At last, if also information on the virtual orbitals is included, such that part of the correlation energy can be recovered in a MP2-like fashion, the functionals are called *double hybrids*. These functionals usually perform the best in standard benchmark calculations, however they are considerably more expensive than all other functionals, as one basically performs an MP2 calculation to obtain part of the correlation energy. The most famous of such functionals is probably the B2PLYP¹¹⁷ functional.

One of the biggest shortcomings of DFT is the inability of common functionals to correctly describe dispersion interactions. In general, the interaction energy of non-covalently bound complexes is largely underestimated or, in extreme cases, the fragments do not even result bound to each other. To obviate to this problem, several schemes have been proposed in the last 20 years or so, with one approach particularly standing out, namely the DFT-D method^{108,118}. The idea is very simple and straightforward, where the missing dispersion energy is added through the following general formula

$$E_{disp} = - \sum_{AB} \sum_{n=6,8,\dots} s_n \frac{C_n^{AB}}{R_{AB}^n} f_{damp}(R_{AB}) \quad (2.117)$$

Here, the sum goes over all atoms A and B , C_n^{AB} are the n -th order dispersion coefficients of the atom pair AB , s_n is a scaling factor and f_{damp} is a damping function which depends on the AB interatomic distance. Typically, the C_6 coefficients contribute the most part of the dispersion energy and coefficients of order higher than $n = 8$ are seldom included. Three-body effects are also present in this classical description of dispersion interactions, however they are generally excluded from this approach as they do not significantly improve the result, while increasing considerably the computational cost of the method. The DFT-D approach has proven very effective, and has been improving at each generation (from DFT-D1 to the latest DFT-D4). Arguably, the major downsides of this scheme are the inherent empiricism used to obtain the parameters and the fact that the dispersion correction does not affect the electron density of the system, at least up to the DFT-D3 version of the method.

To close the section on DFT, a few general and important remarks are made. From a strict theoretical point of view, DFT is an exact theory, however within the practical Kohn-Sham form, a certain degree of arbitrariness is introduced through the approximation of the exchange-correlation functional. These functionals are obtained, broadly speaking, in two main different ways. On one side, the functionals are made such that they obey *exact constraints*, on the other side, some of them are simply fitted to empirical data. Another important aspect regards the wave function obtained with the KS system. In KS DFT, one optimizes the electron density and therefore the KS wave function (i.e. the Slater determinant made of KS orbitals) does not represent an approximation of the true wave function.

2.1.8 Basis Sets in Quantum Chemistry

The notion of *basis set* in electronic structure theory is of fundamental importance in order to obtain accurate and meaningful results. Basis sets are one of the two main sources of errors introduced into the approximations required to solve the Schrödinger equation for a many-particle system.

In electronic structure methods, the typical choice is to use atom-centered basis functions called *atomic orbitals*. These are typically *Gaussian type orbitals (GTOs)*, either in *spherical*

harmonic form

$$\chi_{\zeta,n,l,m}(r, \theta, \phi) = NY_{l,m}(\theta, \phi)r^{2n-2-l}e^{-\zeta r^2} \quad (2.118)$$

or Cartesian

$$\chi_{\zeta,l_x,l_y,l_z}(x, y, z) = Nx^{l_x}y^{l_y}z^{l_z}e^{-\zeta r^2} \quad (2.119)$$

where N is a normalization factor, $Y_{l,m}(\theta, \phi)$ are spherical harmonic functions, the exponent ζ is a system- and basis-dependent parameter. In the Cartesian coordinates notation, the sum $l_x + l_y + l_z$ determine the angular momentum quantum number l . There is always less than or an equal number of spherical harmonic GTOs than Cartesian GTOs (1, 3, 5, 7, ... vs 1, 3, 6, 10, ...).

Although modern computational chemistry softwares generate the atomic orbital basis in Cartesian coordinates, the functions are usually transformed to spherical coordinates prior the actual computation since working with spherical functions has two main advantages: first, especially in the presence of high angular momentum, there are less functions to handle leading to important computational savings, and second, it reduces the problem of linear dependence for large basis sets⁹⁰.

The main reason for the adoption of GTOs is the simplicity with which two-electron integrals can be computed since their analytical expression is known. However, the term r^2 appearing in the exponential function provides for a wrong behavior of the GTO near the nucleus, where the orbital becomes flat with zero derivative in contrast to a cusp in the real wavefunction with a discontinuous derivative, and for large distances from the nucleus, where the orbital decays too quickly. In general, to circumvent these problems and try to reproduce the physically correct behavior of a Slater type orbital (STO), several GTOs are used to approximate a single STO. This leads to the definition of *contracted* basis sets, where typically a single atomic orbital is defined by the following contraction of several GTOs

$$\chi_{\mu} = \sum_{k=1}^K d_{k\mu} \kappa_k \quad (2.120)$$

The functions κ_k are called *primitive* GTOs, or just *primitives*. In general quantum-chemical calculations, one does not optimize the parameters of Equation (2.120), instead preoptimized values are used and kept fixed during the actual simulation. The set of contraction coefficients $d_{k\mu}$ and exponents hidden in κ_k are one of the features characterizing standard basis sets. The other being the number of AOs of a given angular momentum l . A *minimal* or *single zeta* (SZ) basis set contains just one contracted function for each atomic type, e.g. for the hydrogen atom it consists of one contracted *s*-type AO that describes the 1s atomic orbital. However, a minimal basis set is sufficient to provide acceptable results only for atomic systems. In order to deviate from the atomic spherical symmetry of orbital functions and to be able to describe chemical bonds, or to have virtual orbitals for the wave function expansion in correlated methods, one has to add at least a second set of contracted functions for each type. Such types of basis sets are called *double zeta* (DZ) basis sets. If three AOs per atom are used, we have a *triple zeta* (TZ) basis set, and so on. In general, just increasing the number of contractions of the same type is not the most

efficient way to improve the quality of the basis set. Before increasing from DZ to TZ, it is more effective to first add a set of higher angular momentum functions, called *polarization functions*, which accounts for, as the word suggests it, polarization effects. These functions turn out to be fundamental for describing the electron correlation. In a similar way, one can add polarization functions to higher quality basis sets too. In certain cases, such as for non-covalent interactions or when dealing with negatively charged systems, particularly diffuse AOs are required in order to cover appropriately all the space. These functions are denoted *diffuse functions* and are added to the basis sets similarly to the polarization functions.

By working with a finite basis set, the accuracy of any quantum-chemical result is limited by the size of the basis (besides the electronic structure method used). Ideally, one would like to work in a *complete basis set (CBS)*, thus allowing the wave function to have full flexibility and be faithfully represented in the space spanned by the basis. Since in practical calculations this is not possible but for the smallest systems, the CBS limit can instead be reached by performing the same calculation few times with an increasingly large basis set and then applying extrapolation formulas to reach this limit^{119–121}. This fact was noted early on, such that the creation and optimization of new basis sets has been carried out taking this point in consideration, thus providing basis sets with a well-defined hierarchy of qualities depending on the number and the angular momentum of the basis functions constituting it. This hierarchy is particularly important in order for smoothly improving the value of any desired molecular property when going from a basis set of a given quality to another one of a higher one.

Popular basis sets constructed in this way are the correlation consistent basis set of Dunning^{122,123}, the polarization consistent of Jensen^{124–126} and the Def2 of Ahlrichs¹²⁷. Among the basis sets that were not constructed in this manner, we count the very famous family of basis sets by Pople^{128,129}. Most of the standard basis sets also have preoptimized polarization and diffuse functions available that can be easily included in the calculation. For comprehensive review and a full list of references of the most popular basis sets is available in Ref. 130.

One of the biggest shortcomings of using finite basis sets is the basis set superposition error (BSSE), which arises in particular in the calculation of interaction energies in weakly bounded systems. As an example consider the complex AB , formed by fragments A and B . When computing the energy for the entire complex, the fragment A will take advantage of the presence of the basis functions centered on B , providing more flexibility compared to that obtained when only functions centered on A are available (the same holds the other way around for B). This results in an artificial lowering of the total energy of the complex. When computing the energy for the fragments alone, this flexibility is lost since the basis of the other fragment is not present in the calculation¹³¹. This problem may seem innocent, but it can actually account for a large deviation from the true value, especially when the basis set used is small. The most widely used solution

to this problem is the counterpoise correction proposed by Boys and Bernardi¹³², where the energy of the fragments is obtained in the full basis used for the complex.

To finish this section, we note that atom-centered basis sets are only *one* possible option in which molecular wave functions can be expanded. For instance, during the course of this thesis an alternative approach was investigated, in which a combination of atom-centered and distributed GTOs are used. This should, despite increasing the total number of functions in the basis set, provide major flexibility to the wave function and alleviate in part the BSSE problem. See Appendix A.4 for more information.

2.2 Molecular Dynamics

Another field of theoretical and computational chemistry is that of *molecular dynamics* (MD) simulations. Instead of considering the fine details of the electronic structure of atoms and molecules and (typically) their static properties, in MD simulations the molecular system is treated from a classical point of view and the dynamics, i.e. the evolution of the system in time, is studied by applying the classical equations of motion. The classical approximation allows to consider much bigger systems compared to those tractable by standard quantum chemical methods, albeit the degree of empiricism introduced into the formalism is usually higher. Molecular dynamics techniques simulate the movement of individual particles in a deterministic fashion. This in contrast to Monte Carlo (MC) techniques, where the configuration space is explored by successive snapshots of the systems which are generated stochastically and accepted probabilistically. While both MD and MC approaches provide information about the instantaneous structure of the system, only MD can be used to investigate the actual dynamics.

In a purely classical approach, in which both the dynamics of the nuclei as well as the potential energy of a system are calculated based on a parametrized force field¹⁵, a considerable amount of work is put into the choice of the latter and its parameters. In situations where the electronic structure of the species in the system generates complicated types of interaction, sophisticated potential energy functions have to be defined in order to reproduce the correct physics.

During a classical molecular dynamics simulation, a set of particles is allowed to evolve in time according to the laws of classical mechanics. Each individual particle trajectory is not particularly informative if considered by itself, but the strength of the methodology lies in the fact the complete set of trajectories is distributed according to a statistical ensemble, and thus the application of statistical physics laws permits to extract thermodynamic properties from the microscopic description of the system.

In the following we shall present a general overview of molecular dynamics, its principles and practical realization, whereas in the Results section we shall discuss the particular potential energy function derived and implemented as part of this thesis.

2.2.1 The Model System

The definition of the model system constitutes the first ingredient of a MD simulation. In general, within the MD framework there are different possible *resolutions* that can be defined for the system, depending on the type of application. The finest resolution is obtained by explicitly specifying all atoms present in the system, this choice provides the largest number of degrees of freedom. On the other hand, coarser models are an option too, e.g. when treating particularly large molecules such as proteins or, in general, biomolecules, where parts of the system can be defined as single entities instead of their constituting atoms, thus decreasing the total number of degrees of freedom; for instance

¹⁵For instance, one could compute the potential energy of the system using *ab initio* methods and then apply a classical equation of motion to carry out the dynamics of the nuclei.

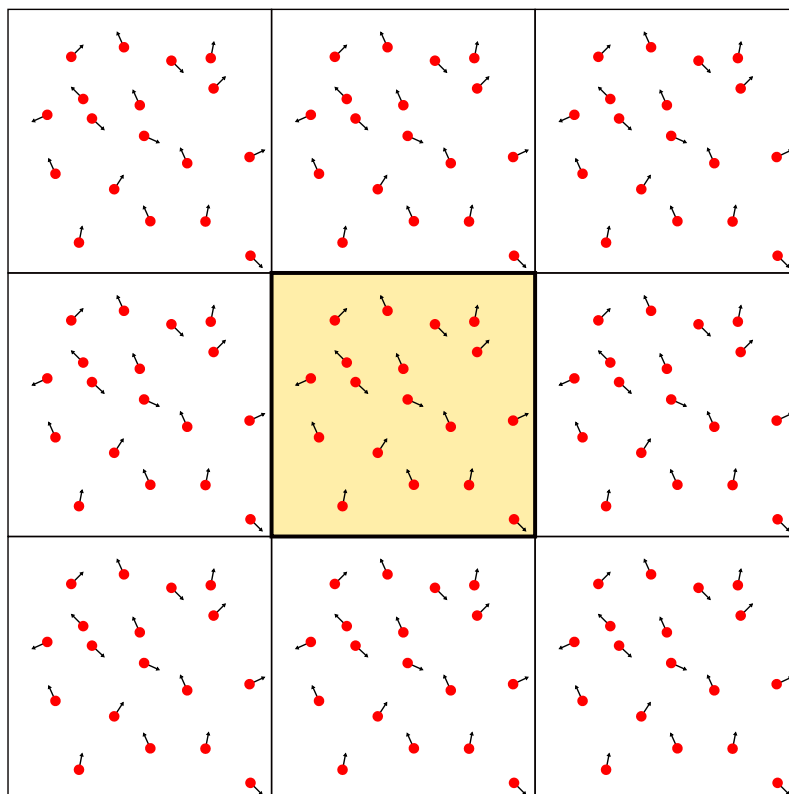


FIGURE 2.2: Model system example in a two-dimensional square box with periodic boundary conditions. Red discs represent the position of the particles, black arrows their velocity vector. As can be seen, the central highlighted box is replicated in both dimensions.

functional groups or solvent molecules can be approximated as a single particle. As far as we are concerned, we will assume for the rest of this thesis that the system is entirely composed by atoms.

In general atomistic simulations, the explicitly defined atoms are constrained to molecules, which are treated as unbreakable entities, such that no chemical reactions can occur during the simulation and thus the types of molecular species in the system cannot change in the course of a calculation.

The molecules constituting the system are placed in a simulation *box* (also called *cell*), which can have different shapes, most commonly cubic or parallelepiped ones. Associated to the simulation cell there the boundary conditions. Two options are available in principle: *PBC* and *OBC*. Although *OBC* can be useful in certain circumstances, the main interest of running MD simulations is in obtaining the bulk properties of a molecular system. This is reflected in the necessity of dealing with an enormous number molecules, which in practice is solved with the application of *PBC*. The simulation box is filled with a finite number of molecules and is then replicated through the entire space, along the three Cartesian directions. This allows to treat a virtually infinite system that does not suffer of any border effect. A two-dimensional representation of a model system as described so far is exemplified in Figure 2.2, which is in all intents and purposes analogous to the three-dimensional case. Clearly, all atomic properties can be (arbitrarily) specified,

such as masses, charges, polarizabilities and so on. Moreover, fictitious particles can also be defined, having e.g. zero mass but nonzero charge.

To summarize, the model system is composed by a number of molecules, treated as indivisible particles which are made up of atoms, each with their own atomic properties. The molecules are placed in a simulation box that has well defined dimensions, shape and boundary conditions. At this point, we shall see how atoms are held together in molecules during a calculation as well as how the latter interact with each other.

2.2.2 Classical Force Fields

The particles in the model system are governed by a classical force field which defines their total configuration energy V_{tot} .

The most general form of such a force field is given by the sum of two terms, i.e.

$$V_{tot} = V_b + V_{nb} \quad (2.121)$$

where V_b and V_{nb} stand for *bonded* and *non-bonded* interactions, respectively. Since all molecules are manually defined in an MD simulation, we emphasize again that no chemical reactions in which bonds are broken or created can happen. Consequently, the term V_b is an *intramolecular* potential, effectively accounting for the potential energy stored in all molecular entities and it depends on the atomic positions. The functional form of V_b is (typically) further decomposed in several contributions involving two, three and four atoms, describing the potential energy of bonds, bond angles and dihedral angles, respectively. The general expression for V_b can thus be mathematically expressed as

$$\begin{aligned} V_b(\vec{r}_1, \vec{r}_2, \dots, \vec{r}_N) = & \sum_{i=1}^{N_{bond}} V_{bond}(\vec{r}_{a_i}, \vec{r}_{b_i}) \\ & + \sum_{i=1}^{N_{angle}} V_{angle}(\vec{r}_{a_i}, \vec{r}_{b_i}, \vec{r}_{c_i}) \\ & + \sum_{i=1}^{N_{dihe}} V_{dihe}(\vec{r}_{a_i}, \vec{r}_{b_i}, \vec{r}_{c_i}, \vec{r}_{d_i}) \\ & + \sum_{i=1}^{N_{other}} V_{other}(\vec{r}_{a_i}, \vec{r}_{b_i}, \vec{r}_{c_i}, \vec{r}_{d_i}) \end{aligned} \quad (2.122)$$

where the sums of the different types of potentials go through all bonds N_{bond} , bond angles N_{angle} , dihedral angles N_{dihe} and any other type of intramolecular degrees of freedom N_{other} . Note that the term V_{other} is very general, for instance it can represent restrictions of the molecular geometry which do not strictly fall into a well-defined category of chemical conformation, such as inversion through a point in the case of molecular isomers.

The form of these terms is chosen according to the particular chemical species studied, such that it best reproduces the true physical interaction. As an example, consider the

term V_{bond} . A very common choice of potential energy function describing the bond energy, is given by an harmonic oscillator, i.e.

$$V_{bond}(\vec{r}_{a_i}, \vec{r}_{b_i}) = \frac{1}{2}k(r_{ab} - r_e)^2 \quad (2.123)$$

where r_{ab} is the distance between the two atoms forming the bond and r_e is the equilibrium distance of that bond. The stiffness of the bond is dictated by the harmonic (force) constant k . Equation (2.123) is only one possible form for the potential energy term describing a chemical bond, many more options exist, however we shall not list here all the alternatives but rather just illustrate the idea through the above example. Ultimately, the particular choice of these terms comes down to a tradeoff between accuracy and computational cost. It has to be noticed however, that in many occasions it might result more convenient from a computational perspective, but possibly also physical, to freeze some, or all internal degrees of freedom of the molecules, such as to avoid the use of an intramolecular potential. This approximation produces in general acceptable results in the case of very stiff systems, but is probably best avoided when dealing with particularly flexible molecules.

The non-bonded potential energy term V_{nb} models the *intermolecular* interactions of a system. It is often the hardest term to define as its form can vary a lot depending on the nature of the interactions between the molecules. As it is the case for the intramolecular potentials, different functional forms have been proposed during the years which differ in both accuracy and computational cost.

The general expression for V_{nb} can be summarized as follows

$$\begin{aligned} V_{nb}(\vec{r}_1, \vec{r}_2, \dots, \vec{r}_N) &= \sum_{i=1}^N \sum_{j>i}^N V_{2\text{-body}}(\vec{r}_i, \vec{r}_j) \\ &+ \sum_{i=1}^N \sum_{j>i}^N \sum_{k>j}^N V_{3\text{-body}}(\vec{r}_i, \vec{r}_j, \vec{r}_k) \\ &+ \sum_{i=1}^N \sum_{j>i}^N \sum_{k>j}^N \sum_{n>k}^N V_{4\text{-body}}(\vec{r}_i, \vec{r}_j, \vec{r}_k, \vec{r}_n) \\ &+ V_{nonadd}(\vec{r}_1, \vec{r}_2, \dots, \vec{r}_N) \\ &+ \sum_{i=1}^N V_{ext}(\vec{r}_i) \end{aligned} \quad (2.124)$$

where we note the change of indices for the atoms from a, b, c, \dots to i, j, k, \dots to emphasize that the *interacting centers* belong to different molecules. The most important contribution in Equation (2.124) is the sum over the *2-body* terms, which account for the *Van der Waals (VdW)* and the *electrostatic Coulomb* interactions. The *3-* and *4-body* potentials may be necessary in some cases, but are usually not included since are computationally demanding because of the extra nested sums. The potential energy function V_{nonadd} is a particularly challenging term as it accounts for non-additive types of interactions, such

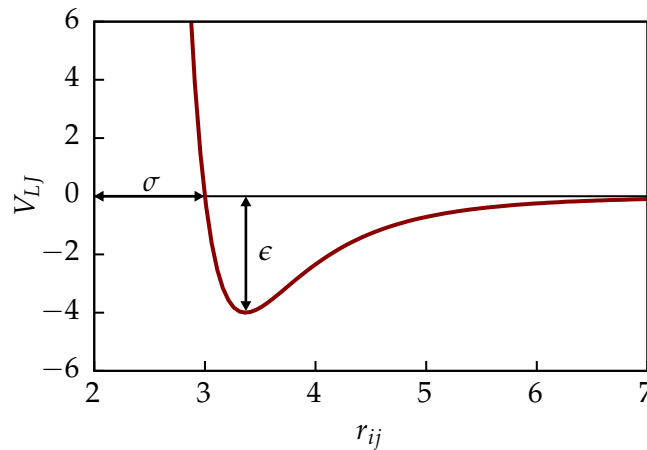


FIGURE 2.3: Example of the Lennard-Jones potential. All values are in arbitrary units.

as the induction interaction. There is no general form for this term because its transferability is very limited. Occasionally, in particular for spherically symmetric interacting units, non-additive effects can be incorporated into the *2-body* part of the potential. The last term, V_{ext} , describes the presence of an external potential acting on the system, such as that of an electric field.

The form of the VdW potential energy function is of utmost importance, and comprises a long-range attractive part and a short-range repulsive wall. The most famous of such potentials is without doubt the *Lennard-Jones (LJ)* potential, given by the following expression

$$V_{LJ}(r_{ij}) = 4\epsilon \left[\left(\frac{\sigma}{r_{ij}} \right)^{12} - \left(\frac{\sigma}{r_{ij}} \right)^6 \right] \quad (2.125)$$

where ϵ is the well depth of the potential and σ is the position at which the repulsive part crosses the zero energy value. An illustrative example to show the typical shape of the LJ potential is given in Figure 2.3 for $\epsilon = 4$ and $\sigma = 3$. The parameters ϵ and σ are set according to the interacting species and are usually obtained by fitting procedures to experimental data or *ab initio* simulations.

Many other functional forms for the VdW potential exist, in particular, we shall consider here a modified version of the LJ potential, named *Improved Lennard-Jones (ILJ)*¹³³. The ILJ potential is an attempt to improve the LJ potential in those places where it underperforms, while keeping it unchanged where it excels. In practice this means to improve the long range regime of the potential curve and its behavior at very short distances. This should be done in a way that affects it as little as possible around the equilibrium position, which is where the LJ potential is known to be accurate.

Such improvements are achieved by using the following expression

$$V_{ILJ}(r_{ij}) = \epsilon \left[\frac{m}{n(r_{ij}) - m} \left(\frac{r_m}{r_{ij}} \right)^{n(r_{ij})} - \frac{n(r_{ij})}{n(r_{ij}) - m} \left(\frac{r_m}{r_{ij}} \right)^m \right] \quad (2.126)$$

where

$$n(r_{ij}) = \beta + 4.0 \left(\frac{r_{ij}}{r_m} \right)^2 \quad (2.127)$$

The parameter r_m is the position of the well depth ϵ . The factor β is a free parameter which relates to the hardness of the system and its value usually varies between 7 and 9. The parameter m , which in particular appears as the exponent of the attractive part of the potential, is set according to the charge of the interacting species. For a neutral-neutral interaction, m is set equal 6, whereas for the ion-neutral case it becomes 4 and $m = 1$ for ion-ion. The introduction of distance-dependent factors and exponent through the function $n(r)$, improves the attractive and the repulsive regions of the potential, while preserving the LJ form around the equilibrium distance. Note how the ILJ potential only comes with an additional parameter, β , compared to the venerable LJ potential.

A practical requirement for the success of a potential function is the availability of the analytical first derivative with respect to the internuclear distance. This is needed, as we will see in the next subsection, to compute the forces acting on the particles. The numerical calculation of the forces requires considerable more computational effort compared to analytical expressions, that can actually be implemented directly into the MD computer program. The overall computational efficiency is a very important factor within the MD formalism, as millions of steps are carried out in a simulation, and it is probably one of the reasons behind the success of the LJ potential. Albeit the more complex functional form, also the ILJ potential admits analytical first derivatives and is thus well suited for this kind of simulations too.

The other important type of *2-body* potential is given by the Coulomb interaction between charged particles. In many cases, atoms within a molecule can be assigned partial charges describing an effective accumulation or depletion of electron density. When this is the case, two centers with charge q_i and q_j interact via

$$V_{els}(r_{ij}) = \frac{q_i q_j}{4\pi\epsilon_0 r_{ij}} \quad (2.128)$$

The contribution from this electrostatic term is in general quite large and of long range nature because of the $1/r$ dependence.

Typically, when particles are far apart, their non-bonded interactions are almost zero and it is thus computationally inefficient to explicitly calculate all of them, considering their overall small contribution. Therefore, it is common to introduce a *cutoff radius* which dictates up to which distance the intermolecular potential has to be computed; to account for the missing long range part an approximate contribution is calculated and added to the total. The cutoff radius cannot be larger than half of the simulation cell, and it effectively defines the range of interaction for all particles. In particular, in the context of PBC, it also helps to rationalize the concept of *minimum image convention* used to obtain the distances between interacting entities. An illustrative example for both the cutoff radius and the minimum image convention are depicted in Figure 2.4. After specifying all interactions within the system, we shall see in the next subsection how the evolution

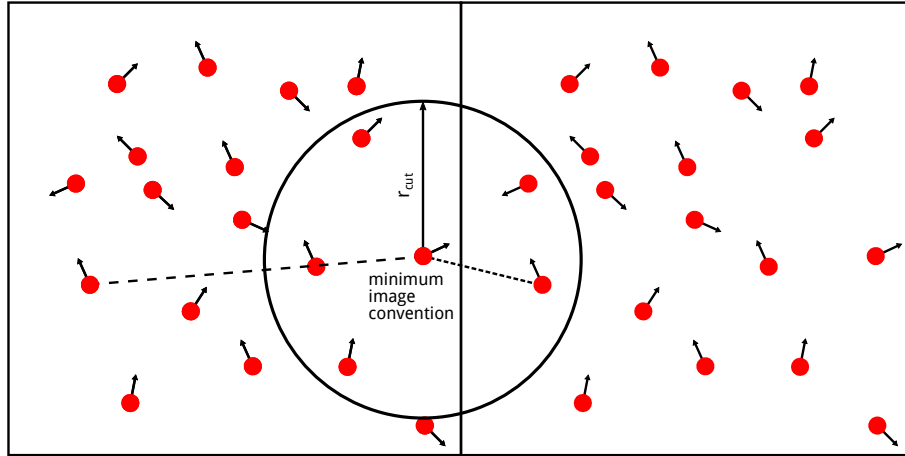


FIGURE 2.4: Example depicting the concept of cutoff radius and minimum image convention.

in time of the system is governed.

2.2.3 Newton's Equation of Motion

As it was mentioned in the introduction to this section, molecular dynamics simulations aim to study the evolution in time of a particular system. This is achieved by integrating Newton's equations of motion. Given a set of positions $\{\vec{r}_i\}$ of all particles, the dynamics is carried out by applying Newton's equations of motion, given by

$$\frac{d\vec{v}_i}{dt} = \frac{1}{m_i} \vec{f}_i \quad (2.129)$$

$$\frac{d\vec{r}_i}{dt} = \vec{v}_i \quad (2.130)$$

for $i = 1, 2, \dots, N_{tot}$, where m_i is the mass of particle i and \vec{f}_i is the total force (vector) acting on it. The force \vec{f}_i is obtained from the potential energy function U upon differentiation. In particular, the vector

$$\vec{f}_i = \begin{pmatrix} f_{i,x} \\ f_{i,y} \\ f_{i,z} \end{pmatrix} \quad (2.131)$$

is obtained for each Cartesian component $w = x, y, z$ by computing

$$f_{i,w} = \sum_{j \neq i} -\frac{\partial U(r_{ij})}{\partial w_i} \quad (2.132)$$

where

$$\frac{\partial U(r_{ij})}{\partial w_i} = \frac{\partial U(r_{ij})}{\partial r_{ij}} \frac{\partial r_{ij}}{\partial w_i} = \frac{\partial U(r_{ij})}{\partial r_{ij}} \frac{w_{ij}}{r_{ij}} \quad (2.133)$$

with $w_{ij} = w_i - w_j$. Therefore, the force in vector notation results

$$\vec{f}_i = \sum_{j \neq i} \vec{f}_{ij} = \sum_{j \neq i} -\frac{1}{r_{ij}} \left(\frac{\partial U(r_{ij})}{\partial r_{ij}} \right) \vec{r}_{ij} \quad (2.134)$$

As it was mentioned in the previous subsection, the derivative of the potential energy function is known in closed form, such that its calculation is straightforward.

The equations of motion in Equation (2.129) have to be integrated in order to carry out the dynamics and obtain the position of the particles as a function of time. In practice, this is done by first discretizing the time dimension in *timesteps* of size Δt and then integrate numerically the equations. Different types of *integrators* can be used, the two most famous being the *velocity verlet* and the *leapfrog* algorithms, both based on a Taylor expansion of the equations of motion. For instance, in the *leapfrog* scheme, forces and position are known at integer timesteps while velocities at half-integer timesteps, i.e.

$$\vec{v}(t + \frac{1}{2}\Delta t) = \vec{v}(t - \frac{1}{2}\Delta t) + \frac{\vec{f}(t)}{m} \Delta t \quad (2.135)$$

and

$$\vec{r}(t + \Delta t) = \vec{r}(t) + \vec{v}(t + \frac{1}{2}\Delta t) \Delta t \quad (2.136)$$

This algorithm is fast and very economical, since one does not need to store the entire history of positions and velocities, but a single set only. Although velocities are known at half integer steps, it is in general useful to know them at integer positions, and this can be achieved by storing an extra set of velocities at a previous timestep and then averaging over the two of them. A disadvantage of the *leapfrog* scheme is that the Taylor series used to derive Equations (2.135) and (2.136) is truncated early, such that positions are accurate up to terms Δt^4 and velocities to Δt^2 only. This implies extra care in the choice of the timestep. The usual length of Δt is thus a crucial parameter for a stable integration of Equation (2.129) and it is usually chosen in the sub-femtosecond regime. The restriction of a short timestep forces an MD simulation to be run for millions of steps in order to reach sensible results, i.e. for a time period which is sufficient to extract relevant information about the system. At last, an important fact regarding the *leapfrog* algorithm is that it shows little long term energy drift since it is time-reversible as it is discussed by Frenkel and Smit¹³⁴.

2.2.4 Statistical Thermodynamics

At last, let us briefly introduce a concept required in practice for molecular dynamics simulations: the *statistical ensemble*. The connection between the *microscopic* view of a system, i.e. at the molecular level, and the *macroscopic* properties that we usually measure in a laboratory, such as temperature, pressure and so on, is given by *statistical physics*. Essentially, the transition from properties of individual particles to the thermodynamics of large groups of molecules happens by recognizing that the latter arises from a collective behavior which can be captured by taking averages over the microscopic system.

TABLE 2.1: Most common statistical ensembles.

name	conserved	non-conserved
canonical	N, V, T	μ, P, E
microcanonical	N, V, E	μ, P, T
grand canonical	μ, V, T	N, P, E

More concretely, a macroscopic observable A can be calculated as the weighted average of the corresponding microscopic variables a_i , i.e.

$$\langle A \rangle = \frac{1}{N} \sum_i^N p_i a_i \quad (2.137)$$

where p_i is the probability of the system to be in microstate i out of N .

In general, an important assumption is made with regard on how the microscopic state i is generated, and correspondingly the microscopic quantity a_i . In both MD and real life experiments, mean values of properties are obtained by averaging over states at different points in time, rather than over an independent ensemble of systems. The assumption that time-averaging is equivalent to ensemble averaging is known as the *ergodic hypothesis*.

An *ensemble* is, broadly speaking, the (infinite) repetition of a closed system with specified thermodynamic properties, in contact with each other. This is very much the situation we constructed ad-hoc in the first subsection, where we introduced the model system with PBC. Within an ensemble, different microscopic states can occur with different probabilities. However, there will be a dominant configuration, such that the ensemble will be most certainly in that configuration most of the time. This particular state practically dominates the properties of the system completely and it naturally comes from the *Boltzmann's distribution*. The extraction of quantitative information from the ensemble then happens through the *partition function*, which describes the thermodynamic system as much as the wave function describes the quantum mechanical one.

In practice, different ensembles exist, defined by the conserved thermodynamic quantities. These are given Table 2.1. Note that the thermodynamic quantities come in pairs: number of particles N and chemical potential μ , volume V and pressure P , energy E and temperature T . Furthermore, the first property of each pair is *extensive* whereas the second is *intensive*.

The microcanonical ensemble: constant N, V, E .

The evolution of time as described in the previous subsections, with the integration of Newton's equations of motion generates in a natural way a series of microscopic states, whose number N , volume V and energy E are conserved throughout the simulation. This situation corresponds to the microcanonical ensemble and consequently this is "natural" ensemble of Molecular Dynamics simulation.

The canonical ensemble: constant N, V, T .

There are practically no real experiments happening at constant energy. It is actually

much more case that the temperature T is held constant. Therefore, different approaches for running MD simulations at constant temperature were developed. Arguably the most notable example is the method developed by Nosé and Hoover, which generates deterministic trajectories according to the canonical ensemble by modifying the equations of motion with the introduction of a frictional coefficient. In this way, the instantaneous kinetic energy is adapted to the desired one according to a specified time constant, usually in the range of 0.5-2.0 picosecond.

We shall not dive further into the topic of statistical thermodynamics as that goes beyond the scope of this section on classical molecular dynamics, it is however important to retain some basic concepts affecting the simulation setup. There are different ensembles, each of which has different conserved quantities. The choice of ensemble defines the type of experimental conditions simulated during the MD calculation. Statistical thermodynamics is the theory connecting the microscopic world to the macroscopic quantities, which ultimately allows to extract meaningful data from atomistic simulations. A series of assumptions, constraints and approximations apply within the framework of molecular dynamics, some of which were presented in this section and some other were not discussed. Nevertheless, the purpose of this section was to provide the basic necessary ingredients to perform an MD simulation and thus merely scratched the surface of the theoretical foundations of atomistic simulations and statistical physics.

2.2.5 Molecular Dynamics Algorithm

We shall finish the theoretical part of MD simulations with a sketch of the algorithm driving them. In very general terms, an algorithm for a molecular dynamics simulation can be summarized as follows:

1. define the ensemble, the corresponding thermodynamic properties, the timestep, the number of steps, the sampling frequency, and any other required parameter
2. select initial positions and velocities for all particles in the system to start the simulation
3. compute the forces on all particles
4. integrate the equations of motion to obtain new position and velocities
5. compute the system properties required and of interest
6. go back to point 3 and iterate until the dynamics has run for the number of steps desired

The system properties which are computed during the simulation are averaged and printed at the end. During the simulation, a large amount of data is also reported, such as the particle positions and velocities, as well as system properties. These are usually written in an output file which can later be used to analyse the trajectory and the time evolution of the properties.

3 Cyclacenes

In this chapter, an extensive theoretical study on the electronic structure and a number of molecular properties of cyclacenes is presented.

All the results reported here and supplementary information are available in the following two scientific articles published during the course of the thesis:

- S. Battaglia, N. Faginas-Lago, D. Andrae, S. Evangelisti and T. Leininger, *Journal of Physical Chemistry A*, 121, 3746–3756, 2017
- S. Battaglia, H.-A. Le, G. L. Bendazzoli, N. Faginas-Lago, T. Leininger and S. Evangelisti, *International Journal of Quantum Chemistry*, 118, e25569, 2018

3.1 Introduction

Cyclacenes, or more appropriately $[n]$ cyclacenes, are a type of carbon nanobelts obtained by wrapping around linear polyacenes with n hexagonal units and by joining the two ends together, as depicted in Figure 3.1. Their first appearance in the literature was in 1954, when Edgar Heilbronner presented these carbon nanostructures in a theoretical study based on Hückel theory¹³⁵.

Despite being known for a long time, these systems are still challenging both experimental and theoretical chemists, due to their difficult (not yet achieved) synthesis and complicated electronic structure.

Besides the many reasons behind the interest on $[n]$ cyclacenes, a major one is certainly due to their remarkable resemblance to carbon nanotubes. In fact, cyclacenes constitute a single unit of zigzag CNTs, i.e. the shortest possible nanotubes. If achieved, a successful synthesis of cyclacenes would allow the controlled production of arbitrarily long zigzag carbon nanotubes in a “bottom-up” fashion⁴². This has been achieved already with larger precursors or for other classes of CNTs, but cyclacenes would give the most flexibility being the shortest possible building units^{36,136–138}.

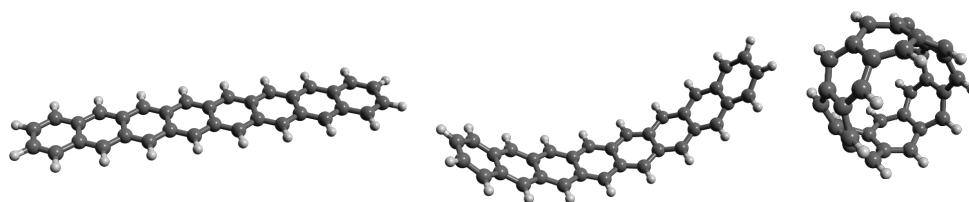


FIGURE 3.1: Wrapping of a linear octacene into an [8]cyclacene.

As it is the case for the closely related linear polyacenes, $[n]$ cyclacenes show very interesting electronic and magnetic properties^{139–142}. The former could be exploited for example for light-harvesting devices and similar applications, in particular due to their size-dependent electronic states gap. The latter, on the other hand, suggest the use of cyclacenes as organic molecular magnets, this time due to the open-shell character of the ground state, in which the number of unpaired electrons depends on the size of the molecule.

Clearly, the particular shape of these systems also suggests them as good candidates for host-guest chemistry applications, as it is the case for carbon nanotubes.

Despite the synthetic interest in $[n]$ cyclacenes, these molecules constitute a fertile ground for theoreticians too; on one side their electronic structure has proven to be difficult to describe by several *ab initio* methods, while on the other side they can be used as conceptual models for understanding more complicated hydrocarbons.

Although several types of carbon nanobelts are experimentally accessible and continues to grow, e.g. a new system was recently successfully obtained^{45,143}, the synthesis of $[n]$ cyclacenes has not been achieved yet. Besides the high strain¹⁴⁴, the crucial obstacle was identified in the high reactivity of these systems due to the radical nature of their electronic ground state^{40,41,46}.

The experimental inaccessibility of cyclacenes thus fosters even more the need for theoretical investigations, which are widely available in the literature.

These systems were extensively investigated using semi-empirical approaches in the late 90s and early 2000s by a number of authors^{145–155} and more recently a few more analytical works based on HMO theory, or variations thereof, were published^{156–159}.

Besides the results based on semi-empirical approximations, several groups have investigated $[n]$ cyclacenes using *ab initio* methods too, providing access to more quantitative results^{139,140,160–164}.

The analysis of most of the semi-empirical studies focused on the geometrical parameters as well as the behavior of electronic properties such as the gap between the highest occupied molecular orbital (HOMO) and lowest unoccupied molecular orbital (LUMO) as a function of the number of rings n . It was found that the gap decreases in an alternating way depending on the parity of n as more units are added to the system. Different types of methodologies predicted slightly different values, although all of them are in agreement with respect to the general trend with respect to the size of the system. The main structural properties studied were the C–C bond lengths perpendicular and parallel to the principal axis passing through the center of the nanobelt. The bonding pattern depends on the parity and the size of n , however different methodologies provide different symmetric properties. The zigzag pattern of C–C bonds forms two parallel polyacetylene ribbons which are connected through the parallel C–C bonds. It was found that the polyacetylene chains undergo dimerization at AM1 level of theory¹⁵⁵, whereas the parallel bonds result longer than the perpendicular ones. The geometrical distortions influence the electronic structure, in particular, the effect of dimerization was found to

uniformly increase the HOMO–LUMO gap with respect to the non-dimerized conformation¹⁵⁵. Albeit the AM1 case, fully symmetric geometries were found or used for the other methodologies.

The large number of semi-empirical investigations are supplemented by a number of *ab initio* studies based on both DFT and wave function approaches. These works focused mainly on the character of the ground state wave function, the energy gap between the ground and the first excited state and the radical nature of the molecule with respect to its size.

Based on DFT calculations, Choi and Kim¹³⁹ investigated the singlet–triplet energy gap, the carbon–carbon bond lengths and the magnetic properties of cyclacenes as a function of the number of rings. A second work based on DFT appeared soon after¹⁴⁰, also reporting the ground–excited state gap with respect to n . In both cases, the authors found a weakly increasing gap as a function of increasing n , and in one case a triplet ground state. However, a few years later, those results were found to be erroneous according to calculations with more sophisticated multireference wave function methods¹⁶⁰. In particular, the ground state of cyclacenes was predicted to be an open-shell singlet state irrespective of the size. These results were further assessed and confirmed by Sadowsky et al.¹⁶¹, who showed that the increasing gap was the result of a singlet instability of the ground state. A recent study by Wu et al.¹⁶² explored a series of electronic properties of $[n]$ cyclacenes by thermally-assisted-occupation DFT (TAO-DFT) and found agreement with the works based on high-level *ab-initio* methods.

In particular, besides establishing the lowest electronic state, the behavior of the electronic gap was calculated for a very large number of system sizes.

In the following, an investigation by semi-empirical and wave function approaches is presented, focusing with the former on a few molecular properties and with the latter on the electronic gap and the radical character of cyclacenes.

3.2 Analytical Tight-Binding

An important feature of $[n]$ cyclacenes is the large presence of molecular symmetries. In particular, these can be exploited within the tight-binding approximation allowing for a substantial simplification of the Hamiltonian, and consequently the eigensolutions.

Cyclacenes can be modeled as n identical units (forming n hexagonal rings) with a unified C–C bond length b and lying on a circumference of radius $R = nb\sqrt{3}/2\pi$ as shown in Figure 3.2. It is convenient to define a unit cell of an $[n]$ cyclacene according to Figure 3.3, with four orthonormal p -like orbitals p_{μ}^{ν} , where $\mu \in [0, n - 1]$ denotes the cell number in the molecule and $\nu \in [1, 4]$ the atom within the cell. The orbitals p_{μ}^{ν} are assumed to be eigenfunctions of the position operator, thus, for $r = x, y, z$, they satisfy

$$\langle p_{\mu}^{\nu} | \hat{r} | p_{\mu'}^{\nu'} \rangle = r_{\mu}^{\nu} \delta_{\nu\nu'} \delta_{\mu\mu'} \quad (3.1)$$

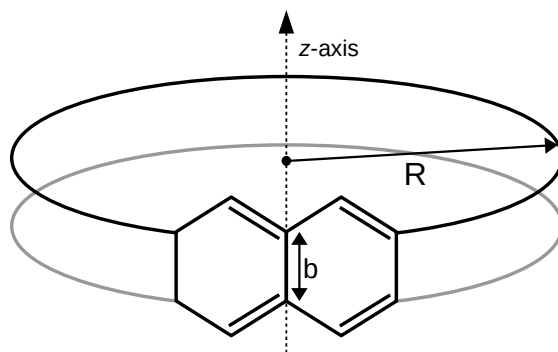


FIGURE 3.2: Simplified scheme of a cyclacene.

3.2.1 The Tight-Binding Energies and Orbitals

The Hamiltonian is defined as presented in the theoretical section of HMO theory, with the Coulomb and resonance integrals given by

$$\langle p_{\mu}^{\nu} | \hat{H} | p_{\mu}^{\nu} \rangle = a \quad (3.2)$$

and

$$\langle p_{\mu}^{\nu} | \hat{H} | p_{\mu'}^{\nu'} \rangle = -t \quad (3.3)$$

if $\nu' = \nu \pm 1$ and $\mu' = \mu \pm 1$ (note that special care has to be taken for the boundary cases).

By exploiting the symmetry properties of the system, it is possible to obtain analytical expressions of the four energy bands (a full derivation is available for instance in Ref.

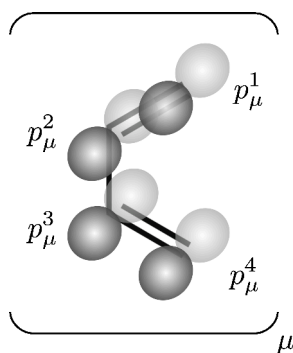


FIGURE 3.3: Scheme of the unit cell μ of the cyclacene with attached basis functions.

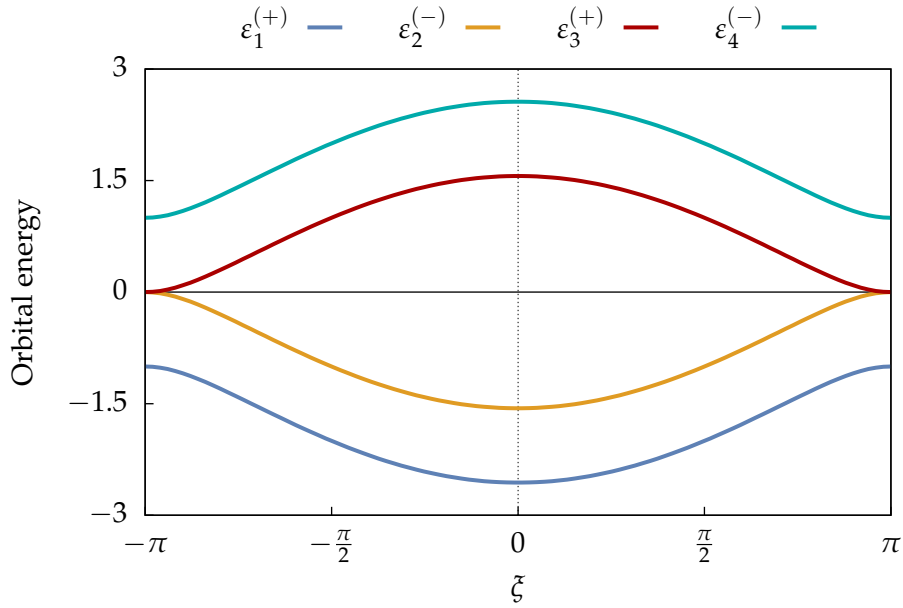


FIGURE 3.4: Energy bands (in t units) at Hückel level of theory for $a = 0$ and $t = 1$.

158), given by

$$\begin{aligned}
 \varepsilon_1(\zeta) &= a - \frac{t}{2}(+1 + \sqrt{9 + 8 \cos \zeta}) \\
 \varepsilon_2(\zeta) &= a - \frac{t}{2}(-1 + \sqrt{9 + 8 \cos \zeta}) \\
 \varepsilon_3(\zeta) &= a - \frac{t}{2}(+1 - \sqrt{9 + 8 \cos \zeta}) \\
 \varepsilon_4(\zeta) &= a - \frac{t}{2}(-1 - \sqrt{9 + 8 \cos \zeta})
 \end{aligned} \tag{3.4}$$

where $\zeta = k\theta$, k is an integer number and $\theta = 2\pi/n$.

Note that because $-t$ is negative, the eigenvalues are labeled in increasing order, i.e. ε_1 is the smallest while ε_4 is the largest for any value of k . Clearly, also the eigenvectors are analytically known and read

$$|m, k\rangle = \frac{1}{\sqrt{n}} \sum_{\mu=0}^{n-1} e^{\frac{2\pi i k \mu}{n}} \left[c_{1,m}(k\theta) p_{\mu}^1 + c_{2,m}(k\theta) p_{\mu}^2 + c_{3,m}(k\theta) p_{\mu}^3 + c_{4,m}(k\theta) p_{\mu}^4 \right] \tag{3.5}$$

where we point out that m and k represent quantum numbers related to the symmetry of the system. In particular, the quantum number m is related to the σ_h plane cutting the cyclacene in half, and note that the eigenvectors with $m = 1, 3$ and $m = 2, 4$ are symmetric and antisymmetric, respectively, upon reflection.

The four energy eigenvalues, which actually represent energy bands in reciprocal space, are plotted in Figure 3.4 for $\zeta \in [-\pi, \pi]$ with $a = 0$ and $t = 1$. Knowing the analytical form of the energy bands allows to obtain the bandgap formula in closed form for the

whole Brillouin zone, which is given by

$$\Delta(\xi) = \varepsilon_3(\xi) - \varepsilon_2(\xi) = t \left(\sqrt{9 + 8 \cos(\xi)} - 1 \right) \quad (3.6)$$

where we notice the closure for $\xi = \pi$ since the eigenvalues $\varepsilon_2(\pi)$ and $\varepsilon_3(\pi)$ are degenerate at this level of theory.

In finite systems, the size of the gap depends on the integer value k : the gap vanishes if and only if there exists a k such that $\xi = k\theta = \pi$. Since $\theta = 2\pi/n$, this implies that n must be even.

For a finite-size [n]cyclacene, the total energy is given by the sum of the occupied orbitals energies as

$$\mathcal{E}_{tot} = 2 \sum_{k=0}^{n-1} \left[\varepsilon_1(k\theta) + \varepsilon_2(k\theta) \right] = 2 \sum_{k=0}^{n-1} \left[2a - t\sqrt{9 + 8 \cos k\theta} \right] \quad (3.7)$$

The factor 2 in front of the sum is due to the double occupancy of each molecular orbital. Note the relation between molecular orbital and band theory, for every allowed point $k\theta$ it corresponds a molecular orbital and the associated energy. In the limit $n \rightarrow \infty$, the orbital energies eventually form the smooth energy bands appearing in Figure 3.4. Within this simple approximation, the discrete expression for the energy in Equation (3.7) can be evaluated in closed form as

$$\mathcal{E}_{tot} = \frac{n}{\pi} \int_{-\pi}^{\pi} \left[\varepsilon_1(\xi) + \varepsilon_2(\xi) \right] d\xi = 4n \left(a - \frac{\sqrt{17}tE\left[\frac{16}{17}\right]}{\pi} \right) \quad (3.8)$$

with the help of the complete elliptic integral of 2nd kind $E[x]$.

3.2.2 Molecular Properties of Cyclacenes

The benefit of working within a simple approximation such that of Hückel theory has, among others, two main advantages. On one side, it is possible to derive analytical expressions for a number of molecular properties, thus obtaining their asymptotic behavior to the thermodynamic limit and predict the property of the bulk. On the other side, in the case such closed-form expressions cannot be found, the low computational complexity of the method allows to reach the thermodynamic regime and extract the asymptotic behavior of the property by repeated numerical calculations on systems of increasing size.

Two, intimately related, interesting properties to investigate are the total position spread (TPS) and the static molecular polarizability.

The TPS tensor was introduced by Resta and co-workers under the name of localization tensor (LT)^{165–167} and defined differently to the TPS by a factor equal to the number of electrons. In molecular systems, it was found that the TPS provides interesting information on the nature of chemical bonding, being able to discern different types of

bonds^{168,169}. On the other hand, in the context of materials, the TPS is able to differentiate insulators from conductors according to its asymptotic behavior with respect to the system size. Concretely, the TPS increases linearly with the system size in the case of insulators, while quadratically when the material behaves as a metal¹⁶⁶. In terms of the LT, in the former case the quantity is constant as a function of the size and in the latter case it diverges (linearly).

The TPS is a tensor quantity defined as the second moment cumulant of the total position operator, i.e.

$$\Lambda_{rr'} = \langle \Phi_0 | \hat{R}_r \hat{R}_{r'} | \Phi_0 \rangle - \langle \Phi_0 | \hat{R}_r | \Phi_0 \rangle \langle \Phi_0 | \hat{R}_{r'} | \Phi_0 \rangle \quad (3.9)$$

where $\hat{R}_r = \sum_{i=1}^N \hat{r}(i)$ is the sum over the one-electron position operators (with $r, r' = x, y$ and z), N the number of electrons and $|\Phi_0\rangle \equiv |0\rangle$ the state of interest (usually the ground state).

By exploiting the resolution of the identity technique, the TPS tensor can be conveniently written in a sum over many-electron excited states $|\Phi_I\rangle \equiv |I\rangle$

$$\Lambda_{rr'} = \sum_I \langle 0 | \hat{R}_r | I \rangle \langle I | \hat{R}_{r'} | 0 \rangle - \langle 0 | \hat{R}_r | 0 \rangle \langle 0 | \hat{R}_{r'} | 0 \rangle \quad (3.10)$$

which in the case of the diagonal components ($r = r'$) simplifies to

$$\Lambda_{rr} = \sum_{I>0} |\langle 0 | \hat{R}_r | I \rangle|^2 \quad (3.11)$$

The form of Equation (3.11) has the advantage to be strictly related to the polarizability, which can be easily obtained by dividing the term $|\langle 0 | \hat{R}_r | I \rangle|^2$ by the energy difference between the state $|I\rangle$ and the state $|0\rangle$, resulting in

$$\alpha_{rr} = \sum_{I>0} \frac{|\langle 0 | \hat{R}_r | I \rangle|^2}{\mathcal{E}_I - \mathcal{E}_0} \quad (3.12)$$

This approach is particularly suited when dealing with model Hamiltonians, since in general the many-particle states $|I\rangle$ spanning the complete space are known. In other words, the use of this technique gives the exact value of the TPS and the polarizability within the approximations introduced by the model Hamiltonian.

Since the operator \hat{r} is mono-electronic, the only non-zero elements appearing in Equations (3.11) and (3.12) are those between the ground state $|0\rangle$ and single excitations thereof. In practice, due to the simple form of the Hückel wave function, they reduce to integrals over occupied and empty orbitals. In particular, for cyclacenes, the total position spread tensor takes the following form

$$\sum_{I>0} |\langle 0 | \hat{R}_r | I \rangle|^2 = 2 \sum_{m=1}^2 \sum_{k=0}^{n-1} \sum_{m'=3}^4 \sum_{k'=0}^{n-1} |\langle m, k | \hat{r} | m', k' \rangle|^2 \quad (3.13)$$

where non-primed indices run over occupied orbitals, primed indices over empty orbitals and the factor 2 in front comes, as before, from the double electron occupancy of the

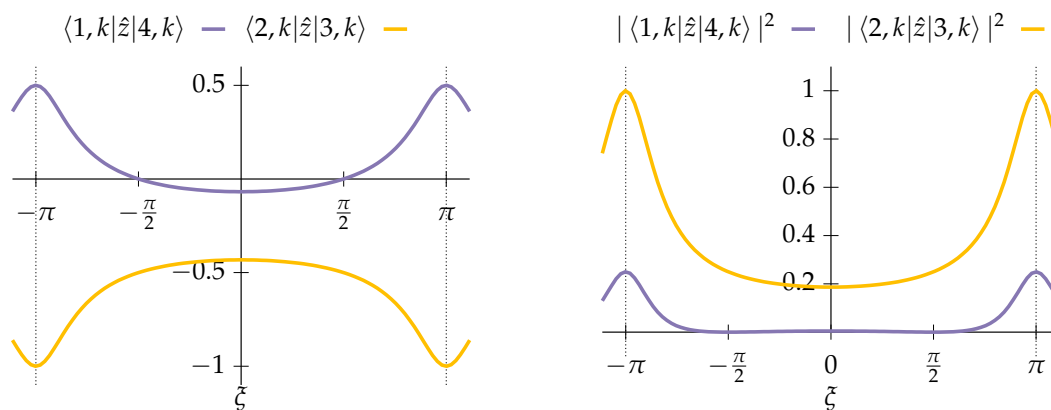


FIGURE 3.5: Nonvanishing integrals (left) and squared integrals (right) in b and b^2 units, respectively, contributing to the axial component of the TPS.

MOs. The polarizability can be obtained in a straightforward manner by simply dividing Equation (3.13) with the energy difference between the states.

3.2.3 Axial Component of TPS and Polarizability

To take advantage of the molecular symmetry, it is convenient to treat the axial component of both tensors, i.e. Λ_{zz} and α_{zz} , separately from the longitudinal ones.

By substituting \hat{r} with \hat{z} in Equation (3.13) we can explicitly find the expressions contributing to the TPS and the polarizability. Given that \hat{z} is an odd function with respect to the reflection plane σ_h , the two orbitals $|m, k\rangle$ and $|m', k'\rangle$ involved in the integration *must* be of different reflection symmetry in order for the integrand to be even. Furthermore, since the position operator is multiplicative, the integral will not vanish only for those states with $k = k'$. Therefore, considering that one of the orbitals has to be empty and the other one occupied, the only non-zero integrals surviving are

$$\langle 1, k | \hat{z} | 4, k \rangle = \frac{b}{4} \left(-1 + \frac{3}{\sqrt{9 + 8 \cos \zeta}} \right) \quad (3.14)$$

$$\langle 2, k | \hat{z} | 3, k \rangle = \frac{b}{4} \left(-1 - \frac{3}{\sqrt{9 + 8 \cos \zeta}} \right) \quad (3.15)$$

which can be seen in the left plot of Figure 3.5 for the arbitrary C–C bond length $b = 1$. Inspecting Equation (3.13) we realize that the actual terms appearing in the sum are the squared values of the integrals, which are instead reported on the right plot appearing in Figure 3.5. The squared integrals of Figure 3.5 have a finite value at every point ζ in the interval delimited by the two vertical dotted lines. Considering Equation (3.13), we notice that Λ_{zz} is a finite sum depending on the number of units n in the system, therefore we also expect a finite value for the axial component of the TPS. On the other hand, at the thermodynamic limit, i.e. for $n \rightarrow \infty$, the TPS will diverge.

By explicitly summing the contributions according to Equation (3.13), we obtain

$$\begin{aligned}\Lambda_{zz} &= 2 \sum_{k=0}^{n-1} \left[|\langle 1, k | \hat{z} | 4, k \rangle|^2 + |\langle 2, k | \hat{z} | 3, k \rangle|^2 \right] \\ &= \frac{b^2}{4} \sum_{k=0}^{n-1} \left(1 + \frac{9}{9 + 8 \cos k\theta} \right)\end{aligned}\quad (3.16)$$

which, in the limit of large values of n can be expressed as the following integral

$$\Lambda_{zz} = \frac{n}{2\pi} \int_{-\pi}^{\pi} 2 \left[|\langle 1, k | \hat{z} | 4, k \rangle|^2 + |\langle 2, k | \hat{z} | 3, k \rangle|^2 \right] d\zeta = \frac{nb^2}{68} \left(17 + 9\sqrt{17} \right) \quad (3.17)$$

Equation (3.17) provides an analytical formula to calculate Λ_{zz} given a large value of n . This result is particularly important because it reveals the dependence of Λ_{zz} on the system size n , which is in this case linear. This means that cyclacenes behave as insulators along the z Cartesian coordinate and is equivalent to have a finite LT for $n \rightarrow \infty$. Roughly speaking, from a subatomic point of view this can be interpreted as electrons fluctuations along the z direction remaining bounded by the system, since the latter only grows in the other two Cartesian coordinates as a function of increasing n .

In a completely similar manner, the α_{zz} component of the polarizability is obtained by dividing $|\langle 1, k | \hat{z} | 4, k \rangle|^2$ and $|\langle 2, k | \hat{z} | 3, k \rangle|^2$ with $\varepsilon_4 - \varepsilon_1$ and $\varepsilon_3 - \varepsilon_2$, respectively. This results in the following two terms

$$\frac{|\langle 1, k | \hat{z} | 4, k \rangle|^2}{\varepsilon_4 - \varepsilon_1} = \frac{b^2 \left(-1 - \frac{3}{\sqrt{9+8 \cos \zeta}} \right)^2}{16t \left(1 + \sqrt{9 + 8 \cos \zeta} \right)} \quad (3.18)$$

and

$$\frac{|\langle 2, k | \hat{z} | 3, k \rangle|^2}{\varepsilon_3 - \varepsilon_2} = \frac{b^2 \left(-1 - \frac{3}{\sqrt{9+8 \cos \zeta}} \right)^2}{16t \left(-1 + \sqrt{9 + 8 \cos \zeta} \right)} \quad (3.19)$$

Equations (3.18) and (3.19), are shown in Figure 3.6 for $b = 1$ and $t = 1$. Differently to the TPS, the $2 \rightarrow 3$ transition element diverges at $\zeta = \pi$ due to the vanishing gap in the denominator. Therefore integrating this quantity will diverge as well, i.e.

$$\int_{-\pi}^{\pi} \frac{|\langle 2, k | \hat{z} | 3, k \rangle|^2}{\varepsilon_3 - \varepsilon_2} d\zeta \rightarrow \infty \quad (3.20)$$

The explicit computation of the total polarizability α_{zz} in the limit of large n proceeds analogously to the TPS one, which results in

$$\alpha_{zz} = \frac{n}{2\pi} \int_{-\pi}^{\pi} 2 \left[\frac{|\langle 2, k | \hat{z} | 3, k \rangle|^2}{\varepsilon_3 - \varepsilon_2} + \frac{|\langle 1, k | \hat{z} | 4, k \rangle|^2}{\varepsilon_4 - \varepsilon_1} \right] d\zeta \quad (3.21)$$

However, in this case the divergence for $n \rightarrow \infty$ is faster than linear since albeit the factor n in front of the expression, the integral itself diverges due to Equation (3.19).

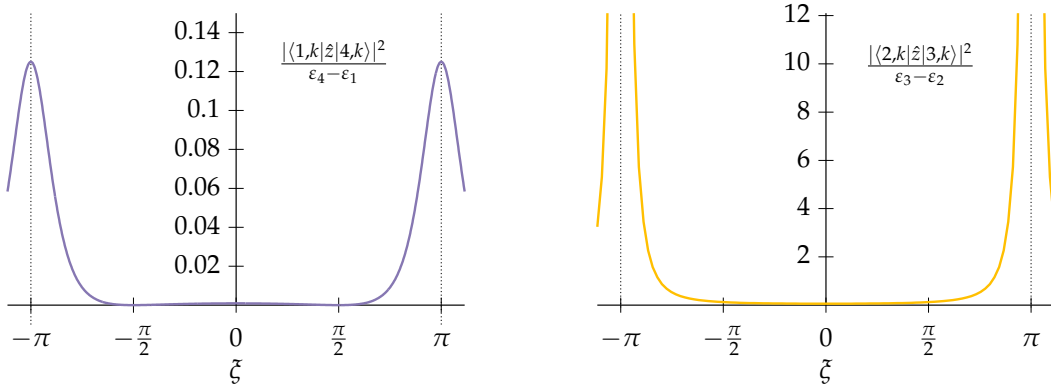


FIGURE 3.6: $1 \rightarrow 4$ (left) and $2 \rightarrow 3$ (right) contribution to α_{zz} in $\frac{b^2}{t}$ units.

The direct consequence of Equation (3.20) is directly observable by considering the per-electron polarizability in the thermodynamic limit, i.e.

$$\frac{\alpha_{zz}}{4n} = \frac{1}{8\pi} \int_{-\pi}^{\pi} 2 \left[\frac{|\langle 2, k | \hat{z} | 3, k \rangle|^2}{\varepsilon_3 - \varepsilon_2} + \frac{|\langle 1, k | \hat{z} | 4, k \rangle|^2}{\varepsilon_4 - \varepsilon_1} \right] d\xi \rightarrow \infty \quad (3.22)$$

A diverging per-electron polarizability is usually associated to a metallic behavior, contradicting the result obtained for the axial component of the per-electron TPS, which approaches a finite value as $n \rightarrow \infty$ and thus is associated to an insulating state.

We argue that the discrepancy of the two quantities is due to the limitation of the tight-binding approximation which artificially predicts a zero bandgap for cyclacenes, ultimately leading to the divergent integral in Equation (3.20).

This issue will be investigated later on in the *ab initio* section.

3.2.4 Planar Components of TPS and Polarizability

The planar components of the TPS and the polarizability are degenerate because of the rotational symmetry around the principal axis of cyclacenes. It turns out that it is more convenient to work with a combined operator $\hat{x} \pm i\hat{y}$ in the polar form given by $\hat{R}e^{\pm i\hat{\varphi}}$ rather than in the two Cartesian coordinates separately. In this notation, φ corresponds to the angle of rotation about the z axis, whereas R represents the radius of the cyclacene. The angle φ formally depends on the cell index μ and is defined as

$$\varphi = \begin{cases} \frac{2\pi\mu}{n} & \text{if } \nu = 2, 3 \\ \frac{2\pi(\mu + \frac{1}{2})}{n} & \text{if } \nu = 1, 4 \end{cases} \quad (3.23)$$

while $R = \frac{nb\sqrt{3}}{2\pi}$ remains a simple multiplicative constant. The application of this operator to the many-particle state $|m, k\rangle$ of Equation (3.5) results in

$$Re^{\pm i\hat{\varphi}} |m, k\rangle = \frac{R}{\sqrt{n}} \sum_{\mu=0}^{n-1} e^{\frac{2i\pi\mu}{n}(k\pm 1)} \left[e^{\pm \frac{i\pi}{n}} c_{1,m} p_{\mu}^1 + c_{2,m} p_{\mu}^2 + c_{3,m} p_{\mu}^3 + e^{\pm \frac{i\pi}{n}} c_{4,m} p_{\mu}^4 \right] \quad (3.24)$$

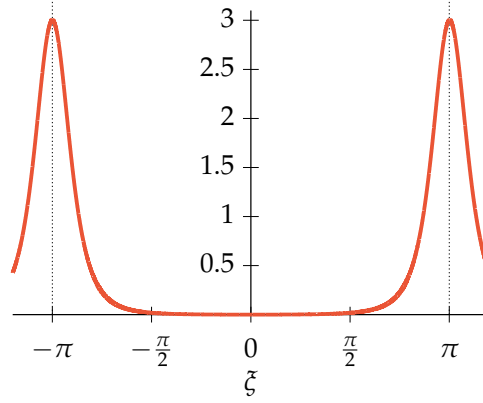


FIGURE 3.7: Squared integral in b^2 units contributing to the planar components of the TPS.

where the presence of a shift $k \pm 1$ in the exponential factor inside the sum implies that the non-vanishing matrix elements are given by

$$\langle m, k | \hat{x} + i\hat{y} | m', k - 1 \rangle \quad \text{and} \quad \langle m, k | \hat{x} - i\hat{y} | m', k + 1 \rangle \quad (3.25)$$

Furthermore, differently to the axial case, $|m, k\rangle$ and $|m', k'\rangle$ must be of the same symmetry with respect to σ_h for the contributions to be different from zero. The nonvanishing elements contributing to the planar components of the TPS are hence $1 \rightarrow 3$ and $2 \rightarrow 4$. This accounts to a total of four integrals, given by

$$\begin{aligned} \langle 1, k | \hat{x} + i\hat{y} | 3, k - 1 \rangle \quad \text{and} \quad \langle 1, k | \hat{x} - i\hat{y} | 3, k + 1 \rangle \\ \langle 2, k | \hat{x} + i\hat{y} | 4, k - 1 \rangle \quad \text{and} \quad \langle 2, k | \hat{x} - i\hat{y} | 4, k + 1 \rangle \end{aligned} \quad (3.26)$$

These elements were derived in closed form, however are not explicitly presented here since they are quite cumbersome and their analytical expression does not reveal much. For their analytical form we point to the Appendix of Ref. 158.

Because of the rotational symmetry, the individual integrals of the operators \hat{x} and \hat{y} can be obtained with the following simple relations

$$\begin{aligned} \langle m, k | \hat{x} | m', k - 1 \rangle = \langle m, k | \hat{y} | m', k - 1 \rangle = \frac{1}{2} \langle m, k | \hat{x} + i\hat{y} | m', k - 1 \rangle \\ \langle m, k | \hat{x} | m', k + 1 \rangle = \langle m, k | \hat{y} | m', k + 1 \rangle = \frac{1}{2} \langle m, k | \hat{x} - i\hat{y} | m', k + 1 \rangle \end{aligned} \quad (3.27)$$

It is also the case that the squared integrals contributing to the planar components of the TPS are the same for both transitions $1 \rightarrow 3$ and $2 \rightarrow 4$. These terms are reported in Figure 3.7, using $\frac{1}{4} \cdot |\langle 2, k | \hat{x} + i\hat{y} | 4, k - 1 \rangle|^2 = |\langle 2, k | \hat{x} | 4, k - 1 \rangle|^2 = |\langle 2, k | \hat{y} | 4, k - 1 \rangle|^2$ as an example with $b = 1$ and $t = 1$. The planar components of the TPS tensor are obtained

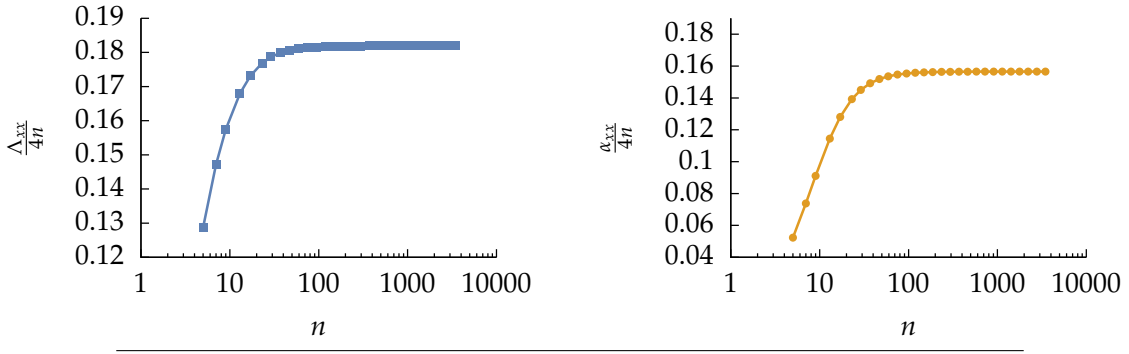


FIGURE 3.8: Planar component of the per-electron TPS (left) and per-electron polarizability (right) in b^2 units and $\frac{b^2}{t}$, respectively.

by inserting the elements of Equation (3.26) into Equation (3.13), resulting in

$$\Lambda_{xx} = \Lambda_{yy} = \frac{1}{2} \sum_{k=0}^{n-1} \left[|\langle 2, k | \hat{x} + i\hat{y} | 4, k-1 \rangle|^2 + |\langle 2, k | \hat{x} - i\hat{y} | 4, k+1 \rangle|^2 + |\langle 1, k | \hat{x} + i\hat{y} | 3, k-1 \rangle|^2 + |\langle 1, k | \hat{x} - i\hat{y} | 3, k+1 \rangle|^2 \right] \quad (3.28)$$

Following the same approach, the polarizabilities α_{xx} and α_{yy} are obtained by dividing the matrix elements with the energy differences, i.e.

$$\alpha_{xx} = \alpha_{yy} = \frac{1}{2} \sum_{k=0}^{n-1} \left[\frac{|\langle 2, k | \hat{x} + i\hat{y} | 4, k-1 \rangle|^2}{\varepsilon_4(k\theta - \theta) - \varepsilon_2(k\theta)} + \frac{|\langle 2, k | \hat{x} - i\hat{y} | 4, k+1 \rangle|^2}{\varepsilon_4(k\theta + \theta) - \varepsilon_2(k\theta)} + \frac{|\langle 1, k | \hat{x} + i\hat{y} | 3, k-1 \rangle|^2}{\varepsilon_3(k\theta - \theta) - \varepsilon_1(k\theta)} + \frac{|\langle 1, k | \hat{x} - i\hat{y} | 3, k+1 \rangle|^2}{\varepsilon_3(k\theta + \theta) - \varepsilon_1(k\theta)} \right] \quad (3.29)$$

Differently to the axial case, closed formulas for both the TPS elements Λ_{xx} , Λ_{yy} and the polarizability elements α_{xx} , α_{yy} were not found. Therefore, in order to investigate their behavior as a function of the system size, numerical calculations of the sums appearing in Equations (3.28) and (3.29) were carried out for systems consisting of up to few thousands hexagonal rings. The results for the per-electron total position spread and per-electron polarizability are reported in logarithmic scale for the xx component in Figure 3.8. From the plots, it appears clear that the planar components of both quantities tend to a finite value as the number n of units increases. The limit is reached quite quickly, and it does not change significantly beyond a critical system size. The convergence to a finite value for both quantities together with the results for the axial component are a signature of an insulating behavior for this type of systems. This is a remarkable result, considering the zero gap of the band structure. Nevertheless, the approximations introduced by the tight-binding approach are substantial and therefore more sophisticated methods are required in order to confirm the obtained results.

3.3 *Ab Initio*

Albeit the insight given by the tight-binding method, higher level calculations are required in order to provide a quantitative treatment and a more detailed description of the system. In the following, a series of properties calculated using *ab initio* methods are reported and, where applicable, compared to the tight-binding results of the previous subsection. In particular, we report the singlet–triplet energy gap, the radical character of the ground state, the TPS and the polarizability as a function of the system size, for the series of even-numbered [n]cyclacenes with $n = 6, 8, \dots, 22$.

3.3.1 Methodology

For all the *ab initio* calculations, we used a double- ζ atomic natural orbital (ANO) basis set by Roos and coworkers¹⁷⁰, either with (ANO-DZP) or without (ANO-DZ) a set of polarization functions on the carbon atoms. The only exception is made for the calculation of the polarizability which is usually quite sensitive to the presence of diffuse functions, for which the aug-cc-pVDZ basis set^{122,123} was employed, in combination with the corresponding auxiliary basis set for the density fitting technique used in the molecular orbital transformation step¹⁷¹. Although the ANO basis set is relatively large (in terms of primitives), to ensure the quality of the double- ζ basis, calculations on an [8]cyclacene and a [20]cyclacene using a larger triple- ζ basis set (ANO-TZ and ANO-TZP) were carried out, comparing well with the double zeta results.

All the geometries were relaxed at RHF/ANO-DZ level of theory, and their quality was extensively assessed against a series of optimizations on selected system sizes at both restricted and unrestricted DFT level of theory with the three-parameter Becke exchange energy functional^{105,112} and the Lee-Yang-Parr correlation energy functional¹⁰⁶ (B3LYP), as well as using MP2 perturbation theory with several different contraction patterns of the ANO basis set. More information is provided in the supplementary material of Ref. 163.

The full D_{nh} molecular point group of cyclacenes was enforced during the geometry optimization by imposing specific constraints on the coordinates, although the symmetry of the wave function used was D_{2h} , as only abelian symmetries are available in the program used to carry out the calculations. The geometry was optimized for the totally symmetric 1A_g closed-shell state (note that in the following the electronic states will be labeled according to the D_{2h} subgroup and not to the full D_{nh} group) and the MOs occupation pattern was set manually for each value of n to ensure the correct electronic configuration.

The single point calculations were performed using the CASSCF method^{172,173} and *partially contracted* NEVPT2^{95–97}, where computationally feasible. During the CASSCF procedure, two states of different spin multiplicity were optimized simultaneously (state-average CASSCF), namely the lowest singlet 1A_g state and the lowest triplet $^3B_{1u}$ state. All MOs were included in the optimization, thus also the core orbitals. Two sets of active spaces were chosen: i) the minimal (2,2) AS and ii) a dynamically sized space generated

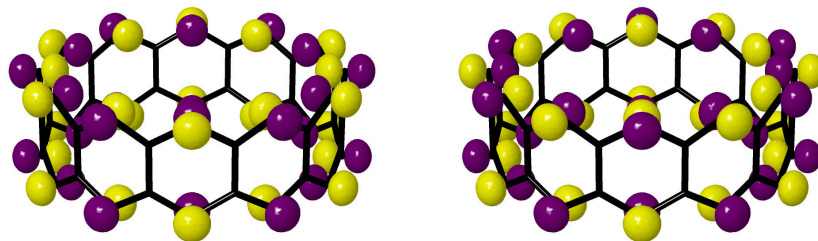


FIGURE 3.9: Symmetric (left) and antisymmetric (right) MOs constituting the HOMO–LUMO pair for a [12]cyclacene. Hydrogen atoms are omitted.

by a selection rule based on the Hückel approximation (denoted in the following as (k,k)). Surprisingly *wrong* results were obtained for calculations with the AS i) and an investigation on the nature of this failure is carried out. On the other hand, the results obtained with the AS ii) are in agreement with the most recent data available in the literature¹⁶². For systems up to $n = 16$, it was possible to account for dynamic electron correlation by performing state-specific NEVPT2 calculations using the CASSCF wave functions as the reference states, freezing excitations from the core orbitals.

The vertical singlet–triplet energy gaps reported throughout this section are calculated according to

$$\Delta E_{ST} = E(^3B_{1u}) - E(^1A_g) \quad (3.30)$$

All the calculations were performed using the 2015.1 version of the MOLPRO program package^{174,175}, applying the default convergence thresholds. The polarizability was instead obtained using the version 4.0 of the ORCA¹⁷⁶ program package, applying the convergence threshold “verytight” and an electric field perturbation of 0.0001 au to obtain the polarizability via finite differences of the dipole moment.

3.3.2 Minimal Active Space

The electronic structure of $[n]$ cyclacenes shares some similarities with that of linear polyacenes. At RHF level of theory, the HOMO and the LUMO are completely delocalized over the two zigzag edges, as shown in Figure 3.9 for a [12]cyclacene. The HOMO–LUMO pair of all even-numbered $[n]$ cyclacenes features the same structure and symmetry properties. In particular, we will denote from now on the symmetric (with respect to the σ_h reflection plane) MO as π_+ and the antisymmetric MO as π_- . Note that the nature and shape of these orbitals remains virtually unchanged with respect to methodology used to obtain them: Hückel, canonical or natural. The minimal active space is composed by two electrons and the HOMO and LUMO orbitals for all system sizes.

The CASSCF/ANO-DZ results (the ANO-DZ is used for all calculations with the (2,2) AS) are shown in Table 3.1. The singlet–triplet energy gap is surprisingly increasing as a function of the system size n . Besides the three smallest systems, starting at $n = 12$ the gap steadily increases proportionally to the number of hexagonal rings. In the central columns, the natural orbital occupation numbers (NOONs) of the two AS orbitals

TABLE 3.1: ΔE_{ST} , NOONs of π_+ and π_- and configuration weights C_+ and C_- of the ground state CASSCF(2,2) wave function.

n	ΔE_{ST} [eV]	NOON		weight	
		π_+	π_-	C_+	C_-
6	0.07	1.32	0.68	-0.81	0.58
8	0.02	1.22	0.78	-0.78	0.62
10	-0.003	1.01	0.99	-0.71	0.70
12	0.03	0.71	1.29	-0.60	0.80
14	0.12	0.43	1.57	-0.46	0.89
16	0.24	0.25	1.75	-0.35	0.94
18	0.37	0.15	1.85	-0.27	0.96
20	0.50	0.10	1.90	-0.22	0.98
22	0.62	0.07	1.93	-0.18	0.98
24	0.73	0.05	1.95	-0.15	0.99
28	0.91	0.03	1.97	-0.11	0.99

are listed, showing a clear tendency of the ground state to gradually become of closed-shell character as n increases. In particular, the occupation of the antisymmetric π_- MO reaches almost two for the largest system. The CASSCF ground state wave function for this small AS is composed by two SDs only, one in which the π_+ MO is doubly occupied, whereas the other one where the π_- MO is instead doubly occupied. The resulting wave function is effectively the linear combination of these two SDs each multiplied by a coefficient, accordingly labeled as C_+ and C_- , respectively. The last two columns of Table 3.1 show the value of these coefficients as a function of n , which, broadly speaking, provide the importance (the weight) of each SD in the wave function. As can be inferred, together with an increasing NOON for π_- there is a large weight for the corresponding configuration C_- . This corresponds to a wave function which is substantially dominated by a single SD and thus apparently of closed-shell nature.

For $n = 6, 8$ the situation is reversed, π_+ is more occupied than its antisymmetric counterpart and $n = 10$ is the “inversion” point, in which the two SDs have equal weight.

For all cyclacenes there is a clear trend: the occupation number of π_+ monotonically decreases towards zero, while that of π_- increases towards two as the system grows in size. This trend goes hand in hand with a decrease of the weight C_+ and an increase of the weight C_- .

The results presented so far are in contradiction with the most recent theoretical studies^{161,162} and our results using larger active spaces which will be discussed later on. Although $[n]$ cyclacenes are known to possess an open-shell ground state¹⁶⁰⁻¹⁶², calculations with this AS fail to correctly describe the nature of the wave function as the size of the system grows: instead of an increase of the multireference character, the ground state becomes increasingly more closed-shell in character. To investigate what drives this failure, we studied the contribution to the correlation energy introduced by the active space part of the wave function.

In general, a CASSCF wave function $|\Psi^{CAS}\rangle$ can be factorized into a core determinantal

part, $|\Phi_c\rangle$, and an active space part, $|\Psi_a\rangle$, such that it can be expressed as the following antisymmetrized tensor product

$$|\Psi^{CAS}\rangle = |\Phi_c\rangle \otimes |\Psi_a\rangle = |\Phi_c\Psi_a\rangle \quad (3.31)$$

For our particular case, the active space part of the 1A_g ground state is given by

$$|\Psi_a\rangle = C_+ |\Phi_+\rangle + C_- |\Phi_-\rangle = C_+ |\psi_+\bar{\psi}_+\rangle + C_- |\psi_-\bar{\psi}_-\rangle \quad (3.32)$$

where $\psi_{\{+,-\}} = \alpha\pi_{\{+,-\}}$ and $\bar{\psi}_{\{+,-\}} = \beta\pi_{\{+,-\}}$ denote the alpha and the beta spin orbitals of the corresponding symmetric and antisymmetric $\pi_{\{+,-\}}$ molecular orbitals, respectively. Note that although $|\psi_+\bar{\psi}_-\rangle$ and $|\bar{\psi}_+\psi_-\rangle$ have spin multiplicity equal to one, they do not contribute to the 1A_g state because they do not belong to the same symmetry as $|\Psi_a\rangle$.

The CASSCF total energy is given by

$$\langle \Psi^{CAS} | \hat{H} | \Psi^{CAS} \rangle = E_{core} + \langle \Psi_a | \hat{H} | \Psi_a \rangle = E_{core} + E_{corr} \quad (3.33)$$

where the electron correlation energy E_{corr} due to the active space part of the wave function can be further decomposed into one- and two-electron contributions according to

$$\langle \Psi_a | \hat{H} | \Psi_a \rangle = E_{corr} = E_1 + E_2 \quad (3.34)$$

with E_1 and E_2 given by

$$E_1 = 2C_+^2 (\pi_+ |h| \pi_+) + 2C_-^2 (\pi_- |h| \pi_-) \quad (3.35)$$

$$E_2 = C_+^2 (\pi_+ \pi_+ | \pi_+ \pi_+) + C_-^2 (\pi_- \pi_- | \pi_- \pi_-) + 2C_+ C_- (\pi_- \pi_+ | \pi_- \pi_+) \quad (3.36)$$

The terms enclosed in round brackets are one- and two-electron integrals over the two orbitals of the active space.

The two-electron integrals over a delocalized basis set tend to zero in the limit of large systems: the larger the cyclacene, the more the energy is dominated by the one-electron terms. Hence, the values of $(\pi_+ |h| \pi_+)$ and $(\pi_- |h| \pi_-)$ are crucial to determine the character of the wave function in the limit of large n . If their difference is significant, the wave function will be predominantly described by the determinant including the orbital with the associated largest (in absolute value) one-electron integral.

The two-electron integrals $(\pi_+ \pi_+ | \pi_+ \pi_+)$ and $(\pi_- \pi_+ | \pi_- \pi_+)$ are plotted against the system size n in Figure 3.10. Note that the integral $(\pi_- \pi_- | \pi_- \pi_-)$ is omitted since it is practically indistinguishable from $(\pi_+ \pi_+ | \pi_+ \pi_+)$. Both integrals rapidly decay according to a power law, which is confirmed by the numerical results. The model function $f(n) = bn^{-c}$ falling towards zero is fitted to the integrals, with optimal exponents $c = 0.65$ for $(\pi_+ \pi_+ | \pi_+ \pi_+)$ and $c = 1.0$ for $(\pi_- \pi_+ | \pi_- \pi_+)$.

The one-electron terms depicted in Figure 3.11 show a negative gap at $n = 8$, which becomes positive at $n = 12$ and steadily increases with n , up to $n = 28$. There is a di-

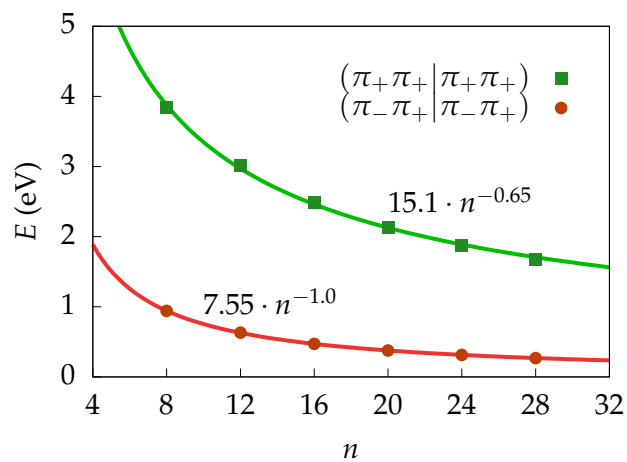


FIGURE 3.10: Two-electron integrals as a function of the system size n .

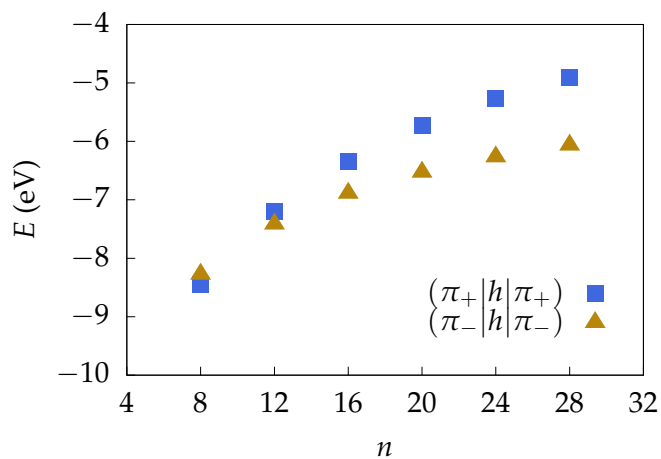


FIGURE 3.11: One-electron integrals as a function of the system size n .

TABLE 3.2: ΔE_{ST} , NOONs of π_+ and π_- and configuration weights C_+ and C_- of the CASCI(2,2) wave function using the orbitals obtained from CASSCF calculations with larger ASs. Note that the first column labeled (2,2) corresponds to full CASSCF(2,2) calculations.

n	ΔE_{ST} [eV]		NOON		weight	
	(2,2)	(k,k)	π_+	π_-	C_+	C_-
8	0.021	0.015	1.20	0.80	0.77	-0.63
20	0.50	0.61	0.08	1.92	0.20	-0.98

rect relationship between the gap $\delta = (\pi_+|h|\pi_+) - (\pi_-|h|\pi_-)$ and both the coefficients C_+, C_- and the occupation numbers of π_+, π_- . An increasing positive gap δ corresponds to an increase of the weight C_- and the occupation number of π_- . Apart from $n = 8$, there is also a relationship between δ and the energy gap ΔE_{ST} , since both increase as a function of n . The trends of the one- and two-electron integrals with respect to the size of the cyclacenes thus explain from a numerical perspective why we observe the gradual drift of the ground state electronic structure towards a closed-shell character for the largest systems.

The numerical values of the one-electron integrals depend on the particular form of the MOs π_+ and π_- ; different orbitals give different energies. The orbitals optimized within the small AS and using a small double- ζ basis set might lack the flexibility to correctly describe the wave function, ultimately producing an artificially increasing one-electron gap δ . Therefore, to investigate the influence of the orbitals, CASCI(2,2) calculations with preoptimized orbitals were carried out. In particular, two exemplary systems, a small [8]cyclacene and a large [20]cyclacene, were considered, in which the orbitals used for the CASCI were obtained by CASSCF(8,8) and CASSCF(16,16) calculations, respectively. The quality of the orbitals obtained with the larger ASs was assured by the fact that the corresponding CASSCF calculations produced results in agreement with those present in the existing literature. The first two columns of Table 3.2 show the gap ΔE_{ST} obtained with the two different sets of orbitals. For $n = 8$ a discrepancy of 0.006 eV is observed, while for $n = 20$ the gap goes from 0.50 eV to 0.61 eV. A notable effect of changing the orbitals is thus visible on the singlet–triplet energy gap, highlighting some limitations of the minimal active space. Corroborating this picture, the one-electron integrals computed using the orbitals from the CASSCF(8,8) and CASSCF(16,16) calculations shift the gap δ by +0.03 eV and +0.12 eV for [8]cyclacene and [20]cyclacene, respectively, as shown in Table 3.3. On the other hand, the two-electron integrals appear to be unaffected by the type of orbitals, as their values remain virtually unchanged.

Albeit the small differences observed in the gaps, the analysis of the correlation energy and the integrals contributions suggests that the failure of the minimal AS is in large extent “AS-driven” and only slightly caused by insufficiently relaxed orbitals, perhaps as a consequence of the small AS. The AS with two electrons in two orbitals is simply too small to capture the essential physics of the system.

TABLE 3.3: Two-electron integral for [8]cyclohexene and [20]cyclohexene and one-electron integral gap δ . All values are given in eV.

integral	[8]cyclohexene		[20]cyclohexene	
	AS(2,2)	AS(8,8)	AS(2,2)	AS(16,16)
$(\pi_+ \pi_+ \pi_+ \pi_+)$	3.8436	3.8627	2.1327	2.1447
$(\pi_- \pi_+ \pi_- \pi_+)$	0.9416	0.9556	0.3765	0.3847
δ	-0.17	-0.14	0.81	0.93

3.3.3 Dynamical Active Space

Besides not providing enough flexibility to the wave function, the minimal active space misses another crucial feature. The series of systems investigated here consists in the same molecule increasing in size, it is therefore to expect that the amount of static electron correlation increases with its size. With more hexagonal rings added to the cyclohexene, correspondingly more energetically near-degenerate configurations should enter in the wave function. To obtain a balanced and comparable description of the ground and excited states throughout the series of systems studied, it is hence important to find a systematic procedure to enlarge the AS and incorporate all important SDs as the system grows in size.

In recent years, a common approach applied to linear polyacenes is to include all valence π orbitals in the AS^{141,177,178}. However, such a choice is not a viable option in our case since the resulting active spaces were too large to be computationally tractable, and therefore we have devised an alternative selection scheme based on Hückel theory.

Recalling the results obtained within the tight-binding approximation in the first part of this chapter, it is possible to exploit the energy bands plot depicted in Figure 3.4 to develop an (unbiased) strategy determining how many electron and orbitals should be part of the active space for a given $[n]$ cyclohexene. Note in particular that for a finite size system, the energy bands reported in Figure 3.4 consist actually in a discrete set of points which is proportional to the n , as exemplified in Figure 3.12 for a [6]cyclohexene and a [16]cyclohexene, where the origin has been shifted to $k\theta = \pi$ for convenience. Every band is formed by $n + 1$ points, each of which corresponds to an energy associated with a Hückel orbital. By increasing the number of units n , more electrons are present in the system and correspondingly also more MOs. Eventually, for $n \rightarrow \infty$, the smooth bands reported in Figure 3.4 obtained from the analytical expressions of Equation (3.4) are reproduced, as there are infinitely many orbitals and associated energies. When n is even, four molecular orbitals *always* appear at $k\theta = \pi$, and at the Fermi level, although not visible from the plots in Figure 3.12, there are two overlapping energies corresponding to the degenerate HOMO–LUMO pair.

The orbitals at $k\theta = \pi$ are of particular interest for our scheme. First, we point out that the HOMO and the LUMO associated to $\varepsilon_2(k\theta = \pi) = \varepsilon_3(k\theta = \pi) = 0$ correspond qualitatively to the π_+ and π_- orbitals discussed in the previous section, as shown in Figure 3.9. The other two MOs at $k\theta = \pi$, i.e. those associated to $\varepsilon_1(k\theta = \pi)$ and $\varepsilon_4(k\theta = \pi)$, also

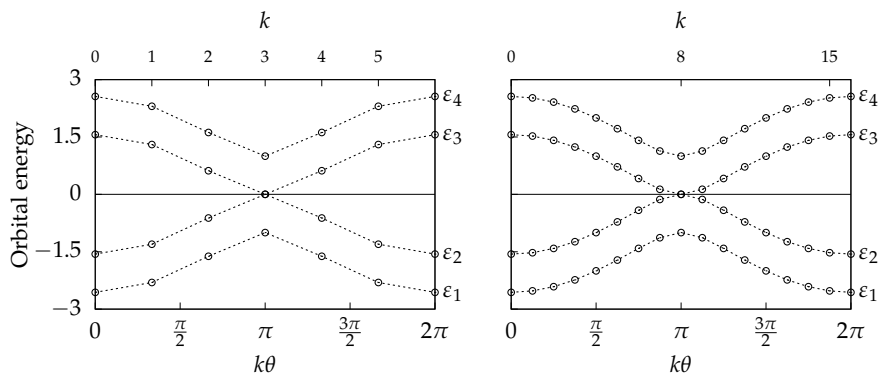


FIGURE 3.12: Hückel energy bands in t units for a [6]cyclacene (left) and for a [16]cyclacene (right). Note that the points at $k\theta = 2\pi$ are the same as those at $k\theta = 0$ because of periodic boundary conditions.

have a characteristic shape which is depicted in Figure 3.13. From now, we shall refer to

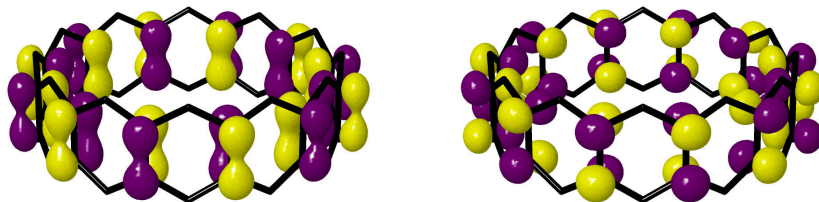


FIGURE 3.13: Symmetric (left) and antisymmetric (right) MO associated to the energies $\varepsilon_1(k\theta = \pi)$ and $\varepsilon_4(k\theta = \pi)$ for a [12]cyclacene. Hydrogen atoms are omitted.

these two orbitals as π'_+ and π'_- , respectively. Note that the difference between the orbitals $\pi_{\{+,-\}}$ and $\pi'_{\{+,-\}}$ is the position of the p -like atomic orbitals on the carbon atoms, in the latter case being non-zero only on the central carbons, whereas in the former only on the external ones.

By drawing two horizontal lines passing through π'_+ and π'_- in Figure 3.12, a delimited energetic zone containing a finite number of points is defined as shown in gray in Figure 3.14. The active space can be defined by selecting all orbitals associated to the energy points appearing within the window highlighted in gray in Figure 3.14, including the π'_+ and π'_- orbitals lying on the boundaries. As the size of the system increases, more points appear along the bands, correspondingly providing a larger number of active orbitals and electrons in an “automatic” manner. It is important to remark that such a selection method is possible because the nature of the π'_+ and π'_- does not change for systems of different sizes, provided that n is even, thus making them easily identifiable. Furthermore, the particular shape of these orbitals is the same irrespective of the method used to obtain them. For the series of cyclacenes considered here, the dynamical active space procedure was applied to canonical orbitals. More specifically, the MOs obtained after an HF calculation were inspected, and all those MOs lying energetically within π'_+ and π'_- were included in the active space. This choice generated active spaces enlarging by four

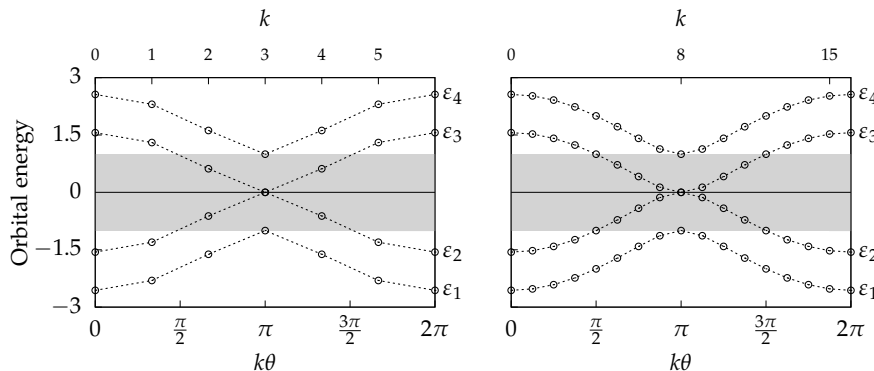


FIGURE 3.14: Hückel energy bands in t units for a [6]cyclohexene (left) and for a [16]cyclohexene (right).

orbitals and four electrons for each increase of six hexagonal units, i.e.

$$n \rightarrow n + 6$$

$$(k, k) \rightarrow (k + 4, k + 4)$$

With this approach, the active space sizes summarized in Table 3.4 were generated.

TABLE 3.4: Active space sizes resulting from the selection scheme.

n	(k, k)
6, 8, 10	(8,8)
12, 14, 16	(12,12)
18, 20, 22	(16,16)

The CASSCF vertical singlet–triplet energy gap calculated using both the ANO-DZ and the ANO-DZP basis sets, along with the NOONs of π_+ and π_- and the configuration weights C_+ and C_- of the ANO-DZP results are shown in Table 3.5. A monotonically

TABLE 3.5: ΔE_{ST} , NOONs of π_+ and π_- and configuration weights C_+ and C_- of the 1A_g ground state CASSCF(k, k) wave function.

n	ΔE_{ST} [eV]		NOON		weight	
	ANO-DZ	ANO-DZP	π_+	π_-	C_+	C_-
6	0.65	0.76	1.61	0.39	0.85	-0.36
8	0.59	0.72	1.62	0.38	0.84	-0.33
10	0.50	0.62	1.58	0.42	0.82	-0.33
12	0.39	0.44	1.39	0.61	0.67	-0.34
14	0.30	0.32	1.31	0.69	0.60	-0.34
16	0.24	0.24	1.25	0.75	0.53	-0.33
18	0.23	0.20	1.18	0.82	0.36	-0.29
20	0.20	0.18	1.18	0.83	0.32	-0.26
22	0.18	0.16	1.17	0.83	0.28	-0.24

decreasing ΔE_{ST} is predicted as a function of n for both basis sets. The NOON of π_+ is always greater than that of π_- , contrary to the CASSCF(2,2) case, together with the weight of the configuration doubly occupying π_+ , which is always greater than that doubly occupying π_- . Interestingly, the increase of size of the cyclacene has a greater impact on the weight of the symmetric configuration than that of the antisymmetric one. From $n = 6$ to $n = 22$ the absolute value of the coefficient C_+ goes from 0.85 to 0.28, while that of C_- only goes from 0.36 to 0.24. In addition, both C_+ and C_- decrease in magnitude as n increases. As the ASs get larger along the sequence of sizes, the two dominant configurations $(\pi_+)^2$ and $(\pi_-)^2$ become less and less important.

For small $[n]$ cyclacenes, the decrease of the gap does not follow the same decaying behavior observed for the larger ones; in particular for $n = 6$ to $n = 10$ the decay is clearly different from the one seen for $n > 10$, as can be seen from Figure 3.15. The best fit to the

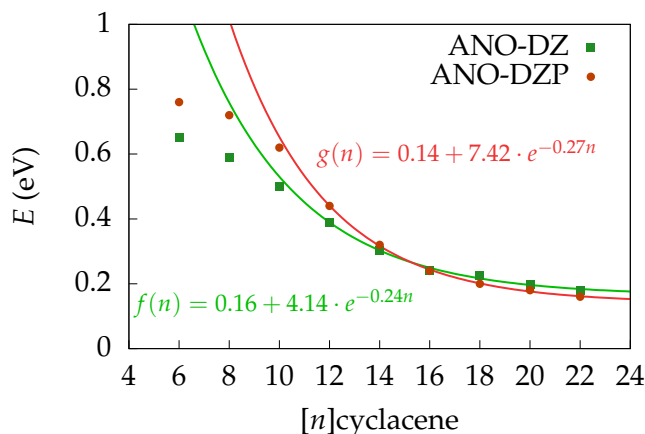


FIGURE 3.15: CASSCF(k, k) singlet–triplet energy gaps calculated with the ANO-DZ (green squares) and the ANO-DZP (red circles) basis sets as a function of n .

energy gap is given by the exponentially decaying function $f(n) = a + be^{-cn}$, excluding the first two points $n = 6$ and $n = 8$ in the parameters estimation. Of special interest is the limit of the singlet–triplet energy gap as n approaches infinity, predicting a value between 0.14 and 0.16 eV at the thermodynamic limit.

For systems with n up to 16, dynamic electron correlation was accounted for by an additional NEVPT2 calculation, in order to study its effect on the singlet–triplet energy gap. We should point out that since we are working with a limited AS on relatively large systems, the choice of method to introduce the dynamic correlation has to be taken carefully. The well-known second order complete active space perturbation theory (CASPT2) method^{179,180} suffers from the so-called intruder state problem, which appears in general when insufficiently large active spaces are used in the underlying CASSCF calculation. This problem can be removed by the introduction of an energy shift^{181,182}, however the choice of the parameter is to a certain extent arbitrary and a series of tests has to be conducted in order to assess the quality of the results. On the contrary, the NEVPT2 approach is much less sensible to this problem; in practice, the problem of intruder states is almost

TABLE 3.6: Predicted singlet–triplet energy gap by the NEVPT2 and CASPT2 methods.

n	ΔE_{ST} [eV]		
	ANO-DZ	ANO-DZP	CASPT2 ^a
6	0.34	0.36	0.52
8	0.36	0.41	0.63
10	0.37	0.44	0.49
12	0.29	0.33	0.60
14	0.24	0.25	-
16	0.19	0.18	-

^a from Sadowsky et al.¹⁶¹, 6-31G(d) basis

never present.

The energy gaps obtained with the NEVPT2 methods are listed in Table 3.6 along with a few values obtained using the CASPT2 method, reported from Sadowsky et al.¹⁶¹. The inclusion of polarization functions on the carbon atoms seems to have an insignificant effect on the qualitative behavior of the gap, as it was observed for the CASSCF method too. The gap slightly increases for the first three cyclacenes and only from $n = 10$ it begins to decrease, again in agreement with the calculated gap at CASSCF level of theory. For all cyclacenes the effect of dynamic electron correlation reduces the gap.

The results for $n = 6, 8, 10$ appear qualitatively different than for the rest of the series, with an increase as high as 0.08 eV, which we shall discuss by comparing our results with those present in the literature.

Previous theoretical studies on [n]cyclacenes using wave function theory did not investigate the asymptotic limit of the singlet–triplet gap; this was only proposed recently by Wu et al.¹⁶² in a study based on TAO-DFT. Our prediction for the gap is in contrast with the results of Houk et al.¹⁴⁰, who obtained a nearly vanishing ΔE_{ST} , actually slightly increasing as a function of n . In this case the 1A_g state was calculated using restricted DFT and the B3LYP hybrid functional, while the $^3B_{1u}$ state using unrestricted time-dependent DFT. This choice clearly overestimates the energy of the singlet state, which we here argue is an open-shell singlet, hence requiring a multiconfigurational approach with a sufficiently large AS in order to be correctly described. Furthermore, the comparison of energies calculated using restricted and unrestricted methodologies is in general unbalanced. In this particular case, the triplet state might be favored by the additional flexibility provided by the unrestricted approach, while the restricted singlet remains energetically too high since it is not properly described by the method.

In another study, Chen et al.¹⁶⁰ applied both unrestricted DFT and the CASSCF method combined with second order multireference Møller-Plesset (MRMP2). Even if in this case unrestricted DFT was used for the 1A_g state too, the gap still showed the opposite behavior to the wave function trend, i.e. increasing as a function of n . On the other hand their CASSCF result for a [6]cyclacene with eight electrons in eight orbitals was 0.65 eV using the 6-31G* basis set. This result is in very good agreement with our predicted gap of 0.65

eV using the same AS size and the ANO-DZ basis set. Inclusion of polarization functions (ANO-DZP) lifts the gap to 0.75 eV, thus resulting 0.1 eV higher. The MRMP2 gap of 0.32 eV is also in good agreement with our results, it is 0.02 eV smaller than NEVPT2 using the ANO-DZ basis set and 0.04 eV lower compared to the ANO-DZP one.

The work of Sadowsky et al.¹⁶¹ provides, to the best of our knowledge, the most recent wave function data on $[n]$ cyclacenes. Both unrestricted DFT as well as CASSCF and CASPT2 were applied to the series of $[n]$ cyclacenes, for n going from 6 to 12. Using the B3LYP functional, an erroneous positive and increasing ΔE_{ST} gap was predicted, while by employing the M06-L functional, they found an increasing gap for $n = 6, 8, 10$, which dropped down for $n = 12$ yielding the smallest value in the series. The active space for the CASSCF calculations was of 8 electrons in 10 MOs, but unfortunately no numerical values were provided, neither for the energy gap nor for the natural orbital occupation numbers. The CASPT2 values listed in the last column of Table 3.6 show an oscillating behavior as n increases. This behavior is not observed in the case of NEVPT2, where for the first three cyclacenes the gap increases from 0.36 eV to 0.44 eV for the ANO-DZP basis set. In particular, it was argued that the increase from a gap of 0.49 eV for $n = 10$ to a gap of 0.60 eV for $n = 12$ was probably the result of the limited size of the AS. This increase was indeed not observed in the case of NEVPT2, probably because of the increase of the AS from (8,8) to (12,12). Given the different choice of methods, basis sets and active spaces, a quantitative comparison between CASPT2 and NEVPT2 values does not provide any additional insight.

The most recent study on $[n]$ cyclacenes was carried out by Wu et al.¹⁶², using TAO-DFT¹⁸³ on systems with n values ranging from 4 to 100. The behavior observed for the *adiabatic* singlet–triplet energy gap is qualitatively the same as in the NEVPT2 case, with a monotonically decreasing gap as a function of the cyclacene size. No extrapolation to the thermodynamic limit was done, but for a [100]cyclacene, the observed gap of 0.02 eV (0.49 kcal/mol) provides a good estimate for such a limit. This value is well below our prediction for $n \rightarrow \infty$, which is ≈ 0.15 eV. This discrepancy, although remarkable, should not surprise considering on one hand the different methodologies and basis sets used, and on the other hand the fact that the adiabatic gap was considered in one case and the vertical gap in the other. In general, as the geometry of the triplet state is relaxed, its energy is forcedly less than or equal to the unrelaxed one, implying a narrowing of ΔE_{ST} . At last, for the smallest cyclacenes, TAO-DFT shows an increase of the gap from $n = 6$ to $n = 8$ as it was the case for the NEVPT2 and the CASPT2 data. The gap then decreases from $n = 8$ to $n = 10$ for both TAO-DFT and CASPT2, but not for NEVPT2 where it keeps increasing. The different behavior of NEVPT2 suggests that perhaps, the AS size predicted by our selection method is not large enough in this particular case. Indeed, a calculation with a (12,12) AS (instead of the (8,8) one defined by our Hückel-based selection scheme) shows a lowering of the ΔE_{ST} from 0.62 eV to 0.59 eV at CASSCF/ANO-DZP level of theory. Furthermore, the gap computed using NEVPT2 on this larger active space also provides a lower estimate by going from 0.44 eV to 0.38 eV. This last value

TABLE 3.7: Effect of the active space size on the CASSCF energy gap for a [10]cyclacene and a [16]cyclacene using the ANO-DZP basis. All values are given in eV.

n	(8, 8)	(12, 12)	(16, 16)
10	0.62	0.59	0.55
16	-	0.24	0.24

TABLE 3.8: Effect of the basis set on the CASSCF(k, k) gap for [8]cyclacene and for [20]cyclacene.

n	(k, k)	ΔE_{ST} [eV]			
		ANO-DZ	ANO-DZP	ANO-TZ	ANO-TZP
8	(8,8)	0.59	0.72	0.60	0.72
20	(16,16)	0.20	0.18	0.20	0.18

falls below the gap of [8]cyclacene and thus agrees with the previous works by Sadowsky et al.¹⁶¹ and Wu et al.¹⁶², making the singlet–triplet gap obtained with NEVPT2 monotonically decreasing.

It is known from studies on linear polyacenes as well as on graphene nanoribbons that the inclusion of all valence π orbitals in the active space is important in order to properly account for the large static electron correlation present in this type of systems^{141,177}. This can be expected to be true also for [n]cyclacenes too, although it was never thoroughly tested. Using our active space selection scheme we were able to consider only a fraction of the π valence space, which nevertheless proved sufficient to produce qualitatively correct results in all cases but $n = 10$. Notably, the enlargement of the AS of [12]cyclacene with respect to that of [10]cyclacene is sufficient to predict the decaying behavior of the energy gap using NEVPT2, in contrast to the result obtained by Sadowsky et al.¹⁶¹. Notwithstanding, to assess the influence of the AS on the ΔE_{ST} , two larger spaces were tested for [10]cyclacene and a larger one for [16]cyclacene. The results are shown in Table 3.7, where for the small cyclacene the CASSCF gap decreases by 0.03–0.04 eV and the NEVPT2 one by 0.06. This is however not the case for the large cyclacene, where the gap remains unchanged upon enlargement to the (16, 16) AS, confirming the effectiveness of our devised selection method.

The influence of the basis set size on the energy gap was assessed too. In particular for both a small system with $n = 8$ and a large one with $n = 20$, the calculated gaps using an ANO triple- ζ basis set are virtually unaffected. Moreover, the values listed in Table 3.8 show that this is true irrespective of the presence of polarization functions.

To inspect the *polyradical* character of the open-shell 1A_g ground state, the natural orbital occupation numbers of the CASSCF wave function are plotted in Figure 3.16. For a better readability, the orbitals displayed are all unique empty and doubly occupied valence π orbitals, i.e. only one orbital for each degenerate pair. The occupation of the active orbitals tends towards one as more hexagonal units are added to the cyclacene. In

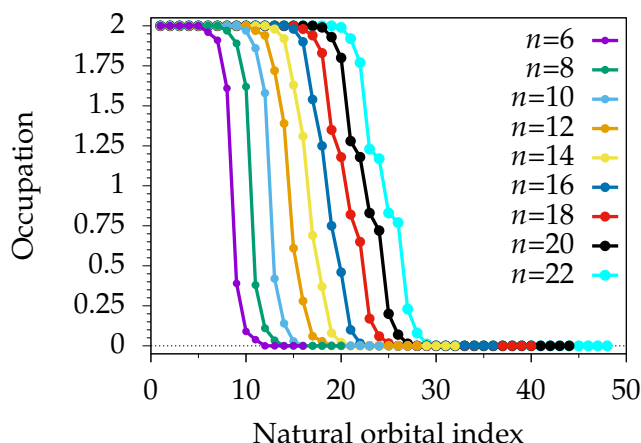


FIGURE 3.16: CASSCF NOONs. Note that all unique π orbitals are plotted, including those not included in the ASs.

particular the occupation number of the highest occupied and the lowest unoccupied orbitals as well as the immediately next ones appears to change rather quickly as a function of the cyclacene size, whereas this behavior is somewhat slower for the other orbitals in the AS. This effect could possibly arise from the limited size of the active space, its sudden change every time n increases by 6, or by the fact that geometries optimized for the closed-shell singlet were used. The occupation numbers approaching one have to be understood in this case as an increase in the radical character of the molecule: pairs of electrons doubly occupying one orbital decouple and localize on either side of the cyclacene (note that this can be seen by a unitary transformation of the orbitals).

As a comparison, the active orbital occupation numbers obtained by TAO-DFT (note that these occupation numbers are an approximation of NOONs¹⁸³) behave differently. Although the tendency is an increasing number of orbitals with fractional occupation approaching one, the way in which this happens is not the same as for CASSCF natural orbitals.

To further assess the *polyradical* character of cyclacenes, we calculated an *effective* number of unpaired electrons using the formula introduced by Head-Gordon¹⁸⁴, which is based on the one-particle reduced density matrix. This measure yields an estimate of the total number of unpaired electrons present in the system and thus characterizes its radical character. This index is given by

$$R = \sum_{i=1}^{n_{orb}} \min(n_i, 2 - n_i) \quad (3.37)$$

where n_i is the NOON of orbital i . It is easy to see that empty and doubly occupied orbitals do not contribute to R , and the sum can therefore be restricted to the orbitals included in the AS only. The values can be visualized in Figure 3.17, where the radical index R highlights the “jumps” to larger active spaces.

Note the clear trend of R : for $n = 6, 8, 10$ the index is between 1 and 2, for $n = 12, 14, 16$

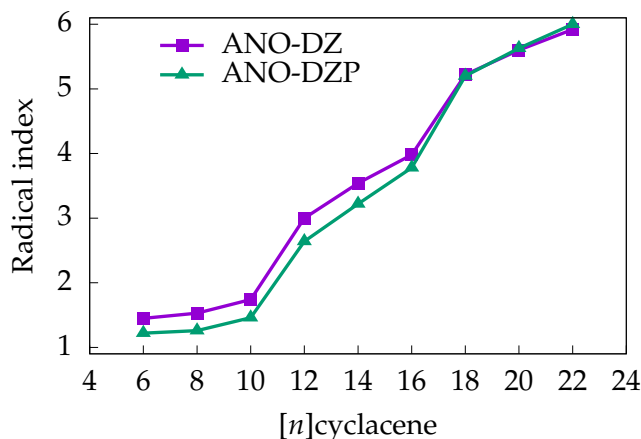


FIGURE 3.17: Effective number of unpaired electrons with respect to the system size.

between 3 and 4 and for $n = 18, 20, 22$ between 5 and 6. For the first three cyclohexenes there is a slightly slower increase of the index than for the larger ones, which is in agreement with the slower decrease of the singlet–triplet energy gap, suggesting a potential relationship between the two quantities. We should remark that that this index provides a lower bound for the number of unpaired electrons, in particular the larger the AS, the more unpaired electrons are predicted by R .

This analysis based on the one-particle density matrix provides strong evidence of polyradical character for systems with $n > 10$ with an open-shell singlet ground state. Similar conclusions were drawn for linear polyacenes^{141,142,177,183,185–188}, although it was argued that for systems up to heptacene, the ground state can be regarded as closed-shell. Consequently, single reference methods should be able to predict the electronic properties of these systems within chemical accuracy¹⁸⁹, if sophisticated methodologies such as CC theory and CBS extrapolation are used. Nevertheless, the increase of the radical character as a function of system size is undeniable and therefore an appropriate method able to account for static electron correlation has to be used when dealing with systems beyond a certain value of n .

At last, in order to provide evidence for the results obtained within the tight-binding approximation, the axial component of the TPS was calculated using the CASSCF wave function^{168,190} expanded in the ANO-DZP basis set. As it is evident from the plot shown in Figure 3.18, the TPS increases linearly with respect to the system size, confirming, already for these relatively small sizes, the thermodynamic behavior obtained analytically. The polarizability has somewhat higher computational requirements. Here, we have computed the polarizability tensor only for cyclohexenes with n equal 6, 8, 10 and 12, using the aug-cc-pVDZ basis set as explained in the Methodology section. The results for the α_{zz} component are reported in Table 3.9. The four available *ab initio* points appear to increase approximately linearly with system size. In particular, there is no sign suggesting the divergence observed at tight-binding level. This is not surprising, since the

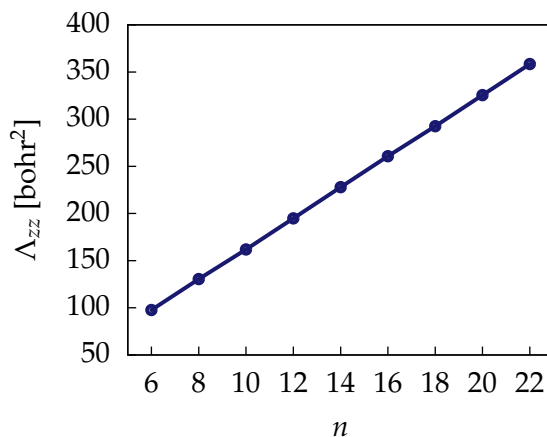


FIGURE 3.18: The total axial component of the TPS computed with the CASSCF wave function.

TABLE 3.9: Axial and longitudinal components of the polarizability (in au) computed with the CASSCF method. The last column lists the NOONs of the HOMO–LUMO pair.

n	α_{xx}	α_{zz}	HOMO/LUMO
6	317.697	251.274	1.63/0.37
8	505.095	334.526	1.64/0.37
10	749.741	419.408	1.60/1.40
12	933.888	479.233	1.41/0.60

problematic term in Equation (3.22) is due to the vanishing denominator of the $2 \rightarrow 3$ transition element. Within HF theory, the HOMO–LUMO pair is non-degenerate. Thus, considering the sum-over-states approach to obtain the static polarizability, the problematic denominator responsible for divergence in Equation (3.22) would have a finite value and not cause any trouble.

A similar argument is probably less accurate at CASSCF level, where the monodeterminantal picture of the wave function is lost and orbital energies are not well-defined anymore. Nevertheless, natural orbital occupation numbers of the HOMO and LUMO (last column of Table 3.9) differ significantly for the cyclacenes considered here, suggesting a clear difference between them, unlike in the case of the degenerate Hückel orbitals. To strictly apply the sum-over-states formula given in Equation (3.12) to the CASSCF formalism, one would have to compute all excited states, which is clearly unfeasible (and likely very inaccurate).

The above arguments however, provide some evidence that the missing electron–electron repulsion within the tight-binding approximation is responsible for the degeneracy at the Fermi level, ultimately producing the unexpected divergence of Equation (3.22). The planar component of the polarizability was also obtained and reported in Table 3.9. However, albeit the linear behavior of α_{xx} for the first few cyclacenes, such a limited number of points is not enough to infer a general trend.

3.4 Conclusions

In this chapter of the thesis, an extensive study on several properties of $[n]$ cyclacenes was carried out both at a semi-empirical and at *ab initio* levels of theory. These fascinating systems show interesting electronic and magnetic properties which make them suitable for technological applications in a variety of domains. Besides that, deepening our understanding in these molecules is also important for their possible use as templates in the controlled growth of zigzag carbon nanotubes, a challenge which we are still facing today.

In the first part of this chapter, the analytical expressions for the eigenvalues and eigenvectors of cyclacenes within the tight-binding approximation were obtained and reported. On this base, the exact expressions of the energy bands, density of states, axial position spread and polarizability tensors were derived in closed form. The energy gap vanishes at the Fermi level, as this is located at the frontier between two different bands. For this reason, the density of states shows the presence of a Van Hove singularity. The axial per-electron TPS remains finite, in accordance with the finite extension of the system in this direction. Quite remarkably however, the corresponding per-electron polarizability diverges, a behavior that is commonly found only in the case of conductors. In general a divergence of the per-electron polarizability is associated to a similar behavior of the corresponding position spread tensor. To our knowledge, this is the only case where the two quantities do not behave in the same way. We argue that the reason is likely due to the missing description of the electron–electron repulsion within the tight-binding approximation, which plays a role in removing the degeneracy at the Fermi level. This is supported by CASSCF calculations of the dipole polarizability for a few small systems as shown in the second part of the chapter. The axial component of the TPS was also computed from the CASSCF wave function for systems with $n = 6, 8, \dots, 22$, remarkably showing the asymptotic linear behavior predicted by Hückel theory, despite being far away from the thermodynamic limit.

We were not able to obtain analytical expressions for the planar components of both the spread and the polarizability tensors. A numerical calculation, however, does not show any evidence of a divergence of these quantities. Therefore the system is predicted to be, at this level of description, an insulator. This result is of particular interest, as this material has a zero gap along with a nonzero density of states at the Fermi level, typically a signature of metallic behavior. The properties computed in our investigation however, which depend on the geometrical details of the system, would characterize it as insulator, meaning that closing a linear polyacene to form a ring appears to change the type of the material from metallic to non-metallic. Nevertheless, more investigation is necessary to confirm or refute this hypothesis.

In the second part of this chapter we have presented the results obtained using first-principles methodologies. In particular, the vertical singlet–triplet energy gap and the polyradical character of $[n]$ cyclacenes were investigated as a function of the system size

in a systematic way. The singlet–triplet gap was found to decrease exponentially with respect to the number n of hexagonal units, and to approach a finite value in the order of a tenth of eV in the limit $n \rightarrow \infty$. We have proposed a criterion to dynamically select the active space as a function of n , based on the tight-binding investigation reported in the first part of this chapter. This approach has allowed a balanced treatment of the *static* electron correlation throughout the series of systems considered. The *ab initio* results presented were compared to previous ones reported in the literature, on one side supporting them and on the other extending them to a larger number of systems. In particular, the open-shell singlet nature of the electronic ground state was firmly confirmed. The polyradical character of cyclacenes was studied by an analysis of the natural orbital occupation numbers as well as an indicator based on the latter.

Calculations using a minimal active space of two electrons in two orbitals were also performed and insight into the failure of this AS was provided through a scrupulous analysis of the integral contributions to the correlation energy. With a *wrong* choice of AS, the ground state of the system tends to be of closed-shell rather than open-shell character for increasing system size. Besides the results provided, this study didactically showed the importance of the active space for this kind of systems and proposed a novel criterion for its systematic selection.

To conclude, although $[n]$ cyclacenes have not been synthesized yet, they remain a fertile ground for theoreticians and experimentalists alike, and their investigation provides a mean to increase the basic understanding of hydrocarbon systems in general.

4 Carbon Nanotubes

In this chapter, several studies centered on carbon nanotubes are presented, spanning some of the possible applications of this class of systems. In the first part, the focus is on the confinement of a number of pure nitrogen clusters inside CNTs, with the intent to investigate on one side the stabilization effects of the nanotubes on these highly energetic molecules and on the other side the nature of the interaction between the fragments.

In a second, shorter part, a study proposing the encapsulation of beryllium chains inside the cavity of CNTs of different diameters is presented, aiming to preserve the linear structure of the chain and study the influence of the nanotube on its characteristic magnetic properties.

Large parts of the results presented here are available in the literature in form of scientific articles published during the course of the thesis:

- S. Battaglia, S. Evangelisti, N. Faginas-Lago and T. Leininger, *Journal of Molecular Modeling*, 23, 294, 2017
- S. Battaglia, S. Evangelisti, T. Leininger and N. Faginas-Lago, In: Gervasi O. et al. (eds) *Computational Science and Its Applications – ICCSA 2018. Lecture Notes in Computer Science*, vol. 10964, 2018

4.1 N_3^- Confinement in Carbon Nanotubes

The hollow structure of CNTs and the low reactivity of the internal wall provide an ideal environment to confine a wide variety of systems in its cavity, making them suitable for different types of applications. As early as 1993, 2 years later the first successful synthesis of CNTs², Ajayan and Iijima⁶⁵ experimentally demonstrated the possibility to fill CNTs by capillary suction, proving the theoretical predictions to be feasible in practice.

Since then, a lot of work has been carried out in this domain both experimentally and theoretically, and a large variety of confined and composite systems were investigated. Among others, the encapsulation of fullerenes and metallofullerenes^{67,68}, a long list of different types of metal^{69,72-77}, energetic molecules⁷⁸⁻⁸¹, and many more. The limited space inside the cavity of CNTs can also induce new phases of materials; the most notable example is certainly that water. Novel “ice” phases arising from encapsulated water were first predicted from theoretical calculations⁸² and then observed experimentally over the years^{83,84,191}.

Searching for alternative and environmentally friendly energy sources, a promising class of systems is that of all-nitrogen molecules^{192,193}. Accounting for as much as 78%,

nitrogen is the most abundant species in Earth's atmosphere and is therefore widely and easily accessible. It is virtually only present as di-molecular N_2 , which is by far the most stable form and it is not harmful for the environment. The reason why nitrogen naturally arises only as N_2 is identified in its peculiar bond energy, with the N–N triple bond characterized by an energy of 229 kcal/mol, that of the double bond by 100 kcal/mol and the single bond one by 38.4 kcal/mol¹⁹². Thermodynamically, three times the energy of a single bond or one and half times the double bond one do not reach the energetic stability of the triple bond, hence the ubiquity of N_2 . Consequently, this energy distribution is such that singly- and doubly-bonded nitrogen allotropes have the potential to release a large amount of energy upon decomposition into molecular nitrogen. For this reason, pure nitrogen clusters are considered as high energy-density materials^{192,193}.

The first and most famous polynitrogen molecule is the N_3^- azide anion, known since the end of the nineteenth century¹⁹⁴. It took more than a 100 years to enlarge this family, with the successful synthesis of the N_5^+ cation¹⁹⁵ in 1999, which renewed the interest in this class of systems as people envisioned the possibility of a pure nitrogen crystal composed by N_3^- and N_5^+ ion pairs^{196–198}. However, experimental attempts to stabilize the two ions resulted unsuccessful¹⁹⁹, highlighting the major obstacle towards the realization of pure nitrogen allotropes, i.e. their intrinsic instability with respect to decomposition into N_2 .

More recently, molecular confinement was explored as a possible strategy to overcome this problem. By encapsulating a polymeric nitrogen chain inside CNTs, it was predicted by molecular dynamics simulations that the nitrogen species remains stable up to high temperatures, preserving, in theory, the structure of these molecules and providing at the same time a way to store them^{79,80,200}. Additional theoretical investigations based on the same idea predicted the same nitrogen chain to be stable in silicon carbide and boron nitride nanotubes^{201–203}. With a similar approach, a comprehensive density functional theory study on the encapsulation of nitrogen clusters of different sizes in a C_{60} fullerene was carried out too, predicting stable structures for molecules of up to 13 atoms before the latter started to be chemically bound to the confining cage²⁰⁴.

From an experimental perspective, an N_8^- anionic species adsorbed on the inner side of a multi-wall carbon nanotube was observed at ambient conditions²⁰⁵; a result that was recently corroborated by the successful synthesis on a carbon nanotube substrate of the cubic gauche phase (cg-N) near ambient conditions²⁰⁶. In the latter work, besides the presence of signature peaks in Raman and infrared spectra corresponding to the cg-N phase, high resolution transmission electron microscopy images clearly show the encapsulated nitrogen clusters.

Besides the relatively large number of works on nitrogen chains, not so many other species were considered in a confined environment. In particular, besides the large amount of literature investigating the spectroscopic features of the azide ion in crystal or gas phase^{207–215} as well as solvated^{216–228}, it has never been studied in a confined environment. Considering that N_3^- often represents a precursor in the synthesis of energetic

molecules, e.g. the aforementioned cg-N phase synthesis over the CNT substrate starts from sodium azide, or it appears as an intermediate structure during the dissociation reaction of larger nitrogen clusters, e.g. the barrierless dissociation of the N_5^- ion, it is certainly of great interest to study its behavior in a constrained environment such as that provided by CNTs, and in particular to understand the type of interactions between the confining and the confined fragments.

In the following, the results obtained on the confinement of the azide anion inside carbon nanotubes of different lengths and diameters are presented. A large part is devoted to an *ab initio* study of this system, providing in the first place important insight into the adsorption of the polynitrogen molecule such as the nature of the interaction between the fragments. Secondly, a more systematic approach is undertaken, where the finite size effects are studied by high-level CC calculations, in order to obtain accurate, reference energies.

Building on the knowledge acquired from the static calculations and comparing to the reference *ab initio* data, a novel intermolecular potential modeling the non-covalent interaction between N_3^- and CNTs is presented. The potential is implemented in the molecular dynamics program DL POLY 4.08^{229,230} and the working equations of the potential as well as its derivatives are reported. The implementation of this potential allows to accurately study the dynamics of the confined ion in carbon nanotubes of any size and type, and in principle solvated in any non-ionic liquid.

As a first approach, a series of *ab initio* calculations on carbon nanotubes of different chiralities, and therefore diameters, but of fixed length were performed, along with an in-depth analysis of the interaction energy, the relaxation effects, the charge density distribution and the nature of the interaction.

In a second part, accurate systematic calculations were performed on nanotubes of increasing length, but of a fixed diameter, in order to provide high-level reference data to compare with the intermolecular potential implemented in the MD program.

4.1.1 *Ab Initio* Methodology – Part I

The carbon nanotubes used in this investigation were treated as finite-size systems and saturated at both ends with hydrogen atoms. Two classes of single-wall nanotubes were used, namely zigzag and armchair, with chiral indices $(n, 0)$ and (m, m) , respectively, assigning values of n equal to 8, 10 and 12, and values of m equal to 4, 5 and 6. The resulting zigzag nanotubes measured ≈ 13.57 Å, whereas armchair ones were ≈ 15.43 Å. The geometries of both the CNTs and the azide were optimized by restricted DFT using the three-parameter Becke exchange functional^{105,112} and the Lee-Yang-Parr correlation functional¹⁰⁶, known as B3LYP. The optimization was performed on the lowest energy state at this level of theory, namely the triplet state for zigzag CNTs and the singlet state for armchair CNTs and N_3^- . For all calculations of this first part, the double- ζ 6-31G basis set¹²⁹ was used for the nanotubes, whereas the 6-31+G* for N_3^- ion²³¹. Note that polarization functions on the carbon atoms do not affect qualitatively the results and

therefore they were not included in this series of calculations.

The interaction energy between the fragments was calculated according to the following formula

$$E_{int} = E_{complex} - E_{cnt} - E_{azide} \quad (4.1)$$

Two sets of energies were obtained, in one case an *unrelaxed* E_{int} was computed using the geometries of the relaxed fragments, whereas in the other case a *relaxed* E_{int} was calculated after optimizing the complex system. For both cases, the BSSE was corrected by the counterpoise procedure¹³².

Single point energies for the complex and the fragments were calculated using the NEVPT2 method on top of a CASSCF wave function in the case of zigzag CNTs, while the MP2 method following a RHF calculation was used in the case of armchair nanotubes. The reason behind the application of different methodologies is the open-shell character of the ground state of $(n,0)$ CNTs, which requires a multireference approach in order to properly account for static electron correlation. Since the armchair nanotubes have a closed-shell ground state, there was no necessity for a multireference approach in that case. The complications to properly describe the wave function of zigzag CNTs also implied that the relaxed interaction energies were computed for systems involving armchair nanotubes only. The optimization of the complex system was carried out using DFT and the dispersion-corrected APFD exchange-correlation functional¹¹⁶, which reproduces the MP2 unrelaxed interaction energies very accurately. Single point calculation on the fully relaxed structures were then obtained by MP2. For this first part, calculations involving zigzag nanotubes were performed using the 2015.1 version of the MOLPRO program package^{174,175} applying default thresholds in all cases, while those involving armchair nanotubes with the Gaussian09 suite of programs²³² and the built-in natural bond orbital (NBO) program²³³. In Gaussian09, the DFT calculations were performed using the “Ultrafine” grid for the numerical integration of the functional.

4.1.2 *Ab Initio* Interaction Energies – Part I

To obtain unrelaxed interaction energies, the azide ion was placed exactly along the principal axis of the CNT and at its midpoint between the two openings as can be seen from Figure 4.1. The calculated energies as a function of the CNTs diameters are depicted in

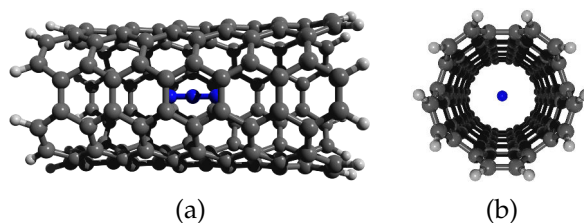


FIGURE 4.1: Side (a) and front (b) view of the geometry used for the unrelaxed interaction energy calculations.

Figure 4.2. For all dimensions considered, the interaction between the two fragments decreases the energy of the total system, resulting in an overall stabilization of the azide ion confined in the CNT. Despite the difference between the two methods used for the two classes of nanotubes, the interaction energy “smoothly” changes as a function of the diameter, suggesting that the nanotube helicity does not play a significant role in the interaction. The most favorable host CNTs have a diameter comprised between 6.26 Å and

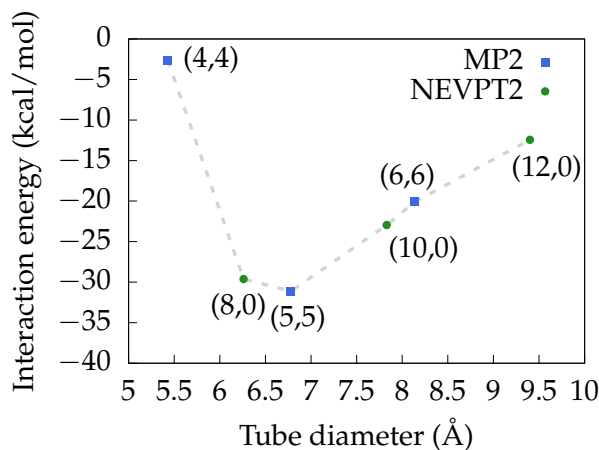


FIGURE 4.2: Unrelaxed interaction energies as a function of the nanotube diameter.

6.78 Å, with E_{int} values of ≈ -30 kcal/mol. A small (6,0) nanotube with a diameter of 4.70 Å was also tested, but the positive interaction energy of more than 100 kcal/mol clearly indicated that the cavity is too small to host the N_3^- ion. By keeping the azide fixed at the center of the nanotube while increasing the diameter of the latter, E_{int} should in principle decrease (in absolute terms) and approach zero for a sufficiently large nanotube.

The (5,5) CNT shows the largest interaction and hence this system was considered in somewhat more details. The relaxation of the complex geometry was started from six different orientations of the N_3^- ion inside the nanotube depicted in Figure 4.3 to ensure that the system did not remain trapped into an energetically high local minimum. The geometry of Figure 4.3a is the same used in the unrelaxed calculation, and after optimization the position of N_3^- remains virtually unchanged. Starting geometries depicted from Figure 4.3b to Figure 4.3d yield final structures similar to that of Figure 4.3a, where the anion ends up in the center of the nanotube, and only slightly displaced from its midpoint along the axis. For the last two cases shown in Figure 4.3e and Figure 4.3f, the N_3^- fragment was initially placed close to one end of the CNT, rotated and shifted closer to the wall. Interestingly, also for the latter cases, the relaxed structures result very similar to the previous ones: during optimization the N_3^- ion moves towards the midpoint of the nanotube instead of remaining near the opening or going out, see Figure 4.4.

In summary, for all relaxed structures, the N_3^- fragment aligns almost perfectly to the CNT axis, with deviations of at most 0.03 Å. On the contrary, its relative position along the axis varies more and in the most extreme case the N_3^- center of mass is displaced

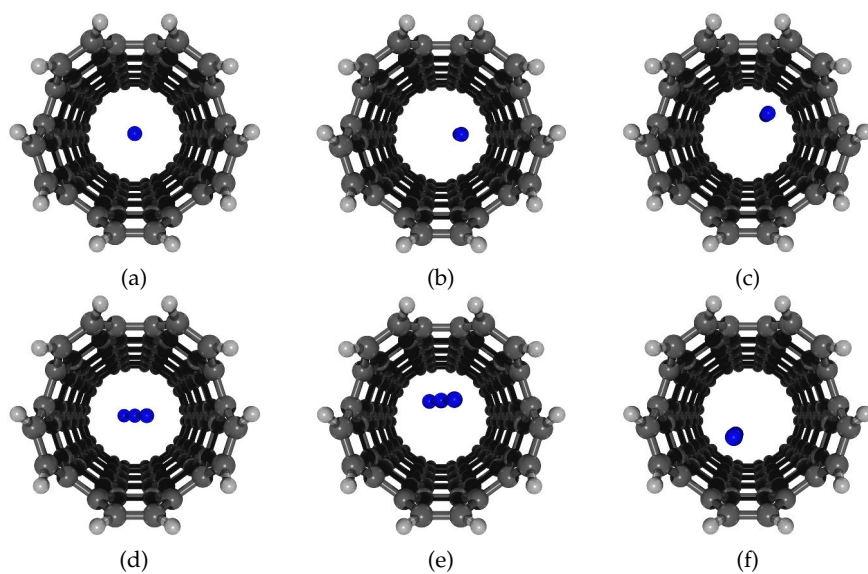


FIGURE 4.3: Starting orientations of the confined N_3^- ion. In the last two cases (e) and (f), N_3^- is closer to the edge of the CNT, while in the other cases is at the midpoint.

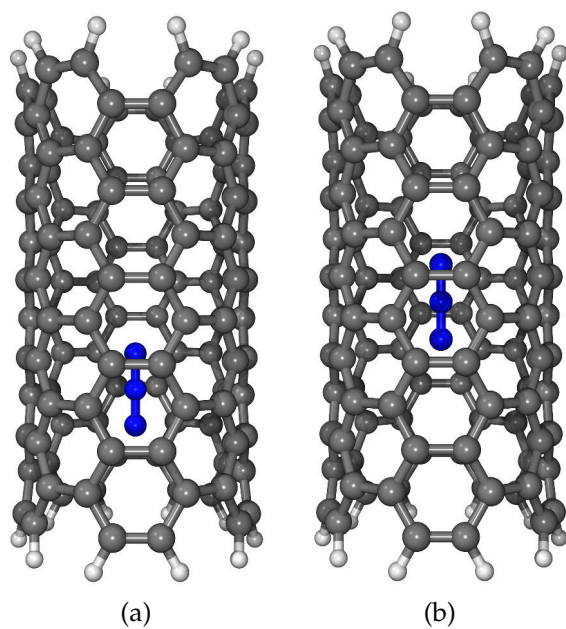


FIGURE 4.4: Starting (a) and final (b) position of the N_3^- ion inside the the (5,5)CNT.

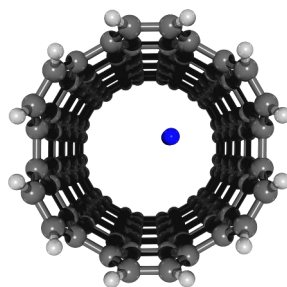
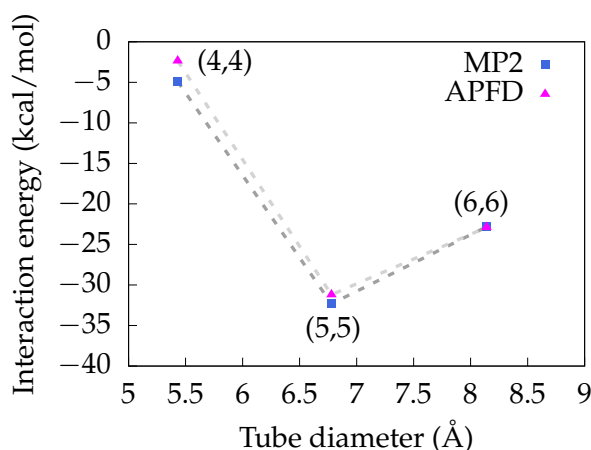
FIGURE 4.5: Relaxed geometry of N_3^- inside a CNT(6,6).

FIGURE 4.6: Relaxed interaction energies as a function of the CNT diameter.

by 0.43 \AA from the midpoint of the CNT. Despite these (small) differences in the relaxed structures, from an energetic perspective the difference is insignificant, with a maximum discrepancy of merely 0.05 kcal/mol .

It is possible that the geometry relaxation induces considerable changes in the interaction energy of nanotubes different than CNT(5,5), therefore the systems with the ion confined inside a (4,4) CNT and a (6,6) CNT were relaxed too, starting from a single geometry similar to the one depicted in Figure 4.3f. For the small (4,4) CNT, the final position of the anion is in the center of the nanotube, parallel to the principal axis and displaced by 0.7 \AA towards one end. In the case of the (6,6) CNT, because of the considerably larger cavity, the N_3^- fragment is adsorbed on the internal wall at a distance of $\approx 3.10 \text{ \AA}$, yet remaining parallel to the principal axis as can be seen in Figure 4.5. For these two geometries and the lowest-energy conformation involving the CNT(5,5), single point MP2 energies were computed and compared to the APFD values, which are again reported as a function of the nanotube diameter in Figure 4.6. The energies obtained with the two methods are in good agreement, with the largest deviation of $\approx 2.60 \text{ kcal/mol}$ for the (4,4) CNT. The comparison with the unrelaxed interaction energies also shows a good match: at MP2 level of theory, E_{int} for the (5,5) CNT slightly decreases from -31.12 kcal/mol to -32.31

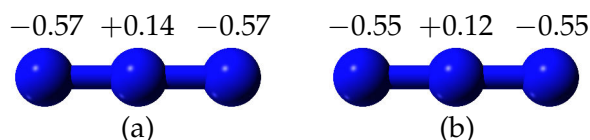


FIGURE 4.7: Partial atomic charges of the isolated (a) N_3^- fragment and confined (b) inside a CNT(5,5).

kcal/mol, whereas for the other two nanotubes it decreases by ≈ 2.5 kcal/mol. Consequently, the optimization of the complex structure has very little impact on E_{int} and does not change the qualitative behavior observed with the unrelaxed geometries.

Most likely, one can expect the relaxation process to affect more the nanotubes with a large diameter, since by fixing N_3^- in the center of the nanotube would decrease the interaction energy for increasing diameter size, whereas allowing for structural relaxation would give the CNT the freedom to adsorb the N_3^- on the inner side of the wall, eventually matching the interaction energy of the azide adsorbed on a graphene sheet in the limit of an infinitely large CNT.

It is interesting to note that the distance between the azide to the CNT(5,5) wall ranges between 3.45 Å and 3.50 Å, a significantly larger value than that measured in the CNT(6,6) case, which was found to be ≈ 3.10 Å. We argue that this is due to a cooperative effect in the case of the (5,5)CNT, whose diameter is such that the distance between the ion and the surrounding wall is just about right to be pulled equally in all directions and ultimately stabilizing in the center.

Regarding the deformation of the fragments due to their interaction, it is observed that the nanotube has virtually no influence on the geometry of the azide ion. The structure remains perfectly linear with the bond length decreasing by only 0.001 Å for all starting geometries, whereas the deformation energy observed never exceeds 0.01 kcal/mol. Similarly, the CNT distortion due to the presence of the anion is also relatively small, with the largest deformation energy calculated being 0.4 kcal/mol.

4.1.3 Charge Distribution and Interaction Nature

The charge distribution of N_3^- is minimally affected by the presence of the carbon nanotube. Partial atomic charges on the nitrogen guest were obtained by a natural population analysis (NPA)²³⁴ for the isolated ion and for the full complex. The analysis for the azide shows a positive excess charge of 0.14 on the central nitrogen and an accumulation of negative charge equal to -0.57 on the two external atoms. This distribution is only weakly affected upon relaxation of the complex, with the partial charge on the central atom decreasing to 0.12 and the one on the external atoms increasing to -0.55 , as shown in Figure 4.7. The fact that the CNT is finite and the presence of hydrogen atoms at the two extremities, induces a polarization on the entire nanotube. In particular, the hydrogen atoms and the carbon atoms to which they are connected are strongly polarized. Quantitatively speaking, a natural population analysis of the CNT(5,5) alone shows a value of 0.26 on each hydrogen and a value of -0.22 on each carbon directly connected.

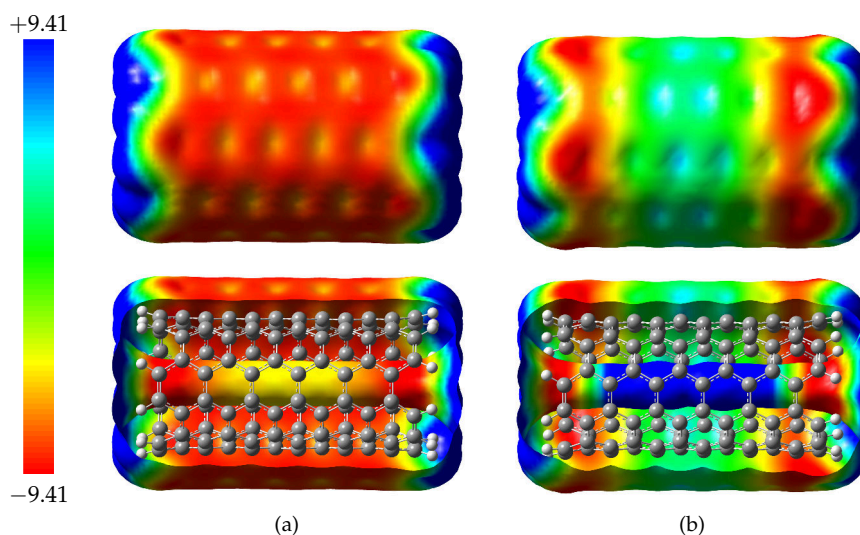


FIGURE 4.8: Molecular electrostatic potential of the unperturbed (5,5) CNT (a) and perturbed (b) by the presence of the azide ion. The isosurface value was set to 0.02. The energy scale is given in kcal/mol.

Moving from the extremities towards the center, the remaining excess negative charge is then relatively homogeneously spread over the rest of the nanotube, with practically neutral carbons around the central region. Important electrostatic effects between the two systems are therefore to expect, however is hard to quantify them.

Furthermore, the presence of the negatively charged ion inside the cavity *induces* an additional polarization on the CNT, which is also confirmed by an NPA on the full complex system, where partial atomic charges of the nanotube around the region of the ion exhibit a change of sign from slightly negative to positive. To investigate the induction effects in more detail, the molecular electrostatic potential (MEP) of the nanotube electron density is calculated for the isolated CNT and compared to the MEP of the electron density perturbed by the presence of the anion. In Figure 4.8a, the MEP of the isolated nanotube is reported, where the aforementioned polarization due to the hydrogen atoms is clearly visible. The isosurface reported in Figure 4.8b was instead obtained from the difference of the total system and N_3^- electron densities, unraveling the effects on the CNT due to the anion. In the central region, around the position of N_3^- , the charge on the CNT changes sign and becomes positive. This is particularly clear from the colormap reported at the bottom of Figure 4.8b, which represents the value of the electrostatic potential inside the cavity. However, the sign flip does not occur everywhere, the carbon atoms at the edges remain negatively charged despite the presence of the ion, suggesting a possible explanation to what was observed during the geometry relaxation. For starting geometries appearing in Figure 4.3e and Figure 4.3f, the negative charge at the CNT edges is such that the N_3^- , which has an excess of electron density around the external nitrogen atoms, is repelled by a strong electrostatic effect and moves back to the midpoint of the nanotube.

According to this analysis, we argue that the confinement of the azide ion inside the

cavity of the nanotube is largely dominated by electrostatic and induction effects. The confined ion induces a polarization on the carbon atoms, which is also favored by the presence of hydrogen atoms at both extremities, resulting in an overall redistribution of the charge on the carbon nanotube. This rearrangement is such that the N_3^- fragment remains *trapped* inside the nanotube, adsorbed on the inner surface.

Of the different types of nanotubes considered, the armchair (5,5) CNT resulted the best host from an energetic point of view, whose cavity has the ideal size to host the linear N_3^- ion parallel to the principal axis at an equal distance in all directions from the CNT wall. In the case of larger and smaller nanotubes, it was found that the azide also remains confined inside the cavity, aligned to the principal axis.

It is to expect that the polarization of the bare nanotube depends on its length, the longer the CNT, the more neutral will be the central sections as the distance from the openings is larger. In the limit of an infinitely long nanotube, there will be no polarization at all. It is important to understand this behavior and investigate its repercussions on the interaction energy calculated for the confined N_3^- inside the carbon nanotube. In particular, a very accurate estimate of E_{int} is crucial in order to compare the performance of a classical intermolecular potential against values obtained from first principles.

In the following, we will present a second series of *ab initio* calculations performed on (5,5)CNT of different lengths, using more accurate quantum chemical methods since the objective is to obtain reference data to compare with the intermolecular potential that we seek to propose for this system later on.

4.1.4 *Ab Initio* Methodology – Part II

As in the previous section, CNTs were treated as finite-size systems with the two open ends capped with hydrogen atoms in order to fill out the valence shell of the carbons. Only one type of armchair nanotube was considered, with chiral indices (5,5). We introduce here the notation Λ -(5,5)CNT to label a nanotube composed by Λ units, where a single unit corresponds to a single [10]cyclophenacene.

The choice of methodology and the length of the nanotubes considered in this part are different with respect to the previous one, however, since the geometry optimization of the individual fragments as well as the complex was already discussed in quite details before, we repropose here only the essential information and provide the rest in Appendix A.1.

The geometries of the nanotubes and the azide anion were optimized using restricted DFT, employing the B97D3 exchange-correlation functional with Becke-Johnson damping^{118,235}. For both fragments, Dunning's triple- ζ cc-pVTZ basis set¹²² was used, with the addition of diffuse functions (aug-) ¹²³ on the the N_3^- fragment. The isolated geometries of the fragments are in good agreement with previous theoretical and experimental results, for a quantitative overview see Appendix A.1.

The different systems composed by the nanotubes and the azide ion were then relaxed by keeping the geometries of the fragments frozen, in order to locate only the optimal

adsorption distance. To ensure that the relaxation process did not remain trapped in a local minimum, similarly to the approach outlined in the previous part, the optimization procedure was started from different geometries. For the geometry optimization only, a total of four different nanotubes were considered, composed by 3, 5, 7 and 9 units and a series of criteria were defined and used to quantify the differences between the optimized structures, these are described in Appendix A.1. Remarkably, for all lengths as well as starting geometries, despite slight differences in the final structures, the interaction energies computed on the different systems were all within 1 kcal/mol from each other. Hence, considering the small impact observed, the simple geometry with the ion placed exactly at the center was used for all single point calculations at higher levels of theory and for longer nanotubes.

The optimizations of the individual fragments were performed using the Gaussian 09 software package, revision d01²³², using the default convergence thresholds, the “ultrafine” grid for the integral quadrature and spherical d and f basis functions. On the other hand, the constrained optimizations were performed using the ORCA 4 program package¹⁷⁶ at the same level of theory, however employing the smaller cc-pVDZ basis set^{122,123} on the nanotube, and the resolution of the identity technique for the Coulomb matrix, using the def2/J auxiliary basis set²³⁶.

The interaction energies were computed according to Equation (4.1) as before, and again it was corrected for the BSSE by the counterpoise scheme¹³².

Single point calculations to obtain accurate energies were performed using wave function methods, in particular using density-fitted spin-component-scaled MP2 (RI-SCS-MP2)²³⁷ and DLPNO-CCSD(T)^{93,238}. The basis sets used were either the cc-pVDZ or, where computationally feasible, the cc-pVTZ, with extra diffuse functions (aug-) on nitrogen atoms in both cases^{122,123}. For all HF calculations on nanotubes longer than 5 units, the chain-of-spheres approximation²³⁹ and the density fitting technique were used. The numerical integration grid was set to “gridx6” while the auxiliary basis set used was the def2/j²³⁶. In the post-HF calculations, either the cc-pVDZ/c or the cc-pVTZ/c auxiliary basis sets fitted against correlated methods were used¹⁷¹. All these calculations were performed using the ORCA 4 program package¹⁷⁶, setting the “tightSCF” convergence criterion and default thresholds for all remaining parameters.

The importance of using a large basis set for quantitative correlated calculation is well known, however in the case of large systems such as carbon nanotubes it is not always feasible. Anyhow, an approximate way to obtain triple- ζ quality results using the DLPNO-CCSD(T) method is possible, relying on an extrapolation technique which is based on energies calculated at a lower level of theory and with a smaller basis set. In our particular case, this was achieved by using the formula

$$E_{CC}(TZ) \approx E_{MP2}(TZ) + (E_{CC}(DZ) - E_{MP2}(DZ)) \quad (4.2)$$

The central assumption of this approach is that the correlation energy difference between two methods remains approximately constant irrespective of the basis set size. Note that

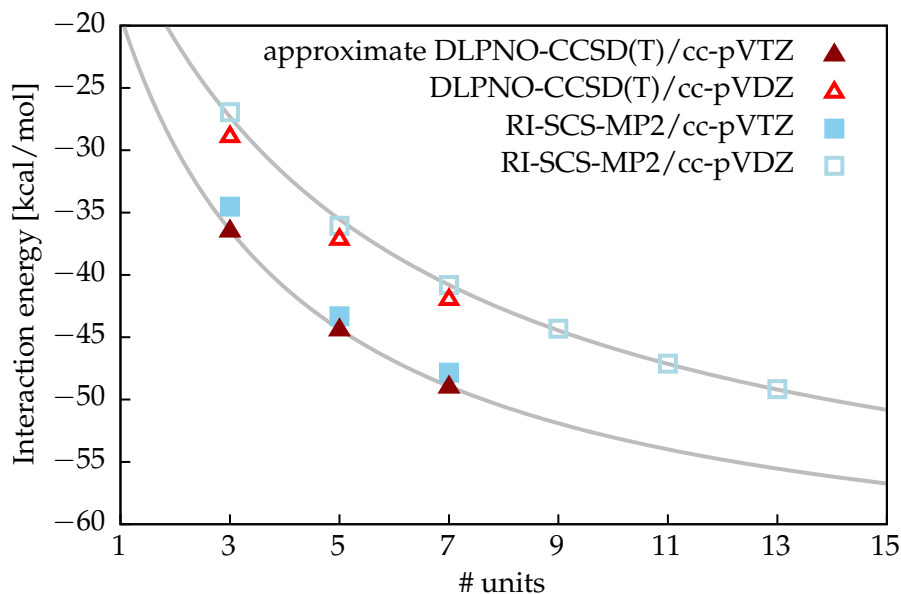


FIGURE 4.9: Interaction energy as a function of tube length. The solid lines are fits to the RI-SCS-MP2/cc-pVDZ and the approximate DLPNO-CCSD(T)/cc-pVTZ points.

E_{CC} in the above equation refers to DLPNO-CCSD(T) energies and E_{MP2} to RI-SCS-MP2, whereas DZ and TZ to the basis sets combinations introduced above. In this way, it was possible to obtain very accurate energies for the shortest nanotubes.

4.1.5 *Ab Initio* Interaction Energies – Part II

The limitation imposed by the size of the systems were such that RI-SCS-MP2/cc-pVTZ and DLPNO-CCSD(T)/cc-pVDZ energies were obtained for nanotubes of length 3, 5 and 7 units only. Accordingly an estimation of the interaction energies for this three cases was possible by application of Equation (4.2). These energies, along with several more points at RI-SCS-MP2/cc-pVDZ level are reported in Figure 4.9 as a function of the nanotube length. The slow convergence of the energy with respect to Λ is evident. The diffuse electron density surrounding the azide anion is such that sizable interaction occurs for every added unit, for all considered lengths. Nonetheless, the RI-SCS-MP2/cc-pVDZ points show that for long CNTs, the relative change between two consecutive points decreases by increasing number of units. It is interesting to see the substantial lowering of the energy for the values obtained with the triple- ζ basis compared to the double- ζ one, highlighting its importance. The good performance of the RI-SCS-MP2 method is also noteworthy, with E_{int} values lying very close to the ones obtained with the CC method.

In principle, the interaction energy points calculated can be fitted to a model function, such that it is possible to extrapolate E_{int} to a nanotube of arbitrary number of units Λ . The simplest function which satisfies the condition $E_{int}(0) = 0$, i.e. in the absence of a nanotube there is no interaction, and provides an estimate for an infinitely long CNT is

given by

$$E_{int}(\Lambda) = \frac{a\Lambda}{b + \Lambda} \quad (4.3)$$

where a and b are the fitting parameters to be determined. Using a non-linear least square procedure, the RI-SCS-MP2/cc-pVDZ energies as well as the approximated DLPNO-CCSD(T)/cc-pVTZ points were fitted and the resulting functions are the solid lines appearing in Figure 4.9. In both cases the fit is qualitatively the same, with the exception for the shortest nanotubes where the constraint $E_{int}(0) = 0$ and the fact that the energies differ by roughly 10 kcal/mol generate different curvatures. In the limit of an infinitely long CNT, the interaction energy at the DLPNO-CCSD(T)/cc-pVTZ level is estimated to be -65.93 kcal/mol, which is remarkably close to the estimate for the RI-SCS-MP2/cc-pVDZ curve, with a value of -64.75 kcal/mol. The values of the other fitting parameter b are 4.11 and 2.43 for the RI-SCS-MP2 and DLPNO-CCSD(T) energies, respectively. Despite the large difference between the two methodologies for the shortest systems, it appears that in the limit of very long nanotubes, where the electrostatic effects due to the finite size are not present anymore, the two methodologies provide results in very good agreement.

Building on the knowledge acquired in the *ab initio* investigations, in particular the rationalization of the interaction nature between the fragments and the behavior of the interaction energy as a function of the nanotube size and length, we shall now propose a novel intermolecular potential to describe this interaction in classical terms.

This is done with the idea that such a potential will allow to study the dynamic properties of the system by performing molecular dynamics simulations.

4.1.6 Intermolecular Potential

In the system under study, three main types of interaction were identified from the previous investigations: VdW interactions (these are always present), induction effects due to the azide ion and electrostatic effects between the polarized nanotube and the azide. We shall see how these different interactions can be accurately modeled and added together to form a complete description of all non-covalent interactions present in the system.

Definition of the Potential Functions

As mentioned in the theoretical methods chapter, VdW interactions can be described by different types of potential functions. Among the most famous ones, there is the Lennard-Jones model, which is particularly efficient from a computational point of view. This fact is crucial for very large systems, however, in our case, given that in a first moment the interest is on a relatively simple system composed by a nanotube and a single azide ion, a (slightly) more complex potential can be used. In particular, an *improved* version of the Lennard-Jones potential was proposed a few years ago by Pirani et al.¹³³, with the

general formula given by

$$V_{ILJ}(r_{ij}) = \epsilon \left[\frac{m}{n(r_{ij}) - m} \left(\frac{r_m}{r_{ij}} \right)^{n(r_{ij})} - \frac{n(r_{ij})}{n(r_{ij}) - m} \left(\frac{r_m}{r_{ij}} \right)^m \right] \quad (4.4)$$

where

$$n(r_{ij}) = \beta + 4.0 \left(\frac{r_{ij}}{r_m} \right)^2 \quad (4.5)$$

The indices i and j represent interaction centers. In principle one can freely choose what constitute such centers, e.g. atoms, bonds, and so on. To simplify the discussion, we assume here that these correspond to the atoms in the system. As Equation (4.4) is modeling non-bonded interactions, atoms i and j do not belong to the same molecule. For each such pair, there are three parameters to be set. The value r_m indicates the position of the minimum of the potential energy surface for the interaction of the two atoms labeled by i and j . The depth of that minimum is given by the value of ϵ and the last parameter is β , appearing in Equation (4.5), which is related to the hardness of the system and usually varies between 7 and 9¹³³. Actually, there is a fourth parameter, m , entering Equation (4.4) as an exponent and prefactor, and is set according to the type and charge of the interacting centers: for atom–atom interactions m is equal 6, for ion–atom interactions is equal 4 and for ion–ion is set to 1.

The ILJ has proven very effective in a number of applications, in particular dealing with polar molecules such as water²⁴⁰, water-carbon systems²⁴¹, ion- π interactions^{242,243}, and in general gases interacting with carbon nanostructures such as graphene and carbon nanotubes^{244–248}.

However, albeit the ability of the ILJ potential to accurately reproduce the potential energy surface of ion-neutral species, it is most often the case that the ions in question are individual atoms. This fact allows for a pairwise treatment of the interaction which might not be true for larger molecular ions. Above all, this is the case for the induction effects, which are non-additive in nature²⁴⁹. The fact that the azide anion is a charged molecular species increases therefore the complexity of the interaction and is therefore considered here as an extra, individual term.

The induction effects generated by the presence of N_3^- can be modeled according to a relatively simple formula, which is a direct consequence of the general induced dipole interaction due to an external electric field, in other words

$$\mu^* = \alpha \mathcal{E} \quad (4.6)$$

where μ^* is the induced dipole, α is the polarizability and \mathcal{E} is the external electric field. In the system we are considering, the external electric field is the one generated by the partial atomic charges of the azide, whereas the polarizability is that of the carbon nanotube. By considering atoms as interacting centers, α actually refers to the atomic polarizability of carbons and hydrogens. The larger is α , the stronger will be the effect of the azide

on the carbon nanotube and therefore stronger will be the interaction between the fragments.

From Equation (4.6), it is possible to obtain the potential by integration, i.e.

$$V_{ind} = - \int_0^{\mathcal{E}} \mu^* d\mathcal{E} = -\frac{1}{2}\alpha\mathcal{E}^2 \quad (4.7)$$

where we note that the electric field on the right-hand side comes squared.

For the specific case of the electric field generated by three point charges, the induction potential is given by

$$V_{ind}(r_{i1}, r_{i2}, r_{i3}) = -\frac{1}{2}\alpha_i \left[\frac{q_1}{r_{i1}^2} + \frac{q_2}{r_{i2}^2} + \frac{q_3}{r_{i3}^2} \right]^2 \quad (4.8)$$

where r_{i1} , r_{i2} and r_{i3} are the distances between atom i of the nanotube and the three nitrogen atoms of the azide anion, q_1 , q_2 and q_3 are their partial atomic charges and α_i is the polarizability per volume of the atom i . Note that the choice of having three partial charges, one for each nitrogen of the azide, is arbitrary, but the most natural. Nevertheless, the fact that the electric field is generated by more than one charge is the mathematical reason why the induction potential is non-additive. In principle, one can model the charge distribution of the azide in a different way, with more or less charge centers, however, due to the very nature of the induction potential, Equation (4.8) would have to be modified accordingly.

The last type of interaction identified in the *ab initio* investigation is the electrostatic one. By using finite, hydrogen-saturated nanotubes, an *artificial* polarization of the CNT wall appear and thus electrostatic effects between this charge accumulation at the extremities and the azide are non-negligible. This type of interactions are quite normal within the context of molecular dynamics, and are usually modeled by the Coulomb potential, given by

$$V_{els}(r_{ij}) = \frac{q_i q_j}{r_{ij}} \quad (4.9)$$

where q_i and q_j are the charges of the interacting atomic centers and r_{ij} is the distance between them. Note that in the absence of hydrogens, the nanotube remains in principle completely unpolarized, hence no partial charges are assigned to the carbon atoms. This makes the contribution of V_{els} essentially zero. Even in the presence of the hydrogen atoms, but in the case that the azide ion confined inside the nanotube is far away from the extremities, the electrostatic contribution should be very small.

The total intermolecular potential describing the interaction between the azide anion and a (arbitrary) carbon nanotube is given by the combination of the three components just introduced, summing over all atoms of both fragments, i.e.

$$V_{tot} = \sum_{i=1}^{N_{cnt}} V_{ind}^{(i)}(r_{i1}, r_{i2}, r_{i3}) + \sum_{i=1}^{N_{azide}} \sum_{j=1}^{N_{cnt}} V_{ILJ}^{(ij)}(r_{ij}) + V_{els}(r_{ij}) \quad (4.10)$$

TABLE 4.1: Potential parameters for carbon and carbon–hydrogen interactions. Polarizability given in \AA^3 , energies in meV and distance in \AA .

(m, m)	$\bar{\alpha}$	C–N _{ext}		C–N _{int}	
		ϵ	r_m	ϵ	r_m
(5, 5)	1.136	5.074	3.984	3.469	3.805
(7, 7)	1.179	5.163	3.991	3.514	3.814
(9, 9)	1.219	5.243	3.997	3.554	3.822

TABLE 4.2: Potential parameters for hydrogen and hydrogen–nitrogen interactions. Polarizability given in \AA^3 , energies in meV and distance in \AA .

(m, m)	$\bar{\alpha}$	H–N _{ext}		H–N _{int}	
		ϵ	r_m	ϵ	r_m
(5, 5)	0.380	2.827	3.644	2.431	3.348

where N_{cnt} , N_{azide} correspond to the total number of atoms in the carbon nanotube and the azide anion, respectively. The superscript (ij) in the ILJ potential term $V_{ILJ}^{(ij)}$ labels the type of interacting atoms, since for every unique pair there is a different set of parameters.

Intermolecular Potential Parameters

With this choice of potential, we are now set to test the accuracy by comparing the interaction energies obtained with the DLPNO-CCSD(T) method with those obtained from Equation (4.10). There exist different possible ways to obtain the parameters required by the potential. In our particular case, we used a combination of experimental and *ab initio* data, together with correlation formulas derived from extensive empirical studies^{250–252}. The most important parameters are the atomic polarizabilities, which are used to determine the ϵ and r_m values for V_{ILJ} as well as enter directly in the induction potential. The nitrogen atomic polarizability is obtained from the experimental total mean polarizability of the azide anion²⁵³, $\bar{\alpha} = 4.65 \text{\AA}^3$, which was distributed on the three atoms according to their partial charges, resulting in a value of 1.9\AA^3 for the external atoms (charges $q_1 = q_3 = -0.56$) and a value of 0.85\AA^3 for the internal one (charge $q_2 = +0.12$). The polarizability of the hydrogen atoms was taken from Ref. 254 and set equal to 0.380\AA^3 , whereas that of carbon atoms from Ref. 58, but the actual value depends on the specific curvature of the nanotube. The polarizability for carbon atoms, along with the calculated ILJ parameters according to Ref. 250 are reported in Table 4.1. Similarly, the parameters for hydrogen and the hydrogen–nitrogen interaction are listed in Table 4.2. The nitrogen partial charges used in the the electrostatic and induction potentials were set equal to $q_1 = q_3 = -0.56$ for the external atoms and $q_2 = +0.12$ for the internal one. For the carbon nanotube, they were obtained through a natural population analysis²³⁴ of the electron density calculated at B97D3/cc-pVTZ level of theory.

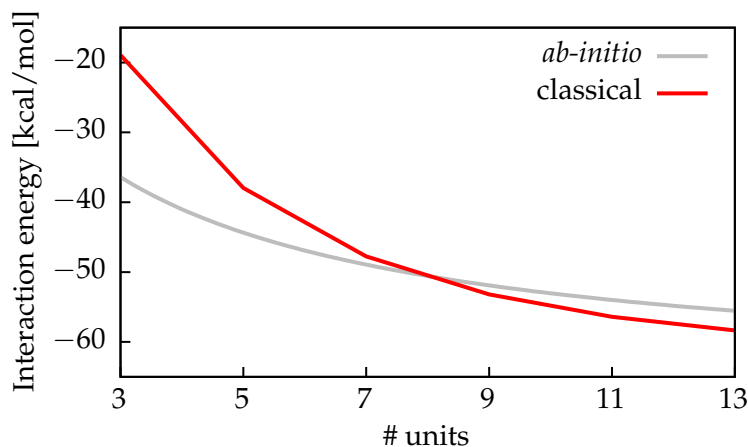


FIGURE 4.10: Comparison of classical and quantum-chemical interaction energies for $\beta = 8$.

Potential Energy Minimum

For all nanotubes considered in the second *ab initio* part, we have computed the interaction energy predicted by the model function extrapolating the DLPNO-CCSD(T)/cc-pVTZ values and compared to the ones obtained by the classical potential. Essentially, the comparison is between the potential energy minimum between the two interacting fragments. In Figure 4.10 the *ab initio* and the classical potential energies are reported for $\beta = 8$ as a function of the nanotube length Λ . As can be seen, for the shortest nanotube, the classical potential largely underestimate the interaction strength, however, starting at 7 units, the agreement is excellent. The fact that different types of interactions are explicitly treated, allows for an approximate energy decomposition analysis. The plot appearing in Figure 4.11 shows the same two curves as in Figure 4.10, however, the relative contributions of the three components V_{ILJ} , V_{ind} and V_{els} are also reported. It is interesting to see the different ranges of the types of interaction. The VdW contribution described by the ILJ potential account for only a fraction of the total interaction energy. Moreover, the convergence with respect to the length of the tube is essentially immediate. Despite the fact that VdW interactions are usually called *long-range* in the QC context, because exchange interactions usually decay exponentially as function of the distance, in this framework they actually should be considered as *short-range* due to their r^{-6} dependence. The induction potential appears to converge also quite quickly with respect to the nanotube length. In this case however, the dependence is given by the inverse fourth power of the distance. What is very surprising here, is the magnitude of this contribution, the explicit modeling of this interaction seems therefore crucial in order to provide a good description of potential well. Furthermore, as the dependence with respect to the distance is different, trying to model induction effects using a standard VdW potential would certainly provide the wrong asymptotic behavior. At last, the really *long-range* interaction is given by the Coulomb potential, whose strength is inversely proportional to the distance between the atomic centers. Here, it is clear how the shape of the total

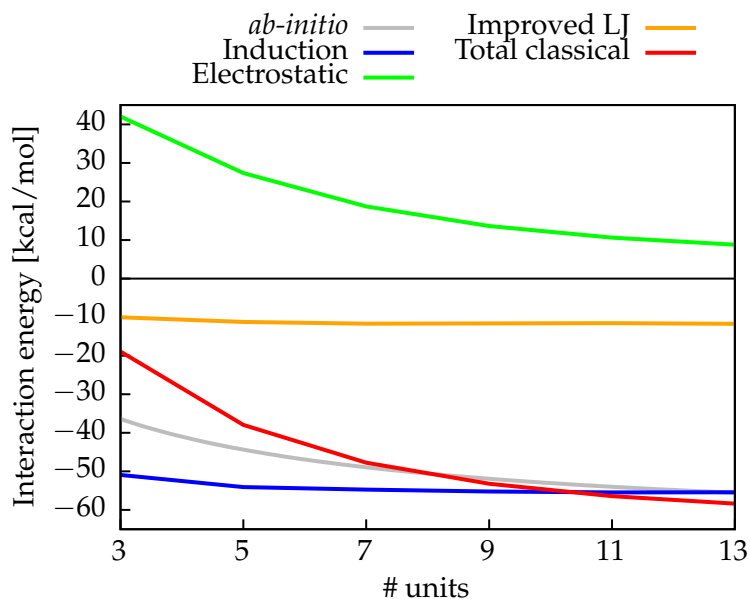


FIGURE 4.11: Individual potential contributions to the interaction energy.

TABLE 4.3: *Ab initio* and classical interaction energies and their difference. All energies are given in kcal/mol, Λ represents the number of units in the nanotube.

Potential	$\Lambda = 3$	$\Lambda = 5$	$\Lambda = 7$	$\Lambda = 9$	$\Lambda = 11$	$\Lambda = 13$
<i>Improved LJ</i>	-10.04	-11.26	-11.71	-11.64	-11.57	-11.74
<i>Electrostatic</i>	+42.02	+27.37	+18.70	+13.64	+10.60	+8.80
<i>Induction</i>	-50.92	-54.06	-54.74	-55.20	-55.44	-55.42
Total	-18.94	-37.95	-47.75	-53.20	-56.41	-58.35
<i>ab initio</i>	-36.42	-44.34	-48.94	-51.91	-53.99	-55.54
Difference	-17.48	-6.39	-1.19	+1.29	+2.42	+2.81

classical potential is dominated by this term. Since between 5 and 7 units, the improved Lennard-Jones and the induction potentials are essentially constant, the convergence behavior of the total is solely determined by the electrostatics.

In order to have a more quantitative insight in the different components, the values plotted in Figure 4.11 are reported in Table 4.3. Most interestingly, the last row shows the difference between the classical and the *ab initio* interaction energies, and as can be clearly seen, the agreement between the two is remarkable.

Potential Energy Profiles

Thanks to the analytical form of the intermolecular potential, the interaction energy profile of the azide ion moving inside and outside nanotubes of arbitrary size can be generated. As an example, we considered in the following three 7-unit long nanotubes, namely

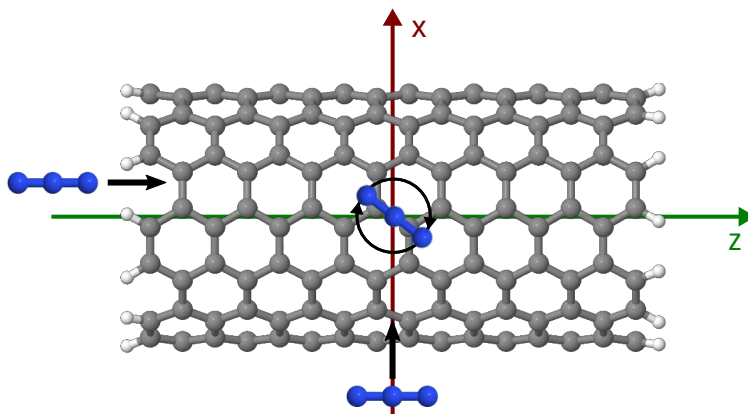


FIGURE 4.12: Scheme showing the three different ways in which the azide was moved to generate the energy profiles.

(5,5), (7,7) and (9,9) CNTs. The parameters used for each nanotube are listed in Table 4.1 and the partial charges assigned to the carbon and hydrogen were obtained by an NPA analysis using the electron density from a B97D3/cc-pVTZ calculation. We investigated the profiles of the azide anion moving in three different ways. In the first case, N_3^- was set parallel to the nanotube axis and moved along the x direction, in the second case it was passed through the nanotube along the z axis at the optimal adsorption distance found in the first profile and in the last case case it was fixed at the center and rotated. A scheme representing the 3 different situations is shown in Figure 4.12. The first potential energy surface that we investigated is that generated along the x axis, such that the optimal adsorption distances could be identified. In Figure 4.13 the results for the three nanotubes are shown stacked on top of each other, starting with the narrowest from the top. The most favorable interaction is always observed inside the CNT, even though a minimum is also found on the external side of the wall in all cases. For the two largest systems there is the appearance of a double well inside the cavity, whereas the optimal adsorption distance for the CNT(5,5) is exactly at the center as was previously found. The different components of the potential behave very similarly across the three systems. Remarkably, by going from the smallest to the largest systems, the overall shape of the total interaction resembles more that of the Van der Waals potential, in particular inside the CNT.

In the second the case, the profile along the nanotube axis was investigated. For the CNT(5,5) case, the azide position coincided with the nanotube axis, for the (7,7) CNT it was placed at a distance of 3.07 Å from the wall, and for the (9,9) nanotube the distance was 3.20 Å. The corresponding profiles are shown in Figure 4.14, where as before the plots are arranged on top of each other, starting from the top with the CNT(5,5). In all cases, if initially placed outside, the azide anion is attracted towards the nanotube. The most interesting result is the flipping of electrostatic interaction, which is attractive when the azide is outside the CNT, since the external hydrogen atoms are positively charged, and repulsive inside, since there is excess negative charge on the carbons.

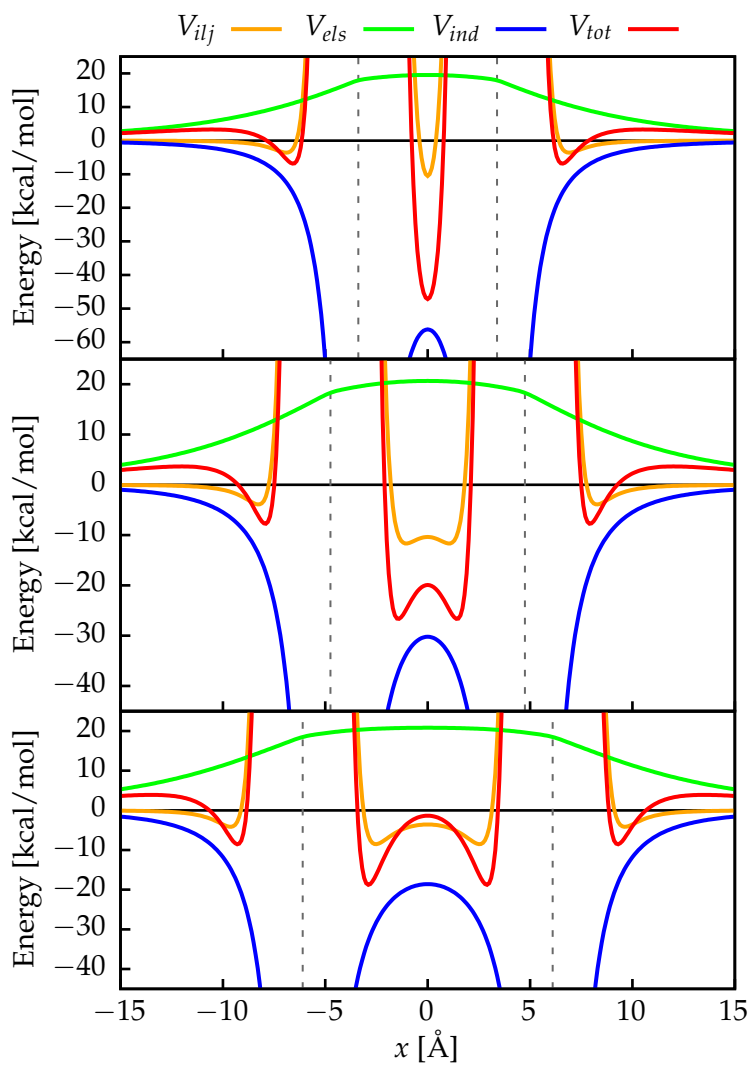


FIGURE 4.13: Potential energy profiles for (5,5), (7,7) and (9,9) CNTs from top to bottom. The dashed vertical lines show the position of the nanotube wall.

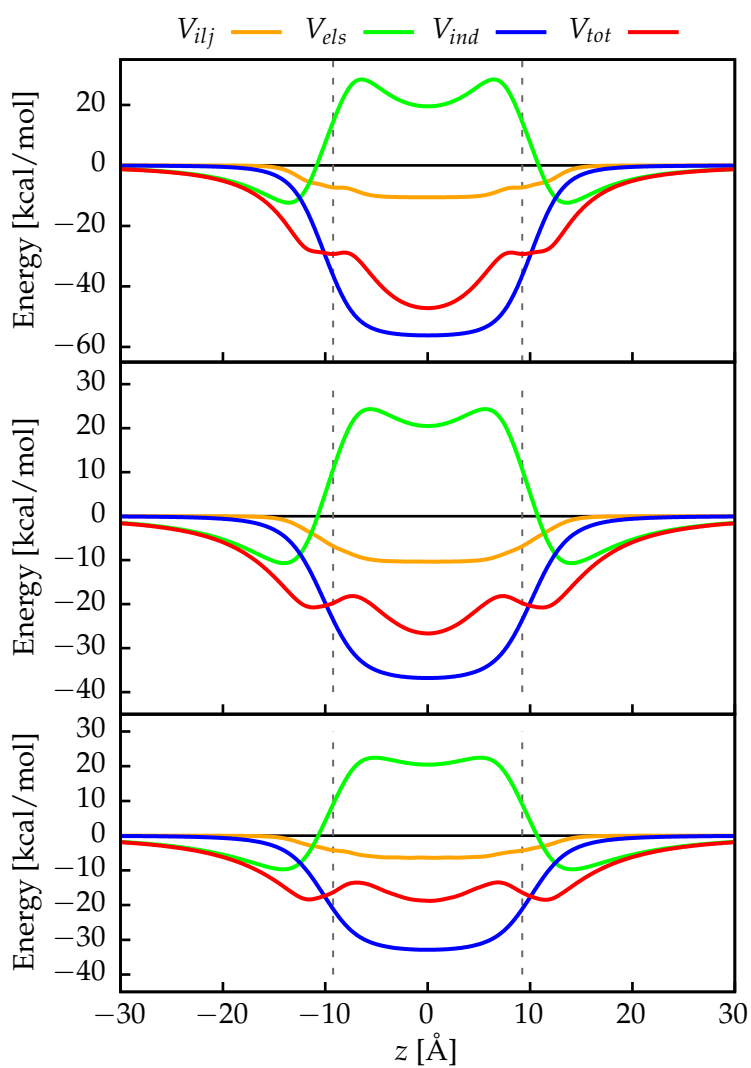


FIGURE 4.14: Potential energy profiles for (5,5), (7,7) and (9,9) CNTs from top to bottom. The dashed vertical lines show the position of the nanotube openings.

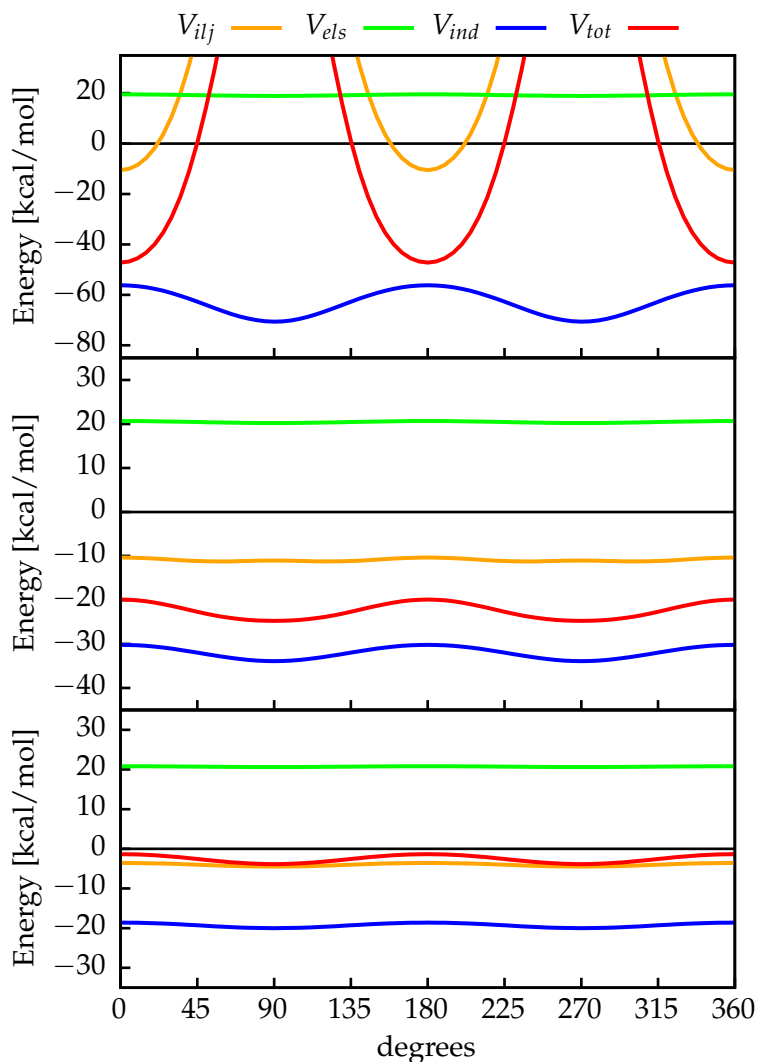


FIGURE 4.15: Potential energy profiles for (5,5), (7,7) and (9,9) CNTs from top to bottom.

The last case analyzed is for the rotation inside the nanotube, whose results are shown in Figure 4.15. This last series of profiles shows very clearly the effects, of spatial confinement provided by the enclosing CNT. In the (5,5) CNT, the ion can barely rotate, and tremendous repulsive walls build around the minimum of the surface. On the other hand, already with the slightly larger CNT(7,7), the effects are only mildly perceived by the ion. For the largest nanotube, the potential is basically flat.

4.1.7 Molecular Dynamics

In order to use this potential for molecular dynamics simulations, we have used the DL POLY 4.08 program^{229,230}. However, both the ILJ and the induction potentials are not mainstream, thus were not available in this software. For this reason they had to be implemented in the code as part of this thesis.

In the following, a brief section describing the implementation is followed by a final part

which discusses some example calculations, showing the potential in action on nanotubes of different sizes.

Implementation of the Potential

It is of paramount importance for the computational efficiency of the simulation that the potential energy gradients can be obtained analytically. This is the case for both the ILJ and the induction potentials. The ILJ potential is essentially as portable as the LJ potential and therefore once it is available, it can be used for any other system. On the other hand, the induction potential, being non-additive in nature, is forcedly hard-coded for the specific case of three point charges. Nevertheless, there is no particular assumption regarding the fact that this potential was implemented for the azide anion, any triatomic ion inducing a polarization to the surrounding molecules can make use of it. The derivation of the gradients is quite tedious, it is therefore only reported in Appendix A.2 at the end of this manuscript.

Another quantity which is required for MD simulations is the *virial*. In this case, for pairwise potential it is already implemented, however an explicit expression to compute it for the induction potential has to be derived. Again, this is reported only in Appendix A.3 as the derivation is quite tedious.

MD Simulations Examples

In order to validate the implementation, a series of MD simulations was carried out on the same systems for which it was presented the energy profiles, i.e. the azide anion confined in a CNT(5,5), a CNT(7,7) and a CNT(9,9). In this case however, the carbon nanotube was considered with PBC and hence without addition of hydrogen atoms at the two ends. This removes the need of electrostatic interactions, since the nanotube is not polarized.

The simulations were carried out with the following choice of parameters:

- NVT ensemble
- Nosé-Hoover thermostat 0.5 ps
- temperature: 300 K
- box size: $40 \times 40 \times 32 \text{ \AA}^3$
- 2000000 equilibration steps
- 3000000 production steps
- timestep: 1 fs
- sampling: every 10000 steps
- rigid molecules

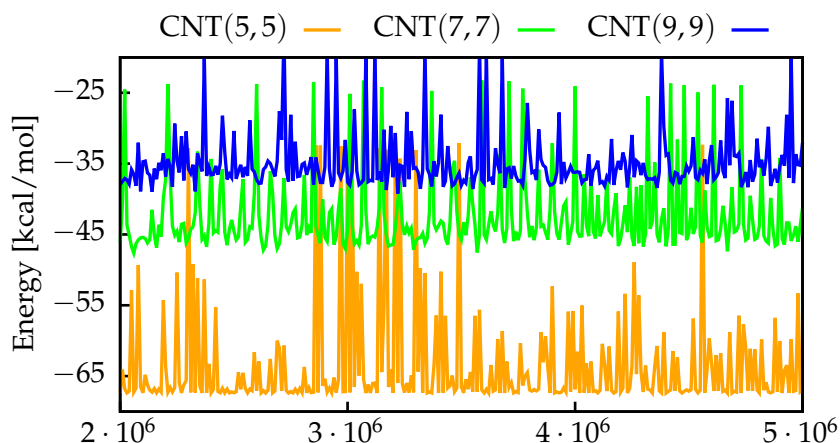


FIGURE 4.16: Adsorption energy of the azide anion inside different carbon nanotubes.

for which we report the adsorption energy sampled every 10000 steps as a function of time in Figure 4.16. Although the fluctuation of the adsorption energy is quite severe (due to the rigid bodies approximation), the mean energy values in kcal/mol of -62.98 , -42.32 and -34.77 for the CNT(5,5), CNT(7,7) and CNT(9,9), respectively, appear to be sensible with respect to what it was observed in the static calculations; in particular, for the CNT(5,5) case the extrapolated DLPNO-CCSD(T)/cc-pVTZ interaction energy was estimated to be -65.93 kcal/mol.

Clearly, this is only an illustrative example to show the correct functioning of the implementation.

4.2 N_5^+ and N_8 Confinement in Carbon Nanotubes

Besides the azide anion discussed so far, there are other, related systems which are of great interest as well. In particular, the pentanitrogen cation N_5^+ , successfully isolated in 1999 by Christe et al.¹⁹⁵, is a good candidate for investigation since combined with the azide anion can lead to the formation of the highly energetic N_8 molecule. In the literature, mostly theoretical and some experimental works investigated on either the individual ions N_3^- , N_5^+ and N_5^- ^{255–259} or compositions thereof^{196–199,260}. On the other hand, the potential energy surface of the N_8 species was also subject of extensive studies^{261–266}. Most notably, in 2001 Fau and Bartlett¹⁹⁶ predicted that the N_8 product of an N_5^+ and N_3^- addition would very likely be too unstable to exist, which was experimentally confirmed in 2004 by Dixon et al.¹⁹⁹. However, it was also suggested that such an allotrope of nitrogen could in principle exist due to the cohesive forces arising from a crystal structure. Indeed, in 2014 it was predicted by Hirshberg et al.²⁶⁷ a stable molecular crystal of N_8 . The confinement of the pentanitrogen cation inside carbon nanostructure has never been investigated, however, a number of theoretical studies predicting a stable polymeric nitrogen chain inside carbon nanotubes is available in the literature^{79,80,200,202}. In the following, the confinement of N_5^+ and selected N_8 linear isomers inside CNTs is investigated and reported.

4.2.1 Methodology

As usual, carbon nanotubes were treated as finite-size systems, saturated by hydrogen atoms at the two extremities. Two types of CNTs were considered, namely zigzag and armchair nanotubes. In the $(n,0)$ case, n was chosen equal to 8, 10 or 12, whereas for (m,m) CNTs, m was either 4, 5 or 6. This choice provided nanotubes with a diameter between 6.26 Å and 9.40 Å. The length of the nanotubes was ≈ 13.57 Å for zigzag and ≈ 15.43 Å for armchair CNTs, respectively.

To compute unrelaxed interaction energies, the fragment geometries were optimized using DFT, using the Becke exchange energy functional^{105,112} and the Lee-Yang-Parr correlation energy functional¹⁰⁶ (B3LYP). Nanotubes geometries were optimized for the lowest electronic state within the restricted approach, i.e. the triplet and singlet state for zigzag and armchair types, respectively. The ground state of the polynitrogen systems is a closed-shell singlet state in all cases.

Calculations of the N_8 as well as the relaxation of any complex system with both fragments were performed with the APFD density functional¹¹⁶.

For this investigation, the double- ζ 6-31G basis set¹²⁹ was used for hydrogen and carbon, while diffuse and polarization functions were added for nitrogen (6-31+G*)²³¹. All interaction energies calculated were corrected for the BSSE using the counterpoise correction scheme¹³². The single point energies involving the pentanitrogen cation were calculated either by MP2 or NEVPT2^{95–97}, while the preliminary study on N_8 was carried out entirely using DFT. As explained before, a multireference approach is necessary to correctly

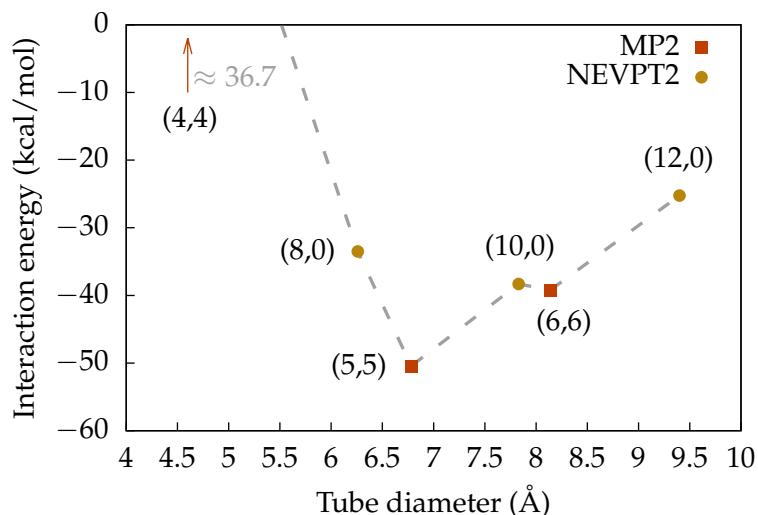


FIGURE 4.17: Unrelaxed interaction energies as a function of the CNT diameter.

describe zigzag nanotubes, whose ground state is of open-shell character. The zeroth order reference for the multireference perturbation treatment was obtained by CASSCF calculations⁹⁴, with an active space of 10 electrons in 10 orbitals, all belonging to the carbon nanotube.

The calculations were performed with either the 2015.1 version of the MOLPRO program package^{174,175} or the Gaussian09 software, version D01²³². Natural population analyses²³⁴ were performed using the NBO program version 3.1²³³ bundled in the Gaussian09 software, while all figures including molecular structures were generated using the Avogadro program²⁶⁸.

4.2.2 N_5^+ Interaction Energy and Relaxation

For the calculation of unrelaxed interaction energies, the N_5^+ cation was placed at the center of the carbon nanotube at an equal distance from both extremities and the surrounding wall. The results obtained in this configuration are reported in Figure 4.17 as a function of the CNT diameter. For all nanotubes except the smallest (4,4) one, the energy is negative, meaning a favorable interaction between host and guest systems. The magnitude of the interaction appears to be independent from the helicity as for the azide anion, and to relate only on the nanotube diameter. A small “bump” in the interaction energy appears between CNTs (10,0) and (6,6), which is however most likely due to the different methodologies used. The most favorable interaction is observed for the (5,5) CNT, with a very large value of -50.44 kcal/mol.

In the case of armchair nanotubes, the ground state of the complex system is a closed-shell singlet state, allowing the relaxation of the geometry using restricted DFT. This is not the case for zigzag nanotubes, where a multireference approach is strictly required, since broken-symmetry DFT fails to accurately describe the electronic structure of the

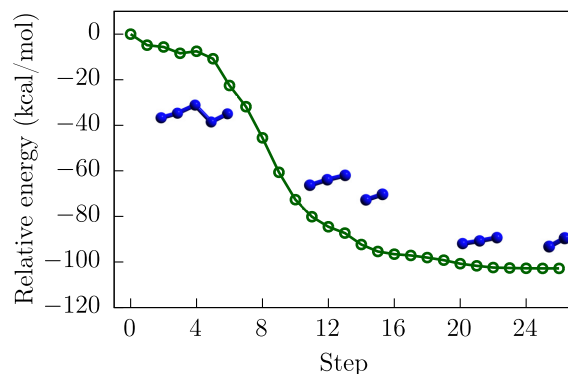


FIGURE 4.18: Relative energies with respect to step zero during the relaxation process. Geometries at steps 7, 11 and 26 are depicted along the curve without the surrounding nanotube for better representation.

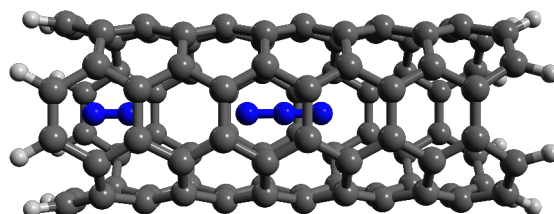


FIGURE 4.19: Final structure of $N_5^+@CNT(4,4)$.

ground state. The $N_5^+@CNT(5,5)$ system was thus relaxed by DFT, surprisingly leading to the breaking of the N_5^+ ion. The decomposition process happens barrierless as can be seen from Figure 4.18, where the relative energies and a few intermediate geometries are also reported along the surface. In order to ensure that the bond breaking was not an artifact due to the choice of functional, the optimization was repeated with the B3LYP density functional with inclusion of the D3 dispersion scheme¹¹⁸. However, also in this case the bond breaks barrierless.

The relaxation process was carried out on the smaller (4,4) and larger (6,6) CNTs too. In both cases, the confined cation breaks again after a few optimization cycles, leading to final conformations exemplified by Figure 4.19 for the CNT(4,4).

In order to investigate the nature of this process, we performed a series of NPAs on the electron density obtained with DFT. The partial atomic charges obtained for the isolated pentanitrogen cation are reported in Figure 4.20. The symmetry of N_5^+ is C_{2v} and therefore the charge distribution is symmetric with respect to the central nitrogen atom.

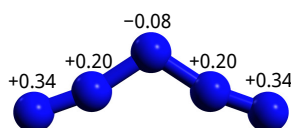


FIGURE 4.20: Partial atomic charges of the isolated N_5^+ cation.

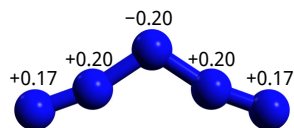


FIGURE 4.21: Partial atomic charges of the N_5^+ cation confined inside the cavity of a (5,5) CNT.

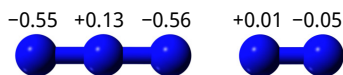
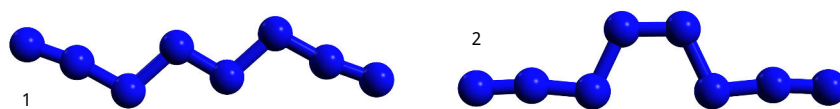


FIGURE 4.22: Partial atomic charges of the decomposed fragments after relaxation inside the cavity of a (5,5) CNT.

By repeating the NPA on the cation confined inside the (5,5) CNT prior to the geometry optimization, a significantly different charge distribution is found, as can be seen in Figure 4.21. Notice how the affected partial charges are those on the two external N atoms and the central one, due to their vicinity to the nanotube wall. By summing all partial charges on the N_5^+ , a total of 0.54 implies a (partial) charge transfer from the nanotube to the cation. A third population analysis on the fully relaxed geometry reveals that, after bond breaking, a total of two electrons were given by the nanotube to the nitrogen species. This charge transfer is quantified in Figure 4.22, showing the charge distribution on the two nitrogen molecules, with a total charge of minus one on the N_3 fragment and of approximately zero on N_2 . In a previous study¹⁹⁹, it was shown that the N_5^\bullet radical dissociates barrierless into an N_3^\bullet radical and N_2 products. We argue that the double electron transfer from the nanotube to N_5^+ is the trigger initiating the decomposition reaction. For the first charge transfer, a possible explanation can be given in terms of the electron affinity (EA) of the pentanitrogen ion and the ionization potential (IP) of the carbon nanotube. The IP of a hydrogen-terminated (5,5) CNT is reported in the work by Buonocore et al.⁶⁰, assigning a value between 4.2 and 5.2 eV depending on the approach used to compute it. The vertical electron affinity of N_5^+ on the other hand, was obtained in this investigation according to the formula $EA = E(N) - E(N + 1)$, where N stands for the number of electrons and $E(N)$, $E(N + 1)$ are total electronic energies computed at the geometry of the system with N electrons. The value for N_5^+ obtained by DFT with the APFD functional is 6.37 eV, thus resulting in a difference between the EA of N_5^+ and the IP of CNT(5,5) in the range ≈ 2.17 – 3.17 eV. Although this is just a qualitative result, it provides some evidence supporting the electron transfer process. It is important to note that this charge transfer could be in principle influenced by the finite length of CNT used in this investigation, since the IP depends on the length of the system. However, it is shown in Ref. 60 that the IP of a CNT decreases as a function of the length of the nanotube, thus this process is expected to be even more favorable in the case of longer and more realistic CNTs. To understand the second charge transfer process, an argument based on EA and IP is certainly harder to make as it is not known a priori at which moment of the reaction the transfer occurs and it would require a more detailed study which goes beyond the

FIGURE 4.23: EEE conformation (1) and EZE conformation (2) of N_8 .

scope of this investigation.

4.2.3 Confinement of N_8

As an attempt to avoid the decomposition, one could pair N_5^+ with a counterion inside the cavity such that their interaction dominates over the competing electron transfer process. Clearly, the ideal candidate in a high energy-density material (HEDM) perspective is the azide anion, which was also previously shown to be favorably stabilized inside CNTs. As mentioned in the introduction of this subsection, the reaction $N_5^+ + N_3^- \rightarrow N_8$ was extensively studied by Fau and Bartlett¹⁹⁶, providing the entire potential energy surface for the isolated system in gas phase. The authors of that study suggested that at ambient conditions, the linear isomers of molecular N_8 are not stable enough due to low activation barriers towards decomposition. Notwithstanding, it was mentioned that the lattice energy of an N_8 molecular crystal could potentially provide the required energy to keep these molecules from breaking apart. A prediction that was subsequently supported by DFT calculations reporting the crystal structure²⁶⁷.

Here, we present some preliminary results on the confinement inside the cavity of a (5,5) carbon nanotube of the two isomers which form the predicted N_8 crystal. Actually, several stable isomers were identified in Ref. 196, however, due to their quasi-linear geometry, in our investigation we only consider two of them. These are called EEE and EZE conformers, by adopting the same nomenclature of Ref. 196, and are illustrated in Figure 4.23. Two decomposition pathways exist for both isomers: in the first one, a terminal N_2 molecule detaches from the chain, resulting in the products $N_6 + N_2$, whereas in the second one, two N_3 radicals simultaneously break apart yielding $2N_3 + N_2$ products. The scheme reported in Figure 4.24 is a representation of the potential energy surface for the two decomposition pathways calculated in gas phase using the APFD functional. The structures depicted correspond to the EZE isomer only, however are representative for the EEE conformer too. The electronic energy difference between the two stable isomers is within 1 kcal/mol and, as can be seen from Figure 4.24, the activation energies for the decomposition reactions are similar for both the EZE and the EEE conformations.

In a similar way to the previous subsection, the interaction energies of both stable geometries confined inside a (5,5) CNT were computed upon relaxation of the complex system. The energies obtained for the EEE and the EZE isomers were -42.48 kcal/mol and -37.34 kcal/mol, respectively, both showing the stabilizing effect of the CNT. Frequency calculations on the entire structures ensured that in both cases we located a true minimum of the potential energy surface. Remarkably, due to the limited space available in the CNT cavity, one of the isomer is favored over the other, with a difference between

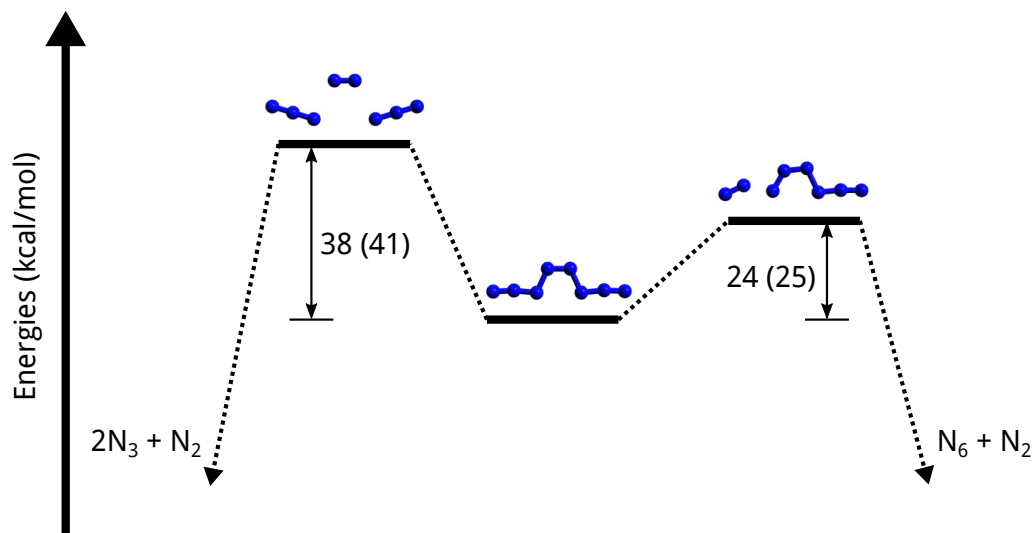


FIGURE 4.24: Potential energy surface showing the N_8 decomposition pathways in gas phase. Molecules and numbers depicted correspond to the EZE conformer, while the values in parenthesis refer to the EEE conformer.

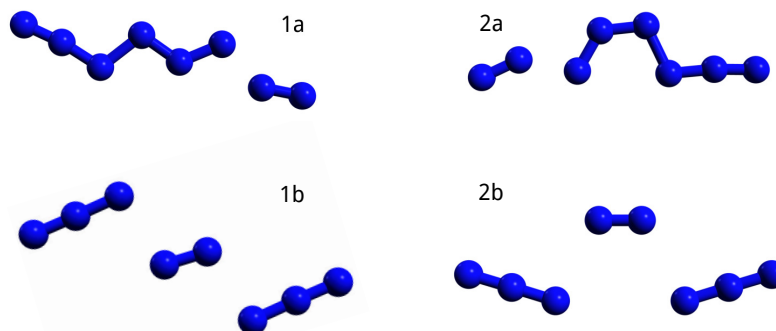


FIGURE 4.25: Transition state structures of the decomposition reactions in gas phase for the EEE conformer (1a and 1b) and the EZE conformer (2a and 2b).

the isomers going from 1 kcal/mol to approximately 5 kcal/mol.

For both systems, the transition states depicted in Figure 4.25 were confined inside the carbon nanotube in order to study the effect of the carbon nanostructure on the height of the activation barriers. In all but one case, the transition states shown in Figure 4.25 were not located inside the CNT(5,5) anymore. In particular, only structure (1a) appears to be a transition state. A possible explanation of this result is the fact that transition state (1a) is more linear than the other ones, thus possibly fitting better inside the cavity, such that its conformation is not overly distorted by the presence of the nanotube. Actually, such an interpretation applies for the stable isomers too: the EEE geometry is more linear than the EZE one, thus favored inside CNT.

From this preliminary results it is clear that steric effects are likely to play a crucial role

here, favoring certain isomers over others and selectively closing some reaction pathways. At the same time, new ones can appear inside the cavity, leading to new transition states or maybe even stable isomers which are not observed for the isolated system. Nevertheless, on the base of these results presented here, it is yet not possible to draw definitive conclusions, and a full exploration of the N_8 potential energy surface inside the carbon nanotube still has to be carried out.

4.3 Be_n Confinement in Carbon Nanotubes

Linear chains of beryllium are a particular conformation of Be_n systems for which interesting magnetic properties were predicted from a theoretical point of view^{269–272}. By sharing two electrons each, beryllium atoms bind together forming single covalent bonds resulting in a linear geometry that leaves two unpaired electrons at both terminal atoms. It was predicted by *ab initio* calculations that two half-filled orbitals are localized at the extremities, giving rise to a ground state which is antiferromagnetically coupled, but with a ferromagnetically coupled triplet state very close in energy. Furthermore, in a following study the same authors found that the magnetic coupling is altered when deposited on a graphene nanoribbon, showing a clear dependence with respect to the distance from the surface²⁷³. Most importantly, the ground state of the system changed from antiferromagnetic to ferromagnetic for a certain range of distances. Be_n chains thus seem to have magnetic properties which can be controlled by non-covalent interactions, with potential applications as molecular magnets.

However, the linear geometry of the chain is only a metastable structure on the Be_n potential energy surface, which tends to fold to a more compact and energetically more favorable cluster conformation²⁷⁴. Deposition on a surface might stabilize the linear geometry, nevertheless, carbon nanotubes certainly provide a more suitable host to preserve their structure as already pointed out in Ref. 273. There is also a second advantage by encapsulating the chains inside CNTs, namely the magnetic coupling of the hybrid system can be tuned according to the diameter of the enclosing nanotube.

The aim of this investigation is therefore to explore the effects of confining beryllium chains of different lengths inside carbon nanotubes of different diameters by means of multireference wave function methods as well as density functional theory. On one hand we are interested in the energetics of beryllium chains compared to their cluster counterparts, and on the other we investigate the magnetic coupling of the chains as a function of both the length of the chain and the diameter of the nanotube.

4.3.1 Methodology

Two Be_n chains with $n = 4, 5$ were considered and encapsulated inside finite-size carbon nanotubes of different diameters. The ground state of the isolated chains is the $^1\Sigma_g$ singlet state irrespective of the length and is always of open-shell character^{269–272}. To correctly describe this type of wave function without breaking the spin symmetry and obtain accurate values of the magnetic coupling, a multireference approach is necessary. Therefore, calculations to predict the coupling were carried out using the CASSCF method⁹⁴, using an active space composed by two electrons and two orbitals, both localized on the terminal atoms of the beryllium chain, see Figure 4.26. Dynamical electron correlation was included in a perturbative fashion using the NEVPT2 approach^{95–97}. For all calculations, the correlation-consistent basis set family by Dunning Jr.¹²² was used, in particular the cc-pVTZ basis for beryllium and the smaller double- ζ cc-pVDZ basis for the nanotube.

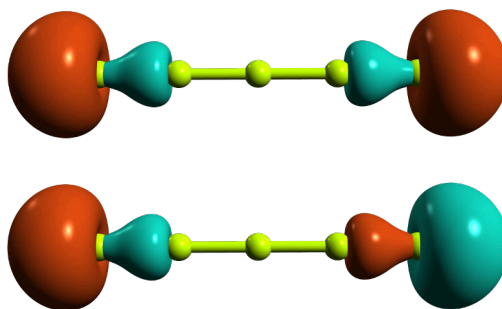


FIGURE 4.26: Edge molecular orbitals included in the active space.

TABLE 4.4: Be_n bond lengths in Å obtained at NEVPT2/cc-pVTZ level of theory.

system	state	Internal bond length	External bond length
Be_4	$^1\Sigma_g$	2.110	2.124
	$^3\Sigma_u$	2.109	2.122
Be_5	$^1\Sigma_g$	2.113	2.126
	$^3\Sigma_u$	2.111	2.123

The geometry of the isolated chains was optimized at NEVPT2/cc-pVTZ level of theory for both the singlet $^1\Sigma_g$ and the triplet $^3\Sigma_u$ states separately. We report in Table 4.4 the optimized bond lengths, which are in good agreement with previous investigations^{269–272}. Given the similar bond lengths for both states, we have used the geometry of the singlet state for all calculations carried out in this work. The carbon nanotubes geometries were generated using the nanotube builder provided by the Avogadro software²⁷⁵, setting a carbon–carbon bond length of 1.421 Å and a carbon–hydrogen bond length of 1.032 Å. It is well known that CNTs are very stiff systems and, since we do not expect the fine details of the nanotube geometry to have a strong effect on the beryllium chain, they were used without optimizing their structure. A total of four carbon nanotubes were used, whose diameters and lengths are listed in Table 4.5. Note that the lengths reported in Table 4.5 are computed from the two extremest carbon atoms and not from the saturating hydrogen atoms.

DFT calculation were carried out in order to compare the structural energy of the linear

TABLE 4.5: Structural parameters of the CNTs used in this work.

(m, k)	diameter [Å]	lengths [Å]
(5, 4)	6.12	17.16
(5, 5)	6.78	16.01
(6, 5)	7.47	17.06
(6, 6)	8.14	16.00

TABLE 4.6: Summary of electronic energy (with and without zero-point vibrational energy correction), enthalpy and free energy differences between the linear and the cluster geometries. All values are given in kcal/mol.

System	ΔE_{el}	ΔE_{el+ZPV}	ΔH	ΔG
Be ₄	56.58	54.34	55.58	52.51
Be ₅	72.82	69.78	71.49	68.03

and cluster conformations, respectively, in combination with the APFD exchange and correlation functional¹¹⁶. In this case, the spin symmetry could not be preserved, however the spin contamination observed was insignificant. The basis set used for these calculations is the same as before.

The wave function calculations were performed using the ORCA program, version 4.0.1.2¹⁷⁶. Given the size of the systems and the basis set used, we relied on the RIJCOSX approximation²³⁹ to perform both the CASSCF and NEVPT2 calculations, employing the universal def2/JK auxiliary basis set by Weigend²⁷⁶. All DFT calculations were performed using the Gaussian 09 software²³², using the “ultrafine” grid option for the functional integration.

Single point energies computed for different electronic states were performed in state-specific mode, as the reliability of the results was assessed in previous studies^{269,270}.

4.3.2 Stability of Be_n Chains

Here we present for the two systems considered in this work, Be₄ and Be₅, the thermodynamic stability of the linear conformation towards the most stable structure. The values reported in Table 4.6 show the thermodynamic energy differences between the linear structure and the cluster geometry which is known to be the global minimum of the singlet manifold²⁷⁴ for both Be₄ and Be₅. As can be seen, the linear conformation is thermodynamically unstable with respect to the cluster one, with free energy differences of 52.51 kcal/mol and 68.03 kcal/mol for Be₄ and Be₅, respectively. The increase of the energy difference observed between $n = 4$ and $n = 5$ is likely to continue for higher n values as well, since in the case of the cluster the atoms have more freedom to rearrange and form new bonds upon increasing n , while in the case of the chain, for each extra atom added to the system only a new single bond is formed. Therefore, given the substantial energy difference, it appears unlikely for the isolated chain to maintain its geometry. Most probably it rather folds into the cluster geometry, consequently losing its peculiar magnetic properties. Nevertheless, the investigation of the potential energy surface of such systems and their kinetics goes beyond the scope of this study and hence is not carried out further here.

Moreover, in order to evaluate in first approximation the feasibility of confining beryllium chains inside carbon nanotubes, the unrelaxed interaction energy between Be₄ and a CNT(5,5) was computed using DFT. The counterpoised corrected¹³² interaction energy

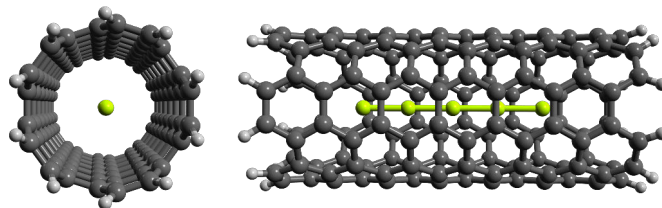


FIGURE 4.27: Front and side view of a Be_5 chain inside a CNT(5,5).

was found to be -53.20 kcal/mol, clearly indicating a favorable overall stabilization of the complex system compared to the separate fragments.

4.3.3 Magnetic Coupling

The structural, electronic and magnetic properties of isolated Be_n chains were studied in a series of works employing high level wave function methods^{269–272}. The most interesting feature of these systems is the presence of two unpaired electrons, one at each terminal beryllium atom. These two electrons reside in the edge orbitals shown in Figure 4.26 and are always antiferromagnetically coupled in the case of the isolated chain irrespective of the number n of atoms. In other words, the magnetic, Heisenberg-type, coupling constant $J = E_S - E_T$ always has a negative value for Be_n chains. The half-filled edge orbitals give rise to two quasi-degenerate states, whose energy split was found to decay exponentially with respect to n , i.e. $J \rightarrow 0$ for $n \rightarrow \infty$.

More recently, beryllium chains deposited on graphene nanoisland were investigated²⁷³ and it was observed that significant dispersion interactions weakly bounded the two systems together. Most interestingly, the magnetic properties of the chain are not lost, but rather influenced by the interaction with the graphene surface. Depending on the distance r between the two fragments, the coupling value J changes and the system switches from an antiferromagnetic to a ferromagnetic ground state for $r < 3.3$ Å. Note however that this inversion happens at a distance shorter than the predicted adsorption distance of 3.6 Å, thus suggesting a difficult practical realization of such systems. Furthermore, we expect such conformation to still be rather unstable even when deposited on a surface.

A possible solution to enforce the linear structure of Be_n and preserve the magnetic properties is to confine it inside a carbon nanotube, limiting its geometrical freedom. An picture showing a Be_5 chain confined in a CNT(5,5) is reported in Figure 4.27. Besides the obvious spatial constraint, the interaction between host and guest fragments is such that the choice of nanotube diameter allows to control the strength of the interaction. The distance between the fragments dictated by the choice of CNT acts as a parameter influencing the coupling of the states. The narrower the tube, the stronger it affects the value of J , and viceversa. We thus have two parameters which modulate the coupling: the length of the chain and the diameter of the CNT.

We report in Table 4.7 and Table 4.8 the values of the coupling obtained using the CASSCF and the NEVPT2 methods for a number of combinations of chain length and nanotube

TABLE 4.7: CASSCF magnetic coupling J for different CNT diameters and chain lengths. All values are given in meV.

host/guest	Be ₄	Be ₅	d [Å]
CNT(5,4)	-1.45	+0.06	3.06
CNT(5,5)	-4.43	-1.81	3.39
CNT(6,5)	-6.99	-0.90	3.74
CNT(6,6)	-7.88	-1.22	4.07
isolated	-8.39	-1.19	∞

TABLE 4.8: NEVPT2 magnetic coupling J for different CNT diameters and chain lengths. All values are given in meV.

host/guest	Be ₄	Be ₅	d [Å]
CNT(5,4)	-4.97	+0.72	3.06
CNT(5,5)	-14.54	-6.07	3.39
CNT(6,5)	-19.64	-2.83	3.74
CNT(6,6)	-20.50	-3.56	4.07
isolated	-16.37	-2.50	∞

diameter, respectively. First of all, note that in all cases the coupling constant is affected by the presence of the nanotube. The CASSCF results for the Be₄ system listed in Table 4.7 show a value of J that gradually increases from -1.45 meV when confined inside the narrowest nanotube to -7.88 meV when the surrounding CNT is the largest. In this case, the antiferromagnetic coupling monotonically approaches the value of the isolated chain. The situation for the longer Be₅ chain is similar, however the difference between the coupling of the isolated chain and the confined one is now extremely small, in the range of 1 meV. The CNT(5,5) case is off the trend, however, again, within such a small energy range it is hard to judge if it is due to numerical noise or not. Anyhow, the overall effect on the longer Be₅ is less visible than to the Be₄ chain.

The NEVPT2 results on the other hand vary on a broader range. For Be₄, although J decreases monotonically for increasingly larger nanotubes, surprisingly it does not converge to the value of the isolated chain. We have no explanation for this behavior. A similar behavior, although within a smaller range, is observed for the magnetic coupling of Be₅. Again, the problematic CNT(5,5) is off the trend, and this time in a more pronounced way. Nevertheless, an interesting result is given by the chain confined in the narrowest nanotube, for which a sign flip of J occurs, meaning that the ground state becomes antiferromagnetic.

To assess the reliability of the minimal active space used to obtain the J couplings, the calculation was repeated for a number of cases using a larger one with 6 electrons in 6 orbitals, with the new electrons and orbitals belonging to the CNT. The results obtained with these parameters are reported in Table 4.9. For Be₄, the effects are barely visible with differences compared to the minimal active space in the order of 0.3–0.5 meV. The J value for the problematic Be₅@CNT(5,5) system on the other hand, deviates by almost 1 meV

TABLE 4.9: Magnetic coupling J for different CNT diameters and chain lengths obtained with a larger (6,6) active space. All values are given in meV.

system	CASSCF(6,6)	NEVPT2
$Be_4@CNT(5,5)$	-4.90	-14.88
$Be_4@CNT(6,6)$	-8.24	-20.70
$Be_5@CNT(5,5)$	-2.72	-8.29

TABLE 4.10: Magnetic coupling J for Be_5 confined in longer CNTs. All values are given in meV.

nanotube	CASSCF(2,2)	NEVPT2	d [\AA]
CNT(5,4)	-0.06	+0.06	3.06
CNT(5,5)	+0.11	+0.48	3.39
CNT(6,5)	-0.93	-2.96	3.74

in the CASSCF case and more than 2 meV in the NEVPT2 case, showing an even stronger antiferromagnetic coupling. In this case too, there is no explanation for the different behavior observed for $Be_5@CNT(5,5)$. Stimulated by this difficult case and considering that we are using finite-size models to represent the carbon nanotubes, we investigated for a selected number of systems the dependence of J with respect to the length of the nanotube. In particular, a unit was added to the three narrowest nanotubes, increasing their length by approximately 2.5 \AA and the J coupling of the confined Be_5 chain was computed again. The results obtained are reported in Table 4.10, where it can be seen that for the two chiral nanotubes, the deviation with respect to the original results is in the range of 0.1 meV apart from the NEVPT2 case, which is off by 0.66 meV, however without disrupting the general behavior. Increasing the length of the nanotube had a different effect on the $Be_5@CNT(5,5)$, whose magnetic coupling changed to ferromagnetic at both CASSCF and NEVPT2 levels of theory, making it off the trend, but in the opposite direction. However, in absolute terms, this result is closer to the ones obtained for the other nanotubes. Finally, for $Be_5@CNT(5,5)$, yet another calculation was carried out with a longer nanotube. The motivation behind this choice is the position of the chain inside the nanotube, for which the particular atomic pattern surrounding Be_n depends on the number of units in the CNT. By adding one unit only, the chain had to be moved inside along the axis of the nanotube in order to be at the same distance from both extremities. On the other hand, adding a second unit increases the length of the nanotube in a symmetric way, thus preserving the particular atomic arrangement around the chain. The coupling obtained in this case is $J = -0.67$ meV and $J = -2.55$ meV for the CASSCF and NEVPT2 methods, respectively. These values perfectly fit in the trend observed in Tables 4.7 and 4.8, however, in principle all cases should be checked using the longest nanotube. Nevertheless, the fact that increasing by one unit the nanotube did not affect significantly the values of the chiral nanotubes as reported in Table 4.10, is reason to believe that the problematic case was the $Be_5@CNT(5,5)$. To summarize, although a

sign change of J is observed for the $\text{Be}_5@\text{CNT}(5,4)$ system, its magnitude, 0.72 meV is significantly lower to the value $J \approx 4.8$ meV obtained for the interaction of Be_5 with the graphene nanoribbon as reported in the work by Evangelisti et al.²⁷³, albeit the different basis sets used. However, as pointed out by the authors, the change of J happens quite rapidly within a limited range of the chain–surface distance. Such a fine control for the chain confined within the nanotube cavity is not possible, assuming that the chain lies on the CNT central axis. This is very likely the case for the two narrowest nanotubes, as their radius is shorter than the adsorption distance measured for the interaction with the graphene nanoisland. On the other hand, this might not be the case for larger nanotubes. To conclude, we notice that a narrower $\text{CNT}(4,4)$ was also considered, having a diameter of 5.43 Å. However, the chain–wall distance was too small and the Be_n edge orbitals hybridized with the nanotube π system, essentially destroying the magnetic properties of the chain.

4.4 Conclusions

In this chapter of the thesis several investigations regarding the encapsulation of nitrogen clusters and beryllium chains inside carbon nanotubes were carried out. The motivation to study all-nitrogen molecules relies in the chemical energy stored by these systems, which makes them a possible source of environmentally friendly energy. Within this perspective, carbon nanotubes were proposed as storage and stabilization devices, in order to protect the nitrogen species from releasing their energy through a decomposition into N_2 . On the other hand, carbon nanotubes were also investigated as possible hosts for materials with other types of properties, such as beryllium chains. Linear Be_n molecules, characterized by two half-filled magnetic orbitals, are weakly antiferromagnetically coupled. Most interestingly, this coupling was found to be affected by non-covalent interactions with carbon nanostructures, suggesting a possible way to control the nature of the ground state.

In the first part of this chapter, the focus was on an *ab initio* investigation of the azide anion confined inside carbon nanotubes. It was found that N_3^- is energetically stabilized by nanotubes of diameters comprised between ≈ 5.5 Å and ≈ 9.5 Å, showing the strongest interaction of -32.31 kcal/mol obtained in the case of a (5,5) CNT, with a diameter of ≈ 6.78 Å. The analysis of the relaxed structures, the partial atomic charges and the molecular electrostatic potential has revealed the nature of the interaction, suggesting an explanation of the results found. In particular, we argue that the guest N_3^- species is stabilized by electrostatic and induction interactions with the nanotube wall, the latter undergoing a remarkable polarization due to the presence of hydrogen atoms used to saturate the CNT extremities. The cavity provided by a $\text{CNT}(5,5)$ is such that the N_3^- fragment aligns perfectly in the center of the nanotube and parallel to its axis, resulting at an optimal distance from its wall in all directions, thus explaining the strong interaction observed.

The shortcomings of using finite-size systems to model carbon nanotubes is that there is

an intrinsic dependence on their length, in particular if charged molecules are considered. Therefore, a thorough investigation on this dependence was carried out too, this time increasing the level of theory as well. The reason was two-fold, on one side we wanted to confirm our previous findings and on the other hand, the aim was to obtain very accurate reference energies. Specifically, the approach used for this study has allowed to obtain interaction energies of unprecedented accuracy, by employing a combined extrapolation and fitting scheme based on RI-SCS-MP2 and DLPNO-CCSD(T) methodologies together with a large triple- ζ quality basis set.

By rationalizing the results obtained at *ab initio* level of theory, we presented a novel intermolecular potential describing the interaction of the azide anion with carbon nanotubes. This model is based on a separation of the three components contributing to the interaction, namely Van der Waals forces, induction effects and electrostatics. The VdW interactions were modeled according to the Improved Lennard-Jones potential, for the induction effects we proposed a new potential based on the general form of an induced dipole due to the presence of an external electric field, whereas the electrostatic component was accounted by the usual Coulomb law. The total potential function presented reproduced the approximate DLPNO-CCSD(T) energies within a few kcal/mol and provided a second way to analyze the results, i.e. by inspecting the relative contributions of the individual components. The latter approach is quite insightful and allows a pedestrian exploration of important features of the potential energy surface which are otherwise hard to grasp. Interestingly, the distance dependence of the various components is also evident in the systematic investigation of the interaction energy as a function of the CNT length: the VdW and induction interactions quickly converge for increasingly long nanotubes and the behavior of the potential energy surface is dominated by the *longer-range* electrostatic force.

The intermolecular potential functions proposed, specifically the ILJ and the induction potentials, were implemented in the MD program DL POLY 4, with which a number of simulations were carried out to demonstrate its functioning.

This in-depth investigation of the azide anion has helped to advance the understanding of this molecule and in particular the ion-CNT interactions in general. Although the azide anion is one of the most stable pure nitrogen molecules, the results obtained here are interesting in the context of alternative energy storage since N_3^- can be used as a precursor for the synthesis of more complex nitrogen clusters. Moreover, this work was also the motivation for the implementation of an accurate intermolecular potential in the DL POLY software, which can now be used for other systems too.

In the second part of this chapter, an investigation of the confinement of other two all-nitrogen molecules was carried out, in particular the cationic species N_5^+ and the neutral N_8 chain. The former, despite the favorable unrelaxed interaction energies with carbon nanotubes, was found to undergo decomposition upon a double charge transfer from the carbon nanostructure to the cation. Actually, as already reported in the literature¹⁹⁹ and confirmed here, a single electron is enough to initiate the barrierless reaction of the

pentanitrogen cation. Such a transfer initially occurs because the electron affinity of N_5^+ is larger than the ionization potential of the carbon nanotube. This process eventually leads to another charge transfer, in which the intermediate N_3 radical gains a second electron from the nanotube resulting in $N_3^- + N_2$ products.

A possible way to circumvent this decomposition is the addition of a counterion in the cavity which may compete with the charge transfer process and stabilize N_5^+ . To this end, we performed some preliminary investigation of the encapsulation of N_8 inside a (5,5) CNT, considering it as the result of the reaction $N_3^- + N_5^+ \rightarrow N_8$. Still, this reaction was not explicitly considered, but instead we focused on the feasibility to encapsulate the N_8 product which might anyhow be formed in other ways.

The results obtained show that two linear isomers of N_8 , which are stable in gas phase, are also stable inside the nanotube with a large interaction energy. The effects of spatial confinement inside the cavity favor the most linear isomer among the two, increasing their relative energy difference by few kcal/mol. Two decomposition pathways for these N_8 isomers exist in gas phase, which were considered here too. Surprisingly, all but one of the known transition states of these reactions did not remain valid when confined inside the nanotube. It is argued that this is due to steric effects, since only the most linear one was located inside the cavity, whereas all the other resulted higher order saddle points. This is corroborated by the stronger interaction energy of the more linear EEE isomer over the EZE one. Furthermore, considering the energy profiles obtained for the azide anion, it results clear how the close vicinity of the nanotube walls to the confined species inside the CNT(5,5) has a strong impact on the geometrical freedom.

Despite still being an ongoing research effort, these findings suggest that steric effects due to the restricted space available in the cavity can close certain reaction pathways and favor certain isomers over others. In this context, the diameter of the nanotube can be used as a tunable parameter providing some degree of control on the encapsulated molecule. In particular, the aim is to either increase the activation energy or even close the reaction pathways leading to decomposition of N_8 , thus favoring selected isomers to remain intact inside the cavity.

In the third and last part of this chapter we have explored the confinement of beryllium chains inside carbon nanotubes of different diameters. On one side, the carbon nanostructure avoid the folding of the chains and the subsequent collapse into a cluster geometry, on the other, the presence of the nanotube clearly has an effect on the characteristic magnetic coupling of these systems. There are indications that the value of J goes towards zero due to the interaction with an increasingly narrower nanotube, however it is not clear if, for sufficiently small CNTs, the composite system becomes ferromagnetic. The behavior of J with respect to the length of the nanotube was tested for a selected number of cases, nevertheless, in order to keep a sufficient accuracy of the calculated property, it was not possible to investigate longer nanotubes in a systematic way.

It would clearly be of great interest to study longer beryllium chains as well, but as was already the case for Be_5 , the length of the nanotube appears to be an important factor,

such that longer CNTs appear to be really needed, yet computationally inaccessible. Finally, we should point out that this work is a preliminary investigation on this type of systems. In the future, relaxation of the complex system should be taken into account so that the chain is allowed to go off the principal axis of the nanotube. This is a major concern, however it is also a very hard problem to deal with from the methodological point of view.

5 General Conclusions

During the course of this PhD thesis, several works involving carbon nanotubes and related structures were carried out. The versatility of these systems is one of their defining features and this was proven by the results proposed here.

Cyclacenes, which are formally zigzag carbon nanotubes composed by a single unit, were studied by semi-empirical and *ab initio* methods, highlighting their interesting electronic properties and the challenges that they pose to modern theoretical approaches. Advancement in the understanding of their electronic structure is essential in order to assess their potential for various technological applications as well as to provide valuable insight to their experimental synthesis, which is yet to be achieved. Furthermore, besides the results obtained by the investigations carried out, this thesis has proven how a combined semi-empirical approach with a higher level *ab initio* treatment provides a powerful tool to understand and characterize a molecular system from different perspectives and at different levels of detail.

Because of the hollow cavity of carbon nanotubes, one of their potential applications is in host-guest chemistry. The confinement of any kind of molecule inside such nanostructures has different kinds of effect and can be exploited in several ways. During this thesis, a type of energetic molecules was considered and their encapsulation inside carbon nanotubes was studied. On one side, the motivation behind this research effort was the potential of pure nitrogen molecules as alternative green energy sources, but on the other hand, the work was also driven by a pure theoretical interest, in particular for understanding the type of interactions involved with carbon nanostructures and how can these be modeled in an accurate, but computationally efficient, way.

The results obtained during the entire PhD period involve essentially three systems, the azide anion, the pentanitrogen cation and the neutral octanitrogen molecule. In all cases, we have investigated the effects exerted by the nanotube on the confined system, focusing on different aspects depending on the system. Specifically, in the case of the azide anion, the stability and the overall stiffness of both the nanotube and the ionic species provided a good base for the development of an intermolecular potential and its implementation in a molecular dynamics program. Furthermore, this system was used as an example to demonstrate the feasibility to accurately model different types of interactions from a classical perspective. The work involving the pentanitrogen cation was centered on the relaxation process, a clear case in which the effect of the nanotube is tremendous. Nevertheless, the latter results provided a starting place for the subsequent study of the N_8 molecule, a system which has sparked a lot of interest in the past and that is still

subject of investigation by several groups nowadays. Here, preliminary results show the importance of spatial confinement in controlling the behavior of the molecule and suggests a way for its storage.

Despite being strictly theoretical, the work carried out in this domain helps to advance the understanding of ion–CNT interactions and provides a solid base for future investigations.

Instead of merely acting as a storage device, carbon nanotubes can form interesting hybrid systems when combined with other types of molecules. This is the case of beryllium chains, whose magnetic properties could be exploited in a number of ways, but their linear geometry limits their applicability. However, when inserted inside the cavity of carbon nanotubes, their structure can be in principle preserved due to the linear conformation of CNTs as well as the limited space available, avoiding the chain to fold into energetically lower isomers. Moreover, the weak interactions between the carbon structure and the chain are such that the properties of the chain may be modulated as a function of the enclosing nanotube diameter. There is evidence that the magnetic coupling of the two unpaired electrons is affected by the presence of the surrounding system, which in some extreme cases appear to change the type of the ground state from antiferromagnetic to ferromagnetic. However, in light of the approximations used in this investigation, we cannot yet provide conclusive proof of this behavior. Nonetheless, carbon nanotubes have once again proven to be a remarkable system that can be exploited in many ways.

Alongside the main projects involving carbon nanotubes, a few other investigations were carried out during the course of this PhD thesis. Most notably, a proposition of a new basis set strategy to perform molecular calculations was explored and reported in Appendix A.4. In practice, the idea is to remain within the domain of Gaussian-based expansions of the wave function, exploiting the well-established machinery developed during the last 50 years, but to mix an atom-centered description with a distributed approach where Gaussian functions are filling the space between and around atoms. This work led to the implementation of a new computer program able to calculate molecular integrals over arbitrarily placed Gaussian-type orbitals, which was used to obtain the numerical results presented in Appendix A.4.

Furthermore, the study from a different perspective of an old problem, namely Wigner localization, was carried out in collaboration with other members of the Toulouse laboratory. This work, which is annexed to this thesis in Appendix A.5, is actually based on the same approach proposed in Appendix A.4, i.e. where distributed Gaussian functions are used for the wave function expansion.

To summarize, in this PhD thesis different approaches were used to study different problems centered on carbon nanotubes. On one side, the driving force was a genuine interest for the possible technological applications of these systems, but on the other, there

was also a methodological curiosity which led to the development of new tools and techniques to tackle old and new problems within the field of theoretical and computational chemistry.

Bibliography

- [1] Kroto, H. W.; Heath, J. R.; O'Brien, S. C.; Curl, R. F.; Smalley, R. E. C₆₀: Buckminsterfullerene. *Nature* **1985**, *318*, 162–163.
- [2] Iijima, S. Helical microtubules of graphitic carbon. *Nature* **1991**, *354*, 56–58.
- [3] Novoselov, K. S.; Geim, A. K.; Morozov, S. V.; Jiang, D.; Zhang, Y.; Dubonos, S. V.; Grigorieva, I. V.; Firsov, A. A. Electric Field Effect in Atomically Thin Carbon Films. *Science* **2004**, *306*, 666–669.
- [4] Ferrari, A. C. et al. Science and technology roadmap for graphene, related two-dimensional crystals, and hybrid systems. *Nanoscale* **2015**, *7*, 4598–4810.
- [5] Iijima, S.; Ichihashi, T. Single-shell carbon nanotubes of 1-nm diameter. *Nature* **1993**, *363*, 603–605.
- [6] Saito, R.; Fujita, M.; Dresselhaus, G.; Dresselhaus, M. S. Electronic structure of chiral graphene tubules. *Applied Physics Letters* **1992**, *60*, 2204–2206.
- [7] Odom, T. W.; Huang, J.-L.; Kim, P.; Lieber, C. M. Atomic structure and electronic properties of single-walled carbon nanotubes. *Nature* **1998**, *391*, 62–64.
- [8] Jorio, A.; Saito, R.; Hafner, J. H.; Lieber, C. M.; Hunter, M.; McClure, T.; Dresselhaus, G.; Dresselhaus, M. S. Structural (n, m) Determination of Isolated Single-Wall Carbon Nanotubes by Resonant Raman Scattering. *Physical Review Letters* **2001**, *86*, 1118–1121.
- [9] Jishi, R. a.; Dresselhaus, M. S.; Dresselhaus, G. Symmetry properties of chiral carbon nanotube. *Physical Review B* **1993**, *47*, 671–674.
- [10] Dresselhaus, M.; Dresselhaus, G.; Saito, R. Physics of carbon nanotubes. *Carbon* **1995**, *33*, 883–891.
- [11] Iijima, S.; Brabec, C.; Maiti, A.; Bernholc, J. Structural flexibility of carbon nanotubes. *The Journal of Chemical Physics* **1996**, *104*, 2089–2092.
- [12] Sánchez-Portal, D.; Artacho, E.; Soler, J. M.; Rubio, A.; Ordejón, P. Ab initio structural, elastic, and vibrational properties of carbon nanotubes. *Physical Review B* **1999**, *59*, 12678–12688.
- [13] Gülseren, O.; Yildirim, T.; Ciraci, S. Systematic ab initio study of curvature effects in carbon nanotubes. *Physical Review B* **2002**, *65*, 153405.

- [14] Matsuo, Y.; Tahara, K.; Nakamura, E. Theoretical Studies on Structures and Aromaticity of Finite-Length Armchair Carbon Nanotubes. *Organic Letters* **2003**, *5*, 3181–3184.
- [15] Zhou, Z.; Steigerwald, M.; Hybertsen, M.; Brus, L.; Friesner, R. A. Electronic Structure of Tubular Aromatic Molecules Derived from the Metallic (5,5) Armchair Single Wall Carbon Nanotube. *Journal of the American Chemical Society* **2004**, *126*, 3597–3607.
- [16] Galano, A. On the influence of diameter and length on the properties of armchair single-walled carbon nanotubes: A theoretical chemistry approach. *Chemical Physics* **2006**, *327*, 159–170.
- [17] Martín-Martínez, F. J.; Melchor, S.; Dobado, J. A. Clar–Kekulé Structuring in Armchair Carbon Nanotubes. *Organic Letters* **2008**, *10*, 1991–1994.
- [18] Martín-Martínez, F. J.; Melchor, S.; Dobado, J. A. Edge effects, electronic arrangement, and aromaticity patterns on finite-length carbon nanotubes. *Physical Chemistry Chemical Physics* **2011**, *13*, 12844–12857.
- [19] Demichelis, R.; Noël, Y.; D’Arco, P.; Rérat, M.; Zicovich-Wilson, C. M.; Dovesi, R. Properties of Carbon Nanotubes: An ab Initio Study Using Large Gaussian Basis Sets and Various DFT Functionals. *The Journal of Physical Chemistry C* **2011**, *115*, 8876–8885.
- [20] Tarighi Ahmadpour, M.; Hashemifar, S. J.; Rostamnejadi, A. Size effects on the structural, electronic, and optical properties of (5,0) finite-length carbon nanotube: An ab-initio electronic structure study. *Journal of Applied Physics* **2016**, *120*, 014303.
- [21] Hamada, N.; Sawada, S.-i.; Oshiyama, A. New One-Dimensional Conductors: Graphitic Microtubules. *Physical Review Letters* **1992**, *68*, 1579–1581.
- [22] Mintmire, J. W.; Dunlap, B. I.; White, C. T. Are Fullerene Tubules Metallic? *Physical Review Letters* **1992**, *68*, 631–634.
- [23] Zhang, Z.; Lieber, C. M. Nanotube structure and electronic properties probed by scanning tunneling microscopy. *Applied Physics Letters* **1993**, *62*, 2792–2794.
- [24] Ebbesen, T. W.; Lezec, H. J.; Hiura, H.; Bennett, J. W.; Ghaemi, H. F.; Thio, T. Electrical conductivity of individual carbon nanotubes. *Nature* **1996**, *382*, 54–56.
- [25] Carroll, D. L.; Redlich, P.; Ajayan, P. M.; Charlier, J. C.; Blase, X.; De Vita, A.; Car, R. Electronic Structure and Localized States at Carbon Nanotube Tips. *Physical Review Letters* **1997**, *78*, 2811–2814.
- [26] Tans, S. J.; Devoret, M. H.; Dai, H.; Thess, A.; Smalley, R. E.; Geerligs, L. J.; Dekker, C. Individual single-wall carbon nanotubes as quantum wires. *Nature* **1997**, *386*, 474–477.

- [27] Bockrath, M.; Cobden, D. H.; McEuen, P. L.; Chopra, N. G.; Zettl, A.; Thess, A.; Smalley, R. E. Single-Electron Transport in Ropes of Carbon Nanotubes. *Science* **1997**, *275*, 1922–1925.
- [28] Wildöer, J. W. G.; Venema, L. C.; Rinzler, A. G.; Smalley, R. E.; Dekker, C. Electronic structure of atomically resolved carbon nanotubes. *Nature* **1998**, *391*, 59–62.
- [29] Ado Jorio, Gene Dresselhaus, M. S. D. In *Carbon Nanotubes*; Jorio, A., Dresselhaus, G., Dresselhaus, M. S., Eds.; Topics in Applied Physics 5; Springer Berlin Heidelberg: Berlin, Heidelberg, 2008; Vol. 111; p 247.
- [30] De Volder, M. F. L.; Tawfick, S. H.; Baughman, R. H.; Hart, a. J. Carbon nanotubes: present and future commercial applications. *Science* **2013**, *339*, 535–539.
- [31] Eatemadi, A.; Daraee, H.; Karimkhanloo, H.; Kouhi, M.; Zarghami, N.; Akbarzadeh, A.; Abasi, M.; Hanifehpour, Y.; Joo, S. Carbon nanotubes: properties, synthesis, purification, and medical applications. *Nanoscale Research Letters* **2014**, *9*, 393.
- [32] Prasek, J.; Drbohlavova, J.; Chomoucka, J.; Hubalek, J.; Jasek, O.; Adam, V.; Kizek, R. Methods for carbon nanotubes synthesis—review. *Journal of Materials Chemistry* **2011**, *21*, 15872.
- [33] Segawa, Y.; Ito, H.; Itami, K. Structurally uniform and atomically precise carbon nanostructures. *Nature Reviews Materials* **2016**, *1*, 15002.
- [34] Segawa, Y.; Yagi, A.; Matsui, K.; Itami, K. Design and Synthesis of Carbon Nanotube Segments. *Angewandte Chemie International Edition* **2016**, *55*, 5136–5158.
- [35] Liu, B.; Wu, F.; Gui, H.; Zheng, M.; Zhou, C. Chirality-Controlled Synthesis and Applications of Single-Wall Carbon Nanotubes. *ACS Nano* **2017**, *11*, 31–53.
- [36] Hitosugi, S.; Yamasaki, T.; Isobe, H. Bottom-up Synthesis and Thread-in-Bead Structures of Finite $(n,0)$ -Zigzag Single-Wall Carbon Nanotubes. *Journal of the American Chemical Society* **2012**, *134*, 12442–12445.
- [37] Li, H.-B.; Page, A. J.; Irle, S.; Morokuma, K. Single-walled Carbon Nanotube Growth from Chiral Carbon Nanorings: Prediction of Chirality and Diameter Influence on Growth Rates. *Journal of the American Chemical Society* **2012**, *134*, 15887–15896.
- [38] Omachi, H.; Nakayama, T.; Takahashi, E.; Segawa, Y.; Itami, K. Initiation of carbon nanotube growth by well-defined carbon nanorings. *Nature Chemistry* **2013**, *5*, 572–576.
- [39] Sanchez-Valencia, J. R.; Dienel, T.; Gröning, O.; Shorubalko, I.; Mueller, A.; Jansen, M.; Amsharov, K.; Ruffieux, P.; Fasel, R. Controlled synthesis of single-chirality carbon nanotubes. *Nature* **2014**, *512*, 61–64.

- [40] Tahara, K.; Tobe, Y. Molecular loops and belts. *Chemical Reviews* **2006**, *106*, 5274–5290.
- [41] Eisenberg, D.; Shenhar, R.; Rabinovitz, M. Synthetic approaches to aromatic belts: building up strain in macrocyclic polyarenes. *Chemical Society Reviews* **2010**, *39*, 2879–2890.
- [42] Omachi, H.; Segawa, Y.; Itami, K. Synthesis of cycloparaphenylenes and related carbon nanorings: A step toward the controlled synthesis of carbon nanotubes. *Accounts of Chemical Research* **2012**, *45*, 1378–1389.
- [43] Lewis, S. E. Cycloparaphenylenes and related nano hoops. *Chemical Society Reviews* **2015**, *44*, 2221–2304.
- [44] Jasti, R.; Bhattacharjee, J.; Neaton, J. B.; Bertozzi, C. R. Synthesis, Characterization, and Theory of [9]-, [12]-, and [18]Cycloparaphenylene: Carbon Nano hoop Structures. *Journal of the American Chemical Society* **2008**, *130*, 17646–17647.
- [45] Povie, G.; Segawa, Y.; Nishihara, T.; Miyauchi, Y.; Itami, K. Synthesis of a carbon nanobelt. *Science* **2017**, *356*, 172–175.
- [46] Gleiter, R.; Esser, B.; Kornmayer, S. C. Cyclacenes: hoop-shaped systems composed of conjugated rings. *Accounts of Chemical Research* **2009**, *42*, 1108–1116.
- [47] Bulusheva, L. G.; Okotrub, A. V.; Romanov, D. A.; Tomanek, D. Electronic Structure of (*n*,0) Zigzag Carbon Nanotubes: Cluster and Crystal Approach. *The Journal of Physical Chemistry A* **1998**, *102*, 975–981.
- [48] Rochefort, A.; Salahub, D. R.; Avouris, P. Effects of Finite Length on the Electronic Structure of Carbon Nanotubes. *The Journal of Physical Chemistry B* **1999**, *103*, 641–646.
- [49] Liang,; Wang, X. J.; Yokojima, S.; Chen, Electronic Structures and Optical Properties of Open and Capped Carbon Nanotubes. *Journal of the American Chemical Society* **2000**, *122*, 11129–11137.
- [50] Cioslowski, J.; Rao, N.; Moncrieff, D. Electronic Structures and Energetics of [5,5] and [9,0] Single-Walled Carbon Nanotubes. *Journal of the American Chemical Society* **2002**, *124*, 8485–8489.
- [51] Li, J.; Zhang, Y.; Zhang, M. The electronic structure and its theoretical simulation of carbon nanotube with finite length. Part II: the energy gap and its oscillation properties of short armchair nanotubes. *Chemical Physics Letters* **2002**, *364*, 338–344.
- [52] Mestechkin, M. M. Finite length nanotubes: Ground state degeneracy and single-electron spectrum. *Journal of Chemical Physics* **2005**, *122*, 074305.

- [53] Chilkuri, V. G.; Evangelisti, S.; Leininger, T.; Monari, A. The Electronic Structure of Short Carbon Nanotubes: The Effects of Correlation. *Advances in Condensed Matter Physics* **2015**, *2015*, 1–14.
- [54] Petrushenko, I. K.; Ivanov, N. A. Ionization potentials and structural properties of finite-length single-walled carbon nanotubes: DFT study. *Physica E: Low-dimensional Systems and Nanostructures* **2013**, *54*, 262–266.
- [55] Kupka, T.; Stachów, M.; Stobiński, L.; Kaminský, J. DFT study of zigzag ($n, 0$) single-walled carbon nanotubes: ^{13}C NMR chemical shifts. *Journal of Molecular Graphics and Modelling* **2016**, *67*, 14–19.
- [56] Kupka, T.; Stachów, M.; Stobiński, L.; Kaminský, J. Calculation of Raman parameters of real-size zigzag ($n, 0$) single-walled carbon nanotubes using finite-size models. *Physical Chemistry Chemical Physics* **2016**, *18*, 25058–25069.
- [57] Baldoni, M.; Sgamellotti, A.; Mercuri, F. Finite-Length Models of Carbon Nanotubes Based on Clar Sextet Theory. *Organic Letters* **2007**, *9*, 4267–4270.
- [58] Torrens, F. Effect of type, size and deformation on the polarizability of carbon nanotubes from atomic increments. *Nanotechnology* **2004**, *15*, S259–S264.
- [59] Ma, S.; Guo, W. Size-dependent polarizabilities of finite-length single-walled carbon nanotubes. *Physics Letters A* **2008**, *372*, 4835–4838.
- [60] Buonocore, F.; Trani, F.; Ninno, D.; Di Matteo, A.; Cantele, G.; Iadonisi, G. *Ab initio* calculations of electron affinity and ionization potential of carbon nanotubes. *Nanotechnology* **2008**, *19*, 025711.
- [61] Mañanes, A.; Duque, F.; Ayuela, A.; López, M. J.; Alonso, J. A. Half-metallic finite zigzag single-walled carbon nanotubes from first principles. *Physical Review B* **2008**, *78*, 1–10.
- [62] Hod, O.; Scuseria, G. E. Half-Metallic Zigzag Carbon Nanotube. *ACS Nano* **2008**, *2*, 2243–2249.
- [63] Lu, W.; Xiong, Y.; Chen, L. Length-Dependent Dielectric Polarization in Metallic Single-Walled Carbon Nanotubes. *The Journal of Physical Chemistry C* **2009**, *113*, 10337–10340.
- [64] Ajayan, P. M.; Ebbesen, T. W.; Ichihashi, T.; Iijima, S.; Tanigaki, K.; Hiura, H. Opening carbon nanotubes with oxygen and implications for filling. *Nature* **1993**, *362*, 522–525.
- [65] Ajayan, P. M.; Iijima, S. Capillarity-induced filling of carbon nanotubes. *Nature* **1993**, *361*, 333–334.
- [66] Khlobystov, A. N.; Britz, D. A.; Briggs, G. A. D. Molecules in carbon nanotubes. *Accounts of Chemical Research* **2005**, *38*, 901–909.

- [67] Smith, B. W.; Monthieux, M.; Luzzi, D. E. Encapsulated C₆₀ in carbon nanotubes. *Nature* **1998**, *396*, 323–324.
- [68] Lee, J.; Kim, H.; Kahng, S. J.; Kim, G.; Son, Y. W.; Ihm, J.; Kato, H.; Wang, Z. W.; Okazaki, T.; Shinohara, H.; Kuk, Y. Bandgap modulation of carbon nanotubes by encapsulated metallofullerenes. *Nature* **2002**, *415*, 1005–1008.
- [69] Ruoff, R. S.; Lorents, D. C.; Chan, B.; Malhotra, R.; Subramoney, S. Single Crystal Metals Encapsulated in Carbon Nanoparticles. *Science* **1993**, *259*, 346–348.
- [70] Guerret-Piécourt, C.; Bouar, Y. L.; Lohseu, A.; Pascard, H. Relation between metal electronic structure and morphology of metal compounds inside carbon nanotubes. *Nature* **1994**, *372*, 761–765.
- [71] Tsang, S. C.; Chen, Y. K.; Harris, P. J. F.; Green, M. L. H. A simple chemical method of opening and filling carbon nanotubes. *Nature* **1994**, *372*, 159–162.
- [72] Choi, W. Y.; Kang, J. W.; Hwang, H. J. Structures of ultrathin copper nanowires encapsulated in carbon nanotubes. *Physical Review B* **2003**, *68*, 193405.
- [73] Che, R. C.; Peng, L.-M.; Duan, X. F.; Chen, Q.; Liang, X. L. Microwave Absorption Enhancement and Complex Permittivity and Permeability of Fe Encapsulated within Carbon Nanotubes. *Advanced Materials* **2004**, *16*, 401–405.
- [74] Liu, Z.; Bando, Y.; Mitome, M.; Zhan, J. Unusual Freezing and Melting of Gallium Encapsulated in Carbon Nanotubes. *Physical Review Letters* **2004**, *93*, 095504.
- [75] Li, L.-J.; Khlobystov, A. N.; Wiltshire, J. G.; Briggs, G. A. D.; Nicholas, R. J. Diameter-selective encapsulation of metallocenes in single-walled carbon nanotubes. *Nature Materials* **2005**, *4*, 481–485.
- [76] Xu, B.; Pan, B. C. Study of Gallium Fragments Encapsulated in Single-Walled Carbon Nanotubes. *The Journal of Physical Chemistry C* **2009**, *113*, 567–570.
- [77] Garg, I.; Sharma, H.; Dharamvir, K.; Jindal, V. K. DFT Study of Al_n (1 – 13) Clusters Encapsulated Inside Single Walled Carbon Nanotubes. *The Journal of Physical Chemistry C* **2010**, *114*, 18762–18772.
- [78] Smeu, M.; Zahid, F.; Ji, W.; Guo, H.; Jaidann, M.; Abou-Rachid, H. Energetic Molecules Encapsulated Inside Carbon Nanotubes and between Graphene Layers: DFT Calculations. *Journal of Physical Chemistry C* **2011**, *115*, 10985–10989.
- [79] Abou-Rachid, H.; Hu, A.; Timoshevskii, V.; Song, Y.; Lussier, L.-S. Nanoscale High Energetic Materials: A Polymeric Nitrogen Chain N₈ Confined inside a Carbon Nanotube. *Physical Review Letters* **2008**, *100*, 196401.
- [80] Ji, W.; Timoshevskii, V.; Guo, H.; Abou-Rachid, H.; Lussier, L. Thermal stability and formation barrier of a high-energetic material N₈ polymer nitrogen encapsulated in (5,5) carbon nanotube. *Applied Physics Letters* **2009**, *95*, 021904.

- [81] Battaglia, S.; Evangelisti, S.; Faginas-Lago, N.; Leininger, T. N_3^- azide anion confined inside finite-size carbon nanotubes. *Journal of Molecular Modeling* **2017**, *23*, 294.
- [82] Koga, K.; Gao, G. T.; Tanaka, H.; Zeng, X. C. Formation of ordered ice nanotubes inside carbon nanotubes. *Nature* **2001**, *412*, 802–805.
- [83] Maniwa, Y.; Kataura, H.; Abe, M.; Suzuki, S.; Achiba, Y.; Kira, H.; Matsuda, K. Phase Transition in Confined Water Inside Carbon Nanotubes. *Journal of the Physical Society of Japan* **2002**, *71*, 2863–2866.
- [84] Agrawal, K. V.; Shimizu, S.; Draushuk, L. W.; Kilcoyne, D.; Strano, M. S. Observation of extreme phase transition temperatures of water confined inside isolated carbon nanotubes. *Nature Nanotechnology* **2017**, *12*, 267–273.
- [85] Nishide, D.; Dohi, H.; Wakabayashi, T.; Nishibori, E.; Aoyagi, S.; Ishida, M.; Kikuchi, S.; Kitaura, R.; Sugai, T.; Sakata, M.; Shinohara, H. Single-wall carbon nanotubes encaging linear chain C_{10}H_2 polyyne molecules inside. *Chemical Physics Letters* **2006**, *428*, 356–360.
- [86] Hart, M.; White, E. R.; Chen, J.; McGilvery, C. M.; Pickard, C. J.; Michaelides, A.; Sella, A.; Shaffer, M. S. P.; Salzmann, C. G. Encapsulation and Polymerization of White Phosphorus Inside Single-Wall Carbon Nanotubes. *Angewandte Chemie International Edition* **2017**, *56*, 8144–8148.
- [87] Szabo, A.; Ostlund, N. S. *Modern Quantum Chemistry: Introduction to Advanced Electronic Structure Theory*, 1st ed.; Dover Publications, 1996; p 480.
- [88] Helgaker, T.; Jørgensen, P.; Olsen, J. *Molecular Electronic-Structure Theory*, 1st ed.; John Wiley & Sons, Ltd, 2000; p 944.
- [89] Cramer, C. J. *Essentials of Computational Chemistry: Theories and Models*, 2nd ed.; John Wiley & Sons, Ltd, 2004; p 618.
- [90] Jensen, F. *Introduction to Computational Chemistry*, 2nd ed.; John Wiley & Sons, Ltd, 2007; p 620.
- [91] Levine, I. N. *Quantum Chemistry*, 7th ed.; Pearson, 2013; p 720.
- [92] Smith, W. *Elements of Molecular Dynamics*, 1st ed.; 2014; p 460.
- [93] Riplinger, C.; Pinski, P.; Becker, U.; Valeev, E. F.; Neese, F. Sparse maps—A systematic infrastructure for reduced-scaling electronic structure methods. II. Linear scaling domain based pair natural orbital coupled cluster theory. *The Journal of Chemical Physics* **2016**, *144*, 024109.
- [94] Roos, B. O.; Taylor, P. R.; Siegbahn, P. E. M. A complete active space SCF method (CASSCF) using a density matrix formulated super-CI approach. *Chemical Physics* **1980**, *48*, 157–173.

- [95] Angeli, C.; Cimiraglia, R.; Evangelisti, S.; Leininger, T.; Malrieu, J.-P. Introduction of n -electron valence states for multireference perturbation theory. *The Journal of Chemical Physics* **2001**, *114*, 10252–10264.
- [96] Angeli, C.; Cimiraglia, R.; Malrieu, J.-P. n -electron valence state perturbation theory: A spinless formulation and an efficient implementation of the strongly contracted and of the partially contracted variants. *Journal of Chemical Physics* **2002**, *117*, 9138–9153.
- [97] Angeli, C.; Pastore, M.; Cimiraglia, R. New perspectives in multireference perturbation theory: The n -electron valence state approach. *Theoretical Chemistry Accounts* **2007**, *117*, 743–754.
- [98] Levy, M. Universal variational functionals of electron densities, first-order density matrices, and natural spin-orbitals and solution of the v -representability problem. *Proceedings of the National Academy of Sciences* **1979**, *76*, 6062–6065.
- [99] Kohn, W.; Sham, L. J. Self-Consistent Equations Including Exchange and Correlation Effects. *Physical Review* **1965**, *140*, A1133–A1138.
- [100] Hohenberg, P.; Kohn, W. Inhomogeneous Electron Gas. *Physical Review* **1964**, *136*, B864–B871.
- [101] Slater, J. C. *The Self-Consistent Field for Molecular and Solids, Quantum Theory of Molecular and Solids, Vol. 4*; McGraw-Hill: New York, 1974.
- [102] Vosko, S. H.; Wilk, L.; Nusair, M. Accurate spin-dependent electron liquid correlation energies for local spin density calculations: a critical analysis. *Canadian Journal of Physics* **1980**, *58*, 1200–1211.
- [103] Perdew, J. P.; Burke, K.; Ernzerhof, M. Generalized Gradient Approximation Made Simple. *Physical Review Letters* **1996**, *77*, 3865–3868.
- [104] Perdew, J. P.; Burke, K.; Ernzerhof, M. Generalized Gradient Approximation Made Simple [Phys. Rev. Lett. *77*, 3865 (1996)]. *Physical Review Letters* **1997**, *78*, 1396–1396.
- [105] Becke, A. D. Density-functional exchange-energy approximation with correct asymptotic behavior. *Physical Review A* **1988**, *38*, 3098–3100.
- [106] Lee, C.; Yang, W.; Parr, R. G. Development of the Colle-Salvetti correlation-energy formula into a functional of the electron density. *Physical Review B* **1988**, *37*, 785–789.
- [107] Miehlich, B.; Savin, A.; Stoll, H.; Preuss, H. Results obtained with the correlation energy density functionals of Becke and Lee, Yang and Parr. *Chemical Physics Letters* **1989**, *157*, 200–206.
- [108] Grimme, S. Semiempirical GGA-type density functional constructed with a long-range dispersion correction. *Journal of Computational Chemistry* **2006**, *27*, 1787–1799.

- [109] Tao, J.; Perdew, J. P.; Staroverov, V. N.; Scuseria, G. E. Climbing the Density Functional Ladder: Nonempirical Meta-Generalized Gradient Approximation Designed for Molecules and Solids. *Physical Review Letters* **2003**, *91*, 146401.
- [110] Zhao, Y.; Truhlar, D. G. A new local density functional for main-group thermochemistry, transition metal bonding, thermochemical kinetics, and noncovalent interactions. *The Journal of Chemical Physics* **2006**, *125*, 194101.
- [111] Peverati, R.; Truhlar, D. G. M11-L: A Local Density Functional That Provides Improved Accuracy for Electronic Structure Calculations in Chemistry and Physics. *The Journal of Physical Chemistry Letters* **2012**, *3*, 117–124.
- [112] Becke, A. D. Density-functional thermochemistry. III. The role of exact exchange. *The Journal of Chemical Physics* **1993**, *98*, 5648–5652.
- [113] Adamo, C.; Barone, V. Toward reliable density functional methods without adjustable parameters: The PBE0 model. *The Journal of Chemical Physics* **1999**, *110*, 6158–6170.
- [114] Staroverov, V. N.; Scuseria, G. E.; Tao, J.; Perdew, J. P. Comparative assessment of a new nonempirical density functional: Molecules and hydrogen-bonded complexes. *The Journal of Chemical Physics* **2003**, *119*, 12129–12137.
- [115] Staroverov, V. N.; Scuseria, G. E.; Tao, J.; Perdew, J. P. Erratum: “Comparative assessment of a new nonempirical density functional: Molecules and hydrogen-bonded complexes” [J. Chem. Phys. 119, 12129 (2003)]. *The Journal of Chemical Physics* **2004**, *121*, 11507.
- [116] Austin, A.; Petersson, G. A.; Frisch, M. J.; Dobek, F. J.; Scalmani, G.; Throssell, K. A Density Functional with Spherical Atom Dispersion Terms. *Journal of Chemical Theory and Computation* **2012**, *8*, 4989–5007.
- [117] Grimme, S. Semiempirical hybrid density functional with perturbative second-order correlation. *The Journal of Chemical Physics* **2006**, *124*, 034108.
- [118] Grimme, S.; Antony, J.; Ehrlich, S.; Krieg, H. A consistent and accurate ab initio parametrization of density functional dispersion correction (DFT-D) for the 94 elements H-Pu. *Journal of Chemical Physics* **2010**, *132*.
- [119] Helgaker, T.; Klopper, W.; Koch, H.; Noga, J. Basis-set convergence of correlated calculations on water. *The Journal of Chemical Physics* **1997**, *106*, 9639–9646.
- [120] Halkier, A.; Helgaker, T.; Jørgensen, P.; Klopper, W.; Koch, H.; Olsen, J.; Wilson, A. K. Basis-set convergence in correlated calculations on Ne, N₂, and H₂O. *Chemical Physics Letters* **1998**, *286*, 243–252.
- [121] Truhlar, D. G. Basis-set extrapolation. *Chemical Physics Letters* **1998**, *294*, 45–48.

- [122] Dunning Jr., T. H. Gaussian basis sets for use in correlated molecular calculations. I. The atoms boron through neon and hydrogen. *The Journal of Chemical Physics* **1989**, *90*, 1007–1023.
- [123] Kendall, R. A.; Dunning Jr., T. H.; Harrison, R. J. Electron affinities of the first-row atoms revisited. Systematic basis sets and wave functions and wave functions. *Journal of Chemical Physics* **1992**, *96*, 6796–6806.
- [124] Jensen, F. Polarization consistent basis sets: Principles. *Journal of Chemical Physics* **2001**, *115*, 9113–9125.
- [125] Jensen, F. Polarization consistent basis sets: II. Estimating the Kohn-Sham basis set limit. *Journal of Chemical Physics* **2002**, *116*, 7372–7379.
- [126] Jensen, F. Polarization consistent basis sets. IV. The basis set convergence of equilibrium geometries, harmonic vibrational frequencies, and intensities. *Journal of Chemical Physics* **2003**, *118*, 2459–2463.
- [127] Weigend, F.; Ahlrichs, R. Balanced basis sets of split valence, triple zeta valence and quadruple zeta valence quality for H to Rn: Design and assessment of accuracy. *Physical Chemistry Chemical Physics* **2005**, *7*, 3297–3305.
- [128] Hehre, W. J.; Ditchfield, R.; Stewart, R. F.; Pople, J. A. Self-Consistent Molecular-Orbital Methods. I. Use of Gaussian Expansions of Slater-Type Atomic Orbitals. *The Journal of Chemical Physics* **1969**, *51*, 2657–2664.
- [129] Hehre, W. J.; Ditchfield, R.; Pople, J. A. Self-Consistent Molecular Orbital Methods. XII. Further Extensions of Gaussian-Type Basis Sets for Use in Molecular Orbital Studies of Organic Molecules. *The Journal of Chemical Physics* **1972**, *56*, 2257–2261.
- [130] Jensen, F. Atomic orbital basis sets. *Wiley Interdisciplinary Reviews: Computational Molecular Science* **2013**, *3*, 273–295.
- [131] Wang, N. X.; Venkatesh, K.; Wilson, A. K. Behavior of density functionals with respect to basis set. 3. Basis set superposition error. *Journal of Physical Chemistry A* **2006**, *110*, 779–784.
- [132] Boys, S. F.; Bernardi, F. The calculation of small molecular interactions by the differences of separate total energies. Some procedures with reduced errors. *Molecular Physics* **1970**, *19*, 553–566.
- [133] Pirani, F.; Brizi, S.; Roncaratti, L. F.; Casavecchia, P.; Cappelletti, D.; Vecchiocattivi, F. Beyond the Lennard-Jones model: a simple and accurate potential function probed by high resolution scattering data useful for molecular dynamics simulations. *Physical Chemistry Chemical Physics* **2008**, *10*, 5489–5503.
- [134] Frenkel, D.; Smit, B. *Understanding Molecular Simulation*; 2002.

- [135] Heilbronner, E. Molecular Orbitals in homologen Reihen mehrkerniger aromatischer Kohlenwasserstoffe: I. Die Eigenwerte von LCAO-MO's in homologen Reihen. *Helvetica Chimica Acta* **1954**, *37*, 921–935.
- [136] Scott, L. T. Conjugated belts and nanorings with radially oriented p orbitals. *Angewandte Chemie - International Edition* **2003**, *42*, 4133–4135.
- [137] Esser, B.; Rominger, F.; Gleiter, R. Synthesis of [6.8]₃Cyclacene: Conjugated Belt and Model for an Unusual Type of Carbon Nanotube. *Journal of the American Chemical Society* **2008**, *130*, 6716–6717.
- [138] Matsui, K.; Fushimi, M.; Segawa, Y.; Itami, K. Synthesis, Structure, and Reactivity of a Cylinder-Shaped Cyclo[12]orthophenylene[6]ethynylene: Toward the Synthesis of Zigzag Carbon Nanobelts. *Organic Letters* **2016**, *18*, 5352–5355.
- [139] Choi, H. S.; Kim, K. S. Structures, magnetic properties, and aromaticity of cyclacenes. *Angewandte Chemie - International Edition* **1999**, *38*, 2256–2258.
- [140] Houk, K. N.; Lee, P. S.; Nendel, M. Polyacene and cyclacene geometries and electronic structures: Bond equalization, vanishing band gaps, and triplet ground states contrast with polyacetylene. *Journal of Organic Chemistry* **2001**, *66*, 5517–5521.
- [141] Hachmann, J.; Dorando, J. J.; Avilés, M.; Chan, G. K.-L. The radical character of the acenes: A density matrix renormalization group study. *The Journal of Chemical Physics* **2007**, *127*, 134309.
- [142] Yang, Y.; Davidson, E. R.; Yang, W. Nature of ground and electronic excited states of higher acenes. *Proceedings of the National Academy of Sciences* **2016**, *113*, E5098–E5107.
- [143] Wegner, H. A. On the Way to Carbon Nanotubes: The First Synthesis of an Aromatic Nanobelt. *Angewandte Chemie International Edition* **2017**, *56*, 10995–10996.
- [144] Segawa, Y.; Yagi, A.; Ito, H.; Itami, K. A Theoretical Study on the Strain Energy of Carbon Nanobelts. *Organic Letters* **2016**, *18*, 1430–1433.
- [145] Gutman, I. Hückel Molecular Orbital Energies and Bond Orders of Cyclacenes. *Polycyclic Aromatic Compounds* **1996**, *8*, 251–257.
- [146] Gutman, I.; Biedermann, P. U.; Ivanov-Petrović, V.; Agranat, I. Cyclic Conjugation Effects in Cyclacenes. *Polycyclic Aromatic Compounds* **1996**, *8*, 189–202.
- [147] Türker, L. Unusual alternation of HMO bond orders in cyclacenes. *Polycyclic Aromatic Compounds* **1996**, *8*, 67–71.
- [148] Türker, L. AM1 treatment of Hückel type cyclacenes. *Journal of Molecular Structure* **1997**, *407*, 217–220.

- [149] Türker, L. Some recursive relationships between acenes and cyclacenes. *Turkish Journal of Chemistry* **1998**, *22*, 109–114.
- [150] Türker, L. MNDO treatment of the Hückel and Möbius types of cyclacenes. *Journal of Molecular Structure: THEOCHEM* **1998**, *454*, 83–86.
- [151] Türker, L. Zigzag cyclopolyacenes: A theoretical study. *Journal of Molecular Structure: THEOCHEM* **1999**, *491*, 275–280.
- [152] Türker, L. The effect of cyclization on acenes. *Journal of Molecular Structure: THEOCHEM* **2000**, *531*, 333–337.
- [153] Türker, L.; Gümüş, S. Cyclacenes. *Journal of Molecular Structure: THEOCHEM* **2004**, *685*, 1–33.
- [154] André, J.-M.; Champagne, B.; Perpète, E. A.; Guillaume, M. Linear, Cyclic, and Möbius Strip Polyacenes: The Influence of the Topology on the Size-Dependent HOMO-LUMO Energy Gap. *International Journal of Quantum Chemistry* **2001**, *84*, 607–616.
- [155] Guillaume, M.; Champagne, B.; Perpète, E. A.; André, J.-M. Möbius strip versus linear and cyclic polyacenes: A Hückel and semiempirical investigation. *Theoretical Chemistry Accounts* **2001**, *105*, 431–436.
- [156] Karmakar, S.; Mondal, S.; Mandal, B. Eigensolutions of cyclopolyacene graphs. *Molecular Physics* **2015**, *113*, 719–726.
- [157] Karmakar, S.; Mandal, B. X, Y-Cyclacene Graphs with Next Nearest Neighbor Interactions. *Polycyclic Aromatic Compounds* **2017**, *0*, 1–13.
- [158] Battaglia, S.; Le, H.-A.; Bendazzoli, G. L.; Faginas-Lago, N.; Leininger, T.; Evangelisti, S. A theoretical study on cyclacenes: Analytical tight-binding approach. *International Journal of Quantum Chemistry* **2018**, *118*, e25569.
- [159] Dias, J. R. Comprehensive study of the correlations that exist among the members of the $[n]$ cyclacene series and the Möbius $[n]$ cyclacene series. *Molecular Physics* **2018**, *116*, 423–448.
- [160] Chen, Z.; Jiang, D. E.; Lu, X.; Bettinger, H. F.; Dai, S.; Schleyer, P. v. R.; Houk, K. N. Open-shell singlet character of cyclacenes and short zigzag nanotubes. *Organic Letters* **2007**, *9*, 5449–5452.
- [161] Sadowsky, D.; McNeill, K.; Cramer, C. J. Electronic structures of $[n]$ -cyclacenes ($n=6-12$) and short, hydrogen-capped, carbon nanotubules. *Faraday Discussions* **2010**, *145*, 507–521.
- [162] Wu, C.-S.; Lee, P.-Y.; Chai, J.-D. Electronic Properties of Cyclacenes from TAO-DFT. *Nature Scientific Reports* **2016**, *6*, 37249.

- [163] Battaglia, S.; Faginas-Lago, N.; Andrae, D.; Evangelisti, S.; Leininger, T. Increasing Radical Character of Large [*n*]cyclacenes Unveiled by Wave Function Theory. *The Journal of Physical Chemistry A* **2017**, *121*, 3746–3756.
- [164] Pérez-Guardiola, A.; Sandoval-Salinas, M. E.; Casanova, D.; San-Fabián, E.; Pérez-Jiménez, A. J.; Sancho-García, J. C. The role of topology in organic molecules: origin and comparison of the radical character in linear and cyclic oligoacenes and related oligomers. *Physical Chemistry Chemical Physics* **2018**, *20*, 7112–7124.
- [165] Resta, R.; Sorella, S. Electron Localization in the Insulating State. *Physical Review Letters* **1999**, *82*, 370–373.
- [166] Resta, R. Kohn's theory of the insulating state: A quantum-chemistry viewpoint. *The Journal of Chemical Physics* **2006**, *124*, 104104.
- [167] Resta, R. The insulating state of matter: a geometrical theory. *The European Physical Journal B* **2011**, *79*, 121–137.
- [168] Brea, O.; El Khatib, M.; Angeli, C.; Bendazzoli, G. L.; Evangelisti, S.; Leininger, T. Behavior of the position-spread tensor in diatomic systems. *Journal of Chemical Theory and Computation* **2013**, *9*, 5286–5295.
- [169] Brea, O.; El Khatib, M.; Bendazzoli, G. L.; Evangelisti, S.; Leininger, T.; Angeli, C. The Spin-Partitioned Total-Position Spread Tensor: An Application To Diatomic Molecules. *The Journal of Physical Chemistry A* **2016**, *120*, 5230–5238.
- [170] Widmark, P.-O.; Malmqvist, P.-Å.; Roos, B. O. Density matrix averaged atomic natural orbital (ANO) basis sets for correlated molecular wave functions. *Theoretica Chimica Acta* **1990**, *77*, 291–306.
- [171] Weigend, F.; Köhn, A.; Hättig, C. Efficient use of the correlation consistent basis sets in resolution of the identity MP2 calculations. *The Journal of Chemical Physics* **2002**, *116*, 3175–3183.
- [172] Werner, H.-J.; Knowles, P. J. A second order multiconfiguration SCF procedure with optimum convergence. *Journal of Chemical Physics* **1985**, *82*, 5053–5063.
- [173] Knowles, P. J.; Werner, H.-J. An efficient second-order MC SCF method for long configuration expansions. *Chemical Physics Letters* **1985**, *115*, 259–267.
- [174] Werner, H.-J.; Knowles, P. J.; Knizia, G.; Manby, F. R.; Schütz, M. Molpro: A general-purpose quantum chemistry program package. *Wiley Interdisciplinary Reviews: Computational Molecular Science* **2012**, *2*, 242–253.
- [175] Werner, H.-J. et al. MOLPRO, version 2015.1, a package of ab initio programs. 2015; <http://www.molpro.net>.
- [176] Neese, F. Software update: the ORCA program system, version 4.0. *Wiley Interdisciplinary Reviews: Computational Molecular Science* **2017**, e1327.

- [177] Mizukami, W.; Kurashige, Y.; Yanai, T. More π electrons make a difference: Emergence of many radicals on graphene nanoribbons studied by *Ab initio* DMRG theory. *Journal of Chemical Theory and Computation* **2013**, *9*, 401–407.
- [178] Schriber, J. B.; Evangelista, F. A. Communication: An adaptive configuration interaction approach for strongly correlated electrons with tunable accuracy. *Journal of Chemical Physics* **2016**, *144*, 161106.
- [179] Andersson, K.; Malmqvist, P.-Å.; Roos, B. O.; Sadlej, A. J.; Wolinski, K. Second-Order Perturbation Theory with a CASSCF Reference Function. *Journal of Physical Chemistry* **1990**, *94*, 5483–5488.
- [180] Andersson, K.; Malmqvist, P.-Å.; Roos, B. O. Second-order perturbation theory with a complete active space self-consistent field reference function. *Journal of Chemical Physics* **1992**, *96*, 1218–1226.
- [181] Roos, B. O.; Andersson, K. Multiconfigurational perturbation theory with level shift – the Cr₂ potential revisited. *Chemical Physics Letters* **1995**, *245*, 215–223.
- [182] Forsberg, N.; Malmqvist, P.-Å. Multiconfiguration perturbation theory with imaginary level shift. *Chemical Physics Letters* **1997**, *274*, 196–204.
- [183] Chai, J.-D. Density functional theory with fractional orbital occupations. *Journal of Chemical Physics* **2012**, *136*, 154104.
- [184] Head-Gordon, M. Characterizing unpaired electrons from the one-particle density matrix. *Chemical Physics Letters* **2003**, *372*, 508–511.
- [185] Ibeji, C. U.; Ghosh, D. Singlet-triplet gaps in polyacenes: a delicate balance between dynamic and static correlations investigated by spin-flip methods. *Physical chemistry chemical physics : PCCP* **2015**, *17*, 9849–9856.
- [186] Fosso-Tande, J.; Nascimento, D. R.; DePrince III, A. E. Accuracy of two-particle *N*-representability conditions for describing different spin states and the single-triplet gap in the linear acene series. *Molecular Physics* **2016**, *114*, 423–430.
- [187] Fosso-Tande, J.; Nguyen, T.-S.; Gidofalvi, G.; DePrince III, A. E. Large-Scale Variational Two-Electron Reduced-Density-Matrix-Driven Complete Active Space Self-Consistent Field Methods. *Journal of Chemical Theory and Computation* **2016**, *12*, 2260–2271.
- [188] Wu, C. S.; Chai, J.-D. Electronic properties of zigzag graphene nanoribbons studied by TAO-DFT. *Journal of Chemical Theory and Computation* **2015**, *11*, 2003–2011.
- [189] Hajgató, B.; Szieberth, D.; Geerlings, P.; De Proft, F.; Deleuze, M. S. A benchmark theoretical study of the electronic ground state and of the singlet-triplet split of benzene and linear acenes. *Journal of Chemical Physics* **2009**, *131*, 224321.

- [190] El Khatib, M.; Leininger, T.; Bendazzoli, G. L.; Evangelisti, S. Computing the Position-Spread tensor in the CAS-SCF formalism. *Chemical Physics Letters* **2014**, *591*, 58–63.
- [191] Maniwa, Y.; Kataura, H.; Abe, M.; Udaka, A.; Suzuki, S.; Achiba, Y.; Kira, H.; Matsuda, K.; Kadowaki, H.; Okabe, Y. Ordered water inside carbon nanotubes: formation of pentagonal to octagonal ice-nanotubes. *Chemical Physics Letters* **2005**, *401*, 534–538.
- [192] Samartzis, P. C.; Wodtke, A. M. All-nitrogen chemistry: how far are we from N_{60} ? *International Reviews in Physical Chemistry* **2006**, *25*, 527–552.
- [193] Zarko, V. E. Searching for Ways to Create Energetic Materials Based on Polynitrogen Compounds (Review). *Combustion, Explosion and Shock Waves* **2010**, *46*, 121–131.
- [194] Curtius, T. Ueber Stickstoffwasserstoffsäure (Azoimid) N_3H . *Berichte der deutschen chemischen Gesellschaft* **1890**, *23*, 3023–3033.
- [195] Christe, K. O.; Wilson, W. W.; Sheehy, J. A.; Boatz, J. A. N_5^+ : A Novel Homoleptic Polynitrogen Ion as a High Energy Density Material. *Angewandte Chemie International Edition* **1999**, *38*, 2004–2009.
- [196] Fau, S.; Bartlett, R. J. Possible Products of the End-On Addition of N_3^- to N_5^+ and Their Stability. *The Journal of Physical Chemistry A* **2001**, *105*, 4096–4106.
- [197] Gagliardi, L.; Orlandi, G.; Evangelisti, S.; Roos, B. O. A theoretical study of the nitrogen clusters formed from the ions N_3^- , N_5^+ , and N_5^- . *Journal of Chemical Physics* **2001**, *114*, 10733–10737.
- [198] Evangelisti, S.; Leininger, T. Ionic nitrogen clusters. *Journal of Molecular Structure: THEOCHEM* **2003**, *621*, 43–50.
- [199] Dixon, D. A.; Feller, D.; Christe, K. O.; Wilson, W. W.; Vij, A.; Vij, V.; Jenkins, H. D. B.; Olson, R. M.; Gordon, M. S. Enthalpies of Formation of Gas-Phase N_3 , N_3^- , N_5^+ , and N_5^- from Ab Initio Molecular Orbital Theory, Stability Predictions for $N_5^+N_3^-$ and $N_5^+N_5^-$, and Experimental Evidence for the Instability of $N_5^+N_3^-$. *Journal of the American Chemical Society* **2004**, *126*, 834–843.
- [200] Li, Y.; Bai, H.; Lin, F.; Huang, Y. Energetics and electronic structures of nitrogen chains encapsulated in zigzag carbon nanotube. *Physica E: Low-dimensional Systems and Nanostructures* **2018**, *103*, 444–451.
- [201] Zheng, F.; Wang, C.; Zhang, P. Polymeric Nitrogen Chain Confined Inside a Silicon Carbide Nanotube. *Journal of Computational and Theoretical Nanoscience* **2012**, *9*, 1129–1133.
- [202] Zheng, F.; Yang, Y.; Zhang, P. Polymeric Nitrogen Chains Confined in Carbon Nanotube Bundle. *International Journal of Modern Physics B* **2012**, *26*, 1250047.

- [203] Liu, S.; Yao, M.; Ma, F.; Liu, B.; Yao, Z.; Liu, R.; Cui, T.; Liu, B. High Energetic Polymeric Nitrogen Stabilized in the Confinement of Boron Nitride Nanotube at Ambient Conditions. *The Journal of Physical Chemistry C* **2016**, *120*, 16412–16417.
- [204] Sharma, H.; Garg, I.; Dharamvir, K.; Jindal, V. K. Structure of Polynitrogen Clusters Encapsulated in C₆₀: A Density Functional Study. *Journal of Physical Chemistry C* **2010**, *114*, 9153–9160.
- [205] Wu, Z.; Benchafia, E. M.; Iqbal, Z.; Wang, X. N₈⁻ Polynitrogen Stabilized on Multi-Wall Carbon Nanotubes for Oxygen-Reduction Reactions at Ambient Conditions. *Angewandte Chemie - International Edition* **2014**, *126*, 12763–12767.
- [206] Benchafia, E. M.; Yao, Z.; Yuan, G.; Chou, T.; Piao, H.; Wang, X.; Iqbal, Z. Cubic gauche polymeric nitrogen under ambient conditions. *Nature Communications* **2017**, *8*, 930.
- [207] Gray, P.; Waddington, T. C. Fundamental vibration frequencies and force constants in the azide ion. *Transactions of the Faraday Society* **1957**, *53*, 901.
- [208] Frech, R.; Decius, J. C. Dipolar Coupling and Molecular Vibrations in Crystals. III. Polarizabilities of Molecular Anions and the Internal Field in Some Rhombohedral Crystals. *The Journal of Chemical Physics* **1969**, *51*, 5315–5322.
- [209] Illenberger, E.; Comita, P. B.; Brauman, J. I.; Fenzlaff, H.-P.; Heni, M.; Heinrich, N.; Koch, W.; Frenking, G. Experimental and Theoretical Investigation of the Azide Anion (N₃⁻) in the Gas Phase. *Berichte der Bunsengesellschaft für physikalische Chemie* **1985**, *89*, 1026–1031.
- [210] Polak, M.; Gruebele, M.; Saykally, R. J. Velocity Modulation Laser Spectroscopy of Negative Ions: The ν_3 Band of Azide (N₃⁻). *Journal of the American Chemical Society* **1987**, *109*, 2884–2887.
- [211] Brazier, C. R.; Bernath, P. F.; Burkholder, J. B.; Howard, C. J. Fourier transform spectroscopy of the ν_3 band of the N₃ radical. *The Journal of Chemical Physics* **1988**, *89*, 1762–1767.
- [212] Tian, R.; Facelli, J. C.; Michl, J. Vibrational and electronic spectra of matrix-isolated nitrogen trimer radical and azide. *The Journal of Physical Chemistry* **1988**, *92*, 4073–4079.
- [213] Polak, M.; Gruebele, M.; Peng, G. S.; Saykally, R. J. Velocity modulation infrared laser spectroscopy of negative ions: The (011)–(001) band of azide (N₃⁻). *The Journal of Chemical Physics* **1988**, *89*, 110–114.
- [214] Maroulis, G.; Hatzis, A.; Haskopoulos, A. Electric properties of the azide ion calculated with a systematic sequence of Gaussian-type basis sets. *Chemical Physics* **2006**, *323*, 451–457.

- [215] Sebald, P.; Stein, C.; Oswald, R.; Botschwina, P. Rovibrational States of N_3^- and CO_2 Up to High J : A Theoretical Study Beyond fc-CCSD(T). *The Journal of Physical Chemistry A* **2013**, *117*, 13806–13814.
- [216] Li, M.; Owrutsky, J.; Sarisky, M.; Culver, J. P.; Yodh, A.; Hochstrasser, R. M. Vibrational and rotational relaxation times of solvated molecular ions. *The Journal of Chemical Physics* **1993**, *98*, 5499–5507.
- [217] Ferrario, M.; Klein, M. L.; McDonald, I. R. Dynamical behavior of the azide ion in protic solvents. *Chemical Physics Letters* **1993**, *213*, 537–540.
- [218] Morita, A.; Kato, S. Vibrational relaxation of azide ion in water: The role of intramolecular charge fluctuation and solvent-induced vibrational coupling. *The Journal of Chemical Physics* **1998**, *109*, 5511–5523.
- [219] Yarne, D. A.; Tuckerman, M. E.; Klein, M. L. Structural and dynamical behavior of an azide anion in water from ab initio molecular dynamics calculations. *Chemical Physics* **2000**, *258*, 163–169.
- [220] Zhong, Q.; Baronavski, A. P.; Owrutsky, J. C. Vibrational energy relaxation of aqueous azide ion confined in reverse micelles. *The Journal of Chemical Physics* **2003**, *118*, 7074–7080.
- [221] Yang, X.; Kiran, B.; Wang, X.-B.; Wang, L.-S.; Mucha, M.; Jungwirth, P. Solvation of the Azide Anion (N_3^-) in Water Clusters and Aqueous Interfaces: A Combined Investigation by Photoelectron Spectroscopy, Density Functional Calculations, and Molecular Dynamics Simulations. *The Journal of Physical Chemistry A* **2004**, *108*, 7820–7826.
- [222] Bondesson, L.; Frediani, L.; Ågren, H.; Mennucci, B. Solvation of N_3^- at the Water Surface: The Polarizable Continuum Model Approach. *The Journal of Physical Chemistry B* **2006**, *110*, 11361–11368.
- [223] Li, S.; Schmidt, J. R.; Piryatinski, A.; Lawrence, C. P.; Skinner, J. L. Vibrational Spectral Diffusion of Azide in Water. *The Journal of Physical Chemistry B* **2006**, *110*, 18933–18938.
- [224] Li, S.; Schmidt, J. R.; Skinner, J. L. Vibrational energy relaxation of azide in water. *Journal of Chemical Physics* **2006**, *125*.
- [225] Li, S.; Schmidt, J. R.; Corcelli, S. A.; Lawrence, C. P.; Skinner, J. L. Approaches for the calculation of vibrational frequencies in liquids: Comparison to benchmarks for azide/water clusters. *The Journal of Chemical Physics* **2006**, *124*, 204110.
- [226] Kuo, C. H.; Vorobyev, D. Y.; Chen, J.; Hochstrasser, R. M. Correlation of the vibrations of the aqueous azide ion with the O–H modes of bound water molecules. *Journal of Physical Chemistry B* **2007**, *111*, 14028–14033.

- [227] Sando, G. M.; Dahl, K.; Owrutsky, J. C. Vibrational Spectroscopy and Dynamics of Azide Ion in Ionic Liquid and Dimethyl Sulfoxide Water Mixtures. *The Journal of Physical Chemistry B* **2007**, *111*, 4901–4909.
- [228] Olschewski, M.; Knop, S.; Lindner, J.; Vöhringer, P. Vibrational relaxation of azide ions in liquid-to-supercritical water. *The Journal of Chemical Physics* **2011**, *134*, 214504.
- [229] Todorov, I. T.; Smith, W.; Trachenko, K.; Dove, M. T. DL POLY 3: New dimensions in molecular dynamics simulations via massive parallelism. *Journal of Materials Chemistry* **2006**,
- [230] Todorov, I. T.; Smith, W. DL POLY 4. 2011.
- [231] Hariharan, P. C.; Pople, J. A. The influence of polarization functions on molecular orbital hydrogenation energies. *Theoretica Chimica Acta* **1973**, *28*, 213–222.
- [232] Frisch, M. J. et al. Gaussian 09 Revision D.01. <http://www.gaussian.com>.
- [233] Glendening, E. D.; Badenhoop, J. K.; Reed, A. D.; Carpenter, J. E.; Weinhold, F. NBO Version 3.1.
- [234] Reed, A. E.; Weinstock, R. B.; Weinhold, F. Natural population analysis. *The Journal of Chemical Physics* **1985**, *83*, 735–746.
- [235] Grimme, S.; Ehrlich, S.; Goerigk, L. Effect of the damping function in dispersion corrected density functional theory. *Journal of Computational Chemistry* **2011**, *32*, 1456–1465.
- [236] Weigend, F. Accurate Coulomb-fitting basis sets for H to Rn. *Physical Chemistry Chemical Physics* **2006**, *8*, 1057.
- [237] Grimme, S. Improved second-order Møller–Plesset perturbation theory by separate scaling of parallel- and antiparallel-spin pair correlation energies. *The Journal of Chemical Physics* **2003**, *118*, 9095–9102.
- [238] Riplinger, C.; Neese, F. An efficient and near linear scaling pair natural orbital based local coupled cluster method. *The Journal of Chemical Physics* **2013**, *138*, 034106.
- [239] Neese, F.; Wennmohs, F.; Hansen, A.; Becker, U. Efficient, approximate and parallel Hartree–Fock and hybrid DFT calculations. A ‘chain-of-spheres’ algorithm for the Hartree–Fock exchange. *Chemical Physics* **2009**, *356*, 98–109.
- [240] Faginas Lago, N.; Huarte Larrañaga, F.; Albertí, M. On the suitability of the ILJ function to match different formulations of the electrostatic potential for water-water interactions. *The European Physical Journal D* **2009**, *55*, 75–85.

- [241] Bartolomei, M.; Carmona-Novillo, E.; Hernández, M. I.; Campos-Martínez, J.; Pirani, F.; Giorgi, G.; Yamashita, K. Penetration Barrier of Water through Graphynes' Pores: First-Principles Predictions and Force Field Optimization. *The Journal of Physical Chemistry Letters* **2014**, *5*, 751–755.
- [242] Albertí, M.; Aguilar, A.; Lucas, J. M.; Pirani, F.; Coletti, C.; Re, N. Atom–Bond Pairwise Additive Representation for Halide–Benzene Potential Energy Surfaces: an Ab Initio Validation Study. *The Journal of Physical Chemistry A* **2009**, *113*, 14606–14614.
- [243] Albertí, M.; Aguilar, A.; Lucas, J. M.; Pirani, F. A Generalized Formulation of Ion– π Electron Interactions: Role of the Nonelectrostatic Component and Probe of the Potential Parameter Transferability. *The Journal of Physical Chemistry A* **2010**, *114*, 11964–11970.
- [244] Bartolomei, M.; Carmona-Novillo, E.; Hernández, M. I.; Campos-Martínez, J.; Pirani, F.; Giorgi, G. Graphdiyne Pores: "Ad Hoc" Openings for Helium Separation Applications. *The Journal of Physical Chemistry C* **2014**, *118*, 29966–29972.
- [245] Faginas-Lago, N.; Yeni, D.; Huarte, F.; Wang, Y.; Alcamí, M.; Martín, F. Adsorption of Hydrogen Molecules on Carbon Nanotubes Using Quantum Chemistry and Molecular Dynamics. *The Journal of Physical Chemistry A* **2016**, *120*, 6451–6458.
- [246] Hauser, A. W.; de Lara-Castells, M. P. Carbon Nanotubes Immersed in Superfluid Helium: The Impact of Quantum Confinement on Wetting and Capillary Action. *The Journal of Physical Chemistry Letters* **2016**, *7*, 4929–4935.
- [247] Hauser, A. W.; Mitrushchenkov, A. O.; De Lara-Castells, M. P. Quantum Nuclear Motion of Helium and Molecular Nitrogen Clusters in Carbon Nanotubes. *Journal of Physical Chemistry C* **2017**, *121*, 3807–3821.
- [248] Wilson, J.; Faginas-Lago, N.; Vekeman, J.; Cuesta, I. G.; Sánchez-Marín, J.; Sánchez de Merás, A. Modeling the Interaction of Carbon Monoxide with Flexible Graphene: From Coupled Cluster Calculations to Molecular-Dynamics Simulations. *ChemPhysChem* **2018**, 1–11.
- [249] Stone, A. *The Theory of Intermolecular Forces*; Oxford University Press, 2013.
- [250] Cambi, R.; Cappelletti, D.; Liuti, G.; Pirani, F. Generalized correlations in terms of polarizability for van der Waals interaction potential parameter calculations. *The Journal of Chemical Physics* **1991**, *95*, 1852–1861.
- [251] Cappelletti, D.; Liuti, G.; Pirani, F. Generalization to ion—neutral systems of the polarizability correlations for interaction potential parameters. *Chemical Physics Letters* **1991**, *183*, 297–303.

- [252] Aquilanti, V.; Cappelletti, D.; Pirani, F. Range and strength of interatomic forces: dispersion and induction contributions to the bonds of dications and of ionic molecules. *Chemical Physics* **1996**, *209*, 299–311.
- [253] Le Borgne, C.; Illien, B.; Beignon, M.; Chabanel, M. Ion association of alkali and alkaline earth metal azides in dimethylsulfoxide. Infrared spectrometry and *ab initio* calculations. *Physical Chemistry Chemical Physics* **1999**, *1*, 4701–4706.
- [254] Gavezzotti, A. Calculation of Intermolecular Interaction Energies by Direct Numerical Integration over Electron Densities. 2. An Improved Polarization Model and the Evaluation of Dispersion and Repulsion Energies. *The Journal of Physical Chemistry B* **2003**, *107*, 2344–2353.
- [255] Wang, X.; Hu, H.-r.; Tian, A.; Wong, N.; Chien, S.-H.; Li, W.-K. An isomeric study of N_5^+ , N_5 , and N_5^- : a Gaussian-3 investigation. *Chemical Physics Letters* **2000**, *329*, 483–489.
- [256] Nguyen, M. T.; Ha, T.-k. Theoretical study of the pentanitrogen cation (N_5^+). *Chemical Physics Letters* **2000**, *317*, 135–141.
- [257] Vij, A.; Wilson, W. W.; Vij, V.; Tham, F. S.; Sheehy, J. A.; Christe, K. O. Polynitrogen Chemistry. Synthesis, Characterization, and Crystal Structure of Surprisingly Stable Fluoroantimonate Salts of N_5^+ . *Journal of the American Chemical Society* **2001**, *123*, 6308–6313.
- [258] Nguyen, M. T. Polynitrogen compounds 1. Structure and stability of N_4 and N_5 systems. *Coordination Chemistry Reviews* **2003**, *244*, 93–113.
- [259] Christe, K. O. Recent Advances in the Chemistry of N_5^+ , N_5^- and High-Oxygen Compounds. *Propellants, Explosives, Pyrotechnics* **2007**, *32*, 194–204.
- [260] Fau, S.; Wilson, K. J.; Bartlett, R. J. On the Stability of $N_5^+N_5^-$. *Journal of Physical Chemistry A* **2002**, *106*, 4639–4644.
- [261] Gagliardi, L.; Evangelisti, S.; Widmark, P.-O.; Roos, B. O. A theoretical study of the N_8 cubane to N_8 pentalene isomerization reaction. *Theoretical Chemistry Accounts: Theory, Computation, and Modeling (Theoretica Chimica Acta)* **1997**, *97*, 136–142.
- [262] Gagliardi, L.; Evangelisti, S.; Roos, B. O.; Widmark, P.-O. A theoretical study of ten N_8 isomers. *Journal of Molecular Structure: THEOCHEM* **1998**, *428*, 1–8.
- [263] Chung, G.; Schmidt, M. W.; Gordon, M. S. An Ab Initio Study of Potential Energy Surfaces for N_8 Isomers. *The Journal of Physical Chemistry A* **2000**, *104*, 5647–5650.
- [264] Gagliardi, L.; Evangelisti, S.; Bernhardsson, A.; Lindh, R.; Roos, B. O. Dissociation reaction of N_8 azapentalene to $4N_2$: A theoretical study. *International Journal of Quantum Chemistry* **2000**, *77*, 311–315.

- [265] Li, Q. S.; Wang, L. J. Theoretical Studies on the Potential Energy Surfaces of N₈ Clusters. *The Journal of Physical Chemistry A* **2001**, *105*, 1979–1982.
- [266] Jie Wang, L.; Li, S.; Li, Q. S. Theoretical studies on a possible synthesis reaction pathway on N₈ (C_s) clusters. *Journal of Computational Chemistry* **2001**, *22*, 1334–1339.
- [267] Hirshberg, B.; Gerber, R. B.; Krylov, A. I. Calculations predict a stable molecular crystal of N₈. *Nature chemistry* **2014**, *6*, 52–56.
- [268] Hanwell, M. D.; Curtis, D. E.; Lonie, D. C.; Vandermeersch, T.; Zurek, E.; Hutchison, G. R. Avogadro: an advanced semantic chemical editor, visualization, and analysis platform. *Journal of Cheminformatics* **2012**, *4*, 17.
- [269] Monari, A.; Vetere, V.; Bendazzoli, G. L.; Evangelisti, S.; Paulus, B. End states and singlet–triplet degeneracy in linear atomic chains. *Chemical Physics Letters* **2008**, *465*, 102–105.
- [270] Pastore, M.; Monari, A.; Angeli, C.; Bendazzoli, G. L.; Cimiraglia, R.; Evangelisti, S. A theoretical study of BeN linear chains: Variational and perturbative approaches. *The Journal of Chemical Physics* **2009**, *131*, 034309.
- [271] Vetere, V.; Monari, A.; Scemama, A.; Bendazzoli, G. L.; Evangelisti, S. A theoretical study of linear beryllium chains: Full configuration interaction. *The Journal of Chemical Physics* **2009**, *130*, 024301.
- [272] Monari, A.; Bendazzoli, G. L.; Evangelisti, S. Theoretical Study of Be N Linear Chains: Optimized Geometries and Harmonic Frequencies. *Journal of Chemical Theory and Computation* **2009**, *5*, 1266–1273.
- [273] Evangelisti, S.; Monari, A.; Leininger, T.; Bendazzoli, G. L. Beryllium chains interacting with Graphene Nanoislands: From anti-ferromagnetic to ferromagnetic ground state. *Chemical Physics Letters* **2010**, *496*, 306–309.
- [274] Šulka, M.; Labanc, D.; Kováč, M.; Pitoňák, M.; Černušák, I.; Neogrady, P. Ab initio study of the stability of beryllium clusters: accurate calculations for Be_{2–6}. *Journal of Physics B: Atomic, Molecular and Optical Physics* **2012**, *45*, 085102.
- [275] Avogadro: an open-source molecular builder and visualization tool. Version 1.2.0. <http://avogadro.cc/>.
- [276] Weigend, F. Hartree–Fock exchange fitting basis sets for H to Rn. *Journal of Computational Chemistry* **2008**, *29*, 167–175.
- [277] Miners, S. A.; Rance, G. A.; Khlobystov, A. N. Chemical reactions confined within carbon nanotubes. *Chemical Society Reviews* **2016**, *45*, 4727–4746.

A Appendix

A.1 Geometry Optimization of N_3^- in CNTs – Part II

The CNT geometries retained the high D_{5d} symmetry, with both parallel and perpendicular (to the principal axis) C–C bonds showing the typical alternation pattern of these systems when treated as finite systems^{15,16}. As the length of the nanotube increases, the average C–C bond length also increases, from 1.4237 Å to 1.4268 Å, which is in agreement with the fact that the bonds get slightly stretched due to the curvature.

The relaxed N_3^- geometry has linear $D_{\infty h}$ symmetry, with an N–N bond length of 1.1874 Å, which is in excellent agreement with the experimental gas phase value of 1.1884 Å²¹⁰.

Three starting geometries were chosen according to possible adsorption sites in which the central nitrogen atom of the azide was placed either over C–C bonds (*bond* (b) and *zigzag* (z) geometries) or in the center of an hexagonal ring of the wall (*hollow* (h) geometry). The three starting sites are shown in Figure A.1, along with their labels that will be used in the following to refer to them. For all three cases, the azide anion was placed at a distance of about 2.25 Å from the nanotube wall. The fourth starting geometry is shown in Figure A.2 and it simply consists in the anion placed exactly in the center of the nanotube. We will refer to this starting geometry as *central* (c) geometry. The structures starting from the (c) conformation correspond to a (local) minimum, since after one optimization step the convergence was reached, with the ion insignificantly (≈ 0.002 Å) shifted out of the principal axis. For this reason we will consider from now on the (c) geometry with the N_3^- moiety perfectly aligned to the principal axis and sitting in the center of the nanotube.

For the three other starting conformations, namely the the (b), (h) and (z) conformations, the optimization led to different minima. In order to quantify these differences, three geometrical and one energetic parameters were defined. The former are depicted in Figure A.3 and consist in the axial distance d_{cm} between the center of mass of the azide anion and the center of mass of the carbon nanotube, the radial distance r_{axis} of the azide anion

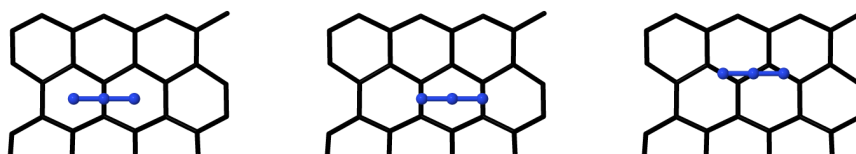


FIGURE A.1: Bond (left), hollow (center) and zigzag (right) starting sites.

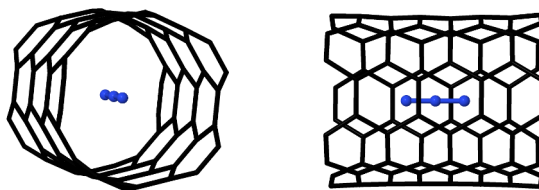


FIGURE A.2: Central starting geometry.

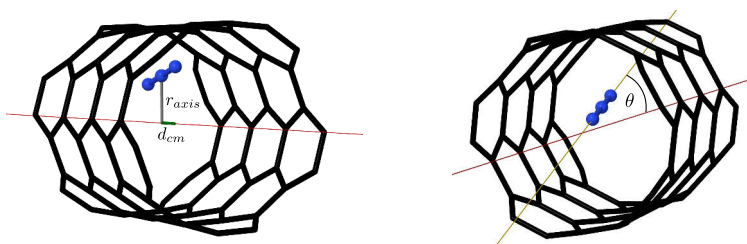


FIGURE A.3: Geometrical parameters.

center of mass from the principal axis of the nanotube and the angle θ formed between the principal axis and an imaginary line passing through the external nitrogen atoms of the azide anion. The energetic parameter is the interaction energy E_{int} between the two fragments.

The computed parameters for all systems are listed in Table A.1. Since the (c) geometry consists in the azide ion being in the exact center of the nanotube, the three geometrical parameters are all zero in this case, and therefore for the cases (b), (h) and (z), the parameters can be considered as *deviations* from the (c) conformation. Accordingly, instead of tabulating the interaction energy for every geometry, the values listed in the last column of Table A.1 correspond to the interaction energy differences between the (c) case and the other three, i.e. $\Delta E_{int} = E_{int}(c) - E_{int}(site)$. A negative value for ΔE_{int} means that the interaction is stronger in the (c) conformation, while a positive value means the opposite. In all cases, the azide anion is found to be almost perfectly aligned to the principal axis of the nanotube, since the angle θ is always very small (below 1° except in one case). Similarly, r_{axis} is always particularly small (most of the times below 0.01 \AA), meaning that the anion has the preference to stay approximately at the same distance from the nanotube wall in all directions, in agreement with our previous findings. In particular, irrespective of the length Λ , the azide ion is adsorbed at a distance of approximately 3.34 \AA (computed as the distance between the N_3^- center of mass and the closest side of the wall). This value is significantly larger than the adsorption distance of 3.17 \AA found for the confinement in a larger 3-CNT(6,6), obtained following the same computational procedure. There are two possible explanations for the difference in the adsorption distance. Either the different curvature of the two nanotubes is such that the forces attracting the ion are stronger in the case of the (6,6) CNT, or, in the case of the (5,5) CNT, there is a competition between the attractive forces exerted by the surrounding wall, which eventually stabilize the guest species at a virtually equal radial distance in any direction.

TABLE A.1: Conformational parameters and interaction energy differences with respect to the (c) geometry. Distances are given in Å, angles in degrees and energies in kcal/mol.

Λ	site	d_{cm}	r_{axis}	θ	ΔE_{int}
3	<i>bond</i>	0.018	0.002	0.06	-0.001
	<i>hollow</i>	0.002	0.003	0.04	0.000
	<i>zigzag</i>	0.000	0.003	0.27	-0.002
5	<i>bond</i>	0.604	0.009	0.32	0.112
	<i>hollow</i>	-0.144	0.002	0.32	0.017
	<i>zigzag</i>	0.000	0.003	0.43	0.000
7	<i>bond</i>	0.470	0.029	1.10	0.588
	<i>hollow</i>	-0.233	0.027	0.54	0.417
	<i>zigzag</i>	0.001	0.038	0.18	0.363
9	<i>bond</i>	0.622	0.015	0.74	0.400
	<i>hollow</i>	-1.304	0.003	0.17	0.030
	<i>zigzag</i>	-0.007	0.004	0.53	0.141

The most fluctuating parameter is d_{cm} . Clearly, the periodic atomic pattern of the carbon nanotube makes the potential energy surface of the fragment full of near-degenerate local minima. Apart from the (z) conformation, for which d_{cm} remains virtually unchanged irrespective to the length, it is hard to rationalize the results for the (b) and (h) cases. The only exception is found for the 3-CNT(5,5), where the two open ends of the nanotube are so close to the azide that the energy barriers to move away from the center are particularly steep and thus block it there.

A.2 Analytical Gradients

In the following, the working equations for the analytical forces of the ILJ and induction potentials are presented as well as their full derivation.

A.2.1 Improved Lennard-Jones Potential

In the main text, the analytical form of the ILJ potential was reported in Equation (4.4). In order to make the derivation easier to follow and implement, the various parts of the potential are labeled as follows

$$V_{ILJ}(r_{ij}) = \epsilon \left[\frac{m}{n(r_{ij}) - m} \cdot \left(\frac{r_m}{r_{ij}} \right)^{n(r_{ij})} - \frac{n(r_{ij})}{n(r_{ij}) - m} \cdot \left(\frac{r_m}{r_{ij}} \right)^m \right] \quad (\text{A.1})$$

$$= \epsilon [f(r_{ij})g(r_{ij}) - h(r_{ij})j(r_{ij})] \quad (\text{A.2})$$

For the implementation of the forces due to a general pairwise potential $V(r)$ in the DL POLY 4.08 program, we are seeking the following intermediate function

$$G(r_{ij}) = -\frac{1}{r_{ij}} \frac{\partial}{\partial r_{ij}} V(r_{ij}) \quad (\text{A.3})$$

where we kept the notation $G(r_{ij})$ used by the authors of the software²³⁰, although it has nothing to do with the function $g(r_{ij})$ appearing in Equation (A.2). The forces on atom i are then evaluated through the following multiplication

$$\begin{aligned} \vec{F}_i(r_{ij}) &= G(r_{ij})\vec{r}_{ij} \\ &= -\frac{1}{r_{ij}} \left[\frac{\partial}{\partial r_{ij}} V(r_{ij}) \right] \vec{r}_{ij} \end{aligned} \quad (\text{A.4})$$

For the sake of lightening the syntax, in the following derivations we will use the notation $r = r_{ij}$.

To begin with, let us compute the derivative of the function $n(r)$ appearing in the potential

$$\frac{\partial}{\partial r} n(r) = \frac{\partial}{\partial r} \left[\beta + 4 \left(\frac{r}{r_m} \right)^2 \right] \quad (\text{A.5})$$

$$= 8 \frac{r}{r_m^2} \quad (\text{A.6})$$

Next, the derivative of the ILJ potential with respect to r is given, in the simplified version introduced above, by

$$\frac{\partial}{\partial r} V_{ILJ}(r) = \epsilon [f'(r)g(r) + f(r)g'(r) - h'(r)j(r) - h(r)j'(r)] \quad (\text{A.7})$$

where the prime signs indicate a derivative with respect to r . The derivative of $f(r)$ is straightforward and has the following form

$$\frac{\partial}{\partial r} f(r) = \frac{\partial}{\partial r} \frac{m}{n(r) - m} = n'(r) \frac{-m}{(n(r) - m)^2} = \frac{-n'(r)}{(n(r) - m)} f(r) \quad (\text{A.8})$$

The derivative of $g(r)$ is more complicated since $n(r)$ appears in the exponent. Therefore we employ the logarithmic differentiation as follows

$$\ln(g(r)) = \ln\left(\frac{r_m}{r}\right) n(r) \quad (\text{A.9})$$

$$\frac{\partial}{\partial r} \ln(g(r)) = \frac{\partial}{\partial r} \left[\ln\left(\frac{r_m}{r}\right) n(r) \right] \quad (\text{A.10})$$

$$g'(r) \frac{1}{g(r)} = \frac{-1}{r} n(r) + \ln\left(\frac{r_m}{r}\right) n'(r) \quad (\text{A.11})$$

$$g'(r) = \frac{\partial}{\partial r} g(r) = g(r) \left[\ln\left(\frac{r_m}{r}\right) n'(r) - \frac{n(r)}{r} \right] \quad (\text{A.12})$$

To obtain $h'(r)$ we carry out the following steps

$$\frac{\partial}{\partial r} h(r) = \frac{\partial}{\partial r} \frac{n(r)}{n(r) - m} \quad (\text{A.13})$$

$$= \frac{n'(r)(n(r) - m) - n(r)n'(r)}{(n(r) - m)^2} \quad (\text{A.14})$$

$$= \frac{n'(r)n(r) - n'(r)m - n(r)n'(r)}{(n(r) - m)^2} \quad (\text{A.15})$$

$$= \frac{-n'(r)m}{(n(r) - m)^2} \quad (\text{A.16})$$

$$= \frac{m}{n(r) - m} \frac{-n'(r)}{n(r) - m} \quad (\text{A.17})$$

Finally, the last derivative reads

$$\frac{\partial}{\partial r} j(r) = \frac{\partial}{\partial r} \left(\frac{r_m}{r}\right)^m = -m \frac{r_m^m}{r^{m+1}} = \frac{-m}{r} j(r) \quad (\text{A.18})$$

By explicitly inserting all the computed terms into Equation (A.7) we obtain the final form for $\frac{\partial}{\partial r} V_{ILJ}$ as

$$\frac{\partial V_{ILJ}(r)}{\partial r} = \epsilon \left[f'(r)g(r) + f(r)g'(r) - h'(r)j(r) - h(r)j'(r) \right] \quad (\text{A.19})$$

$$= \epsilon \left[t_1 t_2 t_3 + t_2 t_3 \left[\ln\left(\frac{r_m}{r}\right) n'(r) - \frac{n(r)}{r} \right] - t_1 t_2 t_4 - \frac{n(r)}{n(r) - m} \frac{-m}{r} t_4 \right] \quad (\text{A.20})$$

where we have introduced intermediates t_1, t_2, t_3 and t_4 , according to

$$t_1 = \frac{-n'(r)}{n(r) - m} \quad (\text{A.21})$$

$$t_2 = \frac{m}{n(r) - m} \quad (\text{A.22})$$

$$t_3 = \left(\frac{r_m}{r}\right)^{n(r)} \quad (\text{A.23})$$

$$t_4 = \left(\frac{r_m}{r}\right)^m \quad (\text{A.24})$$

The ILJ force vectors can now be simply computed through Equation (A.4).

Note that the ILJ potential is completely general and can be used with any molecular species as long as the parameters are accordingly defined.

A.2.2 Induction Potential

The induction potential generated by three point charges is defined in Equation (4.8). In the following we are going to expand the squared term on the right hand side of Equation (4.8) and introduce a more convenient notation for the derivation of the forces,

$$\begin{aligned} V_{ind}(r_{i1}, r_{i2}, r_{i3}) &= -\frac{1}{2}\alpha \left[\frac{q_1}{r_{i1}^2} + \frac{q_2}{r_{i2}^2} + \frac{q_3}{r_{i3}^2} \right]^2 \\ &= -\frac{1}{2}\alpha \left[\frac{q_1^2}{r_{i1}^4} + \frac{q_2^2}{r_{i2}^4} + \frac{q_3^2}{r_{i3}^4} + \frac{2q_1q_2}{r_{i1}^2 r_{i2}^2} + \frac{2q_2q_3}{r_{i2}^2 r_{i3}^2} + \frac{2q_1q_3}{r_{i1}^2 r_{i3}^2} \right] \\ &= -\frac{1}{2}\alpha \left[t_{11}^i + t_{22}^i + t_{33}^i + 2t_{12}^i + 2t_{23}^i + 2t_{13}^i \right] \end{aligned} \quad (\text{A.25})$$

where we note that the terms $t_{jk}^i = t_{kj}^i$ are symmetric.

As before, we are interested in obtaining all the components of the force vector \vec{F}_i acting on atom i . In order to do so, we can differentiate the potential with respect to the individual components of the coordinate vector $\vec{r}_i = [x_i, y_i, z_i]$. For example, for the x component we have

$$\vec{F}_{i,x} = -\frac{\partial V_{ind}}{\partial x_i} \quad (\text{A.26})$$

and similarly for the other two.

The potential V_{ind} depends on the distances r_{i1}, r_{i2} and r_{i3} between atom i and the three nitrogen atoms, thus to obtain the derivative with respect to the Cartesian components we have to apply the chain rule, as exemplified in the following for x_i

$$\frac{\partial V_{ind}}{\partial x_i} = \frac{\partial V_{ind}}{\partial r_{i1}} \frac{\partial r_{i1}}{\partial x_i} + \frac{\partial V_{ind}}{\partial r_{i2}} \frac{\partial r_{i2}}{\partial x_i} + \frac{\partial V_{ind}}{\partial r_{i3}} \frac{\partial r_{i3}}{\partial x_i} \quad (\text{A.27})$$

Let us denote $w_i = \{x_i, y_i, z_i\}$, then we have in general

$$\frac{\partial r_{ij}}{\partial w_i} = \frac{\partial}{\partial w_i} \sqrt{(x_i - x_j)^2 + (y_i - y_j)^2 + (z_i - z_j)^2} = 2(w_i - w_j) \frac{1}{2} \frac{1}{r_{ij}} = \frac{w_{ij}}{r_{ij}} \quad (\text{A.28})$$

where $w_{ij} = w_i - w_j$.

The derivatives of the terms t_{jk}^i introduced in Equation (A.25) can be separated into two possible cases. In the first case, indices j and k are the same

$$\frac{\partial t_{jj}^i}{\partial w_i} = \frac{\partial t_{jj}^i}{\partial r_{ij}} \frac{\partial r_{ij}}{\partial w_i} = \frac{\partial t_{jj}^i}{\partial r_{ij}} \frac{w_{ij}}{r_{ij}} = \left(\frac{\partial}{\partial r_{ij}} \frac{q_j^2}{r_{ij}^4} \right) \frac{w_{ij}}{r_{ij}} = -4q_j^2 r_{ij}^{-5} \frac{w_{ij}}{r_{ij}} = -4 \frac{q_j^2 w_{ij}}{r_{ij}^6} \quad (\text{A.29})$$

In the second case, the indices j and k are different

$$\frac{\partial t_{jk}^i}{\partial w_i} = \frac{\partial t_{jk}^i}{\partial r_{ij}} \frac{\partial r_{ij}}{\partial w_i} + \frac{\partial t_{jk}^i}{\partial r_{ik}} \frac{\partial r_{ik}}{\partial w_i} \quad (\text{A.30})$$

$$= \frac{\partial t_{jk}^i}{\partial r_{ij}} \frac{w_{ij}}{r_{ij}} + \frac{\partial t_{jk}^i}{\partial r_{ik}} \frac{w_{ik}}{r_{ik}} \quad (\text{A.31})$$

$$= \left(\frac{\partial}{\partial r_{ij}} \frac{q_j q_k}{r_{ij}^2 r_{ik}^2} \right) \frac{w_{ij}}{r_{ij}} + \left(\frac{\partial}{\partial r_{ik}} \frac{q_j q_k}{r_{ij}^2 r_{ik}^2} \right) \frac{w_{ik}}{r_{ik}} \quad (\text{A.32})$$

$$= -2q_j q_k r_{ij}^{-3} r_{ik}^{-2} \frac{w_{ij}}{r_{ij}} - 2q_j q_k r_{ij}^{-2} r_{ik}^{-3} \frac{w_{ik}}{r_{ik}} \quad (\text{A.33})$$

$$= -2 \frac{q_j q_k w_{ij}}{r_{ij}^4 r_{ik}^2} - 2 \frac{q_j q_k w_{ik}}{r_{ij}^2 r_{ik}^4} \quad (\text{A.34})$$

The final form of the induction forces can be obtained by inserting all terms just computed into Equation (A.27), by substituting indices 1, 2, 3 with j and k .

Note that due to the non-additive nature of the induction potential, this derivation of the forces only applies to the potential generated by three point charges. Therefore, if more or less charges are the sources of induction, the forces have to be derived and implemented another again.

A.3 Virial

The virial is a quantity required to compute the pressure of a system in a MD simulation. Here, we only demonstrate how the virial is computed for the induction potential, since given that the ILJ potential is a pairwise potential, standard formulas already available in DL POLY 4 naturally apply.

A.3.1 Induction Potential

In the following, we closely follow the derivations provided in Ref. 92. In order to obtain the pressure of a thermodynamic system, we can rely on Clausius' Virial theorem, given by

$$P = \frac{1}{3V} (2\langle K \rangle - \langle \Psi \rangle) \quad (\text{A.35})$$

where $\langle \Psi \rangle$ is the ensemble average of the virial Ψ .

Another method to obtain the pressure is by statistical thermodynamics arguments, through the equation

$$P = - \left\langle \left(\frac{\partial H^N(\vec{r}^N, \vec{p}^N)}{\partial V} \right)_T \right\rangle \quad (\text{A.36})$$

where

$$H^N(\vec{r}^N, \vec{p}^N) = K^N(\vec{p}^N) + \Phi^N(\vec{r}^N) \quad (\text{A.37})$$

is the Hamiltonian of the system.

Note how in Equation (A.36) there is a partial derivative with respect to the system volume V , although in general it does not explicitly appear in the Hamiltonian formula shown in Equation (A.37). In order to introduce the volume and obtain an explicit form of Equation (A.37), we carry out the following substitution

$$\vec{r}^N = V^{1/3} \vec{s}^N \quad (\text{A.38})$$

which introduces the *scaled positions* \vec{s}^N . After some algebraic manipulations, we obtain the derivative of Equation (A.37) with respect to the volume as

$$\frac{\partial H^N(\vec{r}^N, \vec{p}^N)}{\partial V} = \frac{\partial K^N(\vec{p}^N)}{\partial V} + \frac{\partial \Phi^N(\vec{r}^N)}{\partial V} \quad (\text{A.39})$$

$$= \dots \quad (\text{A.40})$$

$$= \frac{-1}{3V} \left(2K^N(\vec{p}^N) - \Psi^N(\vec{r}^N) \right) \quad (\text{A.41})$$

which has the same form as Clausius' virial theorem.

The virial $\Psi^N(\vec{r}^N)$ is then given by

$$\Psi^N(\vec{r}^N) = \frac{\partial \Phi^N(\vec{r}^N)}{\partial \vec{r}^N} \cdot \vec{r}^N \quad (\text{A.42})$$

or, alternatively written as

$$\Psi^N(\vec{r}^N) = 3V \frac{\partial \Phi^N(\vec{r}^N)}{\partial V} \quad (\text{A.43})$$

In order to compute the virial for V_{ind} , we use this last equation, after introduction of the scaled positions in order to have an explicit dependence of the potential with respect to the volume. The induction potential with scaled positions reads then

$$V_{ind}(V^{1/3}s_{i1}, V^{1/3}s_{i2}, V^{1/3}s_{i3}) = -\frac{1}{2}\alpha \left[\frac{q_1}{V^{1/3}s_{i1}^2} + \frac{q_2}{V^{1/3}s_{i2}^2} + \frac{q_3}{V^{1/3}s_{i3}^2} \right]^2 \quad (\text{A.44})$$

By rearranging the terms in Equation (A.44) we have

$$V_{ind}(V^{1/3}s_{i1}, V^{1/3}s_{i2}, V^{1/3}s_{i3}) = -\frac{1}{2}\alpha \frac{1}{V^{4/3}} \left[\frac{q_1}{V^{1/3}s_{i1}^2} + \frac{q_2}{V^{1/3}s_{i2}^2} + \frac{q_3}{V^{1/3}s_{i3}^2} \right]^2 \quad (\text{A.45})$$

and we can now take the derivative as

$$\frac{\partial V_{ind}}{\partial V} = \frac{-4}{3}V^{-7/3} \frac{-1}{2}\alpha \left[\frac{q_1}{s_{i1}^2} + \frac{q_2}{s_{i2}^2} + \frac{q_3}{s_{i3}^2} \right]^2 \quad (\text{A.46})$$

$$= \frac{-4}{3}V^{-1} \frac{-1}{2}\alpha \left[V^{-4/3} \left(\frac{q_1}{s_{i1}^2} + \frac{q_2}{s_{i2}^2} + \frac{q_3}{s_{i3}^2} \right)^2 \right] \quad (\text{A.47})$$

$$= \frac{-4}{3V} \frac{-1}{2}\alpha \left[\frac{q_1}{V^{2/3}s_{i1}^2} + \frac{q_2}{V^{2/3}s_{i2}^2} + \frac{q_3}{V^{2/3}s_{i3}^2} \right]^2 \quad (\text{A.48})$$

$$= \frac{-4}{3V} V_{ind}(r_{i1}, r_{i2}, r_{i3}) \quad (\text{A.49})$$

By comparing Equation (A.46) with Equation (A.43) we see that the virial for particle i due to the induction potential is given by

$$\Psi_{ind}^i(r_{i1}, r_{i2}, r_{i3}) = 3V \frac{\partial V_{ind}}{\partial V} \quad (\text{A.50})$$

$$= 3V \frac{-4}{3V} V_{ind}(r_{i1}, r_{i2}, r_{i3}) \quad (\text{A.51})$$

$$= -4V_{ind}(r_{i1}, r_{i2}, r_{i3}) \quad (\text{A.52})$$

which concludes the derivation.

A.4 Distributed Gaussian Orbitals for Molecular Calculations: Application to Simple Systems

In this work, we propose the combination of atom-centered and distributed Gaussian orbitals to perform molecular calculations. On one side, the atom-centered basis functions provide an accurate description of the core electrons and the electron–nuclear cusp, on the other side, a mesh of distributed *s*-type Gaussian functions fill the space and provides to the wave function the flexibility to represent the more diffuse valence electrons.

To explore this alternative basis set expansion, a custom molecular integrals program was developed based on the McMurchie-Davidson scheme⁸⁸. A tentative draft for the publication of the results obtained with this approach is included in the following.

Distributed Gaussian Orbitals for Molecular Calculations: Application to Simple Systems

Stefano Battaglia,^{a,b} David Bouet,^a Alexis Lecoq,^a Stefano Evangelisti,^a

Noelia Faginas-Lago,^{b,c,*} Thierry Leininger,^a and Andrea Lombardi^{b,c}

^(a) Laboratoire de Chimie et Physique Quantiques - IRSAMC
Université de Toulouse et CNRS
118, Route de Narbonne, F-31062 Toulouse Cedex - France

^(b) Dipartimento di Chimica, Biologia e Biotecnologie, Università degli Studi di
Perugia
Via Elce di Sotto 8
I-06123, Perugia - Italy

^(c) Consortium for Computational Molecular and Materials Sciences (CMS)²
Via Elce di Sotto 8
I-06123, Perugia - Italy

* E-mail: noelia.faginaslago@unipg.it

ARTICLE HISTORY

Compiled September 21, 2018

ABSTRACT

In this article, the possible use of sets of basis functions alternative with respect to the usual atom-centered orbitals sets is considered. The orbitals describing the inner part of the wave function (i.e. the region close to each nucleus) are still atomic Gaussian functions: tight Gaussian orbitals having different angular momenta and large exponential coefficients, centered on each nucleus. On the other hand, the outer part of the wave function is described through a set of *s*-type distributed Gaussian orbitals: *s*-type Gaussians having a *unique fixed exponent*, and whose *fixed* centers are placed on a *uniform mesh of points* evenly distributed in the region surrounding all the atoms of the molecule. The resulting basis sets are applied to various one-electron systems in order to assess the capability to describe different types of one-electron wave functions. Moreover, the hydrogen atom and the dihydrogen cation, for which accurate solutions exist, are also considered for comparison, to assess the effectiveness of the proposed approach. Some preliminary results concerning the introduction of electron correlation, necessary to describe many-electron atoms and

molecules, are also presented.

KEYWORDS

Molecular Basis Sets, Linear Combination of Atomic Orbitals (LCAO), Distributed Gaussian Orbitals, Electron Correlation.

1. Introduction

A common practice in quantum chemistry is the expansion of the molecular orbitals (MO) of the system on a set of fixed basis functions. These can be either orbitals having an atomic character, such as Gaussian-type orbitals (GTOs) [1, 2] and Slater-type orbitals (STOs), or functions distributed on the region surrounding the molecule, such as plane waves, wavelets, etc. (see e.g. Ref. [3]). In particular, GTOs, introduced first by Boys in quantum chemistry [4] are nowadays by far the most common type of orbitals used to perform numerical calculations on atoms and molecules. In principle, a single-center (infinite) set of Gaussian orbitals is enough in order to have a complete basis set, provided the exponents are chosen in a suitable way [5, 6]. From a practical point of view, however, such a single-center expansion has two major problems:

- The basis set becomes quickly quasi-linear dependent.
- The convergence of the expansion to describe the electrons of atoms whose nuclei are not placed on the center of the Gaussians is extremely slow.

In practice, therefore, a single-center Gaussian expansion does not appear to be the most suitable choice to perform actual calculations on multi-atomic systems. In particular, the nuclear cusp of an *s*-type orbital of a given atom can hardly be described unless the expansion contains Gaussians with very large exponents that are centered on the nucleus of the atom itself. For this reason, a very common computational strategy is to expand the molecular orbitals (MOs) of the system on a set of multi-centered atomic orbitals (AOs) of Gaussian type, centered on each one of the atoms that belong to the molecule. This is the very well known linear combination of atomic orbitals (LCAO) strategy first used by Linus Pauling to describe the H_2^+ system, and in a more systematic way by Lennard-Jones, to describe the bonds of atoms belonging to the first main row of the periodic table []. The reason why this choice is so effective is that the intra-molecular interactions are relatively weak, and therefore the different atoms maintain their individuality in a molecular system.

In order to avoid extremely large expansions and to limit quasi-redundancy problems connected to the use of very small exponents on neighboring atoms, a very common practice is to work with linear combinations of the GTOs having *fixed* expansion coefficients. In this way, the contracted Gaussian-type orbitals (CGTOs) are obtained. The set of fixed linear coefficients is usually optimized on atomic calculations involving different states of the atom, and possibly some of its ions. A common practice is to use the atomic natural orbitals (ANOs) of the system in order to define these contraction coefficients [7, 8]. However, this well defined and elegant procedure is by no means the only possibility to obtain a set of CGTOs suitable for molecular calculations.

In the present work, the possible use of an alternative strategy, that can be considered as an extension of the LCAO formalism, will be explored. All the orbitals considered in this approach are Gaussian functions. The essential idea is to use a set of Gaussian-type orbitals that are evenly distributed in the space surrounding the

molecule, as in the floating orbitals scheme. We already noticed, however, that the use of atom-centered tight GTOs can hardly be avoided in order to describe the nuclear cusps. Therefore, we construct a mixed basis set according to the following two guidelines:

- (1) The orbitals describing the inner part of the wave function will be atomic-centered GTOs having different angular momenta and large exponential coefficients.
- (2) The outer part of the wave function, will be described through a set of *s*-type distributed GTOs: *s*-type Gaussians having a *unique fixed exponent* and whose *fixed* centers are placed on a *uniform mesh of points* evenly distributed in the region surrounding all the atoms of the molecule.

A number of previous attempts to construct mixed basis sets are spread among the literature of last decades and proposed, amongst others, mixed atom-centered STOs and floating Gaussians [9], the possible addition of bond functions to an atom-centered Gaussian basis [10] or, more recently, the mixed use of local Gaussians and plane waves for applications to correlated periodic systems [11].

The formalism resulting from the approach described above is here presented and applied to the description of some one-electron systems, to validate it as a method to handle different types of one-electron wave functions. In particular, the proposed approach will be applied to simple analytically soluble systems, like the harmonic oscillator and the hydrogen atom. The dihydrogen cation, for which very precise solutions exist, will also be considered, as an example of multi-center expansion. The introduction of electron correlation, necessary to describe many-electron atoms and molecules, is given in Section 7 along with some preliminary results from applications to simple systems. More complete work is postponed to a forthcoming paper.

This strategy is closely related to the floating spherical Gaussian orbital (FSGO) method, developed long time ago by Frost and coworkers and successfully applied to a series of small molecules [12–16], see also [17]. In the FSGO formalism, a series of additional orbitals of *s* type is added in region of the bond of a molecule in order to improve the wave function flexibility in this region. This approach has never become very popular, and a limited number of applications is found in the literature. It should be noticed however, that recently this formalism was applied in the field of molecular dynamics by Perl *et al.* [18, 19].

This article is organized as follows: in Section 2 we illustrate the basic ideas leading to a linear combination of distributed and atomic orbitals; in Section 3 the Gaussian basis sets required by this approach are formally presented; in Section 4, the problem of the quasi-completeness and quasi-linear dependence of the basis set is addressed; Section 5 describes the details of the numerical calculations, while in Section 6 results concerning one-electron systems are presented and discussed; In Section 7, applications to many-electron systems are considered. Finally, in Section 8, some conclusions are drawn, and the perspective use of such a type of basis sets for realistic molecular calculations is considered.

2. Linear Combination of Distributed and Atomic Orbitals

In this work, we will consider two types of orbitals to be combined for the construction of basis sets for the calculation of the wave functions of atomic and molecular systems:

- (1) Atomic-centered orbitals: these are orbitals whose centers are placed on an atomic nucleus. In this work, we will consider GTOs whose exponents form a geometric series (even-tempered Gaussians).
- (2) Distributed orbitals: evenly distributed identical Gaussian orbitals that occupy the whole molecular region. For the sake of simplicity, only uniformly spaced s -type orbitals having a unique exponent will be considered.

The orbitals at point (1) are the type of orbitals of the usual LCAO approach. Although these orbitals do not form a complete basis set, by choosing the ratio of the series sufficiently close to one, it is possible to construct a suitable linear combination to approximate an atomic orbital to a very high accuracy, provided that it is located in the region of the nucleus. They are very effective for describing the core and inner valence orbitals of an atom. Since the inner atomic shells remain essentially unchanged when a given atom combines with other atoms and gives rise to a molecular structure, the LCAO approach gives a good description of the inner region of the orbitals even in a molecular system. Things are much more complicated for the external regions of the atoms, where, upon bonding, the molecular wave function loses its atomic character. For smoothly varying orbitals, one can adopt the strategy illustrated at point (2) and describe the orbitals through Gaussian functions evenly distributed in the molecular region. As an example, these orbitals can be used to describe a set of electrons placed in a smooth external potential (for instance, the electrons in a quantum dot). However, this approach fails to describe an essential element of any molecule: the cusp of the s orbitals on each nucleus, where the wave function derivative has a singularity. For this reason, for atoms, molecules or real solids a mixed approach would seem preferable: the simultaneous use of tight atomic orbitals in order to describe the inner region of the wave function, with distributed orbitals for the description of the outer region. This technique for the calculation of atomic and molecular orbitals will be indicated as linear combination of distributed and atomic orbitals (LCDAO).

As it will be discussed in detail in the next two sections, a crucial step is represented by the choice of the specific Gaussian-type functions. For nuclear-centered atomic orbitals, there is a large amount of literature concerning even-tempered GTOs and their ability to describe the orbitals of an atom in a satisfactory way. For distributed Gaussians, on the other hand, the situation is much less clear, so we will here focus on this aspect of the problem. It turns out that the key parameter in this case is given by the dimensionless product ξ (formally introduced in the next section) of the Gaussian exponent (whose dimension is a length to the power of minus two) and the square of the intercenter distance. The situation is illustrated in Figures 1, 2 and 3.

If the product is small (Figure 1), the sum of the two Gaussians is a single-peak function, and these functions are in principle suitable to describe a smooth MO. However, if this product is too small, the two Gaussians have a very large overlap, and they quickly become linearly dependent. If the product is too large, on the other hand, the sum of the two Gaussians has a double-peak shape (Figure 2). In this case, a linear combination of such GTOs will necessarily have a large oscillatory behavior while describing any molecular function. This fact introduces a large spurious contribution to the kinetic energy of the system, and the interpolation would be impossible. The bor-

der between these two regimes is found when the product equals two: the sum of two Gaussians with identical exponent still has a single peak, but the second derivative in the mid-point between the two functions is zero. This situation is illustrated in Figure 3. In order to describe a smooth function, Gaussians having a product smaller than 2 have to be used. At the same time, the product should not be much smaller than 1, otherwise we face problems of quasi-linear dependence of the basis set [20].

3. Gaussian Basis Sets

In this section, the properties of the Gaussian orbitals used in this article will be described and detailed. We consider a non-normalized three-dimensional (3D) Gaussian function of the type

$$g_i(\mathbf{r}) = g_{\alpha_i, \mathbf{r}_i}(\mathbf{r}) = \exp(-\alpha_i \|\mathbf{r} - \mathbf{r}_i\|^2) \quad (1)$$

where α_i and \mathbf{r}_i are the exponent and the center of the Gaussian, respectively. The overlap integral between two Gaussians g_i and g_j is given by

$$S_{ij} = S(\alpha_i, \alpha_j, d_{ij}) = \left(\frac{\pi}{\alpha_i + \alpha_j}\right)^{3/2} \exp\left(-d_{ij}^2 \frac{\alpha_i \alpha_j}{\alpha_i + \alpha_j}\right) \quad (2)$$

where d_{ij} is the distance between the two centers \mathbf{r}_i and \mathbf{r}_j , $d_{ij} = \|\mathbf{r}_i - \mathbf{r}_j\|$. For a single Gaussian, the previous equation gives the square norm of the orbital as

$$S_{ii} = S(\alpha_i, \alpha_i, 0) = \left(\frac{\pi}{2\alpha_i}\right)^{3/2} \quad (3)$$

Two cases are particularly relevant for the present work, and will be treated in detail:

- (1) The two Gaussians have the same center (and in general different exponents). In this case, the overlap becomes

$$S(\alpha_i, \alpha_j, 0) = \left(\frac{\pi}{(\alpha_i + \alpha_j)}\right)^{3/2} \quad (4)$$

- (2) The two Gaussians have identical exponents (and in general different centers). In this second case, one gets

$$S(\alpha, \alpha, d_{ij}) = \left(\frac{\pi}{2\alpha}\right)^{3/2} \exp\left(-d_{ij}^2 \alpha/2\right) \quad (5)$$

In the following, it is convenient to work with normalized Gaussian orbitals, by defining the new functions

$$\bar{g}_i(\mathbf{r}) = \bar{g}_{\alpha_i, \mathbf{r}_i}(\mathbf{r}) = \left(\frac{2\alpha_i}{\pi}\right)^{3/4} \exp\left(-\alpha_i(\|\mathbf{r} - \mathbf{r}_i\|^2)\right) \quad (6)$$

The overlap between two normalized Gaussians, denoted as $\bar{S}(\alpha_i, \alpha_j, d_{ij})$, becomes then

$$\bar{S}(\alpha_i, \alpha_j, d_{ij}) = \left(\frac{2\alpha_i}{\pi}\right)^{3/4} \left(\frac{2\alpha_j}{\pi}\right)^{3/4} \left(\frac{\pi}{\alpha_i + \alpha_j}\right)^{3/2} \exp\left(-d_{ij}^2 \frac{\alpha_i \alpha_j}{\alpha_i + \alpha_j}\right) \quad (7)$$

The two particular cases considered earlier therefore become

(1) Two Gaussians with the same center:

$$\begin{aligned}\bar{S}(\alpha_i, \alpha_j, 0) &= \left(\frac{2\alpha_i}{\pi}\right)^{3/4} \left(\frac{2\alpha_j}{\pi}\right)^{3/4} \left(\frac{\pi}{\alpha_i + \alpha_j}\right)^{3/2} \\ &= \left(\frac{4\alpha_i\alpha_j}{(\alpha_i + \alpha_j)^2}\right)^{3/4} \\ &= \left(\frac{2}{1 + \alpha_i/\alpha_j} \frac{2}{1 + \alpha_j/\alpha_i}\right)^{3/4}\end{aligned}\tag{8}$$

(2) Two Gaussians with identical exponents:

$$\begin{aligned}\bar{S}(\alpha, \alpha, d_{ij}) &= \left(\frac{2\alpha}{\pi}\right)^{3/4} \left(\frac{2\alpha}{\pi}\right)^{3/4} \left(\frac{\pi}{2\alpha}\right)^{3/2} \exp\left(-d_{ij}^2\alpha/2\right) \\ &= \exp\left(-d^2\alpha/2\right)\end{aligned}\tag{9}$$

Notice that Equation (8) is manifestly symmetric under the exchange $\alpha_i \leftrightarrow \alpha_j$. Moreover, this equation implies that $\bar{S}(\alpha_i, \alpha_j, 0)$ is a *function of the ratio α_i/α_j only*. The overlap $\bar{S}(\alpha, \alpha, d_{ij})$, on the other hand, depends only on the product $d_{ij}^2\alpha$. These expressions can be further simplified if we consider some particular series of orbitals. For case (1), if a geometric series for the exponents α_i 's is used, $\alpha_j = \alpha_i\gamma^{j-i}$, and we set $\alpha_i = \alpha$ and $j - i = k$, we get

$$\bar{S}(\alpha, \alpha\gamma^k, 0) = \left(\frac{4\gamma^k}{(1 + \gamma^k)^2}\right)^{3/4}\tag{10}$$

where γ is the ratio of the series.

Noticeably, $\bar{S}(\alpha, \alpha\gamma^k, 0)$ does not depend on α . In case (2), by assuming $d_{ij} = (j - i)l = kl$ (with $k \in \mathcal{N}$), and $\xi = \alpha l^2$, one has

$$\bar{S}(\alpha, \alpha, kl) = \exp(-k^2\xi/2)\tag{11}$$

In this case, the overlap does not depend separately on the exponent and the inter-center distance, but only on k and the product ξ .

Equations (10) and (11) have deep consequences on the quasi-degeneracy properties of this Gaussian basis set. In particular, Equation (10) shows that the overlap between two normalized Gaussians tends to zero if the ratio between their exponents is very different from one. This means that the two Gaussians are almost mutually orthogonal, and they approach exact orthogonality if the ratio tends to zero (or infinity). If the ratio approaches unity, on the other hand, the overlap goes to one, and the two Gaussians become the same function.

Equation (11) implies that for any non-zero fixed exponent α and first inter-center distance l , the overlap will go to zero for sufficiently large values of k : well separated Gaussians tend to be orthogonal in this case. The first-neighbor overlap, on the other hand, will become arbitrarily close to one for small values of the product ξ .

Unfortunately, as it is often the case for non-orthogonal basis sets, completeness is associated to quasi-degeneracy: in order to be able to describe accurately a function, one gets into troubles of quasi-linear dependence of the basis sets. The connection between these two properties of the basis set will be made evident by considering the numerical investigations of the two next sections.

4. Completeness and Linear Dependence

From a computational point of view, two issues have a crucial importance for the practical applicability of the present scheme, in order to perform actual accurate calculations. These are the quasi-completeness and quasi-linear dependence of the basis set. For non-orthogonal basis sets, these two aspects are often closely related, since, in trying to improve the description of an orbital, the basis set is pushed toward linear dependency

Quasi-completeness means that, given a molecular orbital, the basis set must be able to reproduce such orbital to an (in principle) arbitrary precision. We will not discuss here about the mathematical aspects of such a property, assuming a pragmatic approach. In practice, a basis set will be considered to be accurate enough, or “quasi-complete”, with respect to a given system if the energy of the system is reproduced up to a fraction of a $\mu Hartree$.

For very large Gaussian expansions ($n \rightarrow \infty$), and either $\gamma \rightarrow 1$ or $\xi \rightarrow 0$ for the two cases, respectively, the numerical evidence seems to indicate that one gets quasi-complete basis sets. These two conditions, however, imply that the overlap between two first-neighbor normalized Gaussians tends to one, and the basis set becomes quasi-linear dependent

$$\lim_{\gamma \rightarrow 1} \bar{S}(\alpha, \alpha\gamma, 0) = \lim_{\gamma \rightarrow 1} \left(\frac{4\gamma}{(1+\gamma)^2} \right)^{3/4} = 1 \quad (12)$$

and

$$\lim_{\xi \rightarrow 0} \bar{S}(\alpha, \alpha, l) = \lim_{\xi \rightarrow 0} \exp(-\xi/2) = 1 \quad (13)$$

From a numerical point of view, therefore, γ and ξ cannot be chosen arbitrarily close to one and zero, respectively, since in these cases the overlap matrix becomes singular. This would mean that the smallest eigenvalue of the $\bar{S}_{i,j}$ matrix, \bar{S}_{\min} , becomes arbitrarily close to zero, and numerical calculations would be impossible. In a next section, it will be shown that there exists a *finite range of exponent values* that allow a good approximation of an atomic or molecular orbital without being plagued by quasi-linear dependence.

We address here the problem of the quasi-singularity of the metric. The analysis becomes much simpler if we assume an infinite number of Gaussians, by working in the limit $n \rightarrow \infty$. The smaller and largest eigenvalues of the overlap matrix are given in this case by the following expressions

$$\bar{S}_{\min} = \bar{S}(0) + 2 \sum_{k=1}^{\infty} (-1)^k \bar{S}(k) \quad (14)$$

and

$$\bar{S}_{\max} = \bar{S}(0) + 2 \sum_{k=1}^{\infty} \bar{S}(k) \quad (15)$$

By using Equations (10) and (11), Equation (14) becomes

$$\bar{S}_{\min}(\gamma) = 1 + 2 \sum_{k=1}^{\infty} (-1)^k \left(\frac{4\gamma^k}{(1 + \gamma^k)^2} \right)^{3/4} \quad (16)$$

for the one-center expansion, and

$$\bar{S}_{\min}(\xi) = 1 + 2 \sum_{k=1}^{\infty} (-1)^k \exp(-k^2 \xi / 2) \quad (17)$$

for the distributed-center one.

The minimum eigenvalue is particularly relevant in the present investigation, since it is precisely \bar{S}_{\min} that, for numerical reasons, must not be too close to zero. For instance, the general-purpose quantum chemistry code MOLPRO [21] does not allow metric eigenvalues smaller than $1.0 \cdot 10^{-6}$. In Figure 4, the lowest eigenvalue $\bar{S}_{\min}(\gamma)$ given by equation (16) is reported as a function of γ . The eigenvalue is a growing function of γ that slowly saturates toward the asymptotic limit of one. The threshold value of 10^{-6} is reached for $\gamma = 1.5$. This leaves a relatively large interval for the choice of the ratio of even-tempered sequences. In Figure 5, a similar behavior is illustrated for $\bar{S}_{\min}(\xi)$. In this case, it appears that the region to which ξ must belong is much narrower than in the previous case. In fact, one must consider that, for a simple cubic arrangement of the Gaussian mesh, the 3D lowest eigenvalue is the *third power* of $\bar{S}_{\min}(\gamma)$ given in Equation (17), since this equation refers to the one-dimensional case. Therefore, in practice the “safe region” is $0.7 < \xi < 1.4$. Nevertheless, as it will be shown in the numerical applications presented in this article, this narrow region is enough to choose a set of distributed Gaussians that describe to a very high degree of accuracy the orbitals of a molecular system.

5. Numerical Investigations: Computational Details

In this work, the proposed scheme is tested through the application to two one-electron systems: the hydrogen atom and the hydrogen dimer cation. The hydrogen atom is an analytically soluble system. Its spherical symmetry implies that only orbitals of s type are required for the atomic expansion. On the other hand, for the H_2^+ molecular cation, that is the simplest molecular system, an exact solution is not known. Because of the lack of isotropy around each nucleus, an accurate wave function description requires in this case the introduction of non spherically symmetric orbitals. In both cases, the presence of the nuclear cusp requires the presence in the basis set of atomic s functions having very large exponents.

5.1. Hydrogen Atom

The hydrogen atom wave function requires the presence of Gaussians with a high exponent, in order to approximate the nuclear cusp. For this reason it can be described by using either atomic or a combination of distributed and atomic GTOs.

A set of s -type even-tempered Gaussian orbitals is suitable to describe the hydrogen atom wave function. The basis set exponents are chosen as

$$\alpha_k = \gamma^k \alpha_0 \quad (18)$$

where k is an *integer* number, either positive, negative or zero. The sequence of exponents defining the Gaussian functions starts at $k = 0$ and is expanded in both positive and negative directions in order to describe both the nuclear cusp and the diffuse region of the electron density. To limit the number of independent parameters to be considered, very large Gaussian expansions were taken until stable values of the energy were reached. In this way, the results coincide, up to an error of about 10^{-10} *Hartree*, with the infinite-expansion ones. We did not investigate the dependence of the approximation quality on the origin α_0 of the even-tempered sequence, that has been arbitrarily chosen to be equal to the best single Gaussian exponent, $\alpha_0 = \frac{8}{9\pi}$ (see Appendix). Notice that, in the limit of $\gamma \rightarrow 1$, the choice of α_0 becomes irrelevant.

The distributed basis functions were chosen as equally spaced s -type Gaussians, having a unique exponent. Again, in order to limit the number of parameters to be considered, the exponent was chosen equal to $\alpha_0 = \frac{8}{9\pi}$. The centers of the Gaussians are located at the corners of a simple cubic network, whose edges contains $2N+1$ functions. Integer values of N from zero to six were considered, giving rise to cubic arrangements of Gaussians going from 1 to 2197 atomic orbitals. The distance d between two first-neighbor centers is related to α_0 via the equation

$$\alpha_0 d^2 = \xi \quad (19)$$

where ξ is a parameter close to one.

In the case of LCDAO basis sets, we used 30 s -type atom-centered even-tempered Gaussians for the atomic basis set, having exponents of the type $\alpha_k = \gamma^k \alpha_0$, with k being a *positive* integer starting at $k = 1$ and the ratio γ equal 2. These Gaussians therefore characterize the inner part of the electron density, being a sequence of increasingly tight functions.

We also investigated the dependence of the results on the position of the atomic center within the cube of distributed Gaussians. To this purpose, the nucleus was moved from the central position towards the cube surface along the three independent directions \mathbf{e}_x , $\mathbf{e}_x + \mathbf{e}_y$ and $\mathbf{e}_x + \mathbf{e}_y + \mathbf{e}_z$. For each independent direction, the energy was calculated at 11 equally spaced points between the position of two Gaussians.

5.2. The H_2^+ Dimer

The hydrogen dimer cation was studied within the LCDAO approach only. A large box containing $9.9 \cdot 21$ distributed orbitals with exponent $\alpha_0 = \frac{8}{9\pi}$ was chosen, in combination with atomic orbitals given by an even-tempered series of Gaussian functions, starting from $\alpha_1 = 2\alpha_0$ and with ratio γ equal to 2. In view of the large number of atomic and distributed functions involved in the expansion, this basis set can be considered converged as far as the s exponents are concerned.

For the atomic part, higher angular momentum functions were also included in the expansion in order to correctly describe the wave function in the bonding region. In particular, the dissociation was performed using a basis comprising 30 s -, 10 p - and 5 d -type orbitals, for a total of 90 atom-centered Gaussians (Cartesian Gaussian functions were used for the d -type orbitals). The dependence on the atomic orbitals was investigated at three different internuclear distances, namely at $R = 1, 2, 4$ bohr.

The reference values were obtained with a standard $v6z$ basis set expansion [21–23], having $6s5p4d3f2g1h$ contracted orbitals.

6. One-Electron Systems

6.1. Hydrogen Atom

The system that will be used to investigate the quality of the one-center atomic basis set is the hydrogen atom. Being a one-electron system that admits an analytical solution, the error in the energy is exactly known, and due to the basis set incompleteness only. If we assume an infinite value for the mass of the nucleus, the ground state wave function depends only on the radial coordinate. For the sake of simplicity, we will limit our investigation to s -type orbitals only. In this case, the energies are given (in atomic units) by

$$\epsilon_n = -\frac{1}{2n^2} \quad (20)$$

while the corresponding wave functions are

$$\psi_n(r, \theta, \phi) = \psi_n(r) = \exp(-r) \quad (21)$$

By using a one-center even-tempered Gaussian expansion, it is possible to approximate the hydrogen atom wave function to an arbitrary accuracy. The results are shown in Table 1 as a function of the even-tempered ratio γ . Notice how the single-center expansion of ratio $\gamma = 2$ provides an energy of -0.499999998129 *Hartree*. If, on the other hand, a ratio $\gamma = 1.8$ is used, the total energy becomes -0.499999999949 *Hartree*. The number of basis functions required to converge to the prescribed accuracy is inversely proportional to γ because for large values of the ratio, extremely tight and very diffuse Gaussians are generated, which do not significantly contribute to the wave function anymore.

In Table 2, the energy of the hydrogen atom obtained within the LCDAO approximation is reported for different values of the product ξ . In order to keep the error associated to the one-center expansion sufficiently small, a ratio $\gamma = 2$ was chosen for the even-tempered series. The nearest-neighbor distance in the mesh is set to

$$d = \sqrt{\frac{\xi}{\alpha_0}} = \frac{\sqrt{8\xi}}{3\sqrt{\pi}} \quad (22)$$

and is listed in the last row of Table 2 for each value of ξ .

Note how the value of ξ limits the achievable accuracy of a distributed basis set for a fixed value of the exponent α_0 . An accuracy in the μ *Hartree* range is only achieved in the case $\xi = 0.7$. For $\xi = 1.4$, the energy starts to saturate already with a cubic mesh with 5 Gaussians on each edge, whereas for $\xi = 0.7$, the energy gains significant digits up to $2N + 1 = 9$. This can be understood from the directly proportional relationship between ξ and the distance d between the Gaussians: the smaller ξ is, the more compact is the cubic mesh, ultimately providing a better achievable accuracy. On the other hand, too smaller values of ξ cannot be chosen without incurring into linear dependency issues (cf. Section 4).

The dependence of the energy on the position of the atom within the box of distributed Gaussians was investigated too, using a cubic mesh of $11 \cdot 11 \cdot 11$ basis functions

and setting $\xi = 0.7$. This box is sufficiently large such that surface effects do not appear. Moving the atom from the center of the cube in three independent directions, a difference δ in the order of 10^{-5} *Hartree* was observed, as reported in Figure 6. In principle, only one parameter plays a role here, which is the distance d between the distributed Gaussians. The smaller the value of d (set according to ξ), the less sensitive is the energy to the actual position of the atom in the cubic mesh. In practice nevertheless, for small boxes, surface effects might appear, in particular for systems described by a diffuse wave function. Small d values imply compact boxes, thus one has to find the right trade-off between ξ and the size of the box of distributed Gaussian in order to balance the errors coming from the different sources.

6.2. The Hydrogen-Dimer Cation

In Figure 7, the dissociation curve of the H_2^+ cation within the LCDAO approximation is shown and compared to the all- s and *spdfgh* curves. The minimum is very close to the internuclear distance $R = 2.0$ *bohr* with all the three basis sets. The dissociation energy, on the other hand, is affected by the basis set in a more noticeable way. Clearly, the all- s expansion does not have much flexibility, such that a large fraction of the dissociation curve lies above the other two cases. On the other hand, the LCDAO approximation is able to practically reproduce the reference curve very accurately at all internuclear distances. In fact, by using the distributed Gaussian expansion one gets for the total energy, at a distance of $R = 2.0$ *bohr*, the value $E = -0.602631$ *Hartree*, while the *spdfgh* value at the same distance is $E = -0.602632$ *Hartree*. By using an all- s basis set, one gets the substantially higher value $E = -0.590900$ *Hartree*.

The dependence of the energy on the GTOs centered on the two nuclei is reported in Table 3. One can see how the presence of p -type orbitals is necessary in order to obtain energies coinciding with the reference at m *Hartree* accuracy at least. Actually, addition of d -type orbitals improves the results compared to the *spdfgh* basis set, as highlighted by the bold digits in Table 3. This is however only observed at interatomic distances $R = 1$ and $R = 4$ and not at the equilibrium.

A second parameter which plays a role regarding the accuracy of the expansion is the square section size of the distributed Gaussians mesh. Accordingly, to study this effect, the energy was computed at the same three distances R as before, but with boxes of different sizes starting from $3 \cdot 3 \cdot 21$ up to $9 \cdot 9 \cdot 21$ and with the largest atom-centered basis. The energies obtained in this case are reported in Table 4. Interestingly, the energy saturates quite fast with respect to the mesh size, and already for the $5 \cdot 5 \cdot 21$ box the energy is better than the reference one at $R = 1$ and $R = 4$, whereas virtually the same at $R = 2$.

These results imply that one has to find an ideal trade-off between the number of distributed and atom-centered Gaussian functions in order to keep the corresponding errors at the same order of magnitude.

Note that in all calculations presented for the H_2 cation the length of the box was kept fixed to account for all internuclear distances, thus resulting in a large number of Gaussians which effectively have no contribution. This was done to reduce the number of parameters to consider in this study. A more effective approach would only require to have a box of distributed Gaussians around each atom, substantially decreasing the size of the basis.

6.3. Computational Complexity

Clearly, the success of any computational approach strongly relies on the efficiency with which calculations can be carried out. The last column of Tables 1 to 4 reports the number of Gaussian-type orbitals in the basis for each case. Evidently, in terms of raw number of basis functions, the LCDAO approach appear rather unfavorable. Nevertheless, a more scrupulous analysis reveals a different picture.

As the LCDAO approximation is a Gaussian basis set expansion only, the actual computational complexity of any calculation is still dictated by the quantum chemical method used, e.g. $\mathcal{O}(\mathcal{N}^5)$ for MP2, $\mathcal{O}(\mathcal{N}^6)$ for CCSD, and so on. On the other hand, as these methods scales with the number of basis functions, it is important to understand what is the advantage of this method over the usual LCAO approach and where further approximation can be introduced.

Besides the large number Gaussians used in the examples presented above, it is possible to estimate the scaling of the number of Gaussians required for larger systems. In particular, for 0-dimensional systems, i.e. single atoms far apart from each other, one has to account for a box of edge M surrounding each atom, i.e. M^3 GTOs times the number of atoms. For 1-D systems, as the length of a bond roughly coincides with the distance d between distributed Gaussians, every extra atom added to a linear system only increases the number of GTOs by one extra square section containing M^2 functions. Similarly for 2-D and 3-D systems one can find similar relations.

Substituting diffuse basis functions of high angular momenta with a set of distributed s -type Gaussian to fill the space brings some computational advantages. Calculation of integrals of high angular momenta relies on the use of recursive relations [24, 25] which are at least an order of magnitude slower than computing integrals over s -type orbitals, for which simple analytical formulas exist [26]. Therefore, one can expect the LCDAO to be much more efficient than the LCAO approach in that respect. Secondly, the fact that the distributed Gaussians are taken relatively compact and far away from each other, implies that a large portion of integrals will contribute insignificantly to the calculation and hence can be discarded by employing prescreening techniques. Lastly, the regular pattern of the 3-dimensional grid of Gaussians is likely to generate a large number of linear dependencies in the bi-electronic integral matrix, which can be therefore efficiently discarded by techniques such as the Cholesky decomposition [27–29].

7. Many-Electron Systems

The present, preliminary investigation is mainly focused on one-electron systems. However, our final aim is the description of atoms, molecules and possibly solids. Therefore, although the systematic treatment of many-electron systems is postponed to future works, it is important to give a preliminary overview of the feasibility of the proposed approach. For this reason, we report in this section the results of calculations on a few many-electron systems.

The first systems that will be discussed are the isoelectronic Helium atom and the H^- negative ion. The Helium atom is a very compact system, due to the closed-shell character and the occupation of $1s$ orbital only. It can be described by a relatively small number of distributed function. On the other hand, because of the excess of negative charge, the H^- system has a very diffuse wave function, and thus requires a large number of distributed Gaussians for an accurate description. Notice that this large number could be substantially reduced at the price of using more diffuse distributed Gaussians, i.e. by taking a smaller value of α_0 . However, since our philosophy is to use a *unique* type of Gaussians for the distributed functions, we did not explore this possibility.

In Table 5, the Hartree-Fock (HF) and full configuration interaction (FCI) total energies for the He atom, obtained by using different boxes, are compared with one-center calculations with a large size basis set containing $28s15p13d11f9g7h5i3j$ uncontracted Gaussians. Both the HF and FCI energies converge quickly as a function of the size of the box, and the difference between the $2N + 1 = 7$ and $2N + 1 = 9$ FCI energies is less than $2 \cdot 10^{-7}$ *Hartree*. With respect to the one-center expansion, and by using the largest basis set, the HF error is less than 10^{-6} *Hartree*, while the FCI error is of the order of $3 \cdot 10^{-6}$ *Hartree*. The cpu time to obtain these energies is at the moment substantial, since the programs we used are not adapted to such distributed basis sets, where a large number of four-center two-electron integrals need to be computed, but are not efficiently prescreened or approximated. In the largest case ($2N + 1 = 9$), the calculation required about ten hours on a medium-size computer.

In Table 6, the FCI energy for the hydrogen anion is reported for a series of boxes of different size and compared with high-accuracy calculations. The situation is similar to the previous one, except for the fact that the wave function is more diffuse due to the excess of negative charge. It can be seen from the table that a cubic box with edge size $2N + 1 = 9$ is able to reproduce the reference energy of this system up to one *mHartree*.

As a more challenging example, we considered the beryllium atom and the polyatomic system Be_4 , whose results, obtained using a completely decontracted cc-pVDZ basis set for Be[30], are reported in Table 7 and Table 8, respectively.

The calculations with atom-centered orbitals were performed by using the complete set of orbitals for each beryllium atom. The LCDAO calculations, on the other hand, were done by taking those atomic functions having a value of the exponent larger than 0.5. Different box sizes were explored for the distributed Gaussians, all having the exponent $\alpha_0 = 8/9\pi$: from 1 to 7 for Be, and from 1 to 9 for Be_4 . For Be_4 , we used a T_d symmetry geometry, where the HF equilibrium distance was chosen for all calculations.

We performed Hartree-Fock and coupled cluster singles and doubles (CCSD) calculations on both systems as well as complete active space self-consistent field (CASSCF)

calculations, with a (2,4) valence active space for the atom, and a comparatively smaller (8,10) active space for the tetramer. In the atomic case, a good $\mu Hartree$ accuracy is achieved for the uncorrelated method and the largest box, whereas the approaches introducing electron correlation deviate significantly from the reference energy.

For the beryllium tetramer, a similar accuracy to the single atom is observed for boxes up to a size of $2N+1 = 7$. However, the CASSCF energy is particularly underestimated for this system. On the other hand, remarkably, the distributed-orbital expansion is capable to outperform the LCAO approach by more than $2 mHartree$ in the CCSD case.

8. Future Perspectives and Conclusions

In this contribution, we investigated the combination of distributed and atomic Gaussian orbitals for the description of molecular orbitals. It was shown that distributed Gaussian functions are well suited to describe orbitals having a smooth dependence on the spatial coordinates, as it is the case for a harmonic oscillator. The presence of the nuclear cusp, on the other hand, requires the use of tight atom-centered Gaussians having large exponents. For this reason, a mixed approach, combining space-fixed distributed Gaussians for the valence region and atom-centered Gaussians to describe the inner shells can be seen as an interesting strategy.

We notice that diffuse orbitals are never introduced in the distributed basis set expansion, a fact that has several advantages. In fact, this strategy should be very little affected by the basis set superposition error (BSSE). The BSSE is mainly due to the presence in the basis set of diffuse orbitals centered on one atom, that artificially improve the description of neighboring atoms only in the case of short interatomic distances. Also the quasi-linear dependence problems at short interatomic distances, associated to the use of very large basis sets, should be substantially reduced. Despite the large number of orbitals in the basis set expansion, their compactness and organized position in a regular mesh can be exploited by prescreening and decomposition techniques applied to very large basis sets, which substantially reduce the number of significant two-electron integrals to compute. Moreover, regarding efficiency, the calculation of integrals over *s*-type GTOs is substantially faster than over functions of higher angular momenta.

At the moment, the main bottleneck for a systematic exploration of the proposed approach is represented by the number of centers of the distributed Gaussians, that are seen in standard *ab initio* codes as dummy atoms not bearing any charge. In fact, while the total number of orbitals in many general-purpose codes can easily be of several thousands, the total number of atoms, and therefore of Gaussian centers, is often limited to a few hundreds. For this reason, in the many-electron applications we were not able to go beyond a box of $9 \cdot 9 \cdot 9$ Gaussians, that is not enough to converge the total energy to more than four digits in general. Work is in progress in order to overcome this limitation, and be able to obtain results using substantially larger distributed basis sets.

9. Appendix : Best Gaussian Orbital for the Hydrogen Atom

Let us consider a Gaussian orbital ϕ_α , centered on the origin of the coordinates. The square of its norm is

$$\|\phi_\alpha\|^2 = \langle \phi_\alpha | \phi_\alpha \rangle = \left(\frac{\pi}{2\alpha} \right)^{3/2} \quad (23)$$

The kinetic and potential mean values on the Gaussian orbital are

$$\langle T \rangle_\alpha = \langle \phi_\alpha | \hat{T} | \phi_\alpha \rangle = \frac{3}{2} \alpha \left(\frac{\pi}{2\alpha} \right)^{3/2} \quad (24)$$

and

$$\langle V \rangle_\alpha = \langle \phi_\alpha | \hat{V} | \phi_\alpha \rangle = - \left(\frac{\pi}{\alpha} \right) \quad (25)$$

respectively (see, for instance, the book by Szabo and Ostlund[26]). The mean value of the energy becomes then

$$E_\alpha = \frac{3}{2} \alpha - \left(\frac{\alpha}{\pi} \right)^{1/2} 2^{3/2} \quad (26)$$

The best variational value for α is found by imposing the first derivative of E_α with respect to α equal to zero, yielding

$$\frac{d}{d\alpha} E_\alpha = \frac{3}{2} - \left(\frac{2}{\pi} \right)^{1/2} \alpha^{-1/2} \quad (27)$$

By setting $\frac{d}{d\alpha} E_\alpha = 0$ we obtain the optimum value for α , namely $\frac{8}{9\pi}$.

Acknowledgements

The authors acknowledge the support of the “Theoretical Chemistry and Computational Modelling” (TCCM) Erasmus-Plus Master program as well as the funding received from the European Union’s Horizon 2020 research and innovation programme under the Marie Skłodowska-Curie grant agreement 642294. We also acknowledge the “Programme Investissements d’Avenir” ANR-11- IDEX-0002-02, reference ANR-10-LABX-0037-NEXT for financial support. N.F-L acknowledges financial support received from Fondazione Cassa di Risparmio di Perugia through Projects “2014/1255, ACT 2014/6167” and “2015.0331.021 Ricerca Scientifica e Tecnologica”. A. L. acknowledges support from the Italian MIUR through PRIN 2015 (contract 2015F59J3R 002). The calculations of this work were performed on the HPC center CALMIP, under the grant 2016-p1048.

References

- [1] F. Jensen, “Atomic orbital basis sets,” *WIREs: Comput. Mol. Sci.*, vol. 3, pp. 275–295, 2013.
- [2] J. Grant Hill, “Gaussian basis sets for molecular applications,” *Int. J. Quantum Chem.*, vol. 113, pp. 21–34, 2013.
- [3] D. Moncrieff and F. Wilson, “Distributed basis sets of s-type gaussian functions in molecular electronic structure calculations,” *Mol. Phys.*, vol. 82, pp. 523–530, 1994.
- [4] S. F. Boys, “Electronic wave functions. i. a general method of calculation for stationary states of any molecular system,” *Proc. R. Soc. London Ser. A*, vol. 200, p. 542, 1950.
- [5] B. Klahn and W. A. Bingel, “The convergence of the rayleigh-ritz method in quantum chemistry,” *Theor. Chim. Acta*, vol. 44, pp. 9–26, 1977.
- [6] B. Klahn and W. A. Bingel, “Completeness and linear independence of basis sets used in quantum chemistry,” *Int. J. Quantum Chem.*, vol. 11, no. 6, pp. 943–957.
- [7] P.-O. Widmark, P.-A. Malmqvist, and B. O. Roos, “Density matrix averaged atomic natural orbital (ano) basis sets for correlated molecular wave functions,” *Theor. Chim. Acta*, vol. 77, pp. 291–306, 1990.
- [8] K. Pierloot, B. Dumez, P.-O. Widmark, and B. O. Roos, “Density matrix averaged atomic natural orbital (ano) basis sets for correlated molecular wave functions,” *Theor. Chim. Acta*, vol. 90, pp. 87–114, 1995.
- [9] G. B. Bacskay and J. W. Linnett, “Mixed basis functions in molecular quantum mechanics,” *Theor. Chim. Acta*, vol. 26, pp. 1–13, 1972.
- [10] D. Neisius and G. Verhaegen, “Bond functions for ab initio calculations on polyatomic molecules. molecules containing c, n, o and h,” *Chem. Phys. Lett.*, vol. 78, pp. 147–152, 1981.
- [11] G. H. Booth, T. Tsatsoulis, K.-L. C. Garnet, and A. Grünes, “From plane waves to local gaussians for the simulation of correlated periodic systems,” *J. Chem. Phys.*, vol. 145, p. 08411, 2013.
- [12] A. A. Frost, B. H. Prentice III, and R. A. Rouse, “A simple floating localized orbital model of molecular structure,” *J. Am. Chem. Soc.*, vol. 89, p. 3064, 1967.
- [13] A. A. Frost, “Floating spherical gaussian orbital model of molecular structure. i. computational procedure. lih as an example,” *J. Phys. Chem.*, vol. 47, p. 3707, 1967.
- [14] A. A. Frost, “Floating spherical gaussian orbital model of molecular structure. ii. one- and two-electron-pair systems,” *J. Phys. Chem.*, vol. 47, p. 3714, 1967.
- [15] A. A. Frost, “A floating spherical gaussian orbital model of molecular structure. iii. first-row atom hydrides,” *J. Phys. Chem.*, vol. 72, p. 1289, 1968.
- [16] A. A. Frost and R. A. Rouse, “A floating spherical gaussian orbital model of molecular structure. iv. hydrocarbons,” *J. Am. Chem. Soc.*, vol. 90, p. 1965, 1968.

- [17] A. A. Frost, R. A. Rouse, and L. Vescelius, "A floating spherical gaussian orbital model of molecular structure v. computer programs," *Int. J. Quantum Chem.*, vol. 2, no. S2, pp. 43–66.
- [18] E. Perlt, M. Brüssel, and B. Kirchner, "Floating orbital molecular dynamics simulations," *Phys. Chem. Chem. Phys.*, vol. 16, pp. 6997–7005, 2014.
- [19] E. Perlt, C. Apostolidou, M. Eggers, and B. Kirchner, "Unrestricted floating orbitals for the investigation of open shell systems," *Int. J. Chem.*, vol. 8, pp. 194–202, 2016.
- [20] B. Klahn and W. A. Bingel, "Completeness and linear independence of basis sets used in quantum chemistry," *Int. J. Quantum Chem.*, vol. 11, p. 943, 1977.
- [21] H.-J. Werner, P. J. Knowles, G. Knizia, F. R. Manby, M. Schütz, P. Celani, W. Győrffy, D. Kats, T. Korona, R. Lindh, A. O. Mitrushenkov, G. Rauhut, K. R. Shamasundar, T. B. Adler, R. D. Amos, A. Bernhardsson, A. Berning, D. L. Cooper, M. J. O. Deegan, A. J. Dobbyn, F. Eckert, E. Goll, C. Hampel, A. Hesselmann, G. Hetzer, T. Hrenar, G. Jansen, C. Köppl, Y. Liu, A. W. Lloyd, R. A. Mata, A. J. May, S. J. McNicholas, W. Meyer, M. E. Mura, A. Nicklass, D. P. O'Neill, P. Palmieri, D. Peng, K. Pflüger, R. Pitzer, M. Reiher, T. Shiozaki, H. Stoll, A. J. Stone, R. Tarroni, T. Thorsteinnsson, and M. Wang, "MOLPRO, version 2015.1, a package of ab initio programs," 2015.
- [22] A. K. Wilson, T. van Mourik, and T. H. Dunning Jr., "Gaussian basis sets for use in correlated molecular calculations. vi. sextuple zeta correlation consistent basis sets for boron through neon," *J. Mol. Struct.: THEOCHEM*, vol. 388, pp. 339–349, 1996.
- [23] H.-J. Werner, P. J. Knowles, G. Knizia, F. R. Manby, and M. Schütz, "Molpro: a general-purpose quantum chemistry program package," *WIREs Comput. Mol. Sci.*, vol. 2, pp. 241–253, 2012.
- [24] T. Helgaker, P. Jørgensen, and J. Olsen, *Molecular Electronic-Structure Theory*. Wiley, 2012.
- [25] S. Reine, T. Helgaker, and R. Lindh, "Multi-electron integrals," *WIREs: Comput. Mol. Sci.*, vol. 2, no. 2, pp. 290–303, 2012.
- [26] A. Szabo and N. S. Ostlund, *Modern Quantum Chemistry: Introduction to Advanced Electronic Structure Theory*. Courier Corporation, 2012.
- [27] S. Wilson, "Universal basis sets and cholesky decomposition of the two-electron integral matrix," *Comp. Phys. Comm.*, vol. 58, pp. 71–81, 1990.
- [28] D. W. O'Neal and J. Simons, "Application of cholesky-like matrix decomposition methods to the evaluation of atomic orbital integrals and integral derivatives," *Int. J. Quantum. Chem.*, vol. 36, pp. 673–688, 1989.
- [29] H. Koch, A. Sánchez De Merás, and T. B. Pedersen, "Reduced scaling in electronic structure calculations using Cholesky decompositions," *J. Chem. Phys.*, vol. 118, no. 21, pp. 9481–9484, 2003.
- [30] B. P. Prascher, D. E. Woon, K. A. Peterson, T. H. Dunning Jr, and A. K. Wilson, "Gaussian basis sets for use in correlated molecular calculations. vii. valence, core-valence, and scalar relativistic basis sets for Li, Be, Na, and Mg," *Theor. Chem. Acc.*, vol. 128, pp. 69–82, 2011.

10. Figure Captions

- (1) The linear combination of two equal-exponent Gaussian orbitals having $\xi < 2$, arbitrary units.
- (2) The linear combination of two equal-exponent Gaussian orbitals having $\xi > 2$, arbitrary units.
- (3) The linear combination of two equal-exponent Gaussian orbitals having $\xi = 2$, arbitrary units.
- (4) The minimum eigenvalue of the metric for a one-dimensional even-spaced infinite set of identical Gaussians as a function of γ . The inset zooms in to small values of γ . Note that values lower than one are omitted.
- (5) The minimum eigenvalue of the metric for a one-dimensional even-spaced infinite set of identical Gaussians as a function of ξ . The inset zooms in to small values of ξ .
- (6) Electronic energy error δ with respect to the position of the hydrogen atom in the box of distributed Gaussians. A total of 11 equidistant points were considered for each direction.
- (7) The H_2^+ potential energy curve as a function of the internuclear distance.

Table 1. Energy of the hydrogen atom calculated using atom-centered GTOs as a function of the harmonic ratio γ . The exact digits are underlined. The last column shows the total number of GTOs in the basis set. All energies are given in *Hartree*.

γ	Energy	# GTOs
16	- <u>0.470197942656</u>	15
8	- <u>0.491985592311</u>	19
4	- <u>0.499656436902</u>	25
2	- <u>0.499999998129</u>	43
1.8	- <u>0.499999999949</u>	51

Table 2. Energy of the hydrogen atom calculated within the LCDAO approximation for different sizes of the box. The exact digits are underlined. The d values represent the distance in *bohr* between the distributed Gaussians along the edges of the cubic mesh. The last column shows the total number of GTOs in the basis set. All energies are given in *Hartree*.

$2N + 1$	ξ			# GTOs
	1.4	1.0	0.7	
1	- <u>0.48858560</u>	- <u>0.48858560</u>	- <u>0.48858560</u>	31
3	- <u>0.49956512</u>	- <u>0.49918847</u>	- <u>0.49864904</u>	57
5	- <u>0.49990338</u>	- <u>0.49995258</u>	- <u>0.49989458</u>	155
7	- <u>0.49992076</u>	- <u>0.49999350</u>	- <u>0.49999371</u>	373
9	- <u>0.49992125</u>	- <u>0.49999431</u>	- <u>0.49999949</u>	759
11	- <u>0.49992139</u>	- <u>0.49999449</u>	- <u>0.49999987</u>	1361
13	- <u>0.49992142</u>	- <u>0.49999452</u>	- <u>0.49999989</u>	2227
d	2.2244	1.8800	1.5729	

Table 3. Dependence of the energy with respect to the atom-centered basis at three different internuclear distances of the H_2^+ dissociation curve. The exact digits are underlined and boldface digits highlight the lower energy obtained with the LCDAO approach. Energies are given in *Hartree* and distances in *bohr*.

basis	$R = 1.0$	$R = 2.0$	$R = 4.0$	# GTOs
30s	<u>-0.44648815</u>	<u>-0.60041608</u>	<u>-0.54588596</u>	1761
30s10p	<u>-0.45174444</u>	<u>-0.60248169</u>	<u>-0.54607627</u>	1821
30s10p5d	<u>-0.45178575</u>	<u>-0.60263066</u>	<u>-0.54608306</u>	1881
ref	-0.45178187	-0.60263209	-0.54603249	182

Table 4. Dependence of the energy with respect to the section of the cubic mesh at three different internuclear distances of the H_2^+ dissociation curve. The exact digits are underlined and boldface digits highlight the lower energy obtained with the LCDAO approach. Energies are given in *Hartree* and distances in *bohr*.

$2N + 1$	$R = 1.0$	$R = 2.0$	$R = 4.0$	# GTOs
3	- <u>0.45178</u> 481	- <u>0.60261</u> 706	- <u>0.54592</u> 175	369
5	- <u>0.45178</u> 574	- <u>0.60263</u> 059	- <u>0.54607</u> 888	705
7	- <u>0.45178</u> 575	- <u>0.60263</u> 063	- <u>0.54608</u> 281	1209
9	- <u>0.45178</u> 575	- <u>0.60263</u> 066	- <u>0.54608</u> 306	1881
ref	-0.45178187	-0.60263209	-0.54603249	182

Table 5. Energy of the He atom obtained using four different boxes at HF and FCI levels of theory. The exact digits are underlined. Energies are given in *Hartree*.

$2N + 1$	E_{HF}	E_{FCI}
3	− <u>2.86165904</u>	− <u>2.90347799</u>
5	− <u>2.86167782</u>	− <u>2.90350148</u>
7	− <u>2.86167842</u>	− <u>2.90350277</u>
9	− <u>2.86167844</u>	− <u>2.90350297</u>
ref	−2.86167906	−2.90350597

Table 6. FCI energy of the H^- anion obtained using five different box sizes. The exact digits are underlined. Energies are given in *Hartree*.

$2N + 1$	E_{FCI}
1	-0.393695
3	-0.490392
5	- <u>0.516930</u>
7	- <u>0.524322</u>
9	- <u>0.526522</u>
ref	-0.527685

Table 7. Ground state energies of the Be atom obtained within the LCDAO approximation for different box sizes and different methods. Exact digits are underlined. Energies are given in *Hartree*.

$2N + 1$	HF	CASSCF(2,4)	CCSD
1	-14.26856824	-14.29070144	-14.28939455
3	- <u>14.54550960</u>	-14.59399663	-14.59533382
5	- <u>14.56978700</u>	- <u>14.61263992</u>	- <u>14.61465921</u>
7	- <u>14.57233219</u>	- <u>14.61484891</u>	- <u>14.61696444</u>
ref	-14.57233763	-14.61593821	-14.61782180

Table 8. Ground state energies of the Be₄ tetramer obtained within the LCDAO approximation. for different box sizes and different methods. Exact digits are underlined and boldface digits highlight the lower energy obtained with the LCDAO approach. Energies are given in *Hartree*.

$2N + 1$	HF	CASSCF(8,10)	CCSD
1	-53.49773025	-54.01994232	-53.94998949
3	-57.99063568	-58.12724099	-58.19390694
5	-58.32481811	-58.45532242	- <u>58.53694478</u>
7	- <u>58.35101973</u>	-58.47700987	- <u>58.56181230</u>
9	- <u>58.35370692</u>	-58.47932424	- <u>58.56512124</u>
ref	-58.35445711	-58.48017161	-58.56252343

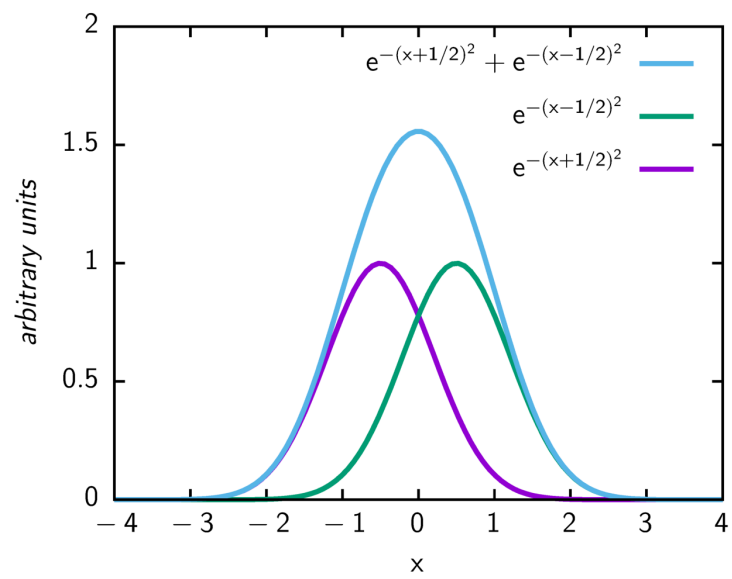


Figure 1. The linear combination of two equal-exponent Gaussian orbitals having $\xi < 2$, arbitrary units.

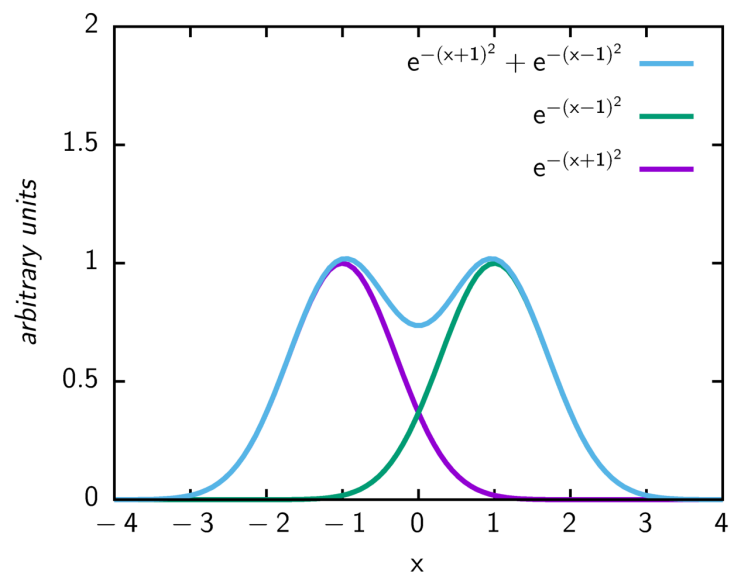


Figure 2. The linear combination of two equal-exponent Gaussian orbitals having $\xi > 2$, arbitrary units.

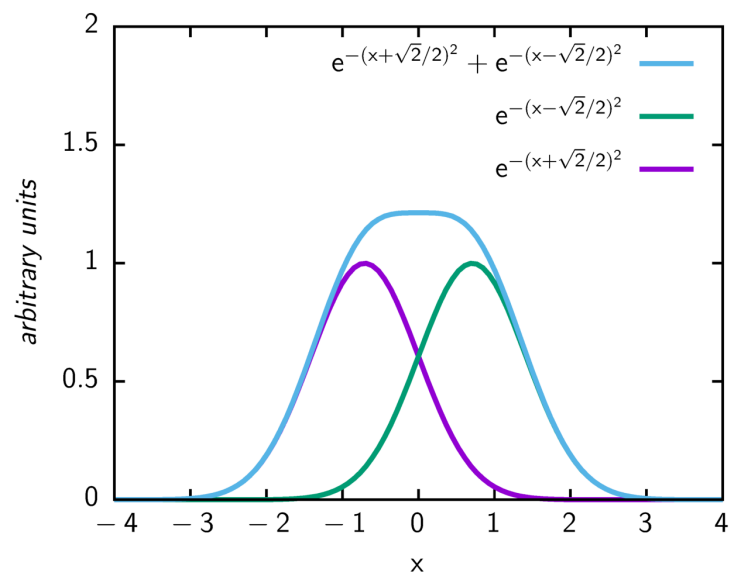


Figure 3. The linear combination of two equal-exponent Gaussian orbitals having $\xi = 2$, arbitrary units.

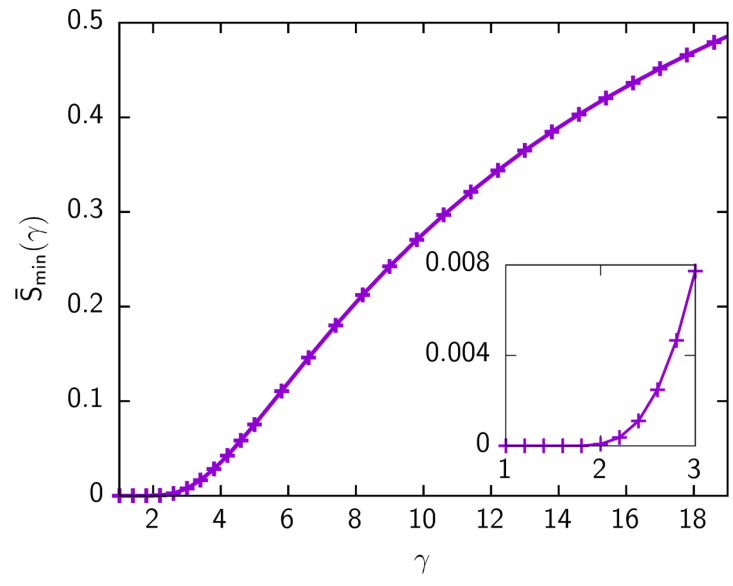


Figure 4. The minimum eigenvalue of the metric for a one-dimensional even-spaced infinite set of identical Gaussians as a function of γ . The inset zooms in to small values of γ . Note that values lower than one are omitted.

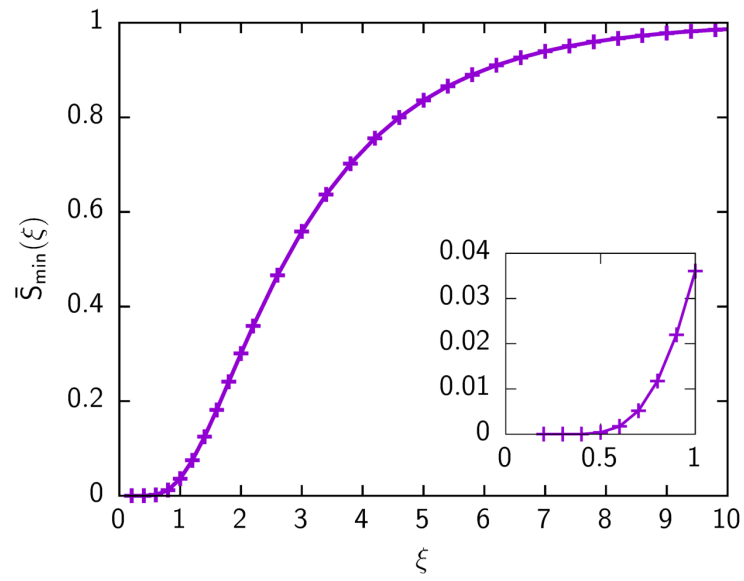


Figure 5. The minimum eigenvalue of the metric for a one-dimensional even-spaced infinite set of identical Gaussians as a function of ξ . The inset zooms in to small values of ξ .

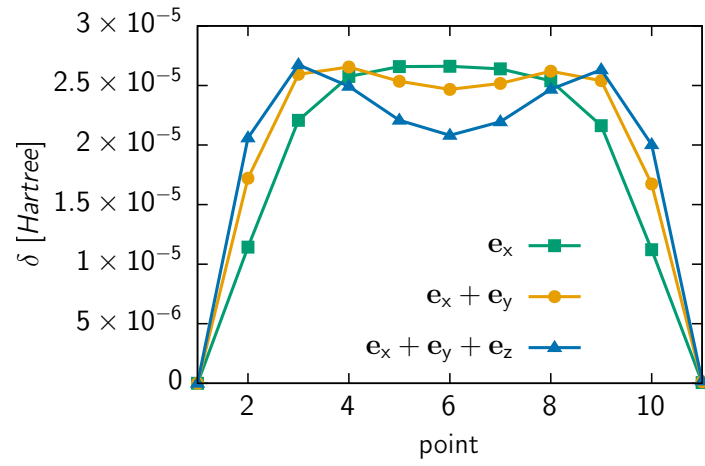


Figure 6. Electronic energy error δ with respect to the position of the hydrogen atom in the box of distributed Gaussians. A total of 11 equidistant points were considered for each direction.

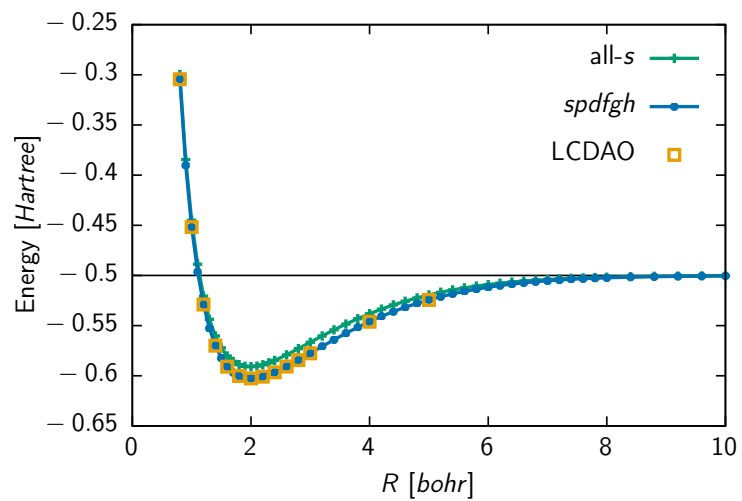


Figure 7. The H_2^+ potential energy curve as a function of the internuclear distance.

A.5 Signatures of Wigner Localization in One-dimensional Systems

The following article was published in the *Journal of Chemical Physics*, volume 148, issue 12, page 124103, 2018.

Signatures of Wigner localization in one-dimensional systems

Alejandro Diaz-Marquez,¹ Stefano Battaglia,^{1,2} Gian Luigi Bendazzoli,³
Stefano Evangelisti,^{1,a)} Thierry Leininger,¹ and J. A. Berger^{1,4,b)}

¹Laboratoire de Chimie et Physique Quantiques, IRSAMC, Université de Toulouse, CNRS, UPS,
31062 Toulouse, France

²Dipartimento di Chimica, Biologia e Biotecnologie, Università degli Studi di Perugia, Via Elce di Sotto 8,
06123 Perugia, Italy

³Università degli Studi di Bologna, Viale Risorgimento 4, I-40136 Bologna, Italy

⁴European Theoretical Spectroscopy Facility

(Received 24 November 2017; accepted 19 February 2018; published online 22 March 2018)

We propose a simple and efficient approach to study Wigner localization in one-dimensional systems using *ab initio* theory. In particular, we propose a suitable basis for the study of localization which consists of equally spaced overlapping gaussians. We illustrate our approach with full-configuration interaction which yields exact results for a given basis set. With our approach, we were able to study up to 8 electrons with full-configuration interaction. Finally, we propose the total-position spread tensor and the total electron entropy as convenient quantities to obtain signatures of Wigner localization. *Published by AIP Publishing.* <https://doi.org/10.1063/1.5017118>

I. INTRODUCTION

When electrons are confined to one dimension (1D), they exhibit remarkable physics. Well-known examples are the quantization of the conductance,^{1,2} fractional conductance,^{3,4} spin-charge separation,^{5–8} and the enhanced localization of electrons at low densities.^{8,9} Due to the latter property, these 1D systems have been shown to be interesting candidates for applications in quantum computation.^{10,11} When only few electrons are involved, these 1D systems are often referred to as Wigner molecules owing to the similarity with Wigner crystallization.^{12,13} Recently, a 2-electron Wigner molecule has been observed experimentally.¹⁴

To treat Wigner molecules numerically, two problems have to be overcome: (i) the non-integrable singularity of the 1D Coulomb potential in the origin^{15–18} and (ii) the lack of a suitable basis in which to express the many-body wave function. In particular, the two most common types of basis sets, i.e., atom-centered basis functions and plane waves, are not convenient. The first problem can be circumvented by modeling the system in three dimensions, in which there is no problem to integrate the Coulomb potential, as a cylinder of infinite length and a radius so small that the transverse motion of the electrons is frozen in the lowest energy state.¹⁹ In this work, we will address the second problem.

Theoretically, Wigner localization can be studied either through phenomenological effective Hamiltonians¹⁴ or by using the non-relativistic electronic *ab initio* Hamiltonian. In almost all studies on finite Wigner systems, the former option is chosen (see, e.g., Refs. 20 and 21), and the phenomenological effective Hamiltonian contains an external potential, often having a harmonic component, to confine the system. The

molecular orbitals (MO's) of the system are then obtained by diagonalizing a one-electron Hamiltonian, given by the kinetic energy plus the confining potential. This is an appropriate strategy for few electrons in a harmonic well. However, it can lead to computational difficulties if the number of electrons (and hence the number of MO's) is large or if the electrons are confined in a spatial region by a very steep potential. This is the case of electrons in boxes of different shapes. In fact, the MO's quickly become strongly oscillating (in 1D systems, the *n*th excited state has *n* nodes), which can be a source of numerical instabilities.

Therefore, in this work we propose to study the non-relativistic electronic *ab initio* Hamiltonian without any *explicit* external potential. Instead, we use a set of equidistant localized orbitals that are distributed in the region of the space where the electrons are confined. This induces an *implicit confining potential* which originates from the basis set itself. We choose the localized orbitals as simple *1s* gaussian orbitals with a common exponent, and electric neutrality is guaranteed by a background of equidistant fractional positive charges. The main advantage of our approach is that, with minor modifications, all standard quantum-chemistry codes can be used to study Wigner localization, since they all deal with gaussian MO's, and the positive background can be realized by placing fractional point charges in the region occupied by the orbitals. Any quantum chemistry approach can thus be used to study Wigner localization. However, since Wigner molecules of few electrons can be treated exactly, we will illustrate our approach mainly with full-configuration interaction (FCI).

Finally, in this work we propose several indicators for the study of localization. Apart from the electron density, we find signatures of Wigner localization also in the total-position spread (TPS) tensor, which is linked to the conductivity as well as the total electron entropy.

^{a)}Electronic mail: stefano.evangelisti@irsamc.ups-tlse.fr

^{b)}Electronic mail: arjan.berger@irsamc.ups-tlse.fr

The manuscript is organized as follows. In Sec. II, we describe the formalism of our approach, while in Sec. III, we discuss the computational details. In Sec. IV, we show and discuss our results, and we draw our conclusions in Sec. V.

II. FORMALISM

In this work, we make use of quantum-chemistry approaches to study the localization of electrons confined in one dimension. In particular, we use the restricted open-shell Hartree-Fock (ROHF) method and full-configuration interaction (FCI) in order to expand the wave function. The FCI expansion is obtained by considering all the Slater determinants that can be generated within a given set of one-electron functions (spin orbitals). The Hamiltonian is the *ab initio* non-relativistic electronic operator describing the kinetic energy and the Coulomb interactions which consists of the electron-background attraction and the electron-electron repulsion.

We choose the orbitals to be equally spaced *s*-type gaussian orbitals with a common exponent and whose equally spaced centers are placed in the region of space where the electrons are confined (in our particular case, we choose the *z* axis). We note that such a 1D arrangement of gaussian orbitals realizes the regularization procedure that is required to treat a 1D Coulomb potential.¹⁹ In fact, the transverse (i.e., orthogonal to the *z* axis) part of the wave function has a gaussian form, as it happens for an electron confined in a harmonic radial potential. It should be noticed that the present approach is able to recover the (analytical) high-density results of the Fermi-gas region, showing the viability of this quantum-chemistry treatment of a set of confined electrons.

The most straightforward way to investigate electron localization in a system with open boundary conditions (OBC's), i.e., a system without translational invariance, is by computing its electron density, given by the diagonal part of the one-body reduced density matrix. Besides the density, we study two other quantities that give information about electron localization and correlation: the total-position spread (TPS) tensor Λ and the total electronic entropy S . The TPS tensor is defined as the second-moment cumulant of the total position operator $\hat{\mathbf{R}}$ according to

$$\Lambda = \langle \Psi | \hat{\mathbf{R}}^2 | \Psi \rangle - \langle \Psi | \hat{\mathbf{R}} | \Psi \rangle^2, \quad (1)$$

where $\hat{\mathbf{R}}$ is defined as

$$\hat{\mathbf{R}} = \sum_{\mu=1}^N \mathbf{r}_{\mu} \quad (2)$$

in which N is the number of electrons. We note that the purpose of the second term in Eq. (1) is to ensure gauge invariance. The *per-electron* TPS tensor is the localization tensor $\lambda = \Lambda/N$ which was introduced by Resta and co-workers^{22,23} following an original idea of Kohn²⁴ (see also Ref. 25). The localization tensor differentiates the behavior of conductors and insulators: in the limit $N \rightarrow \infty$, it diverges for conductors, while it remains finite in the case of insulators.

For this reason, a qualitatively different behavior of the localization tensor is expected in the Fermi-liquid and Wigner-crystal regimes of the electron gas. The localization tensor has

been used to investigate the metallic behavior of finite clusters, at both the *ab initio*^{26–28} and semi-empirical^{29–34} level.

Electron correlation can be related to the natural occupation numbers.³⁵ Therefore, the electron entropy has been proposed as a measure of the presence of correlation in a system.^{36,37} In the case of a pure state described by a wave function Ψ , the particle-hole entropy is defined as

$$S = - \sum_{j=1}^M \left[n_j \ln n_j + (1 - n_j) \ln(1 - n_j) \right], \quad (3)$$

where the sum runs over the M natural spin orbitals of Ψ and n_j is the occupation number of spin orbital j . The first and second terms in the summation are the electron and hole contributions, respectively, to the total entropy. While the entropy of a single determinant is zero, the entropy has its maximum value when all the spin orbitals have equal occupation numbers. For this reason, we expect a very small entropy for the Fermi gas and a much larger entropy in the Wigner regime. In particular, this will be the case for the $S_z = 0$ wave functions because of the large number of Slater determinants that contribute to the wave function with similar weight.

In analogy with the standard quantum-chemistry notation, we will use the expressions “atomic orbital” (AO) and “molecular orbital” in order to indicate, respectively, the primitive non-orthogonal orbitals that are used as a basis set in which we expand the wave function and the orbitals that result from the diagonalization of the Hamiltonian of the system. As is common practice in quantum chemistry, we will use gaussian orbitals for the primitive basis set. In this work, the primitive atomic orbitals (AO's), which we use to expand the molecular orbitals (MO's), are normalized three-dimensional *s*-type gaussian functions, all having a single common exponent α ,

$$\phi_{\alpha, \mathbf{r}_0}(\mathbf{r}) = (2\alpha/\pi)^{3/4} \exp(-\alpha \|\mathbf{r} - \mathbf{r}_0\|^2), \quad (4)$$

where \mathbf{r}_0 is the position of the center of the gaussian orbital.

In order to describe a smoothly varying function in an accurate way, two gaussians must be relatively close together. Therefore, the overlap between two normalized gaussians plays a crucial role in defining a suitable expansion basis set. The overlap S between two normalized gaussians having a common exponent α and with a distance δ between their two centers depending on the dimensionless quantity $\xi = \alpha\delta^2$ only. It is given by the expression

$$S(\alpha, \delta) = S(\xi) = \exp(-\xi/2). \quad (5)$$

A set of sufficiently overlapping gaussian orbitals is able to describe a smoothly varying function in a very accurate way. In order to obtain an accurate description of the wave function, two neighboring gaussians must have a large overlap and, therefore, ξ must be small. In particular, if $\xi > 2$, the sum of the two gaussians which have the same weight yields a function with two peaks, which is unsuitable to provide a smooth description of a wave function. On the other hand, if ξ is too small, and hence the overlap too large, one runs into the problem of a quasi-linear dependent basis set, which can lead to numerical instabilities. In this work, we choose to work with a fixed value for ξ . This means that the width of the gaussian is proportional to the distance between two neighboring

centers. More precisely, we will use the value $\xi = 1$. Previous investigation has shown that this value can recover the energy levels of, for example, a harmonic oscillator with a very high accuracy.³⁸

III. COMPUTATIONAL DETAILS

In this work, we use $g + 1$ equally spaced gaussians in order to describe a single electron confined in a 1D region of the space. If the electron is placed in a region of the z axis of length L , namely, $-L/2 < z < L/2$, the first gaussian will be placed at $z = -L/2$ and the last one at $z = L/2$. In such a way, the distance between two centers is given by $\delta = L/g$. In Fig. 1, the gaussians used to describe a single electron are shown for the case $g = 12$ and $\xi = 1$. We note that, since we choose ξ to be a constant, the length units on the bottom axis in Fig. 1 are arbitrary. By analogy, a total of $Ng + 1$ orbitals are needed to describe N electrons in a region of length NL . In numerical calculations, the choice of g plays a crucial role since the size of the FCI space becomes quickly unmanageable for large values of Ng . We performed benchmark FCI calculations for two and four electrons with $g = 12$. These calculations were used to assess the quality of results obtained with $g = 4$. We verified that by going from $g = 12$ to $g = 4$, the numerical differences are negligible and the qualitative overall picture is left unchanged. In this way, by using such a small value of g , we were able to study systems with 2–8 electrons within the FCI method.

We use a set of point-like fractional positive charges, uniformly distributed on the z axis, in order to simulate the jellium uniform background. The first and last charges of the set coincide with the centers of the first and last gaussian. The point-like charges have been chosen with the same procedure as the gaussian centers. In particular, we used a number of $q + 1$ charges for a segment of length L and hence $Nq + 1$ for the N -electron system. The values of these charges are chosen in such a way to have a system that is globally neutral. This means that each charge has a value of $+N/(Nq + 1)$ in atomic units. We verified that a value of q of the order of ten is needed

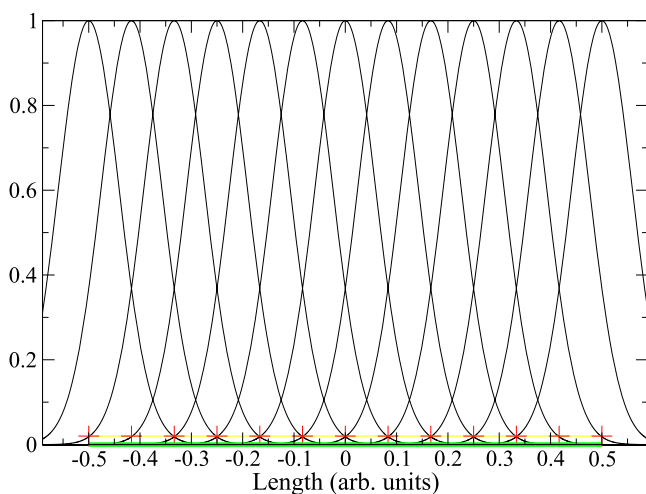


FIG. 1. Example of the tiling of a segment of length $L = 1$ with gaussians to describe 1 electron ($g = 12$). Continuous lines (black): the gaussian functions; plus symbols (red): positions of the fractional positive point charges.

in order to have a converged electronic wave function. For this reason, and to have a maximum number of the point charges coincide with the gaussian centers for the case $g = 12$, all the calculations presented in this work have been obtained by setting $q = 12$.

All the calculations reported in this work have been performed with the packages Neptunus^{39–41} and Molpro.^{42,43} The former is an FCI algorithm that uses the MO integrals computed by the DALTON software package.⁴⁴ It has been used for calculations with $N = 2, 3, 4$ and $g = 12$. For larger number of electrons, the FCI wave function was obtained by using the complete active space self-consistent field (CASSCF) algorithm of the Molpro package.^{45,46}

IV. RESULTS AND DISCUSSION

We express all our results as a function of the formal mean distance d between two electrons, $d = L/N$. We note that d should not to be confused with the mean value of the interelectronic-distance operator. The mean distance d is the inverse of the electron density and twice the Wigner-Seitz radius r_s of the 1D system. We investigated the behavior of the system from an extremely high-density regime ($d = 0.01$ Bohr) to a very low-density regime ($d = 100$ Bohr).

In this work, we focus on the following two spin wave functions:

1. the high-spin (HS) solution, $S_z = N/2$, having a maximum spin multiplicity equal to $N + 1$;
2. the low-spin (LS) solution, $S_z = 0$, for an even number of electrons, having a spin multiplicity equal to one.

To verify our computational approach, we first consider the high-density limit. Since the electron-electron repulsion and, more generally, all the Coulomb interactions present in the system scale as $1/d$, while the kinetic energy of an individual electron scales as $1/d^2$, in the high-density limit, $d \rightarrow 0$, the Coulomb interaction becomes negligible with respect to the kinetic contribution. Therefore the electrons behave as a gas of free non-interacting particles and the wave function of the system becomes the wave function of a set of free fermions in a 1D box, whose behavior is analytically known. For this reason, it is possible to check the quality of our computational approach by comparing our numerical results with analytical expressions.

In Fig. 2, the energy difference per electron between the HS and LS solution as a function of the mean distance d is reported on a bilogarithmic scale. The energy of the LS wave function is below the HS wave function for all values of d in the considered interval. At high density, where the system is well described by a Fermi gas, an analytical expression for the energy difference can be derived from the energy levels of a particle in a 1D box of length L . They are given by the expression $\epsilon_n = n^2\pi^2/2L^2$. By summing the levels of the occupied orbitals in the HS and LS cases and using the identity $\sum_{n=1}^N n^2 = N(N+1)(2N+1)/6 \simeq N^3/3$ for large N , we obtain, for large values of n , the following asymptotic expression:

$$\Delta E/N = (E_{HS} - E_{LS})/N = \pi^2/8d^2. \quad (6)$$

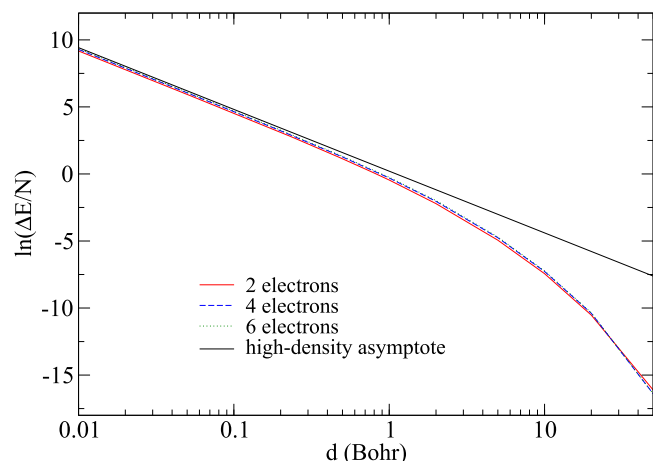


FIG. 2. The natural logarithm of the HS-LS energy-difference per electron obtained within FCI as a function of the mean distance d (please note the logarithmic scale).

We see that in the high-density limit, $d \rightarrow 0$, our numerical results agree with the analytical result. We note that the differences between the various curves for different values of N are not appreciable due to the logarithmic scale.

Now that we have validated our approach we will study the electron localization in the low-density regime. In Figs. 3–6, we report the FCI electron density of the system with six electrons, for both the LS and HS wave functions and for four different values of d : 0.1, 1.0, 10.0, and 100.0 Bohr. We see that for $d = 0.1$ and $d = 1.0$ Bohr, the density is almost a constant and similar to the density of six non-interacting electrons in a one-dimensional box. Indeed, six peaks are observed in the HS case and only three (because of the double occupation of the orbitals) are observed in the LS case. Between $d = 1.0$ and $d = 10.0$ Bohr, the charge distribution completely changes: In the latter case there are six peaks in both the HS and LS cases, separated by deep valleys. At the largest distance shown, $d = 100.0$ Bohr, the density at the bottom of the valleys is almost vanishing, and there is no noticeable difference between the HS and LS densities.

Instead of studying the density for various values of d , it would be more practical to study a single function of d that

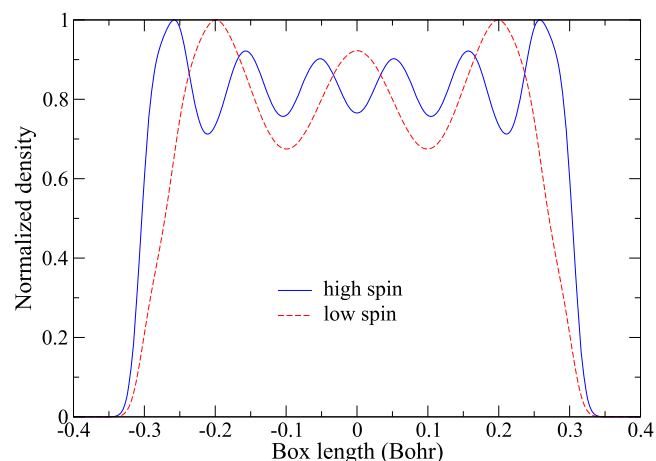


FIG. 3. The electron density for $d = 0.1$ Bohr.

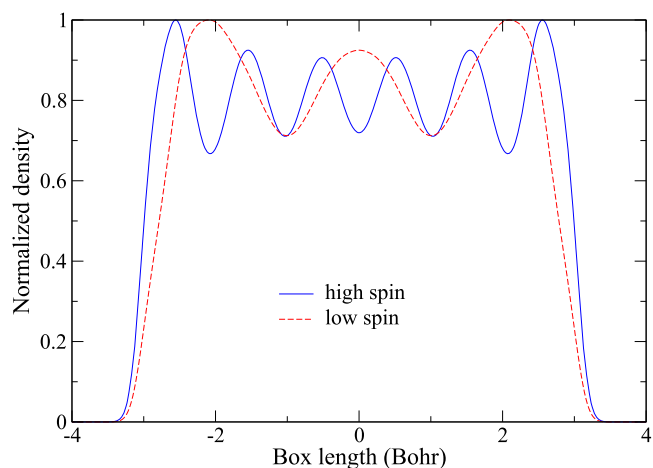


FIG. 4. The electron density for $d = 1.0$ Bohr.

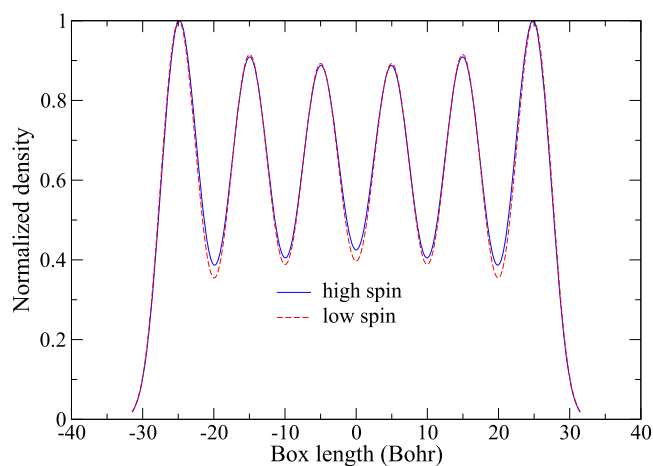


FIG. 5. The electron density for $d = 10.0$ Bohr.

contains similar information about the electron localization. In Fig. 7, we report the values of the HS localization tensor λ for both ROHF and FCI. In order to compare results related to different box sizes, the localization tensor has been divided by d^2 . We note that λd^2 is a dimensionless quantity. There are two important conclusions that can be drawn. First, Fig. 7

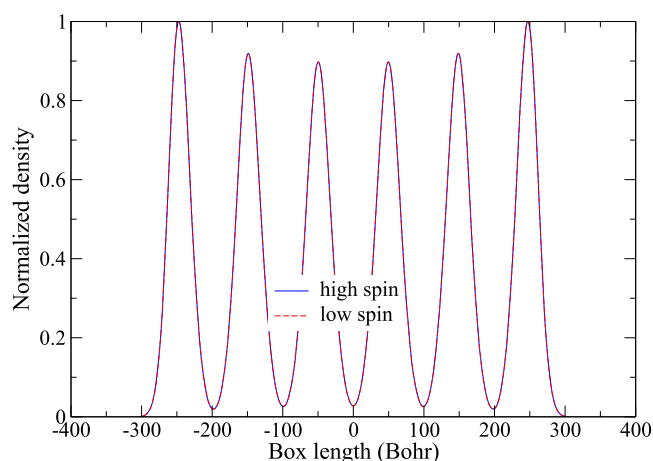


FIG. 6. The electron density for $d = 100.0$ Bohr.

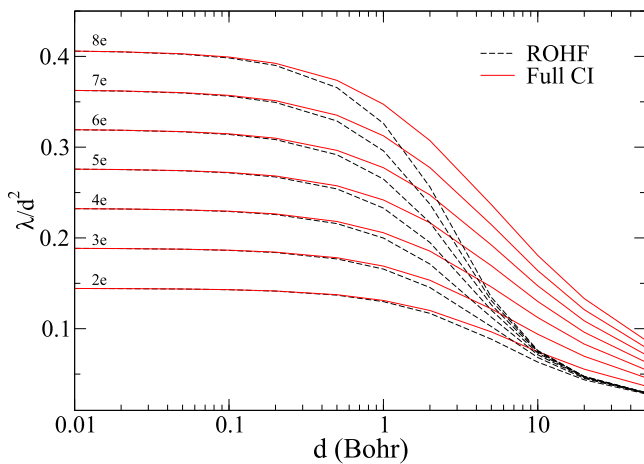


FIG. 7. The scaled HS localization tensor λ/d^2 as a function of the mean distance d (please note the logarithmic scale).

shows a striking decrease of λ/d^2 in the region between $d = 1.0$ and $d = 10.0$ Bohr, which corresponds to the localization that we observed for the electronic density. Therefore, the sudden decrease of λ/d^2 can be considered a signature of Wigner localization. Second, Fig. 7 demonstrates the importance of the accurate treatment of electron correlation in the low-density regime. At high densities, the ROHF and FCI results coincide and become equal to the free-electron high-density limit, as they should. Moreover, in the high-density regime, $d < 1.0$ Bohr, the value of λ/d^2 for both ROHF and FCI is roughly proportional to N , as one would expect for a conducting electron gas. Instead, in the low-density regime the ROHF and FCI results are completely different. The ROHF localization tensor becomes independent of the number of electrons for large d , which would indicate an insulating behavior. However, the FCI localization tensor, i.e., λ/d^2 , is proportional to N also in the low-density regime, indicating the presence of conduction. Therefore, despite the fact that the electrons are localized, the localization tensor shows a behavior that corresponds to a conducting state at least up to $d = 50$ Bohr.

In Fig. 8, the LS and HS FCI values of the localization tensor are compared. For high densities, the LS values are

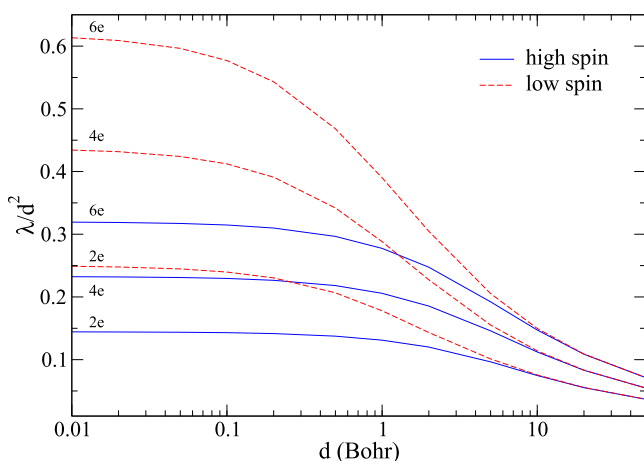


FIG. 8. The scaled FCI localization tensor λ/d^2 as a function of the mean distance d (please note the logarithmic scale).

considerably larger than the HS ones since for the latter case the electron mobility is reduced due to Pauli repulsion. Beyond $d = 10$ Bohr, however, the two sets of curves become perfectly superposed, as one would expect for localized electrons that differ only in their spin coupling.

In Fig. 9, we report the electronic total, i.e., particle+hole, entropy *per electron* as a function of the number of electrons for the lowest HS and LS states. We note that, since the entropy, in general, depends on the spin projection, for the HS state, we report the values for the $S_z = 0$ and $S_z = \max$ components. In all cases, the entropy increases between $d = 1.0$ and $d = 10.0$ Bohr, corresponding to the region in which the electrons become localized. Therefore, the sudden increase of the total entropy can also be considered as a signature of Wigner localization. As mentioned before, the entropy of a single Slater determinant is identically zero, while a nonzero value for S/N means that some kind of correlation is present.

Electron correlation is traditionally split into a dynamical and a non-dynamical (or static) part. Although there is not a clear-cut distinction between the two components, several definitions have been proposed.⁴⁷⁻⁵⁰ We do not want to give an additional definition here. However, broadly speaking, one can say that non-dynamical correlation is a phenomenon associated with the presence of many roughly equivalent Slater determinants in the zero-order description of the wave function. The dynamical part, on the other hand, is related to the huge number of determinants (each one giving a small contribution) that are needed for a correct description of the Coulomb hole in the wave function. In the following discussion, we will use this qualitative distinction between dynamical and non-dynamical correlation.

It is interesting to relate the entropy, as shown in Fig. 9, to the presence of the two types of correlation. Both the LS and HS ($S_z = \max$) FCI entropies vanish for small values of d , i.e., in the Fermi-gas regime, since in both cases the wave function is well represented by the ROHF Slater determinant. This situation corresponds to the absence of both types of correlations. The HS ($S_z = \max$) entropy, on the other hand, goes to a relatively large finite limit when $d \rightarrow 0$. This is due to the fact that many Slater determinants are needed to describe the

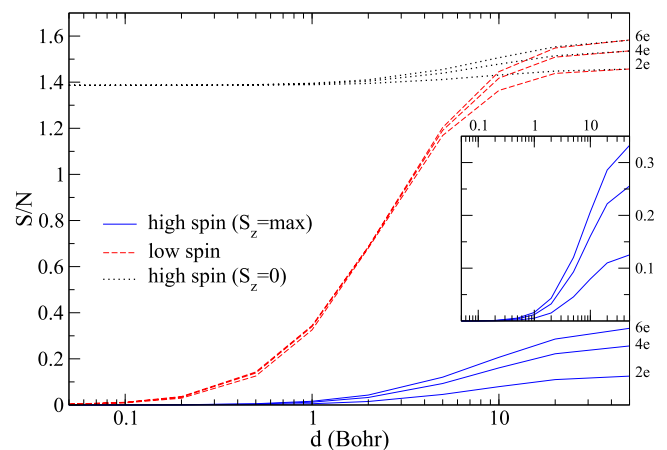


FIG. 9. The total electronic entropy per electron S/N as a function of the mean distance d (please note the logarithmic scale). Inset: a zoom of the entropy of the HS state ($S_z = \max$).

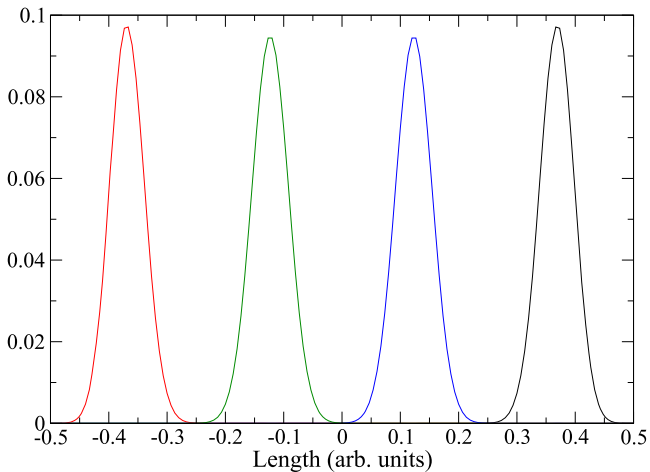


FIG. 10. Four localized orbitals having the largest occupation numbers for the case $N = 4$. Pairs of corresponding orbitals having g and u symmetries have been combined in order to obtain completely localized combinations.

wave function despite the fact that we are in the large-density limit where the Coulomb interactions become negligible with respect to the kinetic energy. This corresponds to the presence of non-dynamical correlation since dynamical correlation is absent. It can be verified from Eq. (3) that the total entropy of N electrons evenly distributed into $2N$ spin orbitals is given by $2N \ln 2$. Therefore, the entropy of the HS($S_z = 0$) state converges towards $2N \ln 2$ in the limit $d \rightarrow 0$ and the entropy per electron converges to $S/N = 2 \ln 2 = 1.386 294$ in this limit. From Fig. 9, we see that the entropies for the LS and the HS($S_z = 0$) state become identical for medium-large distances, when each electron tends to be well localized in space. In this case, the $S_z = 0$ wave functions are dominated by determinants with localized electrons having an equal probability of α and β spins, and the value of $2 \ln 2$ can be interpreted as the entropy per electron due to non-dynamical correlation. The difference $S/N - 2 \ln 2$ can therefore be interpreted as the contribution to the entropy per electron that is due to dynamical correlation.

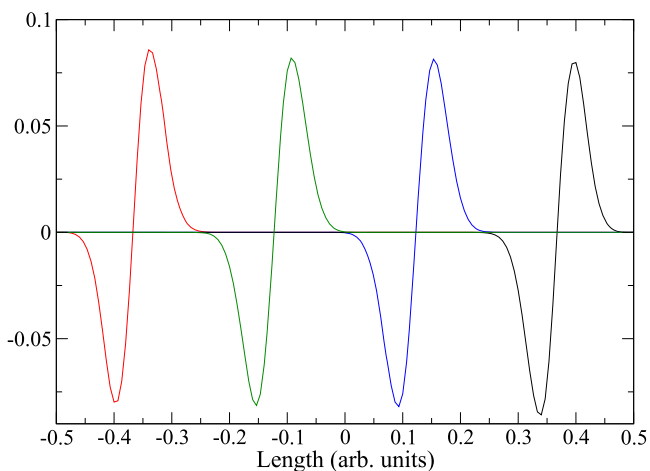


FIG. 11. Four localized orbitals having the 5th to 8th largest occupation numbers for the case $N = 4$. Pairs of corresponding orbitals having g and u symmetries have been combined in order to obtain completely localized combinations.

Because of the $D_{\infty h}$ symmetry of the systems we study here, the natural orbitals are partly delocalized symmetry-adapted pairs, having g and u symmetries. However, by performing a simple combination of the orbitals that correspond to g and u symmetries, we obtain completely localized orbitals. The localized orbitals that account for the overwhelming part of the occupation numbers are symmetric (the most important ones) and antisymmetric orbitals. In the language of three-dimensional atomic orbitals, they correspond to s - and p -type orbitals, respectively. In Fig. 10, localized orbitals corresponding to the four largest occupation numbers are shown. They are s -type orbitals and account for more than 90% of the total orbital occupation numbers. In Fig. 11, localized orbitals corresponding to the four next-largest occupation numbers are shown. They are p -type orbitals that are located in the same region as the s -type orbitals.

V. CONCLUSIONS

We studied the behavior of a small number of electrons confined to a quasi-1D arrangement by the basis set used to expand their wave function. At high density, the wave function of the system is similar to the one of a free-electron system. However, by lowering the density, there is a complete change of the wave function structure. The electrons change from a state where they are essentially delocalized, and well described by a single Slater determinant, to a state where they are localized at fixed positions in space. This is true for both the high-spin and low-spin states.

We obtained a deeper insight in the nature of electron localization by studying the localization tensor and the electron entropy. Indeed, by lowering the electron density, we observe a sudden growth of the entropy and a corresponding drop of the position spread in the density regime where the electrons localize. The drop of the position spread indicates a reduced mobility of the electrons with respect to the Fermi-gas solution. This behavior is a signature of Wigner localization and is reminiscent of the Wigner crystallization in finite systems (Wigner atoms).

The increase of the electronic entropy also indicates that the low-density state is much more correlated than the Fermi-gas state, which tends to a single determinant (zero correlation) in the limit of very high densities. This behavior is not surprising for the low-spin state since a large amount of non-dynamical correlation is needed to account for the multi-determinant singlet wave function. The picture is less obvious in the case of the high-spin solution that is strongly dominated by the high- $|S_z|$ single determinant. Nevertheless, a relatively large amount of dynamical correlation is still present in the localized state, essentially carried by a single p -type orbital located on top of each localized s orbital, even at relatively large distances.

The present investigation shows the usefulness of a quantum-chemistry approach to treat a collection of interacting particles confined to a region of space. Finally, we stress that our method is not restricted to the n -D jellium model but could be used to treat electrons in different confining potentials such as quantum dots.

ACKNOWLEDGMENTS

This work has received funding from the European Union's Horizon 2020 research and innovation programme under the Marie Skłodowska-Curie Grant Agreement No. 642294. The calculations of this work have been partly performed by using the resources of the HPC center CALMIP under Grant No. 2016-p1048. One of us (A.D.M.) acknowledges the support of the "Theoretical Chemistry and Computational Modelling" (TCCM) Erasmus-Plus Master program. This work was supported by the Programme Investissements d'Avenir under the Program No. ANR-11-IDEX-0002-02, Reference No. ANR-10-LABX-0037-NEXT. The authors would like to thank Paola Gori-Giorgi and Pierre-François Loos for fruitful discussions.

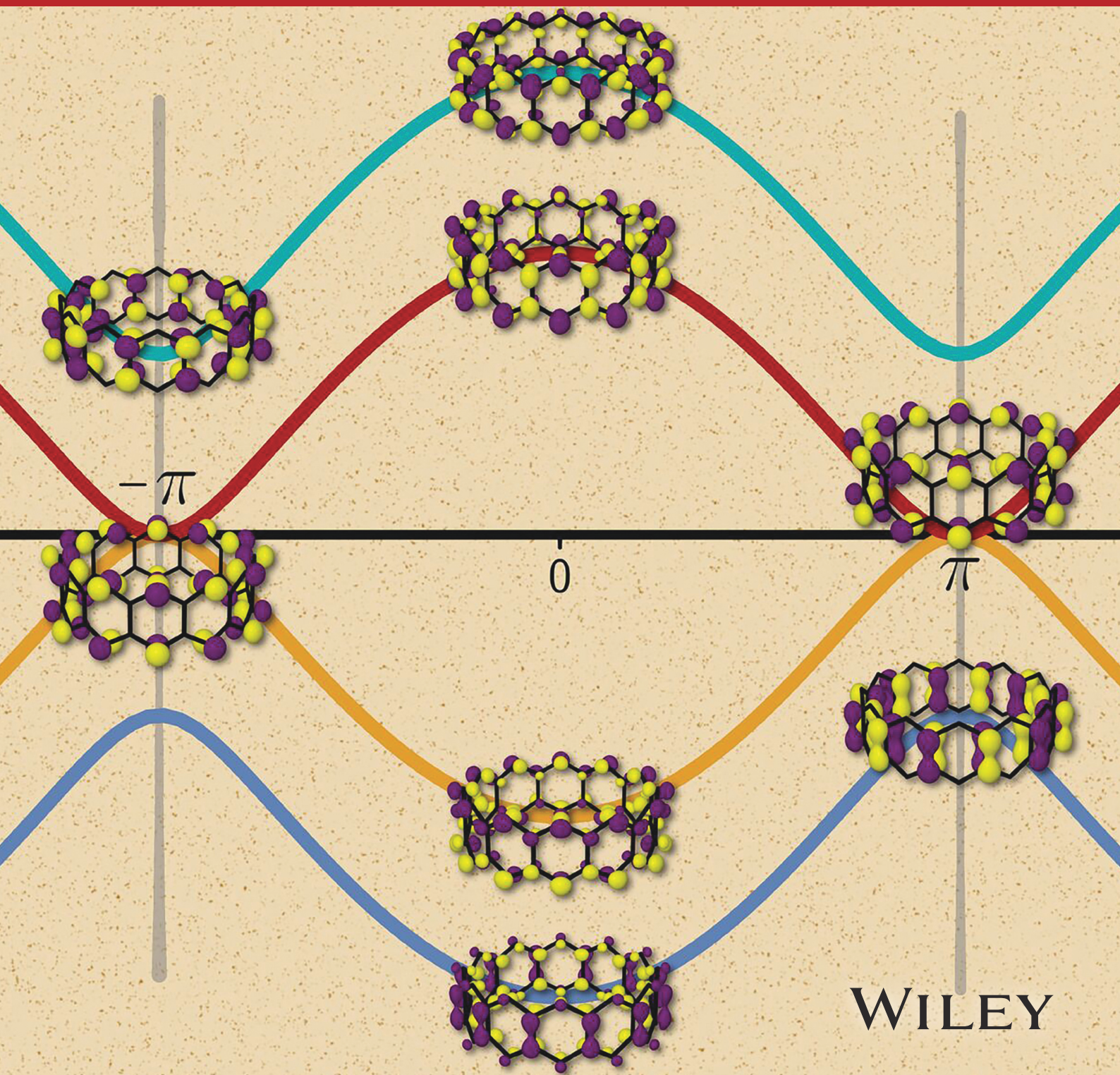
- ¹B. J. van Wees, H. van Houten, C. W. J. Beenakker, J. G. Williamson, L. P. Kouwenhoven, D. van der Marel, and C. T. Foxon, *Phys. Rev. Lett.* **60**, 848 (1988).
- ²D. A. Wharam, T. J. Thornton, R. Newbury, M. Pepper, H. Ahmed, J. E. F. Frost, D. G. Hasko, D. C. Peacock, D. A. Ritchie, and G. A. C. Jones, *J. Phys. C: Solid State Phys.* **21**, L209 (1988).
- ³K. J. Thomas, J. T. Nicholls, M. Y. Simmons, M. Pepper, D. R. Mace, and D. A. Ritchie, *Phys. Rev. Lett.* **77**, 135 (1996).
- ⁴K. J. Thomas, J. T. Nicholls, N. J. Appleyard, M. Y. Simmons, M. Pepper, D. R. Mace, W. R. Tribe, and D. A. Ritchie, *Phys. Rev. B* **58**, 4846 (1998).
- ⁵S.-i. Tomonaga, *Prog. Theor. Phys.* **5**, 544 (1950).
- ⁶J. M. Luttinger, *J. Math. Phys.* **4**, 1154 (1963).
- ⁷F. D. M. Haldane, *J. Phys. C: Solid State Phys.* **14**, 2585 (1981).
- ⁸O. Auslaender, H. Steinberg, A. Yacoby, Y. Tserkovnyak, B. Halperin, K. Baldwin, L. Pfeiffer, and K. West, *Science* **308**, 88 (2005).
- ⁹H. Steinberg, O. M. Auslaender, A. Yacoby, J. Qian, G. A. Fiete, Y. Tserkovnyak, B. I. Halperin, K. W. Baldwin, L. N. Pfeiffer, and K. W. West, *Phys. Rev. B* **73**, 113307 (2006).
- ¹⁰V. V. Deshpande and M. Bockrath, *Nat. Phys.* **4**, 314 (2008).
- ¹¹J. M. Taylor and T. Calarco, *Phys. Rev. A* **78**, 062331 (2008).
- ¹²E. Wigner, *Phys. Rev.* **46**, 1002 (1934).
- ¹³J. Jang, B. M. Hunt, L. N. Pfeiffer, K. W. West, and R. C. Ashoori, *Nat. Phys.* **13**, 340 (2016).
- ¹⁴S. Pecker, F. Kuemmeth, A. Secchi, M. Rontani, D. Ralph, P. L. McEuen, and S. Ilani, *Nat. Phys.* **9**, 576 (2013).
- ¹⁵L. Calmels and A. Gold, *Phys. Rev. B* **56**, 1762 (1997).
- ¹⁶S. Bednarek, B. Szafran, T. Chwiej, and J. Adamowski, *Phys. Rev. B* **68**, 045328 (2003).
- ¹⁷P. F. Loos and P. M. W. Gill, *Phys. Rev. Lett.* **108**, 083002 (2012).
- ¹⁸P. F. Loos and P. M. W. Gill, *J. Chem. Phys.* **138**, 164124 (2013).
- ¹⁹G. F. Giuliani and G. Vignale, in *Quantum Theory of the Electron Liquid* (Cambridge University Press, 2005), Appendix A.
- ²⁰M. Rontani, C. Cavazzoni, D. Bellucci, and G. Goldoni, *J. Chem. Phys.* **124**, 124102 (2006).
- ²¹F. Malet, A. Mirtschink, J. C. Cremon, S. M. Reimann, and P. Gori-Giorgi, *Phys. Rev. B* **87**, 115146 (2013).
- ²²R. Resta, *Rev. Mod. Phys.* **66**, 899 (1994).
- ²³R. Resta, *J. Chem. Phys.* **124**, 104104 (2006).
- ²⁴W. Kohn, *Phys. Rev.* **133**, A171 (1964).
- ²⁵E. Kudinov, *Fizika Tverdogo Tela* **33**, 2306 (1991).
- ²⁶V. Vetere, A. Monari, G. L. Bendazzoli, S. Evangelisti, and B. Paulus, *J. Chem. Phys.* **128**, 024701 (2008).
- ²⁷G. L. Bendazzoli, S. Evangelisti, and A. Monari, *Int. J. Quantum Chem.* **111**, 3416 (2011).
- ²⁸E. Giner, G. L. Bendazzoli, S. Evangelisti, and A. Monari, *J. Chem. Phys.* **138**, 074315 (2013).
- ²⁹A. Monari, G. L. Bendazzoli, and S. Evangelisti, *J. Chem. Phys.* **129**, 134104 (2008).
- ³⁰S. Evangelisti, G. L. Bendazzoli, and A. Monari, *Theor. Chem. Acc.* **126**, 257 (2010).
- ³¹G. L. Bendazzoli, S. Evangelisti, A. Monari, and R. Resta, *J. Chem. Phys.* **133**, 064703 (2010).
- ³²G. L. Bendazzoli, S. Evangelisti, and A. Monari, *Int. J. Quantum Chem.* **112**, 653 (2012).
- ³³M. El Khatib, O. Brea, E. Fertitta, G. L. Bendazzoli, S. Evangelisti, T. Leininger, and B. Paulus, *Theor. Chem. Acc.* **134**, 29 (2015).
- ³⁴E. Fertitta, M. E. Khatib, G. L. Bendazzoli, B. Paulus, S. Evangelisti, and T. Leininger, *J. Chem. Phys.* **143**, 244308 (2015).
- ³⁵S. D. Sabatino, J. A. Berger, L. Reining, and P. Romaniello, *J. Chem. Phys.* **143**, 024108 (2015).
- ³⁶P. Gori-Giorgi and P. Ziesche, *Phys. Rev. B* **66**, 235116 (2002).
- ³⁷A. D. Gottlieb and N. J. Mauser, *Phys. Rev. Lett.* **95**, 123003 (2005).
- ³⁸L. Brooke, A. Diaz-Marquez, T. Leininger, P. F. Loos, N. Suaud, S. Evangelisti, and J. A. Berger, "Localized electrons without an explicit confining potential" (unpublished).
- ³⁹G. L. Bendazzoli and S. Evangelisti, *J. Chem. Phys.* **98**, 3141 (1993).
- ⁴⁰L. Gagliardi, G. L. Bendazzoli, and S. Evangelisti, *J. Comput. Chem.* **18**, 1329 (1997).
- ⁴¹NEPTUNUS is a Quantum-Chemistry FORTRAN code for the calculation of FCI and CAS-CI energies and properties written by G. L. Bendazzoli and S. Evangelisti, with contributions from L. Gagliardi, E. Giner, A. Monari, F. Passerini, and M. Verdicchio.
- ⁴²H.-J. Werner, P. J. Knowles, G. Knizia, F. R. Manby, and M. Schütz, *Wiley Interdiscip. Rev.: Comput. Mol. Sci.* **2**, 242 (2012).
- ⁴³H.-J. Werner, P. J. Knowles, G. Knizia, F. R. Manby, M. Schütz, P. Celani, W. Györfy, D. Kats, T. Korona, R. Lindh, A. Mitrushenkov, G. Rauhut, K. R. Shamasundar, T. B. Adler, R. D. Amos, A. Bernhardsson, A. Berning, D. L. Cooper, M. J. O. Deegan, A. J. Dobson, F. Eckert, E. Goll, C. Hampel, A. Hesselmann, G. Hetzer, T. Hrenar, G. Jansen, C. Köppl, Y. Liu, A. W. Lloyd, R. A. Mata, A. J. May, S. J. McNicholas, W. Meyer, M. E. Mura, A. Nicklass, D. P. O'Neill, P. Palmieri, D. Peng, K. Pflüger, R. Pitzer, M. Reiher, T. Shiozaki, H. Stoll, A. J. Stone, R. Tarroni, T. Thorsteinsson, and M. Wang, *MOLPRO*, version 2015.1, a package of *ab initio* programs, 2015, see <http://www.molpro.net>.
- ⁴⁴K. Aidas, C. Angeli, K. L. Bak, V. Bakken, R. Bast, L. Boman, O. Christiansen, R. Cimraglia, S. Coriani, P. Dahle, E. K. Dalskov, U. Ekström, T. Enevoldsen, J. J. Eriksen, P. Eitenhuber, B. Fernández, L. Ferrighi, H. Fliegl, L. Frediani, K. Hald, A. Halkier, C. Hättig, H. Heiberg, T. Helgaker, A. C. Hennum, H. Hettner, E. Hjertenæs, S. Høst, I.-M. Høyvik, M. F. Iozzi, B. Jansík, H. J. A. Jensen, D. Jonsson, P. Jørgensen, J. Kauczor, S. Kirpekar, T. Kjærgaard, W. Klopper, S. Knecht, R. Kobayashi, H. Koch, J. Kongsted, A. Krapp, K. Kristensen, A. Ligabue, O. B. Lutnæs, J. I. Melo, K. V. Mikkelsen, R. H. Myhre, C. Neiss, C. B. Nielsen, P. Norman, J. Olsen, J. M. H. Olsen, A. Osted, M. J. Packer, F. Pawłowski, T. B. Pedersen, P. F. Provasi, S. Reine, Z. Rinkevicius, T. A. Ruden, K. Ruud, V. V. Rybkin, P. Salek, C. C. M. Samson, A. S. de Merás, T. Saue, S. P. A. Sauer, B. Schimmelpfennig, K. Sneskov, A. H. Steindal, K. O. Sylvester-Hvid, P. R. Taylor, A. M. Teale, E. I. Tellgren, D. P. Tew, A. J. Thorvaldsen, L. Thøgersen, O. Vahtras, M. A. Watson, D. J. D. Wilson, M. Ziolkowski, and H. Ågren, *Wiley Interdiscip. Rev.: Comput. Mol. Sci.* **4**, 269 (2014).
- ⁴⁵H. Werner and P. J. Knowles, *J. Chem. Phys.* **82**, 5053 (1985).
- ⁴⁶P. J. Knowles and H.-J. Werner, *Chem. Phys. Lett.* **115**, 259 (1985).
- ⁴⁷J. Cioslowski, *Phys. Rev. A* **43**, 1223 (1991).
- ⁴⁸E. Valderrama, E. V. Ludeña, and J. Hinze, *J. Chem. Phys.* **106**, 9227 (1997).
- ⁴⁹E. Valderrama, E. V. Ludeña, and J. Hinze, *J. Chem. Phys.* **110**, 2343 (1999).
- ⁵⁰E. Ramos-Cordoba, P. Salvador, and E. Matito, *Phys. Chem. Chem. Phys.* **18**, 24015 (2016).

A.6 Front Cover Image

The following image was published as the front cover of the *International Journal of Quantum Chemistry*, volume 118, issue 12, **2018**, as a result of the work of Ref. 158.

International Journal of **QUANTUM** **CHEMISTRY**

www.q-chem.org



A.7 Résumé Substantiel

Les vingt-cinq dernières années de la chimie du carbone ont été pleines de surprises, de seulement deux allotropes connus de carbone, le diamant et le graphite, et la conviction d'avoir une connaissance très profonde de l'élément fondamental de la vie, la découverte incroyable de trois nouvelles formes de carbone a essentiellement établi un domaine complètement nouveau de la recherche en chimie. En 1985, la molécule zéro-dimensionnelle fullerène a été identifiée pour la première fois¹, en 1991, la famille des allotropes de carbone s'est agrandie une deuxième fois lorsque les nanotubes de carbone (carbon nanotubes en anglais, CNTs) mono-dimensionnel ont été caractérisés expérimentalement² et en 2004, le cercle a été fermé avec la première synthèse du graphène³: une seule couche de graphite. Une image de ces trois nouveaux types de structures de carbone est présentée dans la Figure A.4. Les propriétés intéressantes de ces matériaux de carbone de faible dimension ont généré une incroyable vague de nouvelles recherches dans le domaine, avec le potentiel de révolutionner plusieurs disciplines scientifiques et industrielles.

Dans cette thèse, les nanotubes de carbone ont été le sujet central de l'étude, pour lequel plusieurs investigations ont été menées, envisageant différentes applications potentielles. Cependant, avant d'examiner les résultats obtenus au cours de ces trois années, nous introduirons plus en détails ce matériau.

Après la première synthèse réussie de nanotubes de carbone en 1991, la recherche sur ces systèmes a décollé assez rapidement et deux ans plus tard, les premiers nanotubes composés par une seule feuille enroulée d'atomes de carbone, en anglais *single-wall* CNTs, ont été obtenus expérimentalement⁵. Ces systèmes ont immédiatement fait

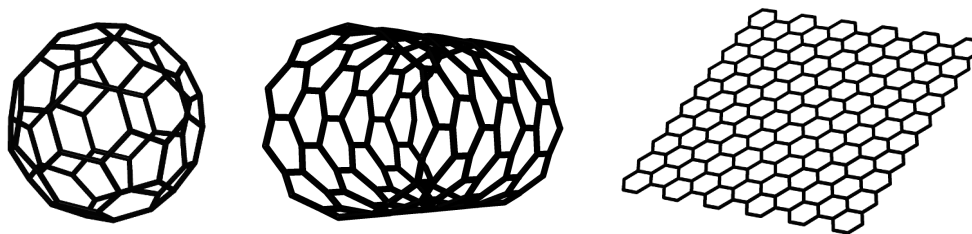


FIGURE A.4: Un fullerène C_{60} (gauche), un nanotube de carbone (centre) et le graphène (droit).

l'objet d'investigations théoriques et la notation utilisée aujourd'hui pour différencier les types possibles de nanotubes provient du travail de Saito et al.⁶. Ayant des arêtes différentes, il existe plusieurs manières de plier une couche de graphène et de la connecter, en formant des nanotubes de trois classes: *armchair*, *zigzag* et *chiral*. La paire de nombres entiers (n, m) avec $n \geq m \geq 0$ est utilisée pour étiqueter le type de nanotube et en fonction de leur valeur, les CNTs se classent dans l'une des trois catégories suivantes: *armchair* pour $n = m$, *zigzag* pour $n \neq 0$ et $m = 0$ et *chiral* pour $n \neq m \neq 0$.

Puisque la géométrie des nanotubes de carbone sans défaut est définie de manière unique par les indices n et m , il était possible de caractériser expérimentalement les CNTs de manière très précise et de déterminer la relation avec les propriétés mesurées. D'un point de vue théorique, les CNTs peuvent être modélisés de deux manières: soit en appliquant des conditions de bord périodiques et en les considérant comme des systèmes de longueur infinie ou par des conditions de bord ouvertes en saturant les atomes de carbone aux extrémités avec des hydrogènes. Dans la seconde approche, les effets de taille finie jouent un rôle très important pour leur géométrie^{14-18,20} et leur structure électronique^{15,25,47-53}, ainsi que pour beaucoup de leurs propriétés, par exemple celles optiques^{20,49,55,56}, aromatiques^{14,17,18,57} et électroniques^{15,16,54,58-63}. Indépendamment de leur modélisation théorique, il est clair que pour faire avancer le développement de nouvelles technologies basées sur les nanotubes de carbone, il est important de trouver un moyen de les fabriquer de manière contrôlée et précise. À cette fin, leur synthèse, leur purification et leur tri jouent un rôle fondamental. Au fil des ans, différentes approches de synthèse ont été explorées, telles que les techniques modernes permettent un contrôle plus fin du type de nanotubes produit²⁹⁻³¹. Pourtant, la synthèse des nanotubes reste le défi majeur malgré les grandes avancées réalisées la dernière décennie³²⁻³⁵. Plus important encore, compte tenu de la relation directe entre la paire (n, m) et les propriétés, la capacité à produire des nanotubes définis par la chiralité est essentielle pour de nombreux types d'applications, d'autant plus que les procédures de tri peuvent introduire des défauts dans les structures et altérer leurs propriétés. Une approche prometteuse consiste à utiliser des précurseurs de carbone à forme de hémisphère sur lesquels le nanotube peut se développer ou des *nanoanneaux* et *nanoceintures* de carbone comme unités modèles pour initier la synthèse du CNT d'une chiralité bien définie^{33,34,36-39}. Un avantage de cette

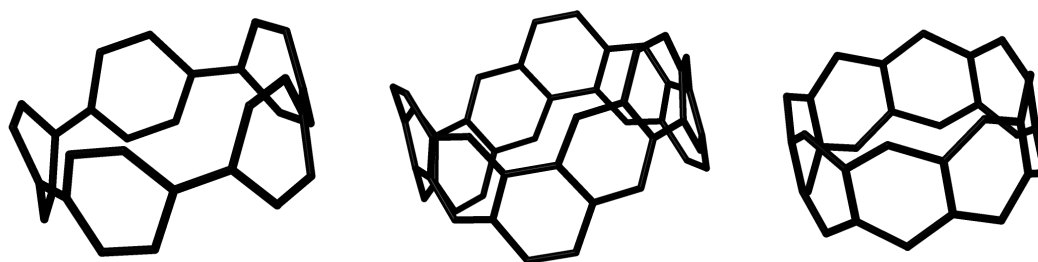


FIGURE A.5: Un cycloparaphénylène (gauche), une nanoceinture de carbone (centre) et un cyclacène (droit).

technique de fabrication ascendante est que la longueur finale du nanotube peut être relativement bien contrôlée. Ces voies de synthèse ont été essentiellement rendues possibles par le grand effort de recherche mis sur les macrocycles de carbone, qui sont généralement très difficiles à obtenir en premier lieu et constituent ainsi un domaine de recherche actif^{40–43}. Par exemple, ce n'est qu'en 2008 que le cycloparaphénylène, l'unité de base du nanotube armchair, a été obtenu expérimentalement⁴⁴ (Figure A.5 à gauche), et en 2017, la première nanoceinture composée de noyaux benzéniques connectés complètement par un bord chacun⁴⁵ (Figure A.5 centre). Les cyclacènes d'autre part, l'unité de base des nanotubes de carbone zigzag, restent encore des structures purement théoriques⁴⁶ (Figure A.5 à droite). Dans cette perspective, il est clair que la théorie joue un rôle important pour ces systèmes: la compréhension acquise par les études *in silico* peut fournir des informations précieuses pour leur découverte expérimentale. En particulier, lors de cette thèse, nous avons contribué à ce domaine de recherche en réalisant deux projets axés sur les cyclacènes.

Pour finir cette partie introductive, nous noterons comment initialement les premiers nanotubes de carbone produits par la méthode "arc-discharge" étaient en général bouchés aux deux extrémités. Considérant la structure creuse de ces systèmes, des applications en chimie "host-guest" étaient évidemment envisagées, de sorte qu'un moyen d'ouvrir les nanotubes de carbone et de les remplir était rapidement découvert^{64,65}. Depuis lors, beaucoup de travail a été effectué dans ce sens, à la fois expérimental mais aussi théorique, et à ce jour les CNTs ont été utilisés pour héberger une grande variété de systèmes, entre autres les fullerènes et similaires^{67,68}, métaux^{69–77}, composés énergétiques^{78–81} et bien d'autres. L'encapsulation de systèmes moléculaires à l'intérieur des nanotubes peut altérer les propriétés chimiques des espèces confinées ou donnent lieu à de nouvelles

phases de matériaux, conduisant à des résultats inattendus. Plus particulièrement, des nouvelles phases d'eau ont été prédites et observées expérimentalement il y a longtemps^{82,83}, mais sont toujours à l'étude aujourd'hui⁸⁴.

Compte tenu de leur structure unidimensionnelle, les candidats idéaux pour le confinement dans les nanotubes de carbone sont des molécules linéaires, des nanofils et similaires. La preuve expérimentale de telles structures confinées est disponible, par exemple des chaînes de polyène linéaires encapsulées dans des CNTs ont été rapportées il y a environ 10 ans⁸⁵, ou la polymérisation du phosphore blanc a été observée récemment à l'intérieur de la cavité du CNTs par la microscopie électronique à transmission⁸⁶. Ce dernier exemple illustre deux propriétés remarquables des nanotubes: d'un côté la paroi du CNT favorise la formation de nouveaux composés au sein de l'hôte, agissant efficacement comme catalyseurs, et de l'autre côté, l'espace limité de la cavité empêche les substances incluses de réagir, se décomposer ou se plier. En effet, parmi les nombreuses applications possibles proposées pour les nanotubes de carbone, leur utilisation comme catalyseurs a augmenté ces dernières années²⁷⁷. Néanmoins, dans cette thèse, nous nous sommes concentrés sur la deuxième propriété que nous venons d'illustrer, i.e. le fait que les nanotubes de carbone constituent un système idéal pour stocker et stabiliser dans leur cavité des substances qui subiraient autrement une décomposition. Il est clair qu'il faut trouver un équilibre entre les contraintes géométriques et les effets catalytiques pour ce dernier point, et en fait, ce n'était pas toujours le cas pour les systèmes présentés ici.

Cyclacènes

Dans la première partie de cette thèse, une étude approfondie sur plusieurs propriétés des cyclacènes a été réalisée au niveau de théorie semi-empirique et *ab initio*. Ces systèmes fascinants montrent des propriétés électroniques et magnétiques intéressantes qui les rendent idéaux aux applications technologiques dans des domaines différents. En plus de cela, approfondir la compréhension de ces molécules est également importante pour leur possible utilisation comme modèles dans la synthèse contrôlée des nanotubes de carbone de type zigzag, un défi auquel nous sommes encore confrontés aujourd'hui.

Les cyclacènes, ou plus précisément les $[n]$ cyclacènes, sont un type de nanoceinture

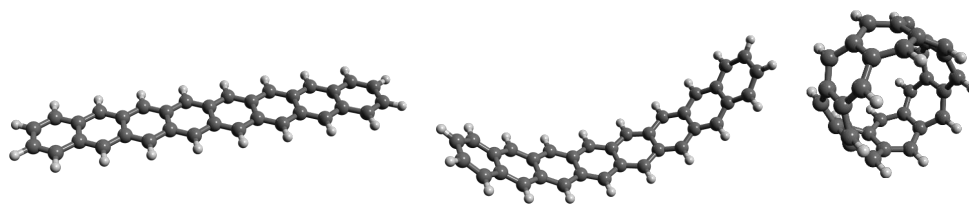


FIGURE A.6: Enroulement d'un octacène dans un [8]cyclacène.

de carbone obtenu en enroulant des polyacènes linéaires composés par n unités hexagonales et en joignant les deux extrémités ensemble, comme représenté dans la Figure A.6. Leur première apparition dans la littérature date le 1954, lorsque Edgar Heilbronner a présenté ces nanostructures de carbone dans une étude théorique basée sur la théorie de Hückel¹³⁵.

L'inaccessibilité expérimentale des cyclacènes a toujours favorisé leur caractérisation théorique, comme les nombreuses recherches disponibles dans la littérature le prouvent. Ces travaux ont été principalement réalisés en utilisant des approches semi-empiriques à la fin des années 90 et début des années 2000 par un certain nombre d'auteurs¹⁴⁵⁻¹⁵⁵. Récemment, quelques études analytiques supplémentaires basées sur la théorie de Hückel, ou des variations de celles-ci, ont été publiés¹⁵⁶⁻¹⁵⁹.

Outre ces résultats, plusieurs groupes ont étudié les [n]cyclacènes en utilisant des méthodes *ab initio*, donnant accès à des résultats plus quantitatifs^{139,140,160-164}.

L'analyse de la plupart des études semi-empiriques a été concentrée sur les paramètres géométriques autant que le comportement de propriétés électroniques simples, telles que l'écart entre le HOMO et le LUMO en fonction du nombre d'unités n dans le système. Par exemple, il a été constaté que l'écart diminue de manière alternée en fonction de la parité de n . Différents types de méthodologies fournissent différentes valeurs, bien que toutes concordent avec la tendance générale en fonction de la taille du système.

Les différentes travaux semi-empiriques sont complétées par un certain nombre des études *ab initio* basées à la fois sur les approches DFT et de fonction d'onde. Ces travaux ont principalement analysés le caractère de la fonction d'onde de l'état fondamental, le gap énergétique de la transition au premier état excité et la nature radicalaire de la molécule en respect de sa taille.

Sur la base de calculs DFT, Choi and Kim¹³⁹ ont étudié le gap d'énergie singulet-triplet, les longueurs des liaisons carbone-carbone et les propriétés magnétiques des cyclacènes.

Un deuxième travail toujours basé sur la DFT est apparu peu après¹⁴⁰, et a également rapporté l'écart entre les états excités en fonction de n . Dans les deux cas, les auteurs ont constaté un écart faiblement croissant en fonction croissante de la taille, et dans un cas, un état fondamental triplet. Cependant, quelques années plus tard, ces résultats se sont avérés être erronés selon des calculs utilisant une méthode fonction d'onde multiréférentielle plus sophistiquée¹⁶⁰. En particulier, l'état fondamental des cyclacènes a été trouvé être de nature singulet à couche ouverte indépendamment de la taille du système. Ces résultats ont été évalués et confirmés par Sadowsky et al.¹⁶¹, qui ont montré que l'écart croissant était le résultat d'une instabilité du singulet de l'état fondamental. Une étude récente par Wu et al.¹⁶² a exploré une série de propriétés électroniques des $[n]$ cyclacènes par l'approche TAO-DFT et a été trouvée en accord avec les travaux basés sur les méthodes de haut niveau *ab initio*. En particulier, outre l'établissement de l'état électronique le plus bas, le comportement du gap électronique a été calculé pour un très grand nombre de tailles de système.

Dans ce qui suit, nous discuterons de notre contribution à la recherche de ce type de systèmes.

Dans un premier travail, les expressions analytiques des valeurs propres et des vecteurs propres des cyclacènes dans l'approximation tight-binding ont été obtenues. Sur la base de ces informations, il était possible de dériver les expressions analytiques exactes des bandes d'énergie, densité d'états, la composante axiale du "total position spread (TPS) tensor" et la polarisabilité axiale. Le gap énergétique disparaît au niveau de Fermi, car il se situe à la frontière entre deux différentes bandes et pour cette raison la densité d'états montre la présence d'une singularité de Van Hove. Le TPS axial par électron reste fini pour $n \rightarrow \infty$, conformément à l'extension finie du système dans cette direction cartésienne. Assez remarquablement cependant, la polarisabilité par électron correspondante diverge, un comportement qui est communément trouvé seulement dans le cas des conducteurs. En général, une divergence de la polarisabilité par électron est associée à un comportement similaire du tenseur TPS correspondante. A notre connaissance, c'est le seul cas où les deux quantités ne se comportent pas de la même manière et nous soutenons que la raison est probablement due à la description manquante de la répulsion électron-électron dans l'approximation tight-binding, qui joue un rôle dans l'élimination

de la dégénérescence au niveau de Fermi. Ceci est pris en charge par les calculs CASSCF de la polarisabilité statique pour un petit nombre des systèmes. La composante axiale du TPS a également été calculée à partir de la fonction d'onde CASSCF pour les systèmes avec $n = 6, 8, \dots, 22$, montrant remarquablement le comportement linéaire asymptotique prédit dans l'approximation tight-binding, bien que loin de la limite thermodynamique. Nous n'avons pas été en mesure d'obtenir des expressions analytiques pour les composantes planes des tenseurs du TPS et polarisabilité, cependant, un calcul numérique ne montre aucune preuve de divergence de ces quantités. Par conséquent, le système devrait être, à ce niveau de description, un isolant. Ce résultat présente un intérêt particulier, car ce matériau a un "bandgap" nul avec une densité d'états différente de zero au niveau de Fermi, généralement une signature du comportement métallique. Les propriétés calculées dans notre étude néanmoins, qui dépendent des détails géométriques du système, le caractérise comme isolant, ce qui signifie que la fermeture d'un polyacène linéaire pour former un anneau semble changer le type de matériau de métallique à non-métallique.

Dans une seconde étude sur ces molécules, nous avons présenté les résultats obtenus en utilisant des méthodologies *ab initio*. En particulier, le gap énergétique vertical singulet-triplet et le caractère polyradical des $[n]$ cyclacènes ont été étudiés de manière systématique en fonction de la taille du système. L'écart singulet-triplet a diminué de façon exponentielle par rapport au nombre n des unités hexagonales et on obtient une valeur finie de l'ordre du dixième de eV dans la limite $n \rightarrow \infty$. Nous avons proposé un critère pour sélectionner dynamiquement l'espace actif (active space en anglais, AS) en fonction de n , basé sur l'étude tight-binding précédemment rapporté. Cette approche a permis un traitement équilibré de la corrélation électronique *statique* dans toute la série des systèmes considérés. Les résultats *ab initio* présentés ont été comparés aux précédents rapportés dans la littérature, soutenant d'un côté les conclusions antérieures et de l'autre les étendant à un plus grand nombre de systèmes. En particulier, la nature singulet à couche ouverte de l'état fondamental électronique a été fermement confirmée. Le caractère polyradical des cyclacènes a été étudié par une analyse des nombres d'occupation des orbitales naturelles ainsi qu'un indicateur basé sur ceux-ci et on a trouvé un signe clair d'une augmentation du caractère radicalaire croissant avec la taille du système. Des

calculs utilisant un espace actif minimal de deux électrons dans deux orbitales ont également été effectués et une investigation des résultats obtenus avec cet AS a été fournie par une analyse scrupuleuse de la contribution des intégrales à l'énergie de corrélation. Avec un choix *erroné* de l'AS, l'état fondamental du système a tendance à être de type couche fermée plutôt qu'ouverte par rapport à la taille du système. Outre les résultats fournis, cette étude a montré de manière didactique l'importance de l'espace actif pour ce type de systèmes et a proposé un nouveau critère pour sa sélection systématique. Pour conclure, bien que les [n]cyclacènes n'aient pas encore été synthétisés, ils restent un terrain fertile tant pour les théoriciens que les expérimentalistes, et leur enquête fournit un moyen d'augmenter la compréhension de base des systèmes d'hydrocarbures en général.

Confinement Dans les Nanotubes de Carbone

Dans la seconde partie de la thèse, plusieurs investigations concernant l'encapsulation des systèmes d'azote pure et des chaînes de béryllium à l'intérieur des nanotubes de carbone ont été réalisées. La structure creuse des CNTs et la faible réactivité de la paroi interne constituent une solution idéale pour confiner une grande variété de systèmes dans leur cavité, les rendant appropriés pour différents types d'applications. Les molécules basées sur l'azote ont la propriété exceptionnelle de stocker une quantité incroyable d'énergie chimique dans leurs liaisons, ce qui en fait une source possible d'énergie green. Cependant, ils souffrent d'une instabilité élevée. Dans cette perspective, des nanotubes de carbone ont été proposés comme dispositifs de stockage et de stabilisation, afin de protéger les espèces d'azote et éviter la libération d'énergie par une décomposition en N_2 . Par ailleurs, les nanotubes de carbone ont également été étudiés comme possibles hôtes de matériaux ayant d'autres propriétés, telles que les chaînes de béryllium, des molécules linéaires caractérisées par deux orbitales magnétiques remplies à moitié, couplées faiblement antiferromagnétiquement. Le plus intéressant, ce couplage s'est avéré être affecté par des interactions non covalentes avec les nanostructures de carbone, suggérant un moyen possible de contrôler la nature de l'état fondamental.



FIGURE A.7: Anion azoture.

Anion Azoture

Dans le cadre de la recherche de sources d'énergie alternatives et respectueuses de l'environnement, une classe prometteuse des systèmes est celui des molécules constituées seulement par l'azote^{192,193}. Comptant jusqu'à 78%, l'azote est l'espèce la plus abondante dans l'atmosphère terrestre et est donc largement et facilement accessible. Il est pratiquement uniquement présent en tant que N₂ di-moléculaire, qui est de loin la forme la plus stable et considérée comme non-nocive pour l'environnement. La raison pour laquelle l'azote ne se produit naturellement que sous la forme N₂ est due à sa liaison chimique particulière, avec la liaison N–N triple caractérisée par une énergie de 229 kcal/mol, celle du double liaison par 100 kcal/mol et la liaison simple par 38,4 kcal/mol¹⁹². Thermodynamiquement, trois fois l'énergie d'un seul lien ou une fois et demie la double liaison n'atteint pas la stabilité énergétique de la triple liaison, d'où l'omniprésence de N₂. Par conséquent, cette distribution d'énergie est telle que les allotropes d'azote à liaison simple et double ont le potentiel de libérer une grande quantité d'énergie lors de la décomposition en azote moléculaire. Pour cette raison, les amas d'azote pur sont considérés comme des matériaux à haute densité énergétique (high energy-density material en anglais, HEDM)^{192,193}. La première et la plus célèbre molécule de polynitrogène est l'anion azoture, avec la formule N₃⁻, représenté dans la Figure A.7, connu depuis la fin du XIXe siècle¹⁹⁴. Il a fallu plus de 100 ans pour agrandir cette famille, avec la synthèse réussie du cation N₅⁺ en 1999 par Christe et al.¹⁹⁵, montré dans la Figure A.8, ce qui a renouvelé l'intérêt pour cette classe de systèmes, envisageant la possibilité de former un cristal d'azote pur composé par des paires ioniques N₃⁻ et N₅⁺^{196–198}. Cependant, des tentatives expérimentales pour stabiliser les deux ions n'ont pas eu de succès¹⁹⁹, mettant en évidence encore une fois l'obstacle majeur à la réalisation d'allotropes d'azote pur, c'est-à-dire leur instabilité intrinsèque par rapport à la décomposition en N₂.

Plus récemment, le confinement moléculaire a été proposé comme une stratégie possible pour surmonter ce problème. En encapsulant une chaîne azotée polymérique à l'intérieur d'un CNT, des simulations de dynamique moléculaire ont montrés que le polymère reste stable jusqu'à des températures élevées, préservant, en théorie, la structure de ces molécules et en fournissant en même temps un moyen de les stocker^{79,80,200}. Des investigations théoriques supplémentaires basées sur la même idée ont prédit la même chaîne d'azote comme stable dans les nanotubes de carbure de silicium et de nitrure de bore²⁰¹⁻²⁰³. Avec une approche similaire, une étude DFT sur l'encapsulation des clusters d'azote de différentes tailles dans un fullerène C₆₀ a également été réalisée, prédisant des structures stables pour des molécules jusqu'à 13 atomes avant que celui-ci a commencé à être lié chimiquement à la cage confinante²⁰⁴.

D'un point de vue expérimental, une espèce anionique N₈⁻ adsorbée à l'intérieur d'un nanotube de carbone à parois multiples a été observée à des conditions ambiantes²⁰⁵; un résultat récemment corroboré par la synthèse réussie sur un substrat de nanotubes de carbone de la phase cubique gauche (cg-N) proche des conditions ambiantes²⁰⁶. Dans ce dernier travail, outre la présence de pics dans les spectres Raman et infrarouge correspondant à la phase cg-N, les images de microscopie électronique à transmission à haute résolution montrent clairement les structures d'azote encapsulées à l'intérieur des CNTs. Malgré le nombre relativement important d'ouvrages sur les chaînes d'azote, peu d'autres espèces ont été considérées dans un environnement confiné. En particulier, outre la grande quantité de littérature examinant les caractéristiques spectroscopiques de l'ion azoture en phase cristalline ou gazeuse²⁰⁷⁻²¹⁵ ainsi que solvaté²¹⁶⁻²²⁸, il n'a jamais été étudié dans un environnement confiné. Considérant que N₃⁻ représente souvent un précurseur dans la synthèse de molécules énergétiques, par exemple la synthèse de la phase cg-N mentionnée ci-dessus sur le substrat CNT part de l'azoture de sodium, où il

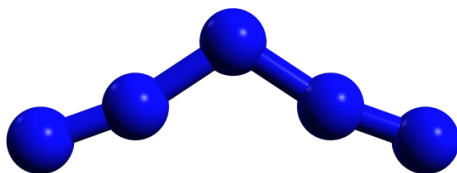


FIGURE A.8: Cation N₅⁺.

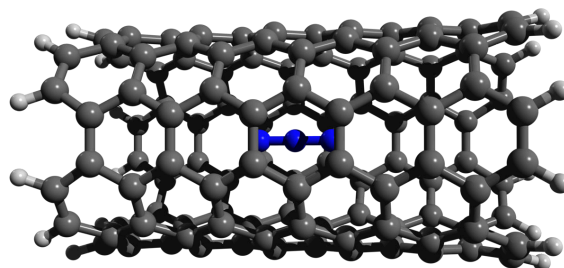


FIGURE A.9: L'anion azoture confiné dans un CNT.

apparaît comme une structure intermédiaire lors de la réaction de dissociation des clusters d'azote plus grands, par exemple la dissociation sans barrière de l'ion N_5^- . Donc, il y a certainement un intérêt à étudier le comportement de l'azoture dans un environnement contraint tel que celui fourni par les CNTs, et en particulier pour comprendre le type d'interactions entre le confinement et les fragments confinés.

A cette fin, le confinement de l'anion azoture à l'intérieur des nanotubes de carbone de différentes longueurs et les diamètres ont été étudiés au cours de cette thèse. Un exemple des systèmes étudiés est montré dans la Figure A.9. Beaucoup d'efforts ont été consacrés à l'étude de ce système, en fournissant dans un premier temps des informations importantes sur l'adsorption de l'ion comme la nature de l'interaction entre les fragments ou les effets de relaxation de l'azoture et du CNT. Deuxièmement, une approche plus systématique a été entreprise, où les effets de taille finie ont été étudiés par la méthode de haut niveau coupled cluster (CC), afin d'obtenir des énergies de référence précises.

En s'appuyant sur les connaissances acquises des calculs statiques et en les comparant à la référence *ab initio*, un nouveau potentiel intermoléculaire modélisant l'interaction non covalente entre N_3^- et CNTs a été présenté. Le potentiel a ensuite été codé dans le programme de dynamique moléculaire DL POLY 4.08^{229,230}, qui permet maintenant d'étudier la dynamique des ions confinés dans des nanotubes de carbone de toute taille et de tout type.

Comme mentionné, dans une première partie, l'accent était mis sur une étude *ab initio* de l'anion azoture confiné à l'intérieur des nanotubes de carbone. On a trouvé que N_3^- est stabilisé énergiquement par des nanotubes de diamètres compris entre ≈ 5.5 Å et ≈ 9.5 Å (voir Figure A.10), montrant la plus forte interaction de -32.31 kcal/mol obtenue dans le cas d'un CNT (5,5), avec un diamètre de ≈ 6.78 Å. L'analyse des structures

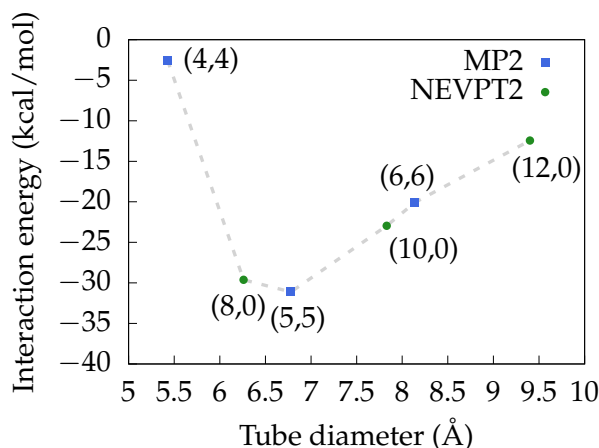


FIGURE A.10: Énergies d'interaction en fonction du diamètre du nanotube.

relaxées, des charges atomiques partielles et du potentiel électrostatique moléculaire a révélé la nature de l'interaction, suggérant une explication des résultats trouvés. En particulier, nous soutenons que l'espèce N_3^- est stabilisée par des interactions électrostatiques et d'induction avec la paroi du nanotube, la dernière subissant une polarisation remarquable due à la présence d'atomes d'hydrogène utilisés pour saturer les extrémités des CNTs. La dimension de la cavité d'un CNT (5,5) est telle que le fragment N_3^- s'aligne parfaitement au centre du nanotube et parallèlement à son axe, résultant en une distance optimale de son mur en toutes directions, expliquant ainsi la forte interaction observée. L'inconvénient de l'utilisation de systèmes de taille finie pour modéliser les nanotubes de carbone est qu'il existe une dépendance intrinsèque à leur longueur, en particulier si on considère des molécules chargées confinées. Par conséquent, une étude approfondie sur cette dépendance a également été menée, cette fois le niveau de la théorie a été augmenté. La raison était double, d'un côté nous voulions confirmer nos résultats précédents et d'autre part, l'objectif était d'obtenir des énergies de référence très précises. Plus précisément, l'approche utilisée pour cette étude a permis d'obtenir des énergies d'interaction avec une précision sans précédent, en employant un schéma combiné d'extrapolation et d'ajustement basé sur les méthodologies RI-SCS-MP2 et DLPNO-CCSD(T) associées à une base de qualité triple- ζ .

En rationalisant les résultats obtenus au niveau de la théorie *ab initio*, nous avons présenté un potentiel intermoléculaire décrivant l'interaction de l'anion azoture avec les nanotubes de carbone. Ce modèle repose sur une séparation des trois composantes

contribuant à l'interaction: les forces de Van der Waals (VdW), les effets d'induction et l'électrostatique. Les interactions VdW ont été modélisées selon le potentiel de Lennard-Jones amélioré (Improved Lennard-Jones en anglais, ILJ), pour les effets d'induction nous avons proposé un nouveau potentiel basé sur la forme générale d'un dipôle induit en raison de la présence d'un champ électrique externe, alors que la composante électrostatique était prise en compte par la loi habituelle de Coulomb. La fonction de potentiel total présentée reproduisait les énergies DLPNO-CCSD(T) approximativement à quelques kcal/mol près et fournit une seconde manière d'analyser les résultats, c'est-à-dire en inspectant les contributions des composants individuels. Cette dernière approche est assez pratique et permet une exploration des caractéristiques importantes de la surface d'énergie potentielle qui sont autrement difficiles à saisir. Fait intéressant, la dépendance à la distance des différentes composantes est également évidente dans l'étude de l'énergie d'interaction en fonction de la longueur des CNTs: le VdW et les interactions d'induction convergent rapidement pour des nanotubes de plus en plus longs et le comportement des la surface d'énergie potentielle est dominée par la force électrostatique à *plus longue portée*.

Les fonctions de potentiel intermoléculaire proposées, en particulier les potentiels ILJ et d'induction, ont été codés dans le programme de dynamique moléculaire DL POLY 4, avec lequel un nombre des simulations ont été effectuées pour démontrer son fonctionnement.

Cette étude approfondie de l'anion azoture a permis de mieux comprendre cette molécule et en particulier les interactions ion-CNT en général. Bien que l'anion azoture soit l'une des molécules d'azote pur les plus stables, les résultats obtenus ici sont intéressants dans le contexte de stockage d'énergie alternatif puisque N_3^- peut être utilisé comme précurseur pour la synthèse des agrégats d'azote plus complexes. De plus, ce travail a également été la motivation pour la mise en œuvre d'un potentiel intermoléculaire précis dans le logiciel DL POLY, qui peut maintenant être utilisé pour d'autres systèmes.

Cation N_5^+ et Chaînes N_8

Outre l'anion azoture dont nous avons parlé jusqu'à présent, ils existent aussi d'autres systèmes d'intérêt. En particulier, le cation N_5^+ (pentazenium), isolé avec succès en 1999

par Christe et al.¹⁹⁵, est un bon candidat à l'investigation car combiné avec l'anion azote, il peut conduire à la formation de la molécule hautement énergétique N_8 . Dans la littérature, plusieurs travaux théoriques et quelques travaux expérimentaux ont étudié les ions N_3^- , N_5^+ et N_5^- soit individuellement²⁵⁵⁻²⁵⁹, soit leurs compositions^{196-199,260}. D'autre part, la surface d'énergie potentielle de l'espèce N_8 était également sujette à des études approfondies²⁶¹⁻²⁶⁶. Plus particulièrement, en 2001, Fau and Bartlett¹⁹⁶ ont prédit que le produit N_8 depuis la réaction entre N_5^+ et N_3^- serait très probablement trop instable pour exister, ce qui a été confirmé expérimentalement en 2004 par Dixon et al.¹⁹⁹. Cependant, il a également été suggéré qu'un tel allotrope d'azote pourrait en principe exister en raison des forces de cohésion résultant d'une structure cristalline. En effet, en 2014, Hirshberg et al.²⁶⁷ avait prédit un cristal moléculaire stable formé par des fragments de N_8 .

Le confinement du pentazenium à l'intérieur de la nanostructure de carbone n'a jamais été étudié, même si un certain nombre des travaux théoriques prédisant une chaîne d'azote polymérique stable à l'intérieur des nanotubes de carbone est disponible dans la littérature^{79,80,200,202}.

Suivant l'approche utilisée jusqu'à présent, une étude sur le confinement des deux autres molécules ont été réalisées, en particulier les espèces cationiques N_5^+ et la chaîne neutre N_8 . Le premier, malgré les énergies d'interaction non liées avec les nanotubes de carbone sont favorables, il a été trouvé qu'il subissait une décomposition lors d'un double transfert de charge de la nanostructure de carbone au cation. En fait, comme déjà rapporté dans la littérature¹⁹⁹ et confirmé ici, un seul électron est suffisant pour déclencher la réaction sans barrière. Un transfert se produit initialement parce que l'affinité électronique de N_5^+ est plus grande que le potentiel d'ionisation du nanotube de carbone. La surface d'énergie potentielle de la décomposition peut être vue dans la Figure A.11. Ce processus conduit finalement à un autre transfert de charge, dans lequel l'intermédiaire radical N_3 gagne un second électron à partir du nanotube, résultant dans des produits $N_3^- + N_2$.

Un moyen possible de contourner cette décomposition est l'ajout d'un contre-ion dans la cavité, ce qui peut concurrencer le processus de transfert de charge et stabiliser finalement N_5^+ . A cette fin, nous avons effectué des investigations préliminaires sur l'encapsulation

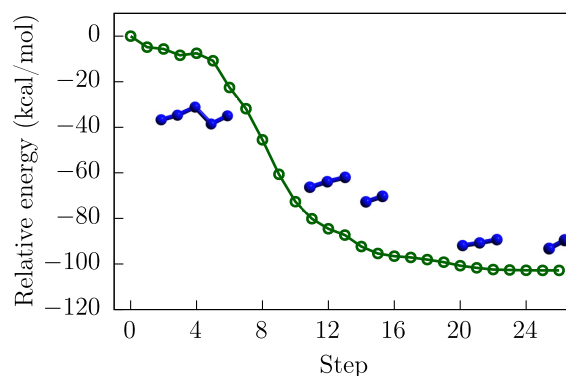


FIGURE A.11: Surface d'énergie potentielle de la décomposition de l'ion N_5^+ . Des géométries intermédiaires sont représentées sans le nanotube pour une meilleure représentation.

de N_8 dans un CNT (5,5), le considérant comme le résultat de la réaction $N_3^- + N_5^+ \rightarrow N_8$. Cependant, cette réaction n'a pas été explicitement considérée, mais nous nous sommes plutôt concentrés sur la faisabilité d'encapsuler le produit N_8 qui pourrait également être formé de toute autre façon.

Les résultats obtenus montrent que deux isomères linéaires de N_8 , représentés à la Figure A.12, qui sont stables en phase gazeuse, sont également stables à l'intérieur du nanotube avec une grande énergie d'interaction. Les effets du confinement spatial à l'intérieur de la cavité favorisent l'isomère le plus linéaire parmi les deux, en augmentant leur différence d'énergie relative de quelques kcal/mol. Il existe deux voies de décomposition en phase gazeuse pour ces isomères de N_8 , qui ont été considérées ici aussi. Étonnamment, tous les états de transition connus de ces réactions, sauf un, ne sont pas restés valables lorsque le système est confiné à l'intérieur du nanotube. On fait valoir que cela est dû à des effets stériques, puisque seul l'existence du plus linéaire a été confirmé à l'intérieur de la cavité, tandis que tous les autres résultaient de points selle d'ordre supérieur (donc pas des états de transition). Ceci est corroboré par l'énergie d'interaction plus forte de l'isomère plus linéaire sur l'autre. En outre, compte tenu des profils énergétiques obtenus pour l'anion azoture, il en résulte une clarification sur la proximité des murs de nanotubes avec les

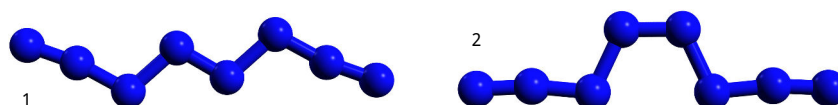


FIGURE A.12: Deux isomères stables de N_8 .

espèces confinées à l'intérieur du CNT (5, 5) a un impact fort sur la liberté géométrique. En dépit d'être encore un sujet de recherche d'actualité, ces résultats suggèrent que les effets stériques dus à l'espace restreint disponible dans la cavité peut fermer certaines voies de réaction et favoriser certaines isomères sur les autres. Dans ce contexte, le diamètre du nanotube peut être utilisé comme paramètre accordable fournissant un degré de contrôle sur la molécule encapsulée. En particulier, l'objectif est soit d'augmenter l'énergie d'activation, soit même de fermer les voies des réaction menant à la décomposition de N_8 , favorisant ainsi le maintien des isomères sélectionnés à l'intérieur de la cavité.

Chaînes de Béryllium

Les chaînes linéaires du béryllium sont une conformation particulière des systèmes Be_n pour lesquels des propriétés magnétiques intéressantes ont été prédites à partir de calculs théoriques^{269–272}. En partageant deux électrons chacun, les atomes de béryllium se lient ensemble pour former des liaisons covalentes uniques résultant en une géométrie linéaire qui laisse deux électrons non appariés aux deux atomes terminaux. On a prédit par des calculs *ab initio* que deux orbitales à moitié remplies, montrées dans la Figure A.13, sont localisées aux extrémités de la chaîne, donnant lieu à un état fondamental qui est couplé antiferromagnétiquement, mais avec un état de triplet couplé ferromagnétiquement très proche en énergie. De plus, dans une étude suivante, les mêmes auteurs ont constaté que ce couplage était altéré si la chaîne est déposée sur un morceau de graphène, montrant une nette dépendance vis-à-vis à la distance de la surface²⁷³. Plus important encore, l'état fondamental du système change de antiferromagnétique à ferromagnétique pour une certaine gamme de distances. Les chaînes Be_n semblent donc avoir des propriétés

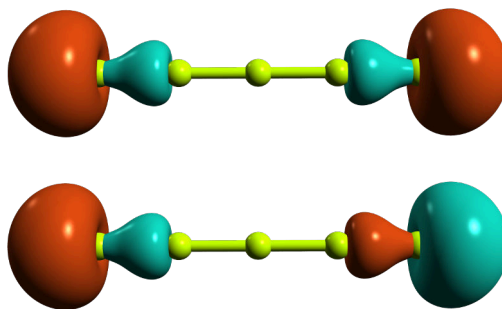
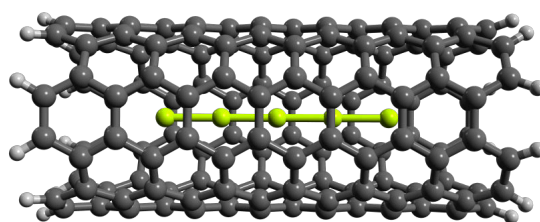


FIGURE A.13: Orbitals magnétiques des chaînes de béryllium.

FIGURE A.14: Be_5 confiné dans un CNT.

magnétiques qui peuvent être contrôlées par des interactions non-covalentes, avec des applications potentielles comme aimants moléculaires. Cependant, la géométrie linéaire de la chaîne n'est qu'une structure métastable sur la surface d'énergie potentielle du système Be_n , qui a tendance à se plier à une conformation plus compacte et énergétiquement plus favorable²⁷⁴. Le dépôt sur une surface peut stabiliser la géométrie linéaire, néanmoins, les nanotubes de carbone fournissent certainement un hôte plus approprié pour préserver leur structure, comme cela a déjà été souligné dans la Référence 273 (une image de ce système est montrée dans la Figure ??). Il existe également un deuxième avantage en encapsulant les chaînes à l'intérieur des CNTs, i.e. le couplage du système hybride peut être accordé en fonction du diamètre du nanotube englobant. En vue de ces objectifs, le but de l'enquête menée dans le cadre de la thèse était donc d'explorer les effets conférés aux chaînes de béryllium des différentes longueurs quand placées à l'intérieur du nanotubes de carbone de différents diamètres au moyen de méthodes de fonction d'onde multi-référencielles ainsi que la théorie de la fonctionnelle de la densité. D'un côté, nous étions intéressés à l'énergétique des chaînes de béryllium par rapport à leurs homologues en forme de cluster, et de l'autre, nous avons concentré l'attention sur le couplage magnétique des chaînes en fonction de la longueur de la chaîne et du diamètre du nanotube.

Il y a des indications que la valeur de J (le couplage magnétique) va vers zéro en raison de l'interaction avec un nanotube de plus en plus étroit (Tableau A.2), mais il n'est pas clair si, pour des CNTs suffisamment petits, le système composite devient ferromagnétique.

Le comportement de J par rapport à la longueur du nanotube a été testé pour un nombre sélectionné des cas, cependant, afin de garder une précision suffisante de la propriété calculée, il était impossible d'étudier de manière systématique des nanotubes plus longs.

TABLE A.2: Couplage magnétique J en fonction du diamètre du CNT et longueur de la chaîne. Les valeurs sont données en meV.

Host	Be ₄	Be ₅	d [Å]
CNT(5,4)	-4.97	+0.72	3.06
CNT(5,5)	-14.54	-6.07	3.39
CNT(6,5)	-19.64	-2.83	3.74
CNT(6,6)	-20.50	-3.56	4.07
isolée	-16.37	-2.50	∞

Il serait manifestement très intéressant d'étudier également les chaînes de béryllium plus longues, mais étant donné que dans le cas Be₅ que la longueur du nanotube semble être un facteur important, des nanotubes plus longs sont vraiment nécessaires, mais inaccessibles d'un point de vue calculatoire. Nous rappelons que à l'avenir, la relaxation du système complexe devrait être prise en compte pour que la chaîne ait la possibilité de sortir de l'axe principal du nanotube. C'est une préoccupation majeure, mais c'est aussi un problème très difficile à résoudre du point de vue méthodologique.

Conclusions

En conclusion de cette discussion, plusieurs travaux impliquant des nanotubes de carbone et des structures connexes ont été réalisés au cours de cette thèse. La polyvalence de ces systèmes est l'une de leurs caractéristiques et cela a été prouvé par les résultats proposés ici.

Les cyclacènes, qui sont formellement des nanotubes de carbone de type zigzag composés par une seule unité, ont été étudiés par des méthodes semi-empiriques et *ab initio*, en mettant en évidence leur propriétés intéressantes et les défis que ces molécules posent aux approches théoriques modernes. L'avancement dans la compréhension de leur structure électronique est essentielle pour évaluer leur potentiel pour diverses applications technologiques ainsi que pour fournir des informations précieuses à leur synthèse expérimentale, qui reste à réaliser. En outre les résultats obtenus par les investigations effectuées, cette thèse a prouvé comment une approche semi-empirique combinée avec un traitement *ab initio* plus élevé fournit un outil puissant pour comprendre et caractériser un système moléculaire de différentes perspectives et à différents niveaux de détail.

En raison de la cavité creuse des nanotubes de carbone, l'une de leurs applications potentielles est la chimie host-guest. Le confinement de tout type de molécule à l'intérieur de ces nanostructures a différents types d'effets et peuvent être exploités de plusieurs manières. Au cours de cette thèse, un type de molécules énergétiques a été envisagé et leur encapsulation à l'intérieur des nanotubes de carbone ont été étudiés. D'un côté, la motivation derrière cet effort de recherche était le potentiel de molécules d'azote pur comme sources d'énergie verte alternatives, mais d'autre part, le travail a également été conduit par un intérêt purement théorique, en particulier pour la compréhension de types d'interaction impliquées dans les nanostructures de carbone et comment celles-ci peuvent être modélisées d'une manière précise, mais efficace par rapport à l'efficacité computationnelle.

Les résultats obtenus pendant toute la période du doctorat concernent essentiellement trois systèmes, l'anion azoture, le cation pentazenium et la molécule neutre N_8 . Dans tous les cas, nous avons étudié les effets exercés par le nanotube sur le système confiné, en se concentrant sur différents aspects en fonction du système. Spécifiquement, dans le cas de l'anion azoture, la stabilité et la rigidité globale des nanotube et de l'espèce ionique constituaient une bonne base pour le développement d'un potentiel intermoléculaire et son implementation dans un programme de dynamique moléculaire. En outre, ce système était utilisé comme exemple pour démontrer la faisabilité de modéliser avec précision différents types d'interactions dans une perspective classique. Le travail sur le cation pentazenium était centré sur le processus de relaxation, un cas clair dans lequel l'effet du nanotube est énorme. Néanmoins, ces derniers résultats ont fourni un point de départ pour l'étude ultérieure de la molécule N_8 , un système qui a suscité un grand intérêt dans le passé et qui fait toujours l'objet d'enquête par plusieurs groupes aujourd'hui. Ici, les résultats préliminaires montrent l'importance du confinement spatial dans le contrôle des comportement de la molécule et suggère un moyen de stockage.

Bien qu'il soit strictement théorique, le travail effectué dans ce domaine contribue à faire avancer la compréhension des interactions ion-CNT et fournit une base solide pour des recherches futures.

Au lieu d'agir simplement comme un dispositif de stockage, les nanotubes de carbone peuvent constituer des systèmes hybrides intéressants lorsqu'ils sont combinés avec des

autres types de molécules. C'est le cas des chaînes de béryllium, dont les propriétés pourraient être exploitées de différentes manières, mais leur géométrie linéaire limite leur applicabilité. Cependant, lorsqu'ils sont insérés dans la cavité des nanotubes de carbone, leur structure peut en principe être préservé en raison de la conformation linéaire du CNT ainsi que de l'espace limité disponible, en évitant que la chaîne ne se plie pas dans des isomères énergétiquement inférieurs. De plus, les faibles interactions entre la structure carbonée et la chaîne sont telles que les propriétés de la chaîne peuvent être modulées en fonction du diamètre du nanotube. Il existe des preuves que le couplage magnétique des deux électrons découplés est affecté par la présence du système environnant, qui semble changer le type de l'état fondamental de antiferromagnétique à ferromagnétique dans certains cas extrêmes. Cependant, à la lumière des approximations utilisées dans cette étude, nous ne pouvons pas encore fournir de preuve concluante de ce comportement. Néanmoins, les nanotubes de carbone se sont révélés être un système remarquable qui peut être exploité en plusieurs façons.

Outre les principaux projets impliquant les nanotubes de carbone, d'autres investigations ont été menées au cours de cette thèse. Plus particulièrement, une proposition d'une nouvelle stratégie d'expansion de la base pour effectuer des calculs moléculaires a été explorée. En pratique, l'idée est de rester dans le domaine des expansions des gaussiennes pour la fonction d'onde, exploitant les moyens bien établis développés au cours des 50 dernières années, mais mélanger une description centrée sur l'atome avec une approche distribuée où les fonctions gaussiennes remplissent l'espace entre et autour des atomes. Ce travail a conduit à la mise en place d'un nouveau programme informatique capable de calculer les intégrales moléculaires sur des orbitales de type gaussien placées arbitrairement, qui a été utilisé pour obtenir les résultats numériques de cette enquête. En outre, l'étude sous un autre angle d'un problème ancien, i.e. la localisation de Wigner, a été réalisée en collaboration avec d'autres membres du laboratoire de Toulouse. Notamment, ce travail est en fait basé sur la même approche que celle que nous venons de mentionner, c'est à dire avec des fonctions gaussiennes pour élargir la fonction d'onde.

En résumé, dans cette thèse de doctorat, différentes approches ont été utilisées pour étudier différents problèmes tournant autour des nanotubes de carbone. D'un côté, le moteur était un véritable intérêt pour les applications technologiques possibles de ces

systemes, mais d'autre part, il y avait aussi une curiosité méthodologique qui a conduit au développement de nouveaux outils et techniques pour aborder de nouveaux problèmes dans le domaine de la chimie théorique et computationnelle.

A.8 Sintesi Sostanziale

Gli ultimi venticinque anni di chimica del carbonio sono stati pieni di sorprese, da solo due allotropi conosciuti, il diamante e la grafite, e la convinzione di avere una conoscenza molto profonda nel elemento di base della vita, l'incredibile scoperta di tre nuove forme cristalline di carbonio ha sostanzialmente generato un campo di ricerca in chimica a sé stante.

Nel 1985 venne identificata per la prima volta la molecola zero-dimensionale chiamata fullerene¹, nel 1991 la famiglia di allotropi di carbonio si allargò una seconda volta quando delle strutture monodimensionali, successivamente denominate nanotubi di carbonio (carbon nanotubes in inglese, CNTs), furono caratterizzate sperimentalmente² e nel 2004 il cerchio fu chiuso con la prima sintesi del grafene³: un singolo strato di grafite. Una immagine di questi tre nuovi tipi di strutture in carbonio è mostrata alla Figura A.15. Le proprietà promettenti di questi materiali carbonici a bassa dimensionalità hanno generato una incredibile ondata di nuove ricerche in materia, con la possibilità di rivoluzionare diverse discipline, sia scientifiche che industriali.

In questa tesi di dottorato i nanotubi di carbonio sono stati il soggetto centrale di studio, sui quali sono state condotte diverse investigazioni teoriche tenendo conto delle possibili applicazioni alla quale si prestano questi sistemi. Tuttavia, prima di discutere i risultati ottenuti durante questi tre anni, introdurremo in maggior dettaglio questo materiale.

Dopo la prima sintesi con successo dei nanotubi di carbonio nel 1991, la ricerca su questi sistemi è decollata abbastanza rapidamente ed è solo due anni dopo che i primi nanotubi composti da un singolo foglio di atomi di carbonio, vale a dire un *single-wall* CNT, fu sperimentalmente ottenuto⁵. Questi sistemi furono immediatamente oggetto di

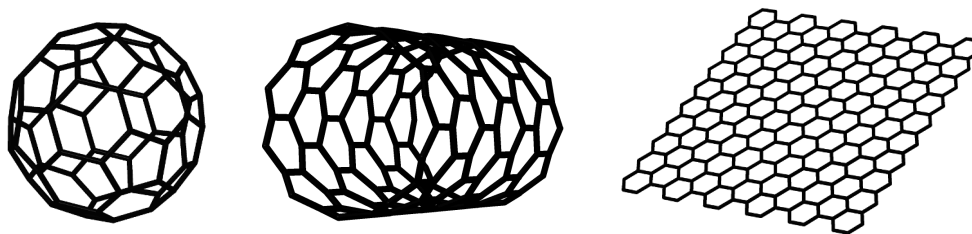


FIGURE A.15: Un fullerene C_{60} (sinistra), un nanotubo di carbonio (centro) ed un pezzo di grafene (destra).

indagini teoriche e la notazione utilizzata ancora oggi per differenziare le tipologie di nanotubi proviene dal lavoro pionieristico di Saito et al.⁶. Poiché i bordi di uno strato di grafene sono differenti gli uni dagli altri, ci sono diversi modi per piegar quest'ultimo e connetterne i bordi, formando nanotubi di tre classi (i cui nomi verranno mantenuti in inglese nel resto di questo riassunto): *armchair*, *zigzag* e *chiral*. La coppia di numeri interi (n, m) con $n \geq m \geq 0$ (chiamati anche *indici chirali*) è usata per identificare la struttura dei nanotubi, ed in base al loro valore i CNTs rientrano in una delle tre categorie elencate poco fa: *armchair* per $n = m$, *zigzag* per $n \neq 0$ e $m = 0$ e *chiral* per $n \neq m \neq 0$.

Poiché la geometria dei nanotubi di carbonio privi di difetti è definita in modo univoco dagli indici chirali n e m , è stato possibile caratterizzare sperimentalmente i CNTs in modo molto preciso, permettendo di associare le proprietà misurate al tipo di nanotubo. Da una prospettiva teorica, i CNTs possono essere modellati in due modi: applicando condizioni di bordo periodiche e considerando i nanotubi come dei sistemi infinitamente lunghi, oppure tramite condizioni di bordo aperte e saturando gli atomi di carbonio alle estremità con degli idrogeni. Nel secondo approccio, gli effetti di dimensione finita giocano un ruolo molto importante per i loro parametri geometrici^{14–18,20} e la loro struttura elettronica^{15,25,47–53}, così come per molte delle loro proprietà, ad esempio quelle ottiche^{20,49,55,56}, aromatiche^{14,17,18,57} ed elettroniche^{15,16,54,58–63}.

Indipendentemente dalla loro modellizzazione teorica, è chiaro che per far avanzare l'attuale sviluppo di nuove tecnologie basate su nanotubi di carbonio, è importante trovare un modo per fabbricarli in modo controllato e preciso. A tal fine, la loro sintesi, purificazione e separazione risultano essere degli aspetti fondamentali. Nel corso degli anni diversi approcci sintetici sono stati esplorati e le tecniche ora disponibili consentono un controllo più preciso sul tipo di nanotubi prodotti^{29–31}. Tuttavia, il processo di sintesi rimane ad oggi il principale ostacolo che ne rallenta la loro diffusione su larga scala, nonostante i grandi passi avanti compiuti nell'ultimo decennio^{32–35}. Soprattutto, considerando la relazione diretta tra chiralità e proprietà, la capacità di produrre nanotubi con una chiralità ben definita è essenziale per molti tipi di applicazioni, in particolare se si considera che le procedure di separazione post-sintesi possono introdurre difetti nelle strutture ed alterare le loro proprietà. Un approccio promettente consiste nell'utilizzare come precursori delle semisfere di carbonio (sostanzialmente dei fullereni tagliati a metà) su cui il nanotubo può "crescere", oppure dei *nanoanelli* o delle *nanocinture* di carbonio come unità

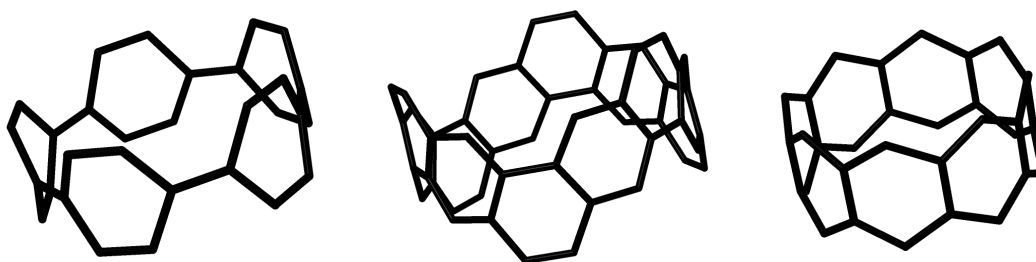


FIGURE A.16: Cicloparafenilene (sinistra), una nanocintura di carbonio (centro) ed un ciclacene (destra).

modello per iniziare la sintesi di un nanotubo con una chiralità ben definita^{33,34,36-39}. Un vantaggio di tale tecnica di fabbricazione “bottom-up” è anche dato dal fatto che la lunghezza finale del nanotubo può essere relativamente ben controllata. Lo sviluppo di questi metodi sintetici è stato essenzialmente reso possibile grazie al grande investimento scientifico nella ricerca di questi strutture “macrocicliche” usate come modello, che sono generalmente molto difficili da ottenere in primo luogo e costituiscono un campo di ricerca molto attivo⁴⁰⁻⁴³. Ad esempio, è stato solo nel 2008 che il cicloparafenilene, l’unità di base di un nanotubo armchair, è stato ottenuto sperimentalmente⁴⁴ (Figura A.16 a sinistra), e nel 2017, la prima nanocintura composta interamente da una serie di anelli benzenoici connessi l’uno all’altro tramite un unico bordo⁴⁵ (Figura A.16 al centro). I ciclaceni invece, l’unità di base dei nanotubi di carbonio zigzag, rimangono ancora una struttura ipotizzata teoricamente ma non ancora ottenuta sperimentalmente⁴⁶ (Figura A.16 a destra). A questo ultimo proposito, è chiaro come la teoria giochi un ruolo importante: la intuizione acquisita dallo studio *in silico* di questi sistemi può fornire preziose informazioni per il loro raggiungimento sperimentale. Durante questa tesi di dottorato, abbiamo contribuito ad espandere questo campo di ricerca svolgendo due progetti focalizzati sui ciclaceni.

Per finire questa parte introduttiva, notiamo come in principio, i nanotubi di carbonio prodotti con il metodo “arc-discharge” risultavano generalmente chiusi alle due estremità (per esempio da due semisfere). Tuttavia, considerando la struttura cava di questi sistemi, risultò chiaro fin da subito il potenziale dei CNTs per applicazioni di chimica “host-guest”, tale per cui un modo per “aprire” i nanotubi alle due estremità e successivamente introdurre una o più molecole “ospite” fu scoperto rapidamente^{64,65}. Da allora, molto lavoro è stato svolto in questa direzione, sia a livello sperimentale che a livello teorico,

ed i CNTs sono stati utilizzati per ospitare una grande varietà di sistemi, tra gli altri i fullereni e metallofullereni^{67,68}, una lunga serie di metalli⁶⁹⁻⁷⁷, molecole energetiche⁷⁸⁻⁸¹ e molti altri ancora. Inoltre, l'incapsulamento di sistemi molecolari all'interno dei nanotubi può alterare le proprietà chimiche delle specie confinate o dare origine a nuove fasi di materiali, portando a risultati inaspettati. In particolare, nuove fasi dell'acqua furono anticipate teoricamente ed osservate sperimentalmente quasi 20 anni fa^{82,83}, ma sono ancora oggi oggetto di studio⁸⁴.

Considerando la loro struttura monodimensionale, i candidati ideali al confinamento dentro nanotubi di carbonio sono molecole lineari, nanofili e sistemi simili. Prove sperimentali di tali strutture confinate è disponibile, ad esempio catene di polietilene confinate in single-wall CNTs sono state riportate una decina di anni fa⁸⁵, o altresì la polimerizzazione del fosforo bianco è stata recentemente osservata avere luogo all'interno della cavità mediante microscopia elettronica a trasmissione⁸⁶. Questo ultimo esempio è illustrativo per due importanti proprietà dei nanotubi: da un lato la parete di un CNT favorisce la formazione di nuovi composti all'interno del nanotubo agendo efficacemente come catalizzatore, d'altra parte invece lo spazio limitato della cavità impedisce alle sostanze confinate di distorcersi eccessivamente, piegarsi o, in alcuni casi, decomporsi. Infatti, delle molte possibili applicazioni proposte per i nanotubi di carbonio, il loro uso come catalizzatori sta avendo crescente successo negli ultimi anni²⁷⁷. Tuttavia, in questa tesi ci siamo concentrati sulla seconda proprietà appena esemplificata, cioè sul fatto che i nanotubi di carbonio costituiscono un sistema ideale per stoccare e stabilizzare al loro interno delle sostanze che altrimenti subirebbero una decomposizione in fase gassosa. Chiaramente, un equilibrio tra i vincoli geometrici e gli effetti catalitici deve essere trovato per rendere questa ultima applicazione possibile, ed in effetti ciò non è sempre stato il caso per i sistemi considerati in questo lavoro.

Ciclaceni

Nella prima parte di questa tesi, è stato condotto uno studio approfondito su diverse proprietà dei ciclaceni sia ad un livello metodologico semi-empirico che *ab initio*. Questi sistemi affascinanti mostrano importanti proprietà elettroniche e magnetiche che li rendono adatti a svariate applicazioni di interesse tecnologico. Oltre a ciò, approfondire

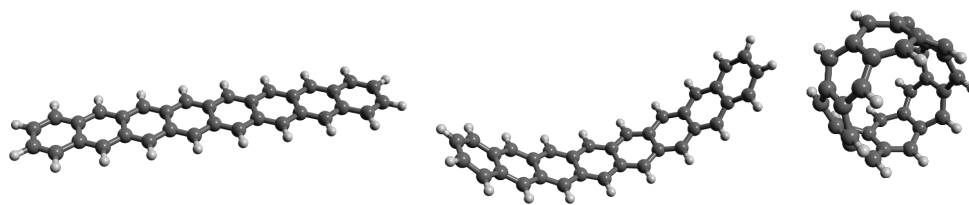


FIGURE A.17: Avvolgimento di un [8]acene lineare in un [8]ciclacene.

la nostra comprensione in queste molecole è anche importante per il loro possibile uso come modelli per la fabbricazione controllata dei nanotubi di carbonio zigzag, una sfida che stiamo affrontando ancora oggi.

I ciclaceni, o più precisamente $[n]$ ciclaceni, sono un tipo di nanostruttura di carbonio ottenuta avvolgendo dei poliaceni lineari formati da n unità esagonali ed unendo le due estremità insieme, come illustrato in Figura A.17. La loro prima apparizione in letteratura fu nel 1954, quando Edgar Heilbronner presentò queste nanostrutture di carbonio in uno studio di ricerca basato sulla teoria di Hückel¹³⁵.

L'inaccessibilità sperimentale dei ciclaceni ha sempre favorito la loro caratterizzazione teorica, come dimostrato dalle numerose investigazioni disponibili in letteratura. Questi lavori sono stati eseguiti principalmente utilizzando approcci semi-empirici alla fine degli anni '90 e agli inizi degli anni 2000 da diversi autori¹⁴⁵⁻¹⁵⁵, mentre più recentemente sono stati effettuati altri studi analitici basati sulla teoria di Hückel o sue varianti¹⁵⁶⁻¹⁵⁹. Oltre a questi risultati, diversi gruppi hanno studiato gli $[n]$ ciclaceni usando metodi *ab initio* che forniscono accesso a dei risultati più quantitativi^{139,140,160-164}.

. L'analisi della maggior parte degli studi semi-empirici si è concentrata sia sui parametri geometrici, così come sul comportamento di semplici proprietà elettroniche come il gap tra HOMO e LUMO in funzione del numero di unità esagonali n . E.g., è stato riscontrato che il divario elettronico diminuisce in modo alternato a seconda della parità di n man mano che vengono aggiunte più unità al sistema. Differenti tipi di metodologie producono valori leggermente diversi, sebbene tutti siano in accordo con la tendenza generale in funzione della dimensione del sistema.

Le varie indagini semi-empiriche sono integrate da un numero di studi *ab initio* utilizzando approcci basati sulla teoria della funzione d'onda e sulla teoria del funzionale della densità (density functional theory in inglese, DFT). Questi lavori erano focalizzati principalmente sul carattere della funzione d'onda nello stato elettronico fondamentale, il gap

energetico della transizione al primo stato eccitato e la natura radicale della molecola in funzione alla sua dimensione.

Sulla base dei calcoli DFT, Choi and Kim¹³⁹ ha riportato lo split fra gli stati di singoletto e tripletto, le lunghezze del legame carbonio-carbonio e le proprietà magnetiche dei ciclaceni in funzione del numero di anelli. Un secondo lavoro basato sulla DFT è apparso poco dopo¹⁴⁰, anche riportando il gap fra lo stato fondamentale e il primo stato eccitato in funzione di n . In entrambi i casi, gli autori hanno trovato un gap debolmente crescente al crescere della dimensione del sistema, ed in un caso hanno riportato uno stato fondamentale di tipo tripletto. Tuttavia, alcuni anni dopo, calcoli basati su metodi di funzione d'onda multireference hanno prodotto risultati in controtendenza rispetto a quelli ottenuti tramite un approccio DFT¹⁶⁰. In particolare, è stato appurato che lo stato fondamentale dei ciclaceni è un singoletto a guscio aperto indipendentemente dalla dimensione del sistema. Questi risultati sono stati poi ulteriormente ampliati e confermati da Sadowsky et al.¹⁶¹, dimostrando che il divario energetico crescente fra singoletto e tripletto era il risultato di una instabilità di singoletto dello stato fondamentale, facendo fallire l'approccio DFT. Uno studio recente da parte di Wu et al.¹⁶² ha esplorato una serie di proprietà elettroniche degli $[n]$ ciclaceni basandosi sulla metodologia TAO-DFT, trovando dei valori in accordo con quelli risultanti da metodi *ab initio* di alto livello. In questo ultimo lavoro, oltre alla conferma della natura dello stato elettronico più basso, il comportamento del gap è stato calcolato per un gran numero di dimensioni del sistema. Di seguito riassumeremo il nostro contributo alla ricerca su questo tipo di sistema.

In una prima indagine, le espressioni analitiche degli autovalori e degli autovettori sono state ottenute per i ciclaceni considerati nella approssimazione tight-binding. Sulla base di queste informazioni, è stato possibile derivare le espressioni in forma chiusa delle bande di energia, la densità degli stati, la componente assiale dei tensori di spread totale della posizione (total position spread in inglese, TPS) e polarizzabilità.

Il bandgap scompare poiché due bande diverse si toccano al livello di Fermi; per questo motivo la densità degli stati mostra la presenza di una singolarità di Van Hove. La componente assiale dello spread della posizione totale per elettrone rimane finito per $n \rightarrow \infty$, in accordo con la estensione finita del sistema in questa direzione cartesiana.

Sorprendentemente tuttavia, la componente della polarizzazione per elettrone corrispondente risulta invece divergere, un comportamento che si trova comunemente solo nel caso di sistemi conduttori. In generale una divergenza della polarizzabilità per elettrone è associata ad un comportamento simile dallo spread della posizione totale. A nostra conoscenza, questo è l'unico caso in cui le due quantità non si comportano nello stesso modo e sosteniamo che la ragione è probabilmente dovuta alla mancata descrizione della repulsione elettrone–elettrone all'interno della approssimazione tight-binding, che gioca un ruolo importante nella rimozione della degenerazione al livello di Fermi. Ciò è supportato da dei calcoli CASSCF della polarizzabilità statica per alcuni piccoli sistemi. La componente assiale del TPS è stata anche calcolata a partire dalla funzione d'onda CASSCF per sistemi con $n = 6, 8, \dots, 22$, mostrando chiaramente lo stesso comportamento lineare asintotico previsto dalla approssimazione tight-binding, nonostante il limite termodinamico sia molto distante.

Non siamo stati in grado di ottenere espressioni analitiche per le componenti planari di entrambi i tensori (TPS e polarizzabilità), tuttavia, un calcolo numerico non mostra alcun segno di divergenza di queste quantità. Pertanto, si prevede che il sistema sia, a questo livello di descrizione, un isolante. Questo risultato è di particolare interesse poiché questo materiale ha un bandgap uguale a zero assieme ad una densità degli stati non-nulla a livello di Fermi, tipicamente segno di comportamento metallico. Tuttavia, le proprietà calcolate nella nostra indagine di ricerca dipendono dai dettagli geometrici del sistema che lo caratterizzano invece come isolante, ovvero chiudendo un poliacene lineare e formando così un anello sembra che il tipo di materiale cambi da metallico a non metallico.

In un secondo studio su queste molecole abbiamo presentato i risultati ottenuti utilizzando le metodologie cosiddette *first principles*. In particolare, il gap energetico vertical fra gli stati di singoletto e tripletto ed il carattere poliradicale degli $[n]$ ciclaceni sono stati studiati in funzione della dimensione del sistema in maniera sistematica. Si è riscontrato che il gap diminuisce esponenzialmente rispetto al numero di unità esagonali che formano il ciclacene e tende ad un valore finito nell'ordine di un decimo di eV per il limite $n \rightarrow \infty$. Abbiamo proposto un criterio per selezionare dinamicamente lo spazio attivo (active space in inglese, AS) in funzione di n , sulla base della indagine svolta nella approssimazione tight-binding discussa precedentemente. Questo approccio ha permesso

un trattamento equilibrato della correlazione elettronica *statica* per tutta la serie di dimensioni considerate. I risultati *ab initio* presentati sono stati confrontati con quelli precedenti riportati in letteratura, da un lato confermando questi ultimi e dall'altro estendendoli ad un numero maggiore di sistemi. In particolare, la natura di singoletto a guscio aperto dello stato fondamentale elettronico è stata confermata fermamente. Il carattere poli-radicalico dei ciclaceni è stato studiato analizzando i numeri di occupazione degli orbitali naturali così come un indicatore basato su questi ultimi, si è trovato un chiaro segno di aumento del carattere radicalico al crescere della dimensione del sistema. Sono stati anche eseguiti calcoli utilizzando uno spazio attivo minimo di due elettroni in due orbitali e la spiegazione del fallimento di questo AS è stata fornita attraverso una scrupolosa analisi dei contributi alla energia di correlazione da parte degli integrali molecolari. Con una scelta *errata* di AS, lo stato fondamentale del sistema tende ad essere un singoletto a guscio chiuso anziché a guscio aperto con l'aumentare delle dimensioni del sistema. Oltre ai risultati forniti, questo studio ha dimostrato didatticamente la importanza dello spazio attivo per questo tipo di strutture ed ha proposto un nuovo criterio per la sua selezione sistematica.

Concludendo, sebbene gli $[n]$ ciclaceni non siano ancora stati sintetizzati, rimangono un terreno fertile per entrambi ricercatori teorici e sperimentali, e la loro indagine fornisce un mezzo per aumentare la conoscenza di base dei sistemi di idrocarburi in generale.

Confinamento in Nanotubi di Carbonio

Nella seconda parte della tesi sono state effettuate diverse indagini di ricerca riguardanti l'incapsulamento di clusters puri di azoto e catene di berillio all'interno di nanotubi di carbonio. La struttura cava dei CNTs e la bassa reattività della parete interna forniscono un ambiente ideale per confinare una ampia varietà di sistemi, rendendoli adatti a differenti applicazioni. Le molecole formate unicamente di azoto hanno la proprietà eccezionale di immagazzinare una incredibile quantità di energia chimica nei loro legami covalenti, rendendole una possibile fonte di energia alternativa. Tuttavia, questi sistemi soffrono in generale di una elevata instabilità. In questa prospettiva, i nanotubi di carbonio sono stati proposti come dispositivi di stoccaggio e stabilizzazione col fine di proteggere le speci azotate dal rilascio della loro energia attraverso la decomposizione in

molecole di N_2 . Seguendo lo stesso principio, i nanotubi di carbonio sono stati studiati per il possibile incapsulamento come di altri materiali, in particolare le catene di berillio. Le molecole lineari Be_n , caratterizzate da due orbitali magnetici singolarmente occupati, si contraddistinguono per l'accoppiamento antiferromagnetico dello stato fondamentale. Particolarmente interessante è il fatto che questo accoppiamento risulta essere influenzato da interazioni non covalenti con nanostrutture di carbonio, suggerendo un possibile modo di controllo della natura dello stato fondamentale.

Anione Azoturo

Nella ricerca di fonti energetiche alternative e rispettose dell'ambiente, una classe promettente di sistemi è quella delle molecole composte unicamente dall'azoto^{192,193}. Comprendone il 78% del totale, l'azoto è la specie più abbondante presente nella atmosfera terrestre e quindi anche ampiamente accessibile. È praticamente presente sotto forma di N_2 di-molecolare, che è di gran lunga la forma più stabile di questo elemento ed è considerata innocua per l'ambiente. Il motivo per il quale l'azoto appare in natura praticamente unicamente come N_2 è dovuto alla peculiare energetica del suo legame chimico: il triplo legame covalente N-N è caratterizzato da una energia di 229 kcal/mol, quella del doppio legame da 100 kcal/mol ed il legame singolo da 38.4 kcal/mol¹⁹². Termodinamicamente, tre volte la energia di un singolo legame o una volta e mezza il doppio legame non raggiungono la stabilità energetica data dal triplo legame, così spiegando la ubiquità di N_2 . Di conseguenza, questa distribuzione di energia è tale che gli allotropi di azoto a legame singolo e doppio hanno il potenziale di liberare una grande quantità di energia se decomposto in azoto molecolare. Per questo motivo, i clusters di azoto puro sono considerati materiali ad alta densità di energia (high energy-density material in inglese, HEDM)^{192,193}.

La molecola formata da più di due atomi di azoto e conosciuta dal maggior tempo è l'anione azoturo, con formula chimica N_3^- , mostrato in Figura A.18 e noto sin dalla fine del diciannovesimo secolo¹⁹⁴. Ci sono voluti più di 100 anni per allargare questa famiglia con la sintesi del catione N_5^+ (noto anche con il nome di pentazenio)¹⁹⁵ nel 1999 (mostrato in Figura A.19) che ha rinnovato l'interesse per questa classe di sistemi stimolando la immaginazione di tanti ricercatori, intravedendo la possibilità di accoppiare N_3^- e N_5^+ e formare un cristallo ionico di puro azoto¹⁹⁶⁻¹⁹⁸. Ciononostante, i tentativi sperimentali di

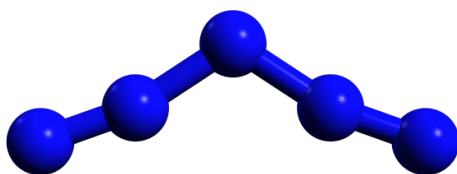


FIGURE A.18: Anione azoturo.

stabilizzare i due ioni hanno avuto esito negativo¹⁹⁹, evidenziando il principale ostacolo alla realizzazione di allotropi di azoto puro, cioè la loro intrinseca instabilità rispetto alla decomposizione in N_2 .

Più recentemente, il confinamento molecolare è stato esplorato come una possibile strategia per superare questo problema. Incapsulando una catena di azoto polimerico all'interno di un CNT, è stato calcolato grazie a simulazioni di dinamica molecolare che la specie azotata rimane stabile fino ad alte temperature, preservando, almeno in teoria, la struttura molecolare e fornendo allo stesso tempo un metodo di stoccaggio^{79,80,200}. Ulteriori indagini teoriche basate sulla stessa idea hanno mostrato che la stessa catena di azoto risulta egualmente stabile in nanotubi di carburo di silicio e nitruro di boro²⁰¹⁻²⁰³. Tramite un approccio simile, uno studio DFT sull'incapsulamento di clusters di azoto di diverse dimensioni in fullereni C_{60} , predice strutture stabili per molecole formate fino a 13 atomi prima che queste inizino ad essere chimicamente legate alla "gabbia" confinante²⁰⁴.

Da una prospettiva sperimentale, una specie anionica di formula N_8^- assorbita sul lato interno della parete di un nanotubo di carbonio è stata osservata a condizioni ambiente²⁰⁵; un risultato che è stato recentemente corroborato dalla sintesi della fase cubic gauche (cg-N) dell'azoto avvenuta con successo su un substrato composto da nanotubi di carbonio a delle condizioni, questa volta, prossime a quelle ambiente²⁰⁶. In questo ultimo lavoro, oltre alla presenza di picchi distintivi negli spettri Raman ed infrarossi corrispondenti alla fase cg-N, immagini ad alta risoluzione ottenute tramite microscopia elettronica a trasmissione mostrano chiaramente le strutture di azoto incapsulate all'interno dei CNTs.

FIGURE A.19: Catione N_5^+ .

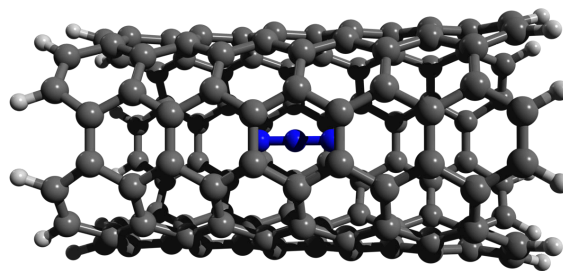


FIGURE A.20: Anione azoturo confinato in un CNT.

Oltre al numero relativamente grande di studi sulle catene di azoto, non si contano molte altre investigazioni di sistemi azotati considerati in confinamento spaziale. In particolare, oltre alla grande quantità di letteratura disponibile sulle caratteristiche spettroscopiche dello ione azoturo in fase cristallina o gassosa²⁰⁷⁻²¹⁵ e solvattato²¹⁶⁻²²⁸, esso non è mai stato studiato in un ambiente a spazio ristretto. Considerando che lo ione N_3^- rappresenta spesso un precursore nella sintesi di molecole energetiche (per esempio la summenzionata sintesi di fase cg-N sul substrato di CNTs parte dall'azoturo di sodio) o appare come una struttura intermedia durante la reazione di dissociazione di sistemi di azoto puri più grandi (per esempio nella dissociazione dello ione N_5^-), è certamente di grande interesse studiare il suo comportamento in un ambiente circoscritto come quello fornito dai nanotubi, ed in particolare per capire il tipo di interazioni che sussiste fra i due frammenti. A tal fine, il confinamento dell'anione azoturo all'interno di nanotubi di carbonio di diverse lunghezze e diametri è stato studiato nel corso di questa tesi. Un esempio di questo tipo di sistema è mostrato in Figura A.20. Un grande sforzo è stato dedicato allo studio *ab initio* di questo sistema, fornendo in primo luogo importanti informazioni sull'assorbimento dello ione, così come la natura della interazione fra i due frammenti o gli effetti di rilassamento dell'intero sistema complesso. In secondo luogo, è stato intrapreso un approccio più sistematico, in cui gli effetti delle dimensioni finite sono stati studiati basandosi su calcoli coupled cluster (CC) al fine di ottenere energie di riferimento con un buon grado di accuratezza.

Basandosi sulle conoscenze acquisite con i calcoli statici e confrontandole con il riferimento *ab initio*, un nuovo potenziale intermolecolare che modella la interazione non covalente tra N_3^- e CNTs è stato presentato. Lo stesso è stato successivamente implementato nel programma di dinamica molecolare (molecular dynamics in inglese, MD) DL POLY 4.08^{229,230}, che ora consente lo studio della dinamica degli ioni confinati in nanotubi di

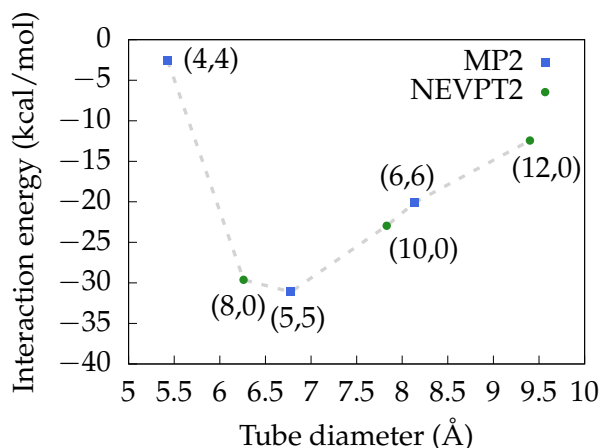


FIGURE A.21: Energie di interazione non rilassate in funzione del diametro del nanotubo.

carbonio di qualsiasi dimensione e tipo.

Come accennato in precedenza, in una prima parte l'accento è stato posto su una indagine *ab initio* dell'anione azoturo confinato all'interno di nanotubi di carbonio. È stato trovato che lo ione N_3^- viene stabilizzato energeticamente da nanotubi di diametri compresi tra ≈ 5.5 Å e ≈ 9.5 Å (vedi Figura A.21), mostrando nel caso più estremo una interazione di -32.31 kcal/mol ottenuta con un CNT(5,5), avente diametro pari a ≈ 6.78 Å. La analisi delle strutture rilassate, le cariche atomiche parziali ed il potenziale elettrostatico molecolare ha rivelato la natura della interazione, suggerendo una spiegazione dei risultati trovati. In particolare, sosteniamo che la specie ospite N_3^- venga stabilizzata da interazioni elettrostatiche e di induzione con la parete del nanotubo, quest'ultima sottoposta ad una notevole polarizzazione dovuta alla presenza di atomi di idrogeno utilizzati per saturare le estremità del CNT. La dimensione della cavità di un CNT(5,5) è tale per cui il frammento N_3^- si allinea perfettamente al centro del nanotubo e parallelo al suo asse, risultando in una distanza di assorbimento dalla sua parete ottimale in tutte le direzioni, spiegando così la forte interazione osservata.

Un punto a sfavore dell'utilizzo di sistemi a dimensione finita per modellare i nanotubi di carbonio è la loro dipendenza intrinseca alla lunghezza, particolarmente nel caso in cui si considerano molecole cariche interagenti. Pertanto, è stata condotta una indagine

approfondita su questa dipendenza, questa volta aumentando anche il livello della teoria. Il motivo era duplice, da un lato si voleva confermare i risultati ottenuti precedentemente e, dall'altro, l'obiettivo era quello di ottenere energie di riferimento di grande accuratezza. Specificatamente, l'approccio utilizzato per questo studio ha permesso di ottenere energie di interazione di accuratezza senza precedenti, utilizzando uno schema combinato di estrapolazione e fitting basato su dei risultati ottenuti coi metodi RI-SCS-MP2 e DLPNO-CCSD(T) insieme ad un grande set di base di qualità triple- ζ .

Razionalizzando i risultati ottenuti a livello *ab initio*, abbiamo presentato un potenziale intermolecolare in grado di descrivere la interazione dell'anione azoturo con nanotubi di carbonio arbitrari. Questo modello si basa sulla separazione delle tre componenti che contribuiscono alla interazione, vale a dire le forze di Van der Waals (VdW), gli effetti di induzione e la azione elettrostatica. Le interazioni VdW sono state modellate secondo il potenziale Improved Lennard-Jones (ILJ)¹³³, per gli effetti di induzione abbiamo proposto un nuovo potenziale basato sulla forma generale di un dipolo indotto dovuto alla presenza di un campo elettrico esterno, mentre la componente elettrostatica è stata rappresentata dalla normale legge di Coulomb. La funzione potenziale totale è in grado di riprodurre le energie di interazione DLPNO-CCSD(T) con un errore nell'ordine di poche kcal/mol e fornisce inoltre un secondo metodo di analisi dei risultati; ovvero ispezionando i contributi dei singoli componenti del potenziale. Quest'ultimo approccio risulta essere molto intuitivo e consente una esplorazione "pedestre" delle caratteristiche importanti della superficie di energia potenziale che altrimenti sarebbe difficile da affermare. È interessante notare come la dipendenza rispetto alla distanza dei vari componenti è evidente. Questa indagine sistematica sulla energia di interazione in funzione della lunghezza del CNT pone in risalto come i contributi da parte delle interazioni di VdW e di induzione convergono rapidamente in funzione della lunghezza del nanotubo, mentre il comportamento generale della superficie è dettato dalla forza elettrostatica *a lungo raggio*.

Le funzioni potenziali intermolecolari proposte, in particolare i potenziali ILJ e di induzione, sono stati implementati nel programma di dinamica molecolare DL POLY 4, con il quale sono state effettuate una serie di simulazioni in dimostrazione del suo corretto funzionamento.

Questa indagine approfondita sull'anione azoturo ha contribuito a far progredire la comprensione di questa molecola ed più in generale delle interazioni anione-CNT. Sebbene lo ione N_3^- sia una delle molecole di azoto pure più stabili, i risultati ottenuti qui sono interessanti nel contesto di stoccaggio di energia alternativa poiché l'azoturo può essere utilizzato come precursore per la sintesi di clusters di azoto più grandi. Inoltre, questo lavoro è stato anche la motivazione per la implementazione di un accurato potenziale intermolecolare all'interno del software DL POLY 4, che può ora essere utilizzato per la simulazione di altri sistemi.

Catione N_5^+ e Catene N_8

Oltre all'anione azoturo discusso finora, esistono altre molecole formate puramente di azoto che sono di grande interesse scientifico. In particolare, il catione N_5^+ , isolato con successo nel 1999 da Christie et al.¹⁹⁵, è un buon candidato per essere combinato con l'anione azoturo per portare alla formazione della molecola neutra ed altamente energetica N_8 . Negli ultimi 20 anni, diversi gruppi di ricerca hanno pubblicato lavori di ricerca sia teorici che sperimentali sui singoli ioni N_3^- , N_5^+ e N_5^- ²⁵⁵⁻²⁵⁹ o composizioni fra essi^{196-199,260}. Inoltre, notiamo che anche la superficie di energia potenziale delle specie N_8 è stata soggetta a diversi studi teorici approfonditi ed estensivi²⁶¹⁻²⁶⁶. Nel 2001, Fau and Bartlett¹⁹⁶ ha suggerito alla luce di calcoli *ab initio* che il prodotto N_8 risultante dalla combinazione degli ioni N_5^+ e N_3^- sarebbe molto probabilmente troppo instabile per esistere a condizioni ambiente, fatto che è stato confermato sperimentalmente nel 2004 da Dixon et al.¹⁹⁹. Tuttavia, nello stesso lavoro, fu suggerito che un simile allotropo di azoto potrebbe in principio esistere sotto forma di materiale in stato solido, dove le forze coesive derivanti dalla struttura cristallina eviterebbero la sua decomposizione. Dieci anni più tardi, nel 2014, una tale conformazione cristallina formata da due isomeri del N_8 è stata infatti riportata da Hirshberg et al.²⁶⁷, sulla base di simulazioni DFT.

Il confinamento del catione pentazenio all'interno di nanostrutture di carbonio non è mai stato studiato, nonostante il buon numero di lavori teorici che riportano dell'incapsulamento di una catena polimerica di azoto in diversi tipi di nanotubi^{79,80,200,202}. Di seguito presentiamo il lavoro svolto in questa direzione come parte di questa tesi di dottorato.

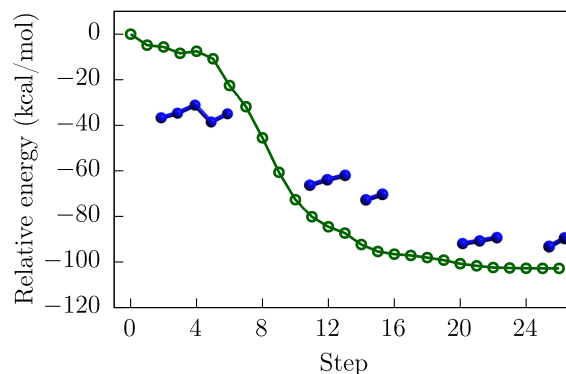


FIGURE A.22: Superficie di energia potenziale della decomposizione dell'ione N_5^+ confinato in un CNT(5,5). Alcune geometrie intermedie sono mostrate lungo la curva senza il nanotubo per una miglior rappresentazione.

Seguendo l'approccio usato finora, è stata condotta una investigazione sul confinamento di altre due forme pure di azoto, in particolare sulla specie cationica N_5^+ e la catena neutrale N_8 . Per il primo dei due sistemi, nonostante la favorevole energia di interazione fra lo ione ed il nanotubo nel caso in cui gli effetti di deformazione non vengono considerati, è stato trovato che la molecola confinata nella cavità si decompone come conseguenza di un doppio trasferimento di carica dalla nanostruttura al catione. Come già riportato in letteratura¹⁹⁹ e confermato qui, un singolo elettrone è sufficiente per iniziare la reazione di decomposizione che avviene senza alcuna barriera di attivazione. Secondo i calcoli effettuati, il primo trasferimento si verifica perché la affinità elettronica del pentazenio è maggiore del potenziale di ionizzazione del nanotubo di carbonio e la cessione dell'elettrone da un frammento all'altro risulta quindi energeticamente conveniente. La superficie di energia potenziale del processo di decomposizione può essere apprezzata alla Figura A.22. La prima cessione di carica porta successivamente ad un secondo trasferimento, in cui la forma radicale intermedia N_3 guadagna un altro elettrone dal nanotubo con i conseguenti prodotti $N_3^- + N_2$.

Una possibile soluzione per aggirare questa decomposizione potrebbe essere la aggiunta di un controione nella cavità del CNT, competendo con il processo di trasferimento di carica e idealmente stabilizzando il catione N_5^+ . A tal fine, abbiamo svolto alcune indagini preliminari sull'incapsulamento della catena N_8 all'interno di un CNT(5,5), considerandola come il risultato della reazione $N_3^- + N_5^+ \rightarrow N_8$. Questa reazione non è stata presa

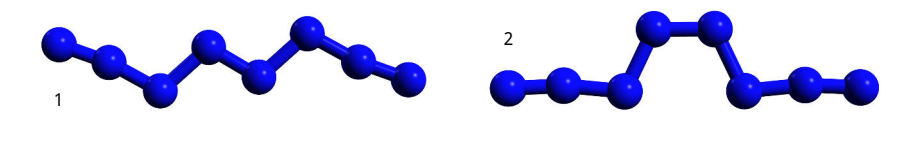


FIGURE A.23: Due isomeri stabili della molecola N_8 .

in considerazione esplicitamente, ma invece ci siamo concentrati sulla fattibilità di incapsulare il prodotto N_8 , che potrebbe comunque essere formato in diversi modi e non strettamente dalla reazione dell'azoturo con il pentazeno.

I risultati ottenuti mostrano che due isomeri lineari della molecola N_8 considerati stabili in fase gassosa secondo calcoli *ab initio* (rappresentati in Figura A.23), sono anche stabili all'interno del nanotubo, mostrando una forte energia di interazione. Gli effetti del confinamento spaziale all'interno della cavità favoriscono l'isomero più lineare tra i due, aumentando la differenza di energia relativa di qualche kcal/mol.

In fase gassosa esistono due canali di decomposizione per questi isomeri che sono stati considerati anche nella nostra indagine. Sorprendentemente, tutti tranne uno degli stati di transizione conosciuti non sono rimasti validi quando considerati confinati all'interno del nanotubo. Sostieniamo che ciò sia dovuto ad effetti sterici, poiché solo la struttura più lineare è stata identificata nella cavità, mentre tutti gli altri hanno generato punti flessi di ordine superiore ad uno (dunque non corrispondenti a degli stati di transizione). Ciò è corroborato dalla più forte energia di interazione osservata per l'isomero più lineare. Inoltre, considerando i profili energetici ottenuti per l'azoturo, risulta chiaro come la stretta vicinanza delle pareti alla specie confinata nella cavità del CNT(5,5) ha un forte impatto sulla loro libertà geometrica.

Nonostante questo sia ancora un lavoro di ricerca aperto, i risultati presentati suggeriscono che gli effetti sterici dovuti allo spazio ristretto disponibile nella cavità può chiudere alcuni canali di reazione e favorire determinati isomeri rispetto ad altri. In questo contesto, il diametro del nanotubo può essere utilizzato come parametro regolabile che ne fornisce un certo grado di controllo sulla molecola incapsulata. In particolare, l'obiettivo è aumentare la energia di attivazione o addirittura chiudere completamente il canale di reazione che porta alla decomposizione, favorendo in tal modo la stabilità di isomeri selezionati all'interno della cavità.

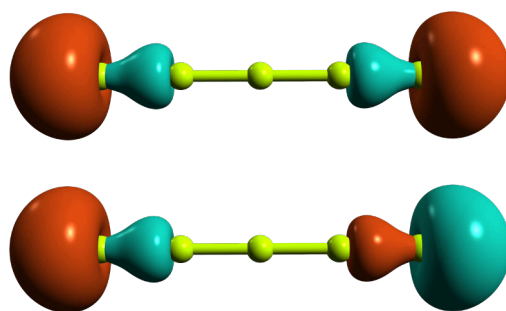
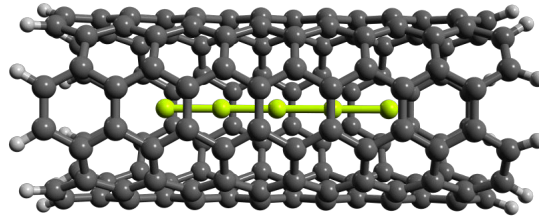


FIGURE A.24: Orbitali magnetici delle catene di berillio.

Catene di Berillio

Le catene lineari di berillio sono una particolare conformazione dei sistemi Be_n per cui delle proprietà magnetiche interessanti sono state riportate in seno ad una serie di calcoli teorici basati su metodi di funzione d'onda^{269–272}. Condividendo due elettroni ciascuno, gli atomi di berillio reagiscono formando singoli legami covalenti, risultando in un sistema con geometria lineare che lascia due elettroni spaiati su entrambi gli atomi terminali. È stato riportato da uno studio teorico basato su calcoli *ab initio* che due orbitali singolarmente occupati, mostrati in Figura A.24, sono localizzati alle estremità dando origine ad uno stato fondamentale che è accoppiato antiferromagneticamente, ma con uno stato di tripletto ferromagnetico molto vicino in energia. Inoltre, in un seguente studio da parte degli stessi autori è stato scoperto che questo accoppiamento viene alterato quando la catena è deposita su una superficie di grafene, mostrando una chiara dipendenza rispetto alla distanza dalla superficie²⁷³. In particolare, lo stato fondamentale del sistema cambia da antiferromagnetico a ferromagnetico per un certo intervallo di distanze. Le catene Be_n sembrano quindi avere proprietà magnetiche che possono essere controllate da interazioni non covalenti, con potenziali applicazioni come magneti molecolari.

Tuttavia, la geometria lineare della catena non rappresenta un minimo globale della superficie di energia potenziale del sistema Be_n , che tende invece a piegarsi in una conformazione più compatta ed energeticamente più favorevole²⁷⁴. La deposizione su una superficie potrebbe stabilizzare la struttura lineare, tuttavia, i nanotubi di carbonio forniscono certamente un ambiente più adatto per preservare la loro geometria come già suggerito nell'articolo originale²⁷³ (una immagine di questo sistema è mostrata in Figura A.25). C'è anche un secondo vantaggio dovuto all'incapsulamento delle catene all'interno dei

FIGURE A.25: Be₅ confinato in un CNT.TABLE A.3: Accoppiamento magnetico J in funzione del diametro del CNT e la lunghezza della catena. Tutti i valori sono dati in meV.

Host	Be ₄	Be ₅	d [Å]
CNT(5,4)	-4.97	+0.72	3.06
CNT(5,5)	-14.54	-6.07	3.39
CNT(6,5)	-19.64	-2.83	3.74
CNT(6,6)	-20.50	-3.56	4.07
isolata	-16.37	-2.50	∞

CNTs, cioè che l'accoppiamento magnetico del sistema ibrido può essere regolato in base al diametro del nanotubo che lo racchiude.

Tenendo conto di questi due punti, lo scopo di questa indagine di ricerca svolta nell'ambito della tesi era quindi di esplorare gli effetti subiti dalle catene di berillio posizionate all'interno di nanotubi di carbonio di diversi diametri per mezzo di metodi di funzioni d'onda multireference e teoria del funzionale della densità. Da una parte abbiamo calcolato la energia relativa delle catene di berillio rispetto alle conformazioni più compatte, e dall'altra abbiamo focalizzato la attenzione sull'accoppiamento magnetico delle catene in funzione sia della lunghezza della catena che del diametro del nanotubo.

Sono state riscontrate indicazioni che il valore di J (la costante di accoppiamento magnetico) tende sempre più verso zero a causa della interazione con nanotubi di diametro sempre più stretto, come mostrato in Tabella A.3. Tuttavia non è chiaro se, per CNTs sufficientemente stretti, il sistema composito diventi ferromagnetico. Il comportamento di J rispetto alla lunghezza del nanotubo è stato testato per un numero selezionato di casi, ciononostante, al fine di mantenere una sufficiente accuratezza della proprietà calcolata, non è stato possibile indagare su nanotubi più lunghi in modo sistematico. Sarebbe chiaramente di grande interesse studiare anche catene più lunghe, ma come è stato già il caso per Be₅, la lunghezza del nanotubo sembra essere un fattore importante, tale per

cui CNTs più lunghi risultano necessari, ma computazionalmente inaccessibili. Sottolineiamo che in futuro si dovrebbe prendere in considerazione il rilassamento del sistema complesso per permettere alla catena di uscire dall'asse principale del nanotubo. Questo è una preoccupazione primaria, tuttavia rimane un problema molto difficile da affrontare dal punto di vista metodologico.

Conclusioni

Finalizzando la discussione, durante questa tesi di dottorato sono stati svolti numerosi lavori che hanno coinvolto nanotubi di carbonio e strutture correlate. La versatilità di questi sistemi è una delle loro caratteristiche principali e ciò è stato dimostrato dai risultati proposti qui.

I ciclaceni, che sono formalmente nanotubi di carbonio zigzag composti da una singola unità, sono stati studiati con metodi semi-empirici ed *ab initio*, evidenziando le loro interessanti proprietà elettroniche e le sfide che pongono agli approcci teorici moderni. L'avanzamento nella comprensione della loro struttura elettronica è essenziale per valutare il loro potenziale in varie applicazioni tecnologiche e per fornire informazioni preziose alla loro sintesi sperimentale, che deve ancora essere raggiunta. Inoltre, oltre ai risultati ottenuti dalle indagini svolte, questa tesi ha dimostrato come un approccio semi-empirico abbinato ad un trattamento di livello teorico superiore come quello *ab initio* fornisce un potente strumento per comprendere e caratterizzare un sistema molecolare da diversi punti di vista ed a diversi livelli di dettaglio.

Grazie alla presenza della cavità nei nanotubi di carbonio, una delle potenziali applicazioni per questi sistemi è la chimica "host-guest". Il confinamento di qualsiasi tipo di molecola all'interno di tali nanostrutture ha diversi effetti che possono essere sfruttati in un gran numero di modi e per svariate applicazioni. Durante questa tesi, è stata considerata una classe di molecole ad alto contenuto energetico ed è stato studiato il loro incapsulamento all'interno di nanotubi di carbonio. Da un lato, la motivazione alla base di questa linea di ricerca è stata il potenziale delle molecole di azoto puro come fonti alternative di energia pulita, ma dall'altro, il lavoro era anche guidato da un puro interesse teorico, in particolare riguardo la caratterizzazione del tipo di interazioni coinvolte con le

nanostrutture di carbonio e come queste possono essere modellate in maniera accurata, ma efficace dal punto di vista computazionale.

I risultati ottenuti durante l'intero periodo di dottorato riguardano essenzialmente tre sistemi, l'anione azoturo, il catione pentazenio e la molecola neutra N_8 . In tutti i casi abbiamo studiato gli effetti esercitati dal nanotubo sul sistema confinato, concentrandoci su aspetti diversi a seconda del sistema. Nello specifico, nel caso dell'azoturo, la stabilità e la rigidità complessiva di entrambi il nanotubo e le specie ionica hanno fornito una buona base per lo sviluppo di un potenziale intermolecolare e la sua implementazione in un programma di dinamica molecolare. Inoltre, questo sistema è stato usato come esempio per dimostrare la fattibilità nel modellare accuratamente diversi tipi di interazione dal punto di vista della meccanica classica. Il lavoro che ha coinvolto il catione pentazenio è stato centrato sul processo di rilassamento del sistema complesso, un caso chiaro in cui l'effetto del nanotubo risulta essere tremendo e distruttivo. Tuttavia, i risultati ottenuti con lo ione N_5^+ hanno fornito un punto di partenza per il successivo studio della catena N_8 , un sistema che ha suscitato molto interesse in passato e che ancora oggi è soggetto di indagine da diversi gruppi di ricerca. In questo ultimo caso, i risultati preliminari mostrano la importanza del confinamento spaziale nel controllo del comportamento della molecola e suggeriscono una via per il suo stoccaggio.

Nonostante sia stato strettamente teorico, il lavoro svolto in questi tre anni aiuta a far avanzare la comprensione delle interazioni ione-CNT e fornisce una solida base per le indagini future.

Al posto di agire semplicemente come dispositivi di stoccaggio, i nanotubi di carbonio possono formare interessanti sistemi ibridi se combinati ad altri tipi di molecole. Questo è il caso delle catene di berillio, le cui proprietà magnetiche possono essere sfruttate in diversi modi, ma la loro geometria lineare ne limita l'applicabilità pratica. Tuttavia, se inseriti all'interno della cavità dei nanotubi di carbonio, la loro struttura può essere, in linea di principio, preservata grazie alla conformazione lineare del CNT ed allo spazio limitato, evitando così che la catena si pieghi in isomeri energeticamente più bassi. Inoltre, le interazioni deboli tra la struttura di carbonio e la catena sono tali che le proprietà elettroniche della catena possono essere modulate in funzione del diametro del nanotubo che lo racchiude. Abbiamo dimostrato con uno studio teorico che l'accoppiamento magnetico dei

due elettroni spaiati della catena è influenzato dalla presenza del sistema circostante, ed in alcuni casi estremi sembra cambiare il carattere dello stato fondamentale da antiferromagnetico a ferromagnetico. Tuttavia, alla luce delle approssimazioni utilizzate in questa indagine, non è ancora possibile fornire una prova conclusiva di questo comportamento. Ciononostante, i nanotubi di carbonio hanno dimostrato ancora una volta di essere un sistema straordinario che può essere sfruttato in molti modi.

Accanto ai principali progetti riguardanti i nanotubi di carbonio, sono stati effettuati alcuni altri studi durante il corso di questa tesi di dottorato. In particolare, è stata esplorata una nuova strategia per eseguire calcoli molecolari, nella quale si propone un nuovo tipo di set di base per la espansione della funzione d'onda. In pratica, la idea è di rimanere nel dominio delle espansioni basate su orbitali di tipo gaussiano, sfruttando così lo sviluppo e gli strumenti consolidati negli ultimi 50 anni per questa tipologia di calcoli, ma unendo una descrizione con funzioni centrate sugli atomi con un approccio basato su funzioni distribuite nello spazio attorno e nel mezzo degli atomi costituenti il sistema molecolare. Questo lavoro ha portato alla implementazione di un nuovo programma in grado di calcolare integrali molecolari fra orbitali di tipo gaussiano in posizioni arbitrarie, che è stato usato per ottenere i risultati numerici di questa indagine di ricerca.

Oltre a questo lavoro, lo studio da una prospettiva diversa della localizzazione di Wigner, un problema tanto vecchio quanto affascinante, è stato realizzato in collaborazione con altri membri del laboratorio di Tolosa. Da notare che questo lavoro è stato anche basato sull'approccio appena citato, cioè utilizzando delle funzioni gaussiane distribuite nello spazio per espandere la funzione d'onda del sistema.

Riassumendo, in questa tesi di dottorato sono stati usati diversi approcci per studiare differenti problemi riguardanti i nanotubi di carbonio. Da un lato, la motivazione è stata il genuino interesse per le possibili applicazioni tecnologiche di questi sistemi, ma dall'altro c'è stata anche una buona porzione di curiosità metodologica che ha portato allo sviluppo di nuovi strumenti e tecniche per affrontare vecchi e nuovi problemi nel campo della chimica teorica e computazionale.